

Electronic Thesis and Dissertation Repository

10-28-2016 12:00 AM

Behavior of Fire-Exposed RC Frames Before and After Jacketing

M. Monir M. Ajan Alhadid, *The University of Western Ontario*

Supervisor: Maged Youssef, *The University of Western Ontario*

A thesis submitted in partial fulfillment of the requirements for the Doctor of Philosophy degree in Civil and Environmental Engineering

© M. Monir M. Ajan Alhadid 2016

Follow this and additional works at: <https://ir.lib.uwo.ca/etd>



Part of the [Civil Engineering Commons](#), and the [Structural Engineering Commons](#)

Recommended Citation

Ajan Alhadid, M. Monir M., "Behavior of Fire-Exposed RC Frames Before and After Jacketing" (2016). *Electronic Thesis and Dissertation Repository*. 4300.
<https://ir.lib.uwo.ca/etd/4300>

This Dissertation/Thesis is brought to you for free and open access by Scholarship@Western. It has been accepted for inclusion in Electronic Thesis and Dissertation Repository by an authorized administrator of Scholarship@Western. For more information, please contact wlsadmin@uwo.ca.

Abstract

Analysis and design of fire-exposed Reinforced Concrete (RC) frames before and after jacketing with concrete layers are commonly performed using prescriptive methods that rely on the concept of fire rating. These methods were developed based on empirical results on individual RC members subjected to certain fire conditions. In typical fire scenarios, the residual capacity, stiffness and thermal deformations affects not only the local performance of each fire-exposed member, but also the load redistribution and global behavior of the entire frame. In terms of fire safety, the philosophy of the new building codes considers objective-based design as an alternative of the current prescriptive methods. Unfortunately, performing full scale experiments and comprehensive numerical analysis on RC frames are expensive and time consuming. Therefore, this thesis aims at developing a simple yet robust analysis procedure for estimating the post-fire behavior of RC frames before and after repair using concrete jackets.

The study encompasses three main phases. Firstly, the influence of interfacial slip in jacketed RC members on the capacity, stiffness and deformation behavior is assessed. An analytical model is developed to analyze the jacketed sections using the sectional analysis method and considering nonlinear material behavior. The validated model is utilized to conduct a parametric investigation aiming at examining the effect of geometrical and mechanical properties on the performance of the jacketed members and to propose modification factors to account for interfacial slip.

In the next phase, the behavior of individual fire-exposed RC members is investigated. The influence of temperature-load history, support type, initial load conditions, material properties and geometrical characteristics on the complete deformation behavior is examined in view of a proposed comprehensive sectional analysis model. The significance of each parameter is captured by performing detailed statistical analysis on the results to determine the different residual characteristics of each member.

The dissertation is culminated by presenting a case study to illustrate the proposed analysis procedure. The global behavior of an intact, fire-exposed and repaired RC frame is discussed

in view of two fire scenarios. The results show the significance of considering the mutual interaction between members to determine load redistribution and residual deformations.

Keywords

reinforced concrete; beams; residual; fire; temperature; stress-block parameters; restraint; frames; columns; jacket, continuous; thermal analysis; sectional analysis; interfacial slip

To My Wonderful Parents Makin and Sana
To My Beloved Wife Hala and Beautiful Daughter Ayla
and
To the Martyrs of the Syrian Uprising (2011 – Present)

Co-Authorship Statement

All analytical work presented in this thesis was performed by Monir Ajan Alhadid. Chapter 3 of this thesis was published in the Engineering Structures Journal. Chapters 4 through 8 of this thesis will be submitted to scholarly journals as manuscripts co-authored by Monir Ajan Alhadid and Maged Youssef.

Acknowledgments

First and foremost, praises and thanks to Allah, the Almighty, for his showers of blessings which he granted me in every step throughout my Doctoral research.

I would like to express my sincere gratitude to my advisor Prof. Maged Youssef for his contribution to a rewarding academic experience by reinforcing my attendance at various conferences, engaging me in new ideas and demanding a high quality of work in all my endeavors. His continuous support during my PhD study and related research has constantly forced me to remain focused on achieving my aspiration. His observations and comments helped me to establish the overall direction of the research and to move forward with investigation in depth. His mentorship was paramount in providing me with a great experience consistent with my long-term career goals.

Special thank also goes to my former supervisor Prof. Amr Sweedan for all the assistance and guidance he provided me with towards pursuing my Doctoral degree at Western University.

My gratitude extends to Mr. Maged Eissa for all the assistance he has provided me with to acquire Mitacs fellowship at INCON company. He has been very helpful, supportive and willing to share his invaluable experience with me from the first day I started my new job.

I would like to thank Ahmad Musa, Ahmad Al-Ansary, Mohammed Diab and all my friends whose encouraging words kept me going when coffee had lost its stimulating effect. My thanks also go to my research group Salah El-Fitiany, Aiham Adawi, Papia Sultana and Emad Ebreik for the constructive discussions we had throughout my study period.

I would like to gratefully thank my amazing family for the love, unending support, and constant encouragement I have gotten over the years. My thank also extends to wife's family, who provided me with continuous inspiration and motivation to pursue my degree.

Finally, and most importantly, I would like to thank my wife Hala. Her continuous support, encouragement, quiet patience and unwavering love were the foundations upon which the past years of my life have been built. She has been my inspiration and motivation for developing my knowledge and moving forward in my life. The past years have proven that Hala is not only my wife; she is also my soul mate, lover and inspiration. Without having her in my life, I could not have completed this dissertation successfully. Every day, I see the beauty of Hala's spirit in the eyes of my little angel, Ayla, who was born amidst this critical time of my life to draw the smile on my face. By the time of completing this dissertation, I will be already spent 18 months of gladness with my beautiful daughter.

Table of Contents

Abstract	i
Co-Authorship Statement.....	iv
Acknowledgments.....	v
List of Tables	xviii
List of Figures.....	xx
List of Abbreviations, Symbols and Notations.....	xxvi
Chapter 1.....	1
1 INTRODUCTION	1
1.1 Research Objectives.....	2
1.2 Methodology.....	3
1.3 Outline of Thesis.....	4
1.3.1 Chapter 2.....	4
1.3.2 Chapter 3.....	4
1.3.3 Chapter 4.....	5
1.3.4 Chapter 5.....	5
1.3.5 Chapter 6.....	6
1.3.6 Chapter 7.....	6
1.3.7 Chapter 8.....	7
1.4 References.....	8

Chapter 2.....	9
2 BACKGROUND AND LITERATURE REVIEW.....	9
2.1 Current Fire Design Practice in Canada.....	9
2.2 Standard Fire.....	10
2.3 Thermal Analysis.....	13
2.4 Responses of Concrete to High Temperatures.....	18
2.5 Materials Residual Behavior.....	20
2.5.1 Concrete Residual Compressive Strength (fcR').....	21
2.5.2 Concrete Residual Tensile Strength (ftR).....	22
2.5.3 Concrete Residual Initial Modulus of Elasticity (EoR).....	23
2.5.4 Concrete Residual Strain at Peak Stress (ϵoR).....	23
2.5.5 Concrete Residual Ultimate Strain (ϵcuR).....	24
2.5.6 Steel Residual Yield Strength (fyR).....	25
2.5.7 Steel Residual Modulus of Elasticity (EsR).....	27
2.6 Literature Review on Residual Strength and Cooling Effects.....	28
2.7 Concrete Jacketing of Reinforced Concrete Members.....	34
2.7.1 Jacketing of Undamaged Reinforced Concrete Members.....	34
2.7.2 Jacketing of Fire-Damaged Reinforced Concrete Members.....	38
2.8 Summary and Conclusions.....	42
2.9 References.....	43

Chapter 3	49
3 ANALYSIS OF REINFORCED CONCRETE BEAMS STRENGTHENED USING CONCRETE JACKETS	49
3.1 Material Models	50
3.2 Typical Strain and Stress Distributions in Jacketed RC Beams	50
3.3 Interfacial Shear Stress (τ) and Slip (S) Relationship	52
3.4 Interfacial Shear Stress (τ) and Slip Strain ($\Delta\varepsilon$) Relationships	54
3.5 Proposed Calculation Algorithm.....	55
3.5.1 Iterations at Mid-Span Section.....	57
3.5.2 Obtaining Moment-Curvature Relationship at Other Beam Segments.....	61
3.6 Validation.....	62
3.6.1 Chalioris and Pourzitidis [1]	62
3.6.2 Chalioris <i>et al.</i> [2]	63
3.6.3 Martinola <i>et al.</i> [3]	63
3.6.4 Hussein <i>et al.</i> [4].....	65
3.6.5 Shehata <i>et al.</i> [5]	66
3.7 Parametric Study.....	67
3.8 Flexural Behavior of the Jacketed Beams.....	67
3.8.1 Effect of Beam Width (b_c)	67
3.8.2 Effect of Jacket Thickness (h_j)	70
3.8.3 Effect of Existing Beam Height (h_c)	70

3.8.4	Effect of Beam Span (L)	71
3.8.5	Effect of Concrete Compressive Strength (f_c').....	72
3.8.6	Effect of Steel Yield Strength (f_y).....	72
3.9	Interfacial Slip Behavior	73
3.9.1	Slip Strain ($\Delta\varepsilon$) Distribution.....	73
3.9.2	Slip (S) Distribution	74
3.9.3	Interfacial Shear Stress (τ) Distribution.....	75
3.9.4	Plastic Hinge Region.....	77
3.10	Proposed Expressions for the Monolithic Factors	78
3.11	Conclusions.....	81
3.12	Appendix.....	83
3.13	References.....	85
Chapter 4	88
4	ANALYSIS OF CONTINUOUS REINFORCED CONCRETE BEAMS STRENGTHENED USING CONCRETE JACKETS.....	88
4.1	Objectives and Scope of Work	89
4.2	Concrete Material Model	90
4.3	Steel Material Model.....	90
4.4	Interfacial Shear Stress (τ) and Slip (S) Relationship	91
4.5	Assumptions.....	92
4.6	Typical Jacketed Section.....	93

4.7 Proposed Calculation Algorithm.....	95
4.7.1 Moment-Curvature at Maximum Moment Sections.....	96
4.7.2 Sectional Analysis in Jacketed Sections.....	98
4.7.3 Moment Redistribution in Continuous Beams.....	98
4.7.4 Load-Deflection Relationship and Equivalent Curvature Distribution ..	101
4.8 Validation.....	102
4.9 Parametric Study.....	104
4.10 Moment-Curvature Behavior.....	104
4.10.1 Effect of Jacket Thickness (h_j).....	108
4.10.2 Effect of Beam Width (b_c).....	110
4.10.3 Effect of Existing Beam Depth (h_c).....	111
4.10.4 Effect of Beam Span (L).....	111
4.10.5 Effect of Concrete Compressive Strength (f_c').....	112
4.10.6 Effect of Steel Grade (f_y).....	113
4.11 Interfacial Slip Behavior.....	113
4.11.1 Slip Strain ($\Delta\varepsilon$) Distribution.....	113
4.11.2 Slip (S) Distribution.....	115
4.11.3 Interfacial Shear Stress (τ) Distribution.....	117
4.12 Proposed Expressions for the Effective Stiffness.....	119
4.13 Summary and Conclusions.....	124

4.14References.....	125
Chapter 5.....	129
5 SIMPLIFIED APPROACH TO ASSESS THE CAPACITY OF FIRE-DAMAGED REINFORCED CONCRETE BEAMS.....	129
5.1 Assumptions.....	130
5.2 Heat Transfer Analysis	130
5.3 Materials Residual Behavior.....	131
5.4 Strength Analysis.....	133
5.5 Validation.....	134
5.5.1 Kodur <i>et al.</i> [36].....	134
5.5.2 Haddad <i>et al.</i> [37]	135
5.6 Parametric Investigation and Discussion.....	136
5.6.1 Influence of Fire Duration	137
5.6.2 Influence of Mechanical Properties	140
5.6.3 Influence of Geometrical Properties	141
5.7 Maximum temperature distribution along the cross-section.....	142
5.8 Stress distribution within the compression zone.....	143
5.9 Proposed Simplified Method	144
5.9.1 Evaluation of the Maximum Temperature (T_{max}) Distribution in Concrete	145
5.9.2 Evaluation of the maximum temperature (T_{max}) in steel bars	147

5.9.3	Evaluation of the residual stress-block parameters (α_{IR} and β_{IR})	148
5.9.4	Evaluation of the residual concrete compressive strength (f_{cR}').....	150
5.9.5	Evaluation of the residual maximum strain at extreme compression fiber (ϵ_{maxR})	151
5.9.6	Evaluation of the residual flexural capacity (M_r)	152
5.10	Summary and Conclusions	153
5.11	References.....	154
Chapter 6	159
6	RESIDUAL AXIAL BEHAVIOR OF RESTRAINED REINFORCED CONCRETE COLUMNS DAMAGED BY A STANDARD FIRE.....	159
6.1	Proposed Analytical Approach	160
6.2	Definition of Cross-Sections.....	164
6.3	Thermal Analysis	166
6.3.1	Rectangular Sections.....	166
6.3.2	Circular Sections.....	167
6.4	Material Models and Strain Components	172
6.5	Strength Analysis	173
6.6	Equivalent Residual Strain.....	173
6.7	Validation of the Proposed Analytical Model	176
6.7.1	Chen <i>et al.</i> [25]	177
6.7.2	Jau and Huang [26]	178

6.7.3	Yaqub and Bailey [27]	179
6.7.4	Elsanadedy <i>et al.</i> [28]	179
6.8	Parametric Study	180
6.8.1	Effect of Fire Duration	183
6.8.2	Effect of Section Size	183
6.8.3	Effect of Mechanical Properties	184
6.8.4	Effect of Steel Reinforcement Ratio	184
6.8.5	Effect of Restraint Conditions	184
6.9	Proposed Simplified Expressions to Obtain Residual Axial Capacity and Stiffness	185
6.9.1	Rectangular Sections	186
6.9.2	Circular Sections	190
6.10	Application of the Proposed Procedure	192
6.11	Conclusions	195
6.12	References	196
Chapter 7	200
7	RESIDUAL BEHAVIOR OF REINFORCED CONCRETE MEMBERS EXPOSED TO FIRE FROM 3 SIDES	200
7.1	Analysis Stages and Assumptions	201
7.2	Thermal Analysis	203
7.3	Influence of Restraints	204

7.3.1	Axial Restraints and Thermal Expansion	205
7.3.2	Rotational Restraints and Thermal Bowing.....	207
7.4	Equivalent Residual Strain of RC Members Heated from 3 Sides	208
7.5	Strength Analysis	211
7.6	Validation.....	212
7.7	Parametric Study.....	213
7.8	Influence of Study Parameters	214
7.8.1	Concrete Compressive Strength (f_c').....	216
7.8.2	Steel Yield Strength (f_y).....	216
7.8.3	Fire Duration (t).....	217
7.8.4	Steel Reinforcement Ratio (ρ)	220
7.8.5	Width of Cross-Section (b).....	220
7.8.6	Height of Cross-Section (h)	221
7.8.7	Restraints against Thermal Expansion.....	221
7.9	Regression Analysis and Proposed Expressions.....	223
7.9.1	Residual Flexural Stiffness of Fire-Exposed Beams-Column Elements	224
7.9.2	Residual Yield Moment of Fire-Exposed Beams	226
7.9.3	Residual Thermal Curvature (ϕ_i) of Fire-Exposed Beams.....	227
7.9.4	Residual Thermal Strain (ε_i) of Fire-Exposed Beams.....	229
7.9.5	Residual Moment-Curvature Diagram of Fire-Exposed Beams	230

7.9.6	Residua Axial Capacity and Stiffness of Columns Heated from 3 Sides	230
7.9.7	Residual Thermal Strain in Columns Heated from 3 Sides	230
7.9.8	Residual Thermal Curvature in Columns Heated from 3 Sides.....	233
7.10	Proposed Procedure to Analyze Fire-Damaged RC Members	234
7.11	Conclusions.....	235
7.12	References.....	237
Chapter 8	240
8	STRUCTURAL PERFORMANCE OF JACKETED FIRE-EXPOSED REINFORCED CONCRETE MEMBERS IN FRAME STRUCTURES CONSIDERING SLIP INFLUENCE	240
8.1	Applicability of the Proposed Method.....	242
8.1.1	Analysis Main Assumptions	242
8.1.2	Mechanical Characteristics Before, During and After Fire	242
8.1.3	Residual Strain Components.....	243
8.1.4	Temperature-Load Interaction	244
8.1.5	Description of the Frame System and Fire Scenarios.....	244
8.2	Local Behavior of the Affected Frame Members	247
8.2.1	Support Conditions of the Considered Members.....	248
8.2.2	Initial Load Level Acting on the Members.....	251
8.2.3	Residual Stiffness and Capacity of Columns Heated from 4 Sides	254
8.2.4	Residual Stiffness and Capacity of Columns Heated from 3 Sides	255

8.2.5	Maximum Temperature Distribution in Beams	256
8.2.6	Residual Flexural Capacity of the Fire-Exposed Beams	259
8.2.7	Residual Stiffness of the Fire-Exposed Beams	261
8.2.8	Residual Thermal Deformations in Beams	262
8.2.9	Residual Thermal Deformations in Columns	263
8.2.10	Behavior of Jacketed Beams	264
8.3	Global Structural Behavior of the Considered Frame	266
8.3.1	Fire Scenario 1	266
8.3.2	Fire Scenario 2	269
8.4	Summary and Conclusions	273
8.5	References	274
Chapter 9	277
9	SUMMARY AND CONCLUSIONS	277
9.1	Background and Literature Review	277
9.2	Analysis of Reinforced Concrete Beams Strengthened using Concrete Jackets	277
9.3	Simplified Approach to Assess the Capacity of Fire-Damaged Reinforced Concrete Beams	278
9.4	Residual Axial Behavior of Restrained Reinforced Concrete Columns Damaged by a Standard Fire	278
9.5	Residual Behavior of Reinforced Concrete Members Exposed to Fire from Three Sides	279

9.6 Structural Performance of Jacketed Fire-Exposed Reinforced Concrete Members in Frame Structures Considering Slip Influence.....	279
9.7 Recommendations for Future Work.....	280
Curriculum Vitae	281

List of Tables

Table 2-1: Indicators values in Equations 4 and 5	15
Table 3-1: Geometry of the Discussed Jacketed Beams	61
Table 3-2: Description of the examined experimental studies.....	62
Table 3-3: Coefficients Used to Calculate $\alpha_{y,J}$, $\alpha_{y,c}$ and α_u in Equations 14 and 15	80
Table 4-1: Geometry of the discussed jacketed beams	105
Table 5-1: Coefficients for Equations 6 through 7	147
Table 5-2: Coefficients for Equations 10 and 11	149
Table 5-3: Coefficients for Equations 15.....	151
Table 5-4: Coefficients for Equations 16.....	152
Table 6-1: Properties of the discussed rectangular and circular column sections	165
Table 6-2: Coefficient of Equation 4 for rectangular sections.....	187
Table 6-3: Coefficient of Equation 5 for rectangular sections.....	188
Table 6-4: Coefficient of Equation 6 for circular sections	191
Table 6-5: Coefficient of Equation 7 for circular sections	192
Table 7-1: Geometrical and mechanical properties of the discussed sections.....	214
Table 7-2: Coefficients for Equation 8	225
Table 7-3: Coefficients for Equations 13 and 14.....	229
Table 7-4: Coefficient for Equation 15.....	232
Table 7-5: Coefficient of Equation 16	233

Table 7-6: Coefficient of Equation 17	234
Table 8-1: Axial spring stiffness and restraint ratios of the considered columns.....	249
Table 8-2: Axial and flexural spring stiffness and restraint ratios of the considered beams	251
Table 8-3: Initial load level and residual properties of the fire-exposed columns.....	252
Table 8-4: Initial load level and residual properties of the fire-exposed beams.....	254
Table 8-5: Initial load level and residual properties of the fire-exposed columns.....	256
Table 8-6: Temperature and residual yield strength in the beams reinforcement.....	259
Table 8-7: Residual thermal strains and curvatures in the considered beams	262
Table 8-8: Residual thermal strains and curvatures in the considered columns	263
Table 8-9: Calculation of yield and ultimate moment capacities of the beams	265

List of Figures

Figure 2-1: Standard fire curves with cooling at various fire durations.	12
Figure 2-2: Residual compressive strength of concrete	22
Figure 2-3: Residual compressive strength of concrete	24
Figure 2-4: Residual yield strength of steel bars	26
Figure 2-5: Residual modulus of elasticity of steel bars.....	27
Figure 3-1: Geometrical properties, strains and stresses of 1-side jacketed beam	51
Figure 3-2: Interfacial slip model	52
Figure 3-3: Definition of jacketed beam segments	56
Figure 3-4: Flowchart showing the calculation algorithm to analyze jacketed beams	57
Figure 3-5: Interfacial slip calculation subroutine	58
Figure 3-6: Moment-curvature (M- ϕ) subroutine.....	59
Figure 3-7: Validation of the proposed analytical model	64
Figure 3-8: Validation of the analytical model (Hussein <i>et al.</i> [4]).....	65
Figure 3-9: Validation of the analytical model (Shehata <i>et al.</i> [5]).....	66
Figure 3-10: Effect of varying b_c on the M- ϕ relationship	68
Figure 3-11: Effect of varying b_c on the P- Δ relationship jacketed along one side.....	69
Figure 3-12: Slip strain ($\Delta\varepsilon$) distribution along beam B-5 jacketed along one side	73
Figure 3-13: Slip distribution (S) along beam B-5 jacketed from one side	75
Figure 3-14: Interfacial shear stress distribution (τ) along beam B-5 from one side.....	76

Figure 3-15: Interfacial shear stress distribution (τ) along beam B-5 from one side.....	77
Figure 3-16: Stiffness reduction model for a typical jacketed beam	78
Figure 3-17: Statistical analysis for the proposed expressions for $\alpha_{y,J}$, $\alpha_{y,c}$ and α_u	81
Figure 4-1: Continuous beam loading scheme and reinforcement configuration.....	93
Figure 4-2: Propped cantilever analytical model.....	94
Figure 4-3: Moment-curvature diagrams for positive and negative moment sections	94
Figure 4-4: Bending moment and deflection profile of the propped cantilever model	96
Figure 4-5: Element forces and displacements	99
Figure 4-6: Longitudinal and cross-sectional views of the beams tested experimentally by Cheong and MacAlevey [15].....	102
Figure 4-7: Validation of the proposed model.....	103
Figure 4-8: Percent difference of initial stiffness by including and neglecting slip effect (sagging)	106
Figure 4-9: Percent difference of initial stiffness by including and neglecting slip effect (hogging).....	106
Figure 4-10: Variation of sagging and hogging initial stiffness with various parameters....	107
Figure 4-11: Effect of varying h_J on the $M-\phi$ relationship (sagging)	108
Figure 4-12: Effect of varying h_J on the $M-\phi$ relationship (hogging).....	109
Figure 4-13: Slip strain ($\Delta\varepsilon$) distribution along beam B-5 ($\mu = 0.4$).....	114
Figure 4-14: Slip strain ($\Delta\varepsilon$) distribution along beam B-5 ($\mu = 1.0$).....	114
Figure 4-15: Slip distribution along beam B-5 ($\mu = 0.4$)	116
Figure 4-16: Slip distribution along beam B-5 ($\mu = 1.0$)	116

Figure 4-17: Interfacial shear stress distribution along beam B-5 ($\mu = 0.4$).....	118
Figure 4-18: Interfacial shear stress distribution along beam B-5 ($\mu = 1.0$).....	118
Figure 4-19: Typical moment-curvature diagram for jacketed beams.....	121
Figure 4-20: Statistical analysis for the proposed expressions	123
Figure 5-1: Development of strain components along the beam cross-section	133
Figure 5-2: Validation of the proposed model in view of load-deflection relationship.....	136
Figure 5-3: Effect of fire duration on $M-\phi$ relationship.....	138
Figure 5-4: Influence of the parameters on the reduction ratios of capacity and stiffness ...	139
Figure 5-5: Temperature distribution and variation of η	139
Figure 5-6: Stress distribution of the examined RC beam.....	143
Figure 5-7: Validation of α_{IR} and β_{IR} for the sagging moment case	149
Figure 6-1: Influence of temperature-stress interaction on the concrete strains.....	161
Figure 6-2: Temperature-stress interaction.....	162
Figure 6-3: Isolation of Columns in Typical RC Frames	163
Figure 6-4: Geometry and Meshing of Rectangular Sections.....	165
Figure 6-5: Geometry and Meshing of Circular Sections.....	168
Figure 6-6: Temperature variation with time at different points along the cross-section.....	169
Figure 6-7: Temperature distribution within the rectangular cross-section of column (R3) at different time increments	170
Figure 6-8: Temperature distribution within the circular cross-section of column (C3) at different time increments.....	171

Figure 6-9: Development of various strain components along the cross-section	174
Figure 6-10: Influence of initial load level on the residual ($P-\varepsilon$) relationship.....	175
Figure 6-11: Residual and equivalent strains distribution along columns R3 and C3 cross-sections.....	176
Figure 6-12: Validation of the proposed analytical model with experimental data.....	177
Figure 6-13: Influence of varying the examined parameters on the axial capacity and stiffness of rectangular columns.....	181
Figure 6-14: Influence of varying the examined parameters on the axial capacity and stiffness of circular columns	182
Figure 6-15: Validation of the proposed Equations 4 and 5 for residual capacity	189
Figure 6-16: Validation of the proposed Equations 4 and 5 for residual axial stiffness.....	189
Figure 6-17: Validation of the proposed Equation 6 for equivalent residual strain.....	190
Figure 6-18: Description of the proposed analysis procedure	193
Figure 7-1: Flow chart summarizing the analysis procedure.....	202
Figure 7-2: A typical RC frame structure illustrating the isolated models	205
Figure 7-3: Restrained beam model after exposure to elevated temperatures	206
Figure 7-4: Strain distributions across a typical beam heated from 3 sides.....	209
Figure 7-5: Validation of the proposed model in view the $M-\phi$ diagram obtained by Guo and Shi (2011).....	213
Figure 7-6: Ambient and residual $M-\phi$ diagrams for a typical member corresponding to different initial loads.	215
Figure 7-7: Effect of the parameters on the residual flexural capacity.	218

Figure 7-8: Effect of the parameters on the average residual thermal strain (including transient strain).....	219
Figure 7-9: Variation of total axial load acting on member 1 during ASTM E119 fire exposure and ($20\%f_c'$) initial axial load level.....	222
Figure 7-10: Variation of $M-\phi$ diagram between ambient and post-fire conditions.	224
Figure 7-11: Validation of Equation 8 to predict $(EI)_R/(EI)_g$ in fire-exposed beams.....	225
Figure 7-12: Validation of Equations 9 and 10 to predict $(M_y)_R/(M_y)$ in beams.	227
Figure 7-13: Validation of Equations 11 and 12 to predict ϕ_i in fire-exposed beams.	228
Figure 8-1: Elevation view of the frame model showing load pattern	245
Figure 8-2: Cross-sectional views of the sections in the analyzed RC frame.....	245
Figure 8-3: Cross-sectional views of the jacketed sections in the RC frame.....	246
Figure 8-4: Elevation view of the frame model showing load pattern	247
Figure 8-5: Isolated models of the different structural members in the frame	248
Figure 8-6: Isolated models of the different structural members in the frame	250
Figure 8-7: Deformation shape and straining actions in the intact frame.....	253
Figure 8-8: Temperature distribution along the beam cross-section	257
Figure 8-9: Strain profile and residual stress-block definition	261
Figure 8-10: Deformation shape and straining actions in the fire-exposed frame (scenario 1)	267
Figure 8-11: Deformation shape and straining actions in the jacketed frame (scenario 1) ..	269
Figure 8-12: Deformation shape and straining actions in the fire-exposed frame (scenario 2)	271

Figure 8-13: Deformation shape and straining actions in the jacketed frame (scenario 2) .. 272

List of Abbreviations, Symbols and Notations

$A'_{s,c}$	area of the compression core reinforcement (mm^2)
$A_{s,c}$	area of the tension core reinforcement (mm^2)
$A_{s,J}$	area of the tension jacket reinforcement (mm^2)
b_c	width of the existing beam section (m)
C_{cR}	residual resultant compressive force (N)
c	compression zone depth (mm)
D_b	diameter of the steel bars (mm)
d	distance measured from the bottom surface along the vertical axis (mm)
d_c	effective depth of the tension core reinforcement (mm)
d'_c	effective depth of the compression core reinforcement (mm)
E_s	elastic modulus of steel (MPa)
E_{sh}	strain hardening modulus of steel (MPa)
f_c	compressive stress of concrete at a given strain ε_c (MPa)
f'_c	compressive strength of concrete at 28 days (MPa)
f_{cR}'	residual compressive strength (MPa)
f_s	stress developed in steel bars at a given strain ε_s (MPa)
f_{su}	ultimate strength of steel (MPa)
f_y	yield strength of steel (MPa)
f_{yR}	residual yield strength (MPa)

F_τ	interfacial shear force (N)
h_c	height of the existing beam section (m)
h_J	thickness of the attached concrete jacket (m)
HL	Layer height used in sectional analysis (mm)
K	global interfacial slip coefficient (MPa)
k_s	secant interfacial stiffness (N/mm ³)
k_δ	axial stiffness of the equivalent spring (N/mm)
L	Beam Span (m)
L_s	Shear Span (m)
L_p	Plastic Hinge Length (m)
M	bending moment (N.mm)
M_f	moment corresponding to maximum curvature (failure moment) (N.mm)
M_r	ultimate moment (flexural capacity) (N.mm)
N_{seg}	Number of beam segments used in the proposed analytical model
NL	Number of sectional analysis layers
P	applied load (N)
P_i	initial applied load (N)
r	radius of circular cross-sections (mm)
R_D	axial restraint ratio
S	interfacial slip (mm)

S_{cu}	slip value at the onset of frictional mechanism failure (mm)
T_{cold}	fire temperature at the end of the cooling phase (°C)
T_o	room temperature (°C)
t_{hot}	fire duration at the end of the heating phase (hr, min)
T_{hot}	fire temperature at the end of the heating phase (°C)
T_{max}	maximum temperature reached (°C)
v_c	interfacial shear stress resisted by concrete (MPa)
v_{cu}	ultimate frictional capacity at the interface (MPa)
V_D	resultant dowel force (N)
V_{Du}	ultimate dowel force (N)
x	distance from support to the section under consideration (mm); or horizontal distance from the edge of the cross-section to the steel bar (mm)
α_1	parameter representing the ratio of average stress in rectangular compression stress block to the concrete compressive strength
β_1	parameter representing the ratio of rectangular compression stress-block depth to the distance between the extreme compression fiber and the neutral axis
y	vertical distance measured from the beam soffit to the steel bar (mm)
γ	factor representing the product of γ_1 and γ_2
γ_1	ratio between the average and maximum values of interfacial shear stress
γ_2	ratio between the average and maximum values of slip strain
$\Delta\varepsilon$	slip strain representing the drop in strain at the interface (mm/mm)
$\Delta\sigma$	change in the applied load level (MPa)

ϵ_c	mechanical strain of concrete (mm/mm)
ϵ_{cr}	creep strain (mm/mm)
ϵ_{cu}	concrete crushing strain at ambient conditions (mm/mm)
ϵ_{cuR}	residual concrete crushing strain (mm/mm)
$\epsilon_{c,bot}$	strain at the bottom fiber of the existing beam section (mm/mm)
$\epsilon_{c,top}$	strain at the top fiber of the existing beam section (mm/mm)
ϵ_{eq}	equivalent thermal strain (mm/mm)
$\epsilon_{J,bot}$	strain at the bottom fiber of the attached concrete jacket (mm/mm)
$\epsilon_{J,top}$	strain at the top fiber of the attached concrete jacket (mm/mm)
ϵ_{LITS}	load induced thermal strain (mm/mm)
ϵ_m	mechanical strain (mm/mm)
ϵ_{max}	strain corresponding to ultimate moment (mm/mm)
ϵ_{maxR}	strain corresponding to residual ultimate moment (mm/mm)
ϵ_o	strain at peak stress of concrete (mm/mm)
ϵ_{oR}	residual strain at peak stress (mm/mm)
ϵ_R	residual thermal strain (mm); total residual strain (mm/mm)
ϵ_s	strain of steel (mm/mm)
$\epsilon_{s,bot}$	strain in the bottom core reinforcement (mm/mm)
$\epsilon_{s,J}$	strain in the jacket reinforcement (mm/mm)
$\epsilon_{s,top}$	strain in the top core reinforcement (mm/mm)

ε_{sh}	strain hardening strain of steel (mm/mm)
ε_t	total strain (mm/mm)
ε_{th}	free thermal strain (mm/mm)
ε_{thR}	residual free thermal strain (mm/mm)
ε_{tr}	transient strain (mm/mm)
ε_{trR}	residual transient strain (mm/mm)
ε_u	strain at ultimate strength of steel (mm/mm)
ε_y	strain at yield strength of steel (mm/mm)
ε_σ	stress-related strain (mm/mm)
$\varepsilon_{\sigma i}$	residual stress-induced strain (mm/mm)
μ	coefficient of shear friction at the interface
η	ratio between T_{max} to T_{hot}
λ	axial load level
ρ_s	steel reinforcement ratio
τ	interfacial shear stress (MPa)
φ	curvature (rad/mm)
ω	residual capacity and axial stiffness ratio

Chapter 1

1 INTRODUCTION

The statistics provided by the Council of Canadian Fire Marshals and Fire Commissioners [1] for the year of 2007 revealed that a total of 42,753 fires incidents across Canada resulted in 226 civilian victims and over \$1.5 billion loss in property damage. These high figures of casualties and economical loss necessitate an inevitable reassessment of the current design philosophy to consider the fire as a loading case acting on the structure rather than just specifying descriptive information about the fire endurance of each element individually.

To the best of the authors' knowledge, the first known steps in the realm of developing a full understanding of concrete behavior at elevated temperatures has been commenced by Lea and Stradling [2]. The structural fire protection legislations aim at maintaining the lives of people, controlling the spread of fire and protecting the surrounding environment. Most concrete structures exposed to fire conditions are not fully deteriorated and their structural integrity and mechanical properties can be restored by applying suitable repair methods. According to the European Concrete Platform [3], a statistical study revealed that only 9% of all burned houses made of reinforced concrete should be demolished and the remaining 91% can be put back to use after repair. The detailed assessment of the structural performance after fire events is an essential key to satisfy the current construction practices by choosing suitable repair and strengthening techniques that conform to the current regulations and provide sufficient fire resistance for other possible fire scenarios.

Understanding the structural behavior of building structures during and after exposure to elevated temperatures is gaining a growing interest instead of relying merely on prescriptive codes. The objective-based approach implies designing the structural components to achieve specified performance levels under various loading and exposure conditions. This method is adopted by engineers to design structural members under various types of static and dynamic loads but still in its infancy when considering fire [4].

The objective-based approach has been introduced by the International Code Council [5] and the National Fire Protection Association [6] as a different alternative to the current prescriptive standards for fire safety [7]. In 2005, objective-based design philosophy was first introduced in the National Building Code of Canada as a supplement to the still commonly used prescriptive methods [8]. Other countries are also implementing the same approach in shifting towards objective-based design.

1.1 Research Objectives

Current methods of considering fire safety are considered in view of prescriptive methods that were derived for individual RC members subjected to fire. However, changes in capacity and stiffness affects not only the fire-exposed members, but also the global behavior of the entire frame they are composing. This study is a continuation of a research work that has been ongoing since 2004 at Western University under the supervision of Dr. Maged Youssef to examine the behavior of RC members exposed to elevated temperatures. The proposed research work encompasses the following:

- 1) Determine the influence of interfacial slip on the flexural behavior of structurally determinate and continuous jacketed RC beams.
- 2) Evaluate the maximum temperature distribution along a concrete cross-section.
- 3) Evaluate the flexural capacity of fire-exposed RC beams.
- 4) Evaluate the residual capacity of axially loaded rectangular and circular RC columns.
- 5) Determine the residual axial capacity of RC members exposed to fire from three or four sides.
- 6) Predict the overall post-fire behavior of indeterminate RC frames before and after jacketing with concrete.

1.2 Methodology

The proposed research work is performed analytically using MATLAB numerical computing environment to examine the behavior of both intact and fire-damaged RC members before and after jacketing with concrete layers. The current study encompasses three main stages as follow:

- 1) Develop an analytical model to capture the influence of various parameters on the flexural behavior of jacketed reinforced concrete beams. These parameters include interfacial slip, materials' mechanical properties, beams' geometrical characteristics, initial applied load level and steel reinforcement ratio. The model is first developed to analyze structurally determinate RC beams subjected to either sagging or hogging moments. The additional concrete layers are applied either from one side or three sides to account for the commonly adopted jacketing practices. The proposed analytical model is then extended to account for jacketing of continuous RC beams. The results are validated against relevant experimental data found in literature to ensure the accuracy and applicability of the proposed analytical model.
- 2) Develop an analytical model to evaluate the post-fire behavior of RC beams and columns. The procedure commences by evaluating the maximum temperature distribution within concrete members after a complete heating-cooling cycle. The residual properties are evaluated considering relevant empirical models available in literature. The residual flexural capacity of fire-exposed beams subjected to either sagging or hogging moments is investigated and a method to predict its value based on the stress-block concept is proposed. After that, the residual axial capacity, stiffness and deformations in axially loaded rectangular and circular columns are evaluated. The influence of varying the initial load level and support conditions as well as the mechanical and geometrical properties on the residual behavior of such columns is investigated. Next, the developed model is extended to cover beam-column members exposed to heat from three sides. The residual flexural and axial stiffness in beams and columns is examined. The residual thermal strains and curvatures are also evaluated after fire. This research phase is culminated by

proposing a calculation procedure to evaluate the residual behavior of both beams and columns in typical RC frames after exposure to fire.

- 3) Propose a practical approach to analyze fire-exposed RC frames before and after repair with concrete jackets. A case study that accounts for two commonly encountered fire scenarios in frame structures is presented. A procedure to evaluate the residual capacity, stiffness and thermal deformations of the individual members is described. The influence of applying concrete jackets on the stiffness and capacity of repaired sections is then discussed. Finally, the global behavior of the entire fire-exposed frame before and after fire is investigated in terms of the deformed shape and the developed straining actions.

1.3 Outline of Thesis

This thesis is prepared in an “Integrated-Article Format” following the guidelines described in Western University – School of Graduate and Postdoctoral Studies (SGPS), General Thesis Regulations.

1.3.1 Chapter 2

A literature review is presented in this chapter to present background pieces of information and part of the ongoing research related to the proposed research work. The topics discussed in Chapter 2 include the current design practice commonly used in Canada, the concept of standard fire, the procedure of thermal analysis in concrete sections and the residual properties of concrete and steel bars after exposure to fire. In addition, discussions concerning the residual behavior of RC members and the structural performance of jacketed intact and fire-damaged RC members are presented.

1.3.2 Chapter 3

Analysis of jacketed Reinforced Concrete (RC) beams considering the interfacial slip effect is a complicated problem. In the current practice, slip influence is neglected in the analysis and monolithic behavior is assumed in the jacketed section resulting in higher estimates of stiffness and/or capacity. Engineers need simplified yet robust tools to

predict the actual behavior of jacketed RC beams. This chapter provides a simplified method to analyze jacketed RC beams taking into account the interfacial slip distribution and the actual nonlinear behavior of both concrete and steel. An iterative calculation algorithm is developed to determine the moment-curvature and load-deflection curves of the jacketed beams. The developed method provides an evaluation of the slip and shear stress distributions, which allow assessing the influence of surface roughness conditions. The developed method is utilized to conduct an extensive parametric study, which resulted into modification factors to calculate the capacity and deformations of strengthened beams while accounting for interfacial slip.

1.3.3 Chapter 4

Analysis of continuous jacketed Reinforced Concrete (RC) beams requires accounting for the nonlinear behavior of the interface and the materials as well as redistribution of moments. This kind of analysis is complex and could only be conducted by academic researchers. Engineers need simplified yet robust tools to predict the actual behavior of jacketed RC beams. In the current practice, slip is neglected in the analysis and monolithic behavior is assumed for the jacketed section, which result in higher estimates of stiffness and/or capacity. This chapter provides a simplified method to analyze continuous jacketed RC beams taking into account the interfacial slip distribution and the actual nonlinear behavior of both concrete and steel. An iterative calculation algorithm is developed to determine the moment-curvature curves of a jacketed beam at different sections. The developed method allows the evaluation of interfacial slip and shear stress distributions. The developed method is utilized to conduct an extensive parametric study, which resulted into modification factors that can be used to calculate the capacity and deformations of a strengthened beam considering the interfacial slip.

1.3.4 Chapter 5

A simplified procedure to predict the flexural capacity of reinforced concrete (RC) beams exposed to a complete heating-cooling cycle experienced during a standard fire exposure is considered in this chapter. A model is proposed to determine the flexural behavior of fire-damaged RC beams subjected to either sagging or hogging moments considering the

finite difference heat transfer method and sectional analysis. The influence of the cooling phase, on the temperature distribution and residual mechanical properties, is considered in the analysis. The ability of the proposed model to predict the flexural behavior of fire-exposed beams is validated using experimental studies by others and shown to be in very good agreement. A parametric study is then conducted to determine the influence of geometrical and mechanical properties on the Moment-curvature ($M-\phi$) relationship assuming different fire durations. The study has led to proposing a procedure to determine the critical temperature distribution within the section and to calculate the equivalent stress-block parameters taking into account the residual properties.

1.3.5 Chapter 6

A simplified procedure to predict the residual axial capacity and stiffness of both rectangular and circular Reinforced Concrete (RC) columns after exposure to a standard fire is considered. The development of an analytical procedure during the design phase provides engineers with flexibility to come up with better designs that ensures safety. In this chapter, finite difference heat transfer and sectional analysis models are combined to determine the axial behavior of such columns with various end-restraint conditions at different standard fire durations. The influence of cooling phase on temperature distribution and residual mechanical properties are considered in the analysis. The ability of the model to predict the axial behavior of the damaged columns is validated in view of related experimental studies and shown to be in very good agreement. A parametric study is then conducted to assess the axial performance of fire-damaged RC columns. A procedure is proposed to determine the residual strength and stiffness of fire-damaged RC columns in typical frame structures.

1.3.6 Chapter 7

This chapter is a continuation of the ongoing work aiming at proposing a simplified procedure for analyzing fire-exposed RC frames subjected to various standard fire scenarios. The residual capacity, stiffness and thermal strains in beams and columns exposed to fire from 3 sides with various end-restraint conditions are considered in the analysis. Thermal and transient strains associated with temperature-load interaction and

heat transfer during the cooling phase are explicitly considered. The validated model is implemented to conduct an extensive parametric study that culminated in proposing simplified equations based on regression analysis.

1.3.7 Chapter 8

A case study is presented in order to investigate the changes in the structural behavior of RC frames associated with exposure to standard fire before and after jacketing. It also examines the influence of interfacial slip on the structural performance of jacketed fire-exposed RC beams. The work described in this chapter is performed as a culmination of previous analytical studies that resulted in proposing simplified calculation procedures that address both the interfacial slip in jacketed members (Chapters 3 and 4) and the residual characteristics of fire-exposed members (Chapters 5, 6 and 7).

1.4 References

- [1] Wijayasinghe, M. “Fire Losses in Canada,” Association of Canadian Fire Marshals and Fire Commissioners, 2011, Calgary, AB.
- [2] Lea, F. “The resistance to fire of concrete and reinforced concrete,” Journal of Chemical Technology and Biotechnology, 1922, Vol. 41, No. 18, pp. 395-396.
- [3] European Concrete Platform ASBL. “Comprehensive Fire Protection and Safety with Concrete,” 2007, Brussel, Belgium.
- [4] Lataille J.I., “Factors in Performance-Based Design of Facility Fire Protection,” 2008, <http://magazine.sfpe.org/fire-protection-design/factors-performance-based-design-facility-fire-protection,Last>, accessed: 27/9/2012.
- [5] International Code Council (ICC), “ICC performance code for buildings and facilities,” 2001, Falls Church, VA.
- [6] National Fire Protection Association (NFPA). “Building Construction and Safety Code,” 2002, Quincy, MA.
- [7] Johann, M.A., Albano, L.D., Fitzgerald, R.W. and Meacham B.J. “Performance-Based Structural Fire Safety,” Journal of Performance of Constructed Facilities, ASCE, 2006, Vol. 20, No. 1, pp. 45-53.
- [8] Norris, M.B. “Performance-Based Design Using the Canadian Model Building Codes,” 2012, Vol. 2, <http://newsletter.aonfpe.com/2012/Volume-2/code.aspx>, accessed: 14/8/2013.

Chapter 2

2 BACKGROUND AND LITERATURE REVIEW

The production of concrete as a superior building material led to a consequent civilian renaissance in construction. Unfortunately, despite the enormous advantages of Reinforced Concrete (RC) structures, they deteriorate and lose part of their strength when exposed to fire. The mechanical properties of concrete and reinforcing steel as well as the interfacial behavior between them pass through several significant changes during the heating and cooling stages as a result of material breakdown and thermal cracks formation. Fortunately, most concrete structures subjected to fire scenarios are not fully damaged and their structural performance can be regained or even increased by applying suitable repair and strengthening methods.

2.1 Current Fire Design Practice in Canada

In Canada, the first National Building Code [1], which was introduced in 1941, treated fire influence on building structures based on prescriptive methods through providing construction requirements for structural fire safety. Buildings subjected to fire scenarios are addressed by the National Building Code of Canada [1] in terms of the fire-resistance rating. It implies the time during which a building member or a structural assembly preserves the capability to resist the passage of flame and the transmission of heat while maintaining their structural performance. The required fire-resistance ratings range from 1 to 4 hours as specified in section 3 of the NBC [1] for different building assemblies. These ratings are set to limit the probability that a person close to the building will be exposed to injury caused directly by fire or indirectly through collapse of physical elements or entrapment inside the building. The ratings provided by NBC [1] are assigned in view of all available literature on the assemblies of common building materials and can be applied more specific test value are not available. The specified fire-resistance ratings are what a particular construction must meet under the specified testing methods but not necessarily the actual time the assembly would endure in a real fire

scenario [1]. When obtaining these ratings, it is important to determine whether it applies to a thermally restrained or unrestrained assembly. Concrete is considered as one of the most highly efficient materials to withstand fire and to provide protection from fire. Thus, the current structural design practices regarding fire recommended by NBC [1] focus on increasing the size of the RC elements and adding more concrete cover to protect the embedded steel bars. Seven various concrete types and the thickness requirements for different structural members are classified Appendix D of the NBC [1] in view of their fire-resistance requirements.

2.2 Standard Fire

The characteristics of a typical real fire spreading in a closed compartment can be classified into three main stages; namely, the growth period, the fully developed period and the decay period [2]. Although the duration of the growth period is relatively small and produces low temperatures, it is crucial in determining the effective operation period of fire brigades to intervene and distinguish the fire with minimal damage to the properties. In this burning stage, the gas temperature increases more rapidly due to the heat accumulation within the enclosure. Once the combustible materials actively burn, a sudden ignition of the accumulated gases and the exposed materials occur causing what is called a flash-over. At this point, the fire is fully developed and the temperature rises in an ascending rate until the peak temperature is reached. The temperature stabilizes when the heat generated from the combustible materials becomes equal to the heat loss to the surroundings. If the fire was not contained during its growth period, then it will be controlled by either the surface area of the exposed contents or the rate of air exchange through the windows depending on the amount of available combustible materials [3]. After that, the temperature falls down gradually within the decay period. The rate of temperature drop in this stage becomes smaller as the duration of the fully developed fire increases. The temperature in any closed area varies with both time and location, and thus the reported temperature is usually taken as the average gas temperature within a certain volume. Real fires are either fuel or ventilation controlled. Initially, the availability of sufficient fuel to reach the flashover point governs the fire spread. After reaching this

point, continuous ventilation into the burning area is mandatory to keep the fire alive. For instance, fire is unlikely to reach severe temperatures if it occurs in a certain enclosure with high fuel load but low ventilation levels. The temperature produced in the growth period is usually neglected in fire analysis as it does not form any significant risk on the structural members. Thus, standard fire curves typically focus on depicting the fully developed period in which temperature reaches extremely high values that could result in severe damage to the structural elements.

The variation of fire severity with time can be simulated numerically depending on many factors such as the type and amount of combustible materials and the presence of oxygen. However, these parameters are hard to predict accurately as they are time dependent and usually vary from one enclosure to another in the building. This implies the unlikelihood of having two real fires sharing the same thermal properties within any enclosure at any given time. Also, the behavior of each structural members is unique when exposed to a single fire based on their location relative to the developed heat flux. This unpredictable nature of fire and its interaction with the structural and non-structural elements assembling the building makes it necessary to rely on statistical data and engineering judgment to predict such severe behavior conservatively. This prediction is performed in view of a standard fire that describes the temperature variation with time for any given enclosure taking into account the little chance it will be exceeded by a real fire scenario during the building lifetime. Tabulated data for temperature increase with time are given in many standards such as the International Organization for Standardization [4] and the American Society for Testing and Materials [5]. Analytical expressions are also proposed to fit these tabulated data such as the ISO 834 [4] and ASTM E119 [5] standard fire curves as shown in Equations 1 and 2, respectively.

$$T - T_o = 345 \log_{10}(480 t + 1) \quad (1)$$

$$T - T_o = 750 [1 - e^{(-3.79553 \sqrt{t})}] + 170.41\sqrt{t} \quad (2)$$

where T is the fire temperature in ($^{\circ}\text{C}$), T_o is the initial temperature in ($^{\circ}\text{C}$) and t is the time in hours. The two standard fire models are almost identical and their difference in severity is negligible [6, 7].

In the cooling phase, temperature decreases gradually with different rates depending on the fire type and cooling method. The ASTM E119 [5] standard fire curve lacks a cooling phase after reaching the peak fire temperature. The ISO [4] standards specify cooling rates as functions of the maximum fire duration reached (t_{hot}) as given by Equation 3. The temperature is assumed to decrease gradually approximating the behavior of natural fires.

$$\Delta T = \begin{cases} -10.417 & , \quad t < 30 \text{ min} \\ -4.167 \left(3 - \frac{t_{hot}}{60} \right) & , \quad 30 \text{ min} \leq t < 120 \text{ min} \\ -4.167 & , \quad t \geq 120 \text{ min} \end{cases} \quad (3)$$

Figs. 2-1(a) and 2-1(b) illustrate the ASTM E119 [5] and ISO 834 [4] standard fire curves obtained from Equations 1 and 2, respectively. The curves terminate at the maximum burning duration specified by the corresponding standard. The cooling phase commences at various pre-defined peak fire temperatures according to Equation 3 as shown in the dashed lines in both figures.

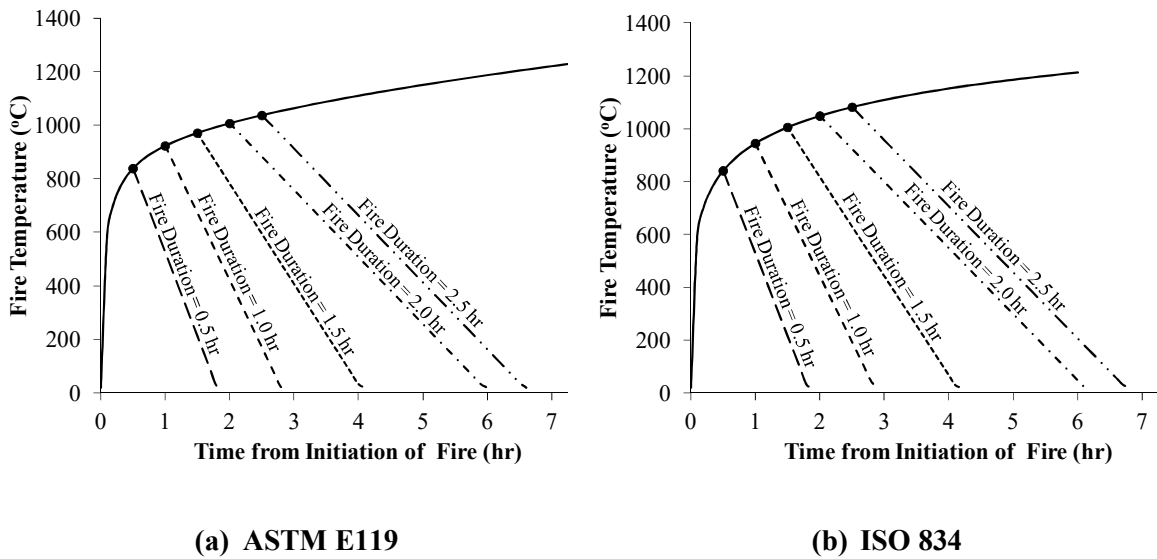


Figure 2-1: Standard fire curves with cooling at various fire durations.

2.3 Thermal Analysis

Temperature distribution within a reinforced concrete section subjected to elevated temperatures can be predicted experimentally or theoretically. The theoretical method implies the analysis of a structural member analytically or numerically based on the knowledge of fire behavior at different scenarios and the response of those members to external temperature variation depending on their thermal properties. The finite difference method [8, 9] is an analytical process which possesses the capability of predicting the temperature variation within a cross-section taking into account the temperature dependence of thermal material properties. It provides relatively accurate predictions for monolithic structural members exposed to fire from one or more sides. However, this process is not practical to be used in design offices as it is laborious and requires enormous amount of time to build and execute an iterative procedure for the analysis.

The calculation procedure is carried out by dividing the concrete section into many interior right angle rhombus elements and boundary right angle triangle elements. The temperature is represented for each rhombus element by its center and for each triangular element by the hypotenuse mid-point. The steel bars are considered as excellent conductors due to their significantly higher thermal conductivity relative to the surrounding concrete material. Thus, the temperature in each steel bar is considered equal to the temperature of the adjacent concrete elements. The heat analysis is carried out in time steps with the aid of a chosen standard fire relationship. At any given time, the temperature in each element is calculated by solving a corresponding heat equation with the knowledge of the temperature at the previous time increment. Under normal environmental conditions, concrete may hold about 3% moisture by volume. The influence of moisture is considered by assuming that at a temperature of 100°C, heat flow to the element is used to evaporate the water rather than increasing its temperature.

Heat is transferred from fire to the boundary elements by both radiation and convection and to the inner elements by conduction [9]. Thermal radiation occurs due to the conversion of thermal energy into electromagnetic energy resulting in the emission of photons and electromagnetic waves away from the fire. This radiated energy results in

rising the temperature of the surrounding objects based on their thermal properties [10]. Convection is the transfer of thermal energy by mass motion of gases or liquids. In this process, fire increases the surrounding air temperature causing it to flow upward towards the ceiling resulting in a heat transfer to the adjacent structural members in contact with this hot air [11]. The heat transferred by convection represents not more than 10% of that transferred by radiation [12]. Conduction, on the other hand, is the transfer of internal energy by diffusion and collision of adjacent molecules, atoms and electrons within an element. The heat flows from the hotter to the colder part of the body until thermal equilibrium is achieved.

The temperature (T) in each element is derived by ensuring heat balance within the section. For the outer concrete elements, the temperature at time $t = (j+1) \Delta t$ is given by Equation 4. In this equation, the left hand term represents the sensible heat absorbed by the element during the specified time increment (Δt). The first term on the right hand side of the equation represents the heat transferred from fire to a boundary element during a time increment of (Δt); whereas the second term represents the heat transmitted by conduction during the same period of time from the neighboring elements to the element under consideration.

$$\begin{aligned}
 & \left(\frac{\Delta \xi^2}{2} \right) [(\rho_c c_c)_{A,B}^j + (\rho_w c_w) \Gamma_{A,B}^j] (T_{A,B}^{j+1} - T_{A,B}^j) \\
 & = (\sqrt{2} \Delta \xi B_o \omega_f \omega_c) \left[(T_f^j + 273)^4 - (T_{A,B}^j + 273)^4 \right] (\Delta t) \\
 & - \left[\left(\frac{k_{C_1, D_1}^j + k_{A,B}^j}{2} \right) (T_{C_1, D_1}^j - T_{A,B}^j) \right. \\
 & \left. + \left(\frac{k_{C_2, D_2}^j + k_{A,B}^j}{2} \right) (T_{C_2, D_2}^j - T_{A,B}^j) \right] (\Delta t)
 \end{aligned} \tag{4}$$

For the inner concrete elements, the temperature at time $t = (j+1) \Delta t$ is given by Equation 5. In this equation, the left hand term represents the sensible heat absorbed by the element during the specified time increment (Δt). The right hand terms represent the heat

transferred by conduction during the same period of time from the neighboring elements to the element under consideration.

$$\begin{aligned}
(\Delta\xi^2)[(\rho_c c_c)_{m,n}^j + (\rho_w c_w)\Gamma_{m,n}^j](T_{m,n}^{j+1} - T_{m,n}^j) \\
= \left[\left(\frac{k_{m-1,n-1}^j + k_{m,n}^j}{2} \right) (T_{m-1,n-1}^j - T_{m,n}^j) \right. \\
+ \left(\frac{k_{m+1,n-1}^j + k_{m,n}^j}{2} \right) (T_{m+1,n-1}^j - T_{m,n}^j) \\
+ \left(\frac{k_{m-1,n+1}^j + k_{m,n}^j}{2} \right) (T_{m-1,n+1}^j - T_{m,n}^j) \\
\left. + \left(\frac{k_{m+1,n+1}^j + k_{m,n}^j}{2} \right) (T_{m+1,n+1}^j - T_{m,n}^j) \right] (\Delta t)
\end{aligned} \tag{5}$$

In Equations 4 and 5, T_f is fire temperature ($^{\circ}\text{C}$); Δt is time increment (s); ρ_c and ρ_w are densities of concrete and water (kg/m^3), respectively; c_c and c_w are the specific heats of concrete and water ($\text{J}/\text{kg}\cdot^{\circ}\text{C}$), respectively; ω_f and ω_c are the emissivity coefficients of fire and concrete, respectively; B_o is Stefan-Boltzmann constant ($\text{W}/\text{m}^2\cdot\text{K}^4$); Γ is the concentration of moisture as a volume fraction; κ is thermal conductivity of concrete ($\text{W}/\text{m}\cdot^{\circ}\text{C}$); $\Delta\xi$ is mesh width (m); M is the total number of mesh points along the horizontal axis; N is the total number of mesh points along the vertical axis; m is the layer number along the horizontal axis; n is the layer number along the vertical axis; j is the time increment number; and the values of A , B , C_1 , C_2 , D_1 and D_2 are given in Table 2-1 as a function of the surface location.

Table 2-1: Indicators values in Equations 4 and 5

Value	Bottom Surface	Top Surface	Left Surface	Right Surface
A	m	m	1	N
B	1	M	n	n
C_1	m-1	m-1	2	M-1
C_2	m+1	m+1	2	M-1
D_1	2	N-1	n-1	n-1
D_2	2	N-1	n+1	n+1

The moisture content (I) in each element is calculated using equations 4 and 5 by replacing the left hand term with the expressions shown in Equations 6 and 7 for boundary and interior elements, respectively. In these expressions, λ_w is the heat of vaporization of water (2.3×10^6 J/kg).

$$(\rho_w \lambda_w) \left(\frac{\Delta \xi^2}{2} \right) (\Gamma_{m,n}^j - \Gamma_{m,n}^{j+1}) \quad (6)$$

$$(\rho_w \lambda_w) (\Delta \xi^2) (\Gamma_{m,n}^j - \Gamma_{m,n}^{j+1}) \quad (7)$$

The thermal properties of concrete are irreversible and do not restore their initial values [13-15]. Thus, during the cooling phase, thermal properties are assumed to have a constant value corresponding to the maximum temperature reached in concrete. This assumption is valid for temperatures above 100°C when most moisture is evaporated and its influence on temperature distribution becomes negligible [13].

Regarding circular sections, the increase in temperature (T) in each layer is derived by applying the heat balance principles between them. For the outer exposed concrete layer of the column, the temperature at time $t = (j+1)\Delta t$ is given by Equation 8.

$$\begin{aligned} T_1^{j+1} = T_1^j + & \left\{ \frac{2(M-1)\Delta t}{(M-1.25)[(\rho_c c_c)_1^j + (\rho_w c_w)\Gamma_1^j] \Delta \xi} \right\} \\ & \times \left\{ B_o \omega_f \omega_c \left[(T_f^j + 273)^4 - (T_1^j + 273)^4 \right] \right\} \\ & + \left\{ \left[\frac{(M-1.5)(\kappa_1^j + \kappa_2^j)\Delta t}{(M-1.25)[(\rho_c c_c)_1^j + (\rho_w c_w)\Gamma_1^j] (\Delta \xi)^2} \right] (T_1^j - T_2^j) \right\} \end{aligned} \quad (8)$$

For the center concrete layer, the change in temperature at the next increment is determined by Equation 9.

$$T_M^{j+1} = T_M^j + \left\{ \frac{2 \Delta t}{[(\rho_c c_c)_M^j + (\rho_w c_w)\Gamma_M^j] (\Delta \xi)^2} \right\} \times \{ (\kappa_{M-1}^j + \kappa_M^j) (T_{M-1}^j - T_M^j) \} \quad (9)$$

For all other internal layers in the concrete column, the temperature variation with time is given by Equation 10.

$$T_m^{j+1} = T_m^j + \left\{ \frac{\Delta t}{2(M-m)[(\rho_c c_c)_m^j + (\rho_w c_w) \Gamma_m^j] (\Delta \xi)^2} \right\} \\ \times \left\{ [(M-m+0.5)(\kappa_{m-1}^j + \kappa_m^j)(T_{m-1}^j - T_m^j)] \right. \\ \left. - [(M-m-0.5)(\kappa_m^j + \kappa_{m+1}^j)(T_m^j - T_{m+1}^j)] \right\} \quad (10)$$

Where $\Delta \xi$ is mesh width (m); M is the total number of layers in the column; m is the layer number; and j is the time increment number. The other parameters are defined in a similar manner to Equations 4 and 5.

The initial volume of moisture in the outer concrete layer (V_1) and the corresponding evaporated moisture volume per unit length (ΔV_1) occurring during a time interval of Δt are given in Equations 11 and 12, respectively.

$$V_1 = \pi(M - 1.25)(\Delta \xi)^2 \Gamma_1 \quad (11)$$

$$\Delta V_1 = \frac{2\pi \Delta t}{\rho_w \lambda_w} \left\{ (M-1)(\Delta \xi)(B_o \omega_f \omega_c) \left[(T_f^j + 273)^4 - (T_1^j + 273)^4 \right] \right. \\ \left. - (M-1.5) \left(\frac{\kappa_1^j + \kappa_2^j}{2} \right) (T_1^j - T_2^j) \right\} \quad (12)$$

The initial volume of moisture in the center concrete layer (V_M) and the corresponding evaporated moisture volume per unit length (ΔV_M) occurring during a time interval of Δt are given in Equations 13 and 14, respectively.

$$V_M = 0.25 \pi (\Delta \xi)^2 \Gamma_M \quad (13)$$

$$\Delta V_M = \frac{\pi \Delta t}{\rho_w \lambda_w} \left\{ \left(\frac{\kappa_{M-1}^j + \kappa_M^j}{2} \right) (T_{M-1}^j - T_M^j) \right\} \quad (14)$$

For any other concrete layer, the initial volume of moisture (V_m) and the corresponding evaporated moisture volume per unit length (ΔV_m) occurring during a time interval of Δt are given in Equations 15 and 16, respectively.

$$V_m = 2\pi (M - m)(\Delta\xi)^2\Gamma_m \quad (15)$$

$$\Delta V_m = \frac{2\pi\Delta t}{\rho_w\lambda_w} \left\{ \left[(M - m + 0.5) \left(\frac{\kappa_{m-1}^j + \kappa_m^j}{2} \right) (T_{m-1}^j - T_m^j) \right] - \left[(M - m - 0.5) \left(\frac{\kappa_m^j + \kappa_{m+1}^j}{2} \right) (T_m^j - T_{m+1}^j) \right] \right\} \quad (16)$$

where λ_w is the heat of vaporization of water (J/kg).

2.4 Responses of Concrete to High Temperatures

Concrete is a heterogeneous material composed of cement paste and aggregate. Influence of elevated temperatures on the integrity of concrete material is mainly governed by the phase transformations taking place in both the cement matrix and the embedded aggregate. Thermal incompatibility between these two constituents further exacerbates the deterioration of concrete when subjected to prolonged fire scenarios. The permanent concrete damage caused by prolonged exposure to elevated temperatures occurs due to the irreversible chemical and physical processes in both the heating and cooling phases of a fire cycle. As the temperature increases, the embedded aggregates will always expand but the cement paste may either expand or shrink depending on whether the thermal expansion or moisture loss is dominant. The heating rate, fire duration and concrete composition are the main factors that affect the incompatibility between the concrete constituents resulting in cracks around the aggregates' transition zone. Although it is easy to define the thermal behavior of each constituent, this variation in thermal properties makes it difficult to model the overall response directly. Cement matrix is composed of various chemical compounds that respond to the increase of temperature differently. As temperature rises, more of the cement constituents undergo decomposition reactions. For

instance, when concrete is heated up to 120°C, the physically adsorbed water particles gain sufficient energy to undergo hydrothermal reactions resulting in loss of bound water from the CSH gel due to evaporation. The mitigation of water particles in both the liquid and gaseous phases results in increasing the porosity and breaking down the hardened cement matrix. Increasing the temperature to 300°C initiates the decomposition of the hydrated calcium silicate and the release of the chemically bonded water particles. The aggregate thermal expansion increases the formation of microcracks as a consequence of the increased internal stresses. Raising the temperature further to 600°C stimulates the decomposition reaction of Portlandite (CH) and the inversion of α -quartz into β -quartz which is accompanied by an expansion of 0.45%. This new phase results in strength reduction and shrinkage of concrete due to the formation of cracks and voids in the cement matrix [16]. Subjecting the concrete to higher temperatures up to 900°C results in the destruction of the CSH gel and the dissociation of calcium carbonate (CaCO_3). At this point, concrete loses its structural usefulness due to the severe strength and stiffness losses. When temperature approaches 1200°C, concrete melts and glassy materials form [13]. The moisture content is the free and absorbed water particles but not the chemically bonded water particles. Its presence in concrete at the time of fire may have a substantial effect on enhancing its fire endurance [1].

The variation in thermal expansion between the aggregate and the cement paste plays another major role in causing damage to concrete subjected to fire. The hardened cement matrix expands when subjected to temperatures up to 200°C and then shrinks. The aggregates, on the other hand, keep expanding with temperature with different expansion rates depending on the type of aggregates used [17]. This strain difference is compensated by the transient creep phenomenon [13, 16] that occurs in loaded concrete subjected to elevated temperature. Concrete subjected to temperature of up to 300°C is capable of restoring its strength after a long period of time (between 1 and 2 years) provided that no large temperature gradient caused by rapid heating occur within the section [18].

Alteration in coloration of concrete as a function of heat serves as an indicator for engineers to estimate the maximum temperature reached at different layers within the

concrete section after a fire incident. The concrete color after cooling provides a visual indication of the maximum temperature reached during the fire scenario. The color variation is caused by the cement paste gradual dehydration and the internal aggregate transformations [19]. Although the type of aggregate affects the intensity of the concrete color variation, the same changes occur to some extent for all types used in typical constructions. For fire temperatures below 300°C, concrete retains its original color but its surface may be blackened as a result of the generated gases from the combustion process. On heating above 300°C to just under 600°C, its color turns into pink or red as a result of changes in the limestone and/or the dehydration or oxidation of the iron compounds presented in the fine or coarse siliceous aggregate. This change in color is a useful indicator in practice to the onset of substantial loss in concrete strength. Increasing the temperature to 900°C turns the cement matrix color into whitish grey and it becomes buff at about 1000°C [20, 21].

2.5 Materials Residual Behavior

This section details the residual mechanical properties and the constitutive relationships of both concrete and steel. The term "residual" indicates the material mechanical properties after undergoing a complete heating-cooling cycle. Strength testing of concrete subjected to fire can be performed in one of three ways; namely, stressed test, unstressed test and unstressed residual strength test [22]. The concrete properties are substantially dependent on the test method adopted [13]. These testing techniques are carried out to determine the concrete compressive strength, stiffness, strain at maximum stress and dissipated energy when exposed to elevated temperatures. In the stressed test, the structural element is preloaded with a maximum of typically 40% of its ultimate compression capacity before heating commences. The temperature is then raised gradually until steady state condition is satisfied. After that, the stress is increased again until element failure occurs. The results obtained from this test simulate the behavior of structural elements subjected to extra loading due to load redistribution resulting from failure of adjacent elements in a fire scenario. The unstressed test follows the same

procedure of the stressed test except that the initial load level is zero indicating that no internal stresses are developed in the concrete before loading. This test is convenient for modeling structural elements developing small straining actions at ambient conditions and loaded when subjected to high temperatures. The unstressed residual strength test is performed by subjecting the structural element to one or more heating cycles before bringing its temperature back to the initial ambient conditions. The load is then applied to the cooled specimen until failure takes place. The observations obtained from this test is suitable for determining the residual properties and post fire performance of concrete members.

2.5.1 Concrete Residual Compressive Strength (f'_{CR})

There are several factors affecting the residual strength of concrete resulting in additional strength loss relative to the minimum strength attained during the heating phase. For instance, post-fire rehydration process results in more deterioration up to one or two months from the time of fire incident as a result of the volume expansion caused by the formation of calcium hydroxide. However, for long durations (a year or more), concrete reaches partial or full strength recovery due to rehydration of the unhydrated cement particles. Moreover, interior temperature in concrete is found to keep increasing after reaching the peak fire temperature due to heat redistribution from the exterior hot surfaces towards both the inner colder concrete core and the surrounding air which results in additional drop in strength. Furthermore, thermal incompatibility between the hardened cement matrix and the embedded aggregates causes more deterioration to concrete during the cooling phase compared to the heating stage. This happens due to the fact that transient creep strain component becomes permanent at the maximum temperature reached and does not alleviate the thermal incompatibility problem as opposed to the first heating phase.

Many experimental investigations [22-26] were carried out to determine the influence of the maximum temperature reached on the residual compressive strength of concrete. Fig. 2-2 summarizes the results obtained from these studies. All test results indicate a continuous residual strength reduction in concrete with increasing temperature. Also, concrete compressive strength at ambient conditions is found to have negligible influence

on the strength reduction rate of concrete provided that explosive spalling is not governing.

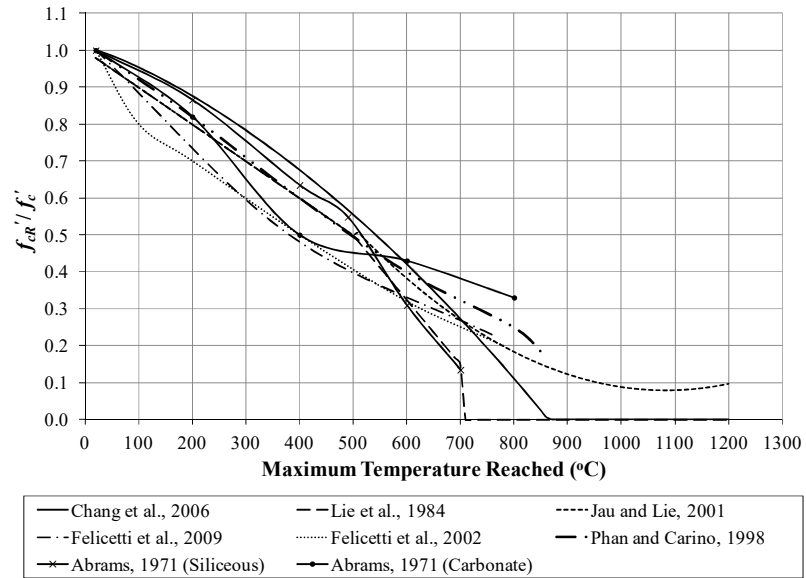


Figure 2-2: Residual compressive strength of concrete

The model proposed by Cheng *et al.* [26], Equation 17, is adopted in this study to predict the residual compressive strength of concrete in terms of the maximum temperature reached.

$$f'_{cR} = 1.008 + \frac{T}{450 \ln\left(\frac{T}{5800}\right)} \geq 0.0 \quad (17)$$

2.5.2 Concrete Residual Tensile Strength (f_{tR})

Studies concerning the residual tensile strength of concrete are limited in literature. The experimental study performed by Chang *et al.* [26] revealed that the residual tensile strength of concrete decreases as the temperature increases according to the empirical expressions in Equation 18 as functions of the original tensile strength (f_t) and maximum temperature reached.

$$f_{tR} = \begin{cases} f_t (1.05 - 0.0025 T) & , 20^\circ\text{C} < T \leq 100^\circ\text{C} \\ f_t (0.80) & , 100^\circ\text{C} < T \leq 200^\circ\text{C} \\ f_t (1.02 - 0.0011 T) \geq 0.0 & , 200^\circ\text{C} < T \leq 800^\circ\text{C} \end{cases} \quad (18)$$

2.5.3 Concrete Residual Initial Modulus of Elasticity (E_{oR})

Exposing concrete to elevated temperature reduces its residual compressive strength and increases its strain at peak stress causing the material to soften. The experimental investigation conducted by Chang *et al.* [26] showed that the residual elastic modulus of concrete decreases in a higher rate than the reduction in compressive strength. The experimental results for normal weight concrete obtained by Felicetti *et al.* [25] are in good agreement with Equation 19.

$$\frac{E_{oR}}{E_o} = \begin{cases} -0.00165 T + 1.033 & , 20^\circ\text{C} < T \leq 125^\circ\text{C} \\ \frac{1}{1.2 + 18(0.0015T)^{4.5}} & , 125^\circ\text{C} < T \leq 500^\circ\text{C} \\ \frac{1 - 0.4 \left(\frac{T - 500}{200} \right)}{1.2 + 18(0.0015T)^{4.5}} & , 500^\circ\text{C} < T \leq 700^\circ\text{C} \\ \frac{0.6 + 0.4 \left(\frac{T - 700}{100} \right)}{1.2 + 18(0.0015T)^{4.5}} & , 700^\circ\text{C} < T \leq 800^\circ\text{C} \end{cases} \quad (19)$$

2.5.4 Concrete Residual Strain at Peak Stress (ε_{oR})

The permanent increase in strain at peak stress is attributed to the cracks developed during the heating-cooling cycle resulting from the thermal incompatibility between the cement matrix and the embedded aggregates. Chang *et al.* [26] observed the formation of a visible cracks network after heating the concrete specimens to 300°C below which cracks were not significant. The cracks were found to grow in size at higher temperature

levels resulting in larger values of strain at peak stress. The original compressive strength of concrete was shown to have a substantial impact on the strain at peak stress when the temperature exceeds 200°C. Both observations were also detected by Felicetti *et al.* [25] at temperatures beyond 250°C. The residual strain at peak stress is determined in this study in view of Change *et al.* [26] model, Equation 20, as a function of concrete compressive strength and maximum temperature reached.

$$\frac{\varepsilon_{oR}}{\varepsilon_o} = \begin{cases} 1.0 & , 20^\circ\text{C} < T \leq 200^\circ\text{C} \\ \left(\frac{-f'_c}{10} + 7.7 \right) \left[\frac{e^{(-5.8+0.01T)}}{1 + e^{(-5.8+0.01T)}} - 0.0219 \right] + 1.0 & , 200^\circ\text{C} < T \leq 800^\circ\text{C} \end{cases} \quad (20)$$

2.5.5 Concrete Residual Ultimate Strain (ε_{cuR})

The ultimate compressive strain (ε_{cu}) of concrete at failure is taken as 0.0035 at ambient conditions according to CSA A23.3-14 [27]. Unfortunately, few information is available in literature regarding the residual ultimate strain of concrete (ε_{cuR}). In this study, the value of ε_{cuR} is proposed as ε_{cu} in addition to the difference between the residual strain at peak stress (ε_{oR}) and its counterpart at ambient conditions (ε_o) as given in Equation 21.

$$\varepsilon_{cuR} = \varepsilon_{cu} + (\varepsilon_{oR} - \varepsilon_o) \quad (21)$$

By comparing the value of ε_{cuR} obtained from the proposed equation with the experimental data obtained by Felicetti *et al.* [25], an excellent match is detected especially at temperatures beyond 350°C as shown in Fig. 2-3.

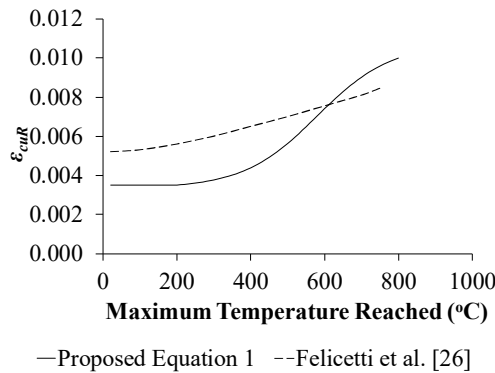


Figure 2-3: Residual compressive strength of concrete

2.5.6 Steel Residual Yield Strength (f_{yR})

When reinforced concrete structures are subjected to fire scenarios, part of the steel reinforcement may be exposed to extremely high temperatures especially if spalling of the concrete cover takes place. The temperature of these bars may be brought back to the ambient conditions by slow cooling in the air or rapid cooling caused by the water jet used to extinguish the fire. The cooling method of these heated bars dictates the extent of mechanical behavior variation and strength loss with respect to the original intact reinforcement. Also, the cross-sectional properties of the steel bars and the reinforcement distribution may play a significant role in determining the cooling rate of the steel mass [28]. In the case of slow cooling, a greater increase in the rupture strain and a decrease in the tensile strength are witnessed indicating a shift towards a more ductile behavior. On the other hand, using water jet to cool steel specimens at temperatures above 700°C resulted in a reduction in rupture strain and consequently a shift towards the brittle behavior. The variation in ductility level relative to the original steel bars becomes more pronounced for the small diameter specimens. A metallographic analysis on steel bars with different diameters and subjected to different cooling techniques was performed by Neves *et al.* [28] to examine the changes that occur to the microstructure of these bars. The examinations revealed that the gradually cooled specimens in the air exhibited an increase in the proeutectoid ferrite grain size relative to the unheated specimens. The rapid cooling performed by water jet resulted in a formation of a Widmanstätten patterns associated to bainite which results from the decomposition of the iron crystal structure after exceeding a critical temperature of 727°C [29].

A complete heating-cooling cycle does not alter the intrinsic shape of steel stress-strain curve including the well-defined yielding plateau and strain hardening behavior. The residual yield strength of mild steel starts to drop when the temperature exceeds 500°C and becomes much more significant beyond 700°C [25, 28, 29]. In this study, the residual yield strength (f_{yR}) is proposed in Equation 22 based on Neves *et al.* [28] and Felicetti *et al.* [25] experimental results as a function of maximum temperature reached. An approximate relationship showing the same trend was also obtained by Kodur *et al.* [30].

$$f_{yR} = \begin{cases} (-1.855 \times 10^{-5}) T + 0.993 & , T \leq 500 \text{ } ^\circ\text{C} \\ (8.237 \times 10^{-7}) T^2 - (1.809 \times 10^{-3}) T + 1.682 & , T > 500 \text{ } ^\circ\text{C} \end{cases} \quad (22)$$

Qiang *et al.* [31] performed tensile tests on high strength steel coupons after exposing them to different temperatures up to 1000°C. The results showed that the residual mechanical properties of high strength steel are different from that of mild steel. Based on these tests, Qiang *et al.* [31] proposed empirical equations to determine the residual yield strength for two grades of high strength steel; namely S460 and S690. Equations 23 and 24 show the residual yield strength for the aforementioned steel grades, respectively.

$$f_{yR} = (-3.24 \times 10^{-10}) T^3 + (4.98 \times 10^{-8}) T^2 + (4.52 \times 10^{-5}) T + 0.998 \quad (23)$$

$$f_{yR} = \begin{cases} 1.0 - \frac{(T - 20)^{1.584}}{9957 T} & , T < 650 \text{ } ^\circ\text{C} \\ (1.8 \times 10^{-8}) T^3 - (4.03 \times 10^{-5}) T^2 + (2.74 \times 10^{-2}) T - 4.711 & , T > 650 \text{ } ^\circ\text{C} \end{cases} \quad (24)$$

Fig. 2-4 illustrates the experimental data [25, 28] along with the proposed model in this study for mild steel. The models proposed by Kodur *et al.* [30] for mild steel and by Qiang *et al.* [31] for high strength steel having grades S460 and S690 are also shown in the same figure.

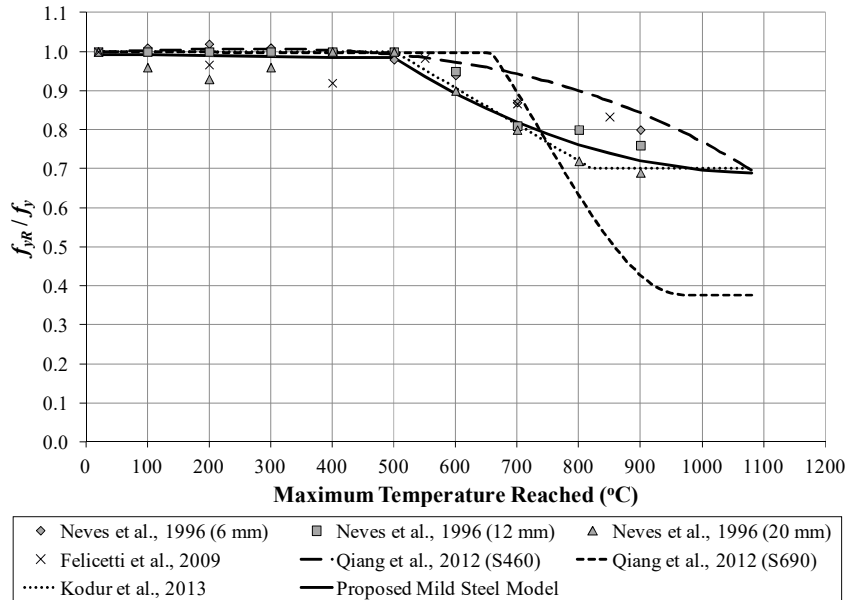


Figure 2-4: Residual yield strength of steel bars

2.5.7 Steel Residual Modulus of Elasticity (E_{SR})

The residual Young's modulus of mild steel is not affected by the heating-cooling cycle at all temperature levels and can be taken equal to its original value before fire [25, 28, 29]. However, for high strength steel, Qiang *et al.* [31] observed a permanent reduction in the elastic modulus after a full heating-cooling cycle. Based on the experimental program carried out by Qiang *et al.* [31], Equations 25 and 26 were proposed to predict the residual elastic modulus (E_{SR}) for two types of high strength steel (i.e. S460 and S690), respectively.

$$\frac{E_{SR}}{E_S} = \begin{cases} -2.69 \times 10^{-7} T^2 + 6.55 \times 10^{-5} T + 0.999 & , 20 < T \leq 600^\circ\text{C} \\ 0.947 - \frac{(T - 600)^{1.618}}{68.84 T} & , 600 < T \leq 800^\circ\text{C} \\ -2.545 \times 10^{-6} T^2 + 3.856 \times 10^{-3} T - 0.598 & , 800 < T \leq 1000^\circ\text{C} \end{cases} \quad (25)$$

$$\frac{E_{SR}}{E_S} = \begin{cases} -1.52 \times 10^{-10} T^3 + 2.70 \times 10^{-8} T^2 - 3.3 \times 10^{-5} T + 1.0 & , T \leq 600 \\ 6.27 \times 10^{-9} T^3 - 1.38 \times 10^{-5} T^2 + 8.95 \times 10^{-3} T - 0.806 & , T > 600^\circ\text{C} \end{cases} \quad (26)$$

Fig. 2-5 illustrates the variation of steel residual modulus of elasticity as a function of maximum temperature reached for mild steel [25, 28, 29] and high strength steel [31].

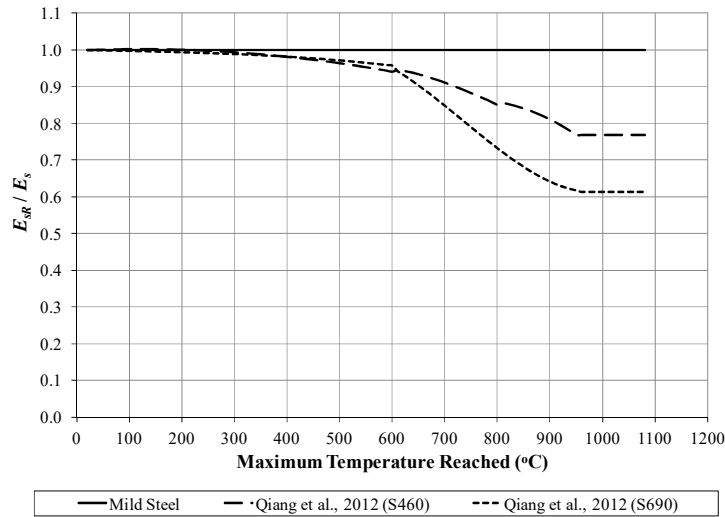


Figure 2-5: Residual modulus of elasticity of steel bars

2.6 Literature Review on Residual Strength and Cooling Effects

In an attempt to provide a better understanding of concrete subjected to various fire scenarios, Youssef and Moftah [32] conducted an extensive literature review which discussed in details the general stress-strain relationship of this material when subjected to high temperatures. The significance of the study emerged from its ability to provide a solid basis for designing concrete structures to account for various possible fire scenarios by presenting and comparing the different models used for predicting both the concrete and steel performances at elevated temperatures. The study came to a conclusion that the main properties affecting the stress-strain relationship of confined concrete are the concrete compressive strength, modulus of elasticity, strain at peak stress, thermal strain, transient creep strain, steel yield strength and bond strength of the reinforcing bars. Also, it was shown that concrete softens as the temperature increases indicating a proportional reduction in its strength and stiffness accompanied by an increase in the absolute strain at maximum stress value. Based on the findings, the authors proposed and verified different simplified analytical models that can be implemented in any finite element code to describe both the compressive and tensile stress-strain relationships of concrete at high temperatures.

Several studies discussing the residual mechanical properties of concrete after being exposed to elevated temperatures and brought back to room temperature are available in the literature. However, quantitative comparison between these studies cannot be performed accurately due to the variation in specimens' geometries, material properties and testing conditions among the researchers. One of the earliest investigations related to strength recovery of concrete exposed to elevated temperatures was carried out by Crook and Murray in 1970. The performance of concrete blocks under different post-fire curing conditions was evaluated after heating concrete specimens to 620°C and cooling them down to room temperature. The authors noticed that concrete compressive strength was decreased remarkably even after bringing the specimens temperature back to the initial state. However, it was observed that by immersing the samples in water after cooling, the strength recovery was much more evident than that evaluated by air treatment. This

observation was justified by knowing that the presence of water motivated the hydration process to reactivate and increase the cement paste strength chemically and physically by forming more hydration products that filled the small pores.

A research by Poon *et al.* [33] was performed in an attempt to figure out the influence of concrete treatment after exposure to various fire scenarios on its mechanical properties and durability. The experimental program encompassed casting and testing concrete cubes of twenty different mixes to cover a wide range of concrete types and curing regimes. The findings showed that the strength and durability regain in the blended concrete was higher than the normal concrete made of Portland cement only. It was also observed that strength recovery of concrete became insignificant when the temperature exceeded 600°C for all specimens as a result of the C-S-H gel decomposition that becomes more pronounced above 550°C. Thus, the authors recommended that in case of any fire scenario, keeping the temperature of concrete members below 600°C would eliminate the need of special repairs to regain the concrete initial strength and durability.

In 2006, Chang *et al.* [26] studied the strain variation with respect to the applied stress on 108 standard concrete cylinders cast with siliceous aggregate. The experimental work commenced by heating the specimens to temperatures ranging from 100°C to 800°C and cooling them gradually to room temperature before testing them in compression to obtain their compressive strength, tensile strength, modulus of elasticity, peak strain ratio and failure patterns. The substantial influence of heat on those mechanical properties was detected by tracking their variation with respect to temperature increase. It was found that the concrete compressive strength decreases in an increasing rate up to 85% loss of the initial compressive strength at 800°C without noticing any effect of the actual compressive strength on this trend. The elastic modulus followed the same behavior of the compressive strength variation until reaching a temperature of 500°C beyond which it kept decreasing but with a decreasing rate. The tensile strength was found to drop steadily from 20% of the initial strength at 200°C to just over 90% at 800°C. Based on the results, the authors recommended the use of a single equation to describe the stress-strain behavior for both heated and unheated concrete by using the same model proposed by Tsai [34] but with modified parameters.

Zega and Di Maio [35] investigated the behavior of concrete made of recycled aggregates in terms of its mechanical properties after a full heating and cooling cycle. The experimental work was performed by testing standard cylindrical specimens casted from various concrete mixes with different water/cement ratios and recycled aggregates replacement rates to evaluate their compressive strength and modulus of elasticity. Part of these samples were heated so that the internal temperature reached an average value of 230°C and the remaining ones were heated until their core reached a mean temperature of 450°C before bringing them back gradually to ambient conditions. For the scope of this work, a similar behavior was observed for both the recycled concrete and the normal concrete as a result of the insignificant differences in thermal properties they possessed.

Xiao and Zhang [36] conducted an experimental study aiming at assessing the residual compressive strength of concrete made of different proportions of recycled aggregates after being exposed to elevated temperatures. All concrete cubes were heated to a predetermined maximum temperature ranging between 200°C and 800°C and then tested after being cooled to room temperature. The results showed a significant effect of the aggregate replacement ratio on the concrete performance in resisting compressive load after cooling. An increase in the concrete strength compared to the normal concrete was detected when the replacement rate exceeded 50% of the original aggregates and vice versa. This observation was more pronounced when the maximum concrete temperature varied between 300°C and 500°C.

Belkacem *et al.* [37] inspected the behavior of high-performance concrete after being exposed to elevated temperatures and cooled down under various cooling regimes. The extensive experimental program was conducted using 114 cylindrical samples to fully determine the concrete residual mechanical properties after being exposed to maximum temperatures ranging from 200°C up to 1000°C. It was observed that the change in these properties was more pronounced in fast cooling conditions compared to the natural ones. The results indicated that under all cooling regimes, the loss initiation of concrete compressive strength was obvious at relatively low fire temperature whereas the loss in splitting tensile strength became remarkable when the temperature exceeded 400°C.

Klingsch *et al.* [38] conducted an experimental study to investigate the concrete compressive strength when exposed to elevated temperatures and after cooling. The experimental program was carried out by heating cylindrical concrete specimens casted from different cement types and testing them at different temperature values. Another set of specimens were heated to the same maximum temperature values of the previous group and then tested in compression after cooling them down to room temperature. By plotting the strength-temperature curves for the different cement types, it was concluded that the concrete compressive strength decreases significantly as the temperature increases and that the residual strength after cooling was further reduced and became more pronounced with higher temperatures. The authors justified this conclusion by the debonding between the aggregates and the surrounding cement paste as was seen from the magnetic resonance imaging.

Tanacan *et al.* [39] studied the influence of different cooling conditions on the mechanical performance of aerated concrete subjected to high temperatures. All specimens were heated to a certain maximum temperature ranging from 100°C to 965°C and tested either before or after being cooled to ambient temperature. All specimens were thermally expanded at first and exhibited a small increase in volume before they shrink as the temperature rises. The results showed that the rapid cooling by water caused thermal shock in the specimens and thus led to less residual strength compared to the ones cooled gradually in air taking into account the high porosity of the aerated concrete and the higher susceptibility for water vapor to influence the concrete strength.

Bingol and Gul [18] underwent an extensive experimental study in an attempt to better understand the influence of cooling regimes on the residual strength of concrete with various water/cement ratios and exposed to high temperatures ranging from 50 °C to 700°C with a heating rate of 12 to 20°C/min. The unit weight of all concrete specimens was shown to decrease slightly as the heating temperature goes up because of the voids left in the cement paste due to the bound water evaporation. A substantial permanent loss of the concrete compressive strength was noticed in all specimens exposed to high temperatures as a consequence of the different types of cracks developed in the specimen. The residual strength observed in the specimens cooled gradually in air was higher than

their counterparts cooled rapidly in water causing thermal shock. Spalling was not encountered in any of the specimens because of the normal density cement paste that contains paths for the water vapor to escape and thus avoid pressure accumulation.

Wu *et al.* [40] studied the performance of reinforced concrete columns exposed to fire scenarios during heating and at the end of the gradual cooling phase emphasizing on both the loading and the axial restraint ratios. The experimental program was carried out under transient heat loading conditions using twelve 2.34 meters long columns with (+), (T) and (L) cross sections. Thermal analysis of the columns was conducted using SAFIR finite element software and revealed that the adopted sections possessed less fire endurance compared to the rectangular columns because of the less sectional thickness they have. Vertical cracks along all columns surfaces were observed at the end of the heating process. The contours of the temperature distribution in the different cross sections varied according to the columns geometry with the (+) section having the least core temperature and the (L) section possessing the highest one. It was also observed that at the initiation of the cooling phase, the concrete outer parts and the steel bars responded promptly whereas the concrete core temperature kept increasing as a result of the continuous heat transfer.

Liu *et al.* [41] studied experimentally the behavior of fire-damaged shear walls after cooling and exposure to seismic loading conditions with a deep focus on the influence of steel reinforcement and the loading scenarios. The shear walls were heated for 90 minutes either under stressed or unstressed conditions prior to testing. The specimens were subjected to cyclic lateral load to simulate the behavior of an earthquake. The cracks distribution demonstrated the influence of the elevated temperatures in reducing the shear walls strength and improves their ductility. The inclined cracks were smaller and in some cases insignificant when the cyclic loading was applied on axially loaded fire-damaged shear walls as opposed to the wider cracks observed in the unstressed shear walls. It was shown from the test results that for certain heating conditions, increasing the steel reinforcement causes higher residual ultimate capacity and stiffness of the shear walls due to strength recovery of steel after cooling. The seismic performance of the shear walls was affected negatively when exposed to fire before the application of the cycling

loading as indicated by the thinner hysteretic loops produced from the fire-damaged specimens with respect to the intact ones.

Sharma *et al.* [42] carried out an extensive experimental study in order to assess the influence of confining steel reinforcement on the residual strength and behavior of RC short columns at high temperatures. All 108 cylindrical concrete specimens were 150 mm in diameter and 450 mm in length and varied in their hoop reinforcement spacing, steel yield strength, concrete compressive strength and maximum temperature they were exposed to. The specimens were tested after a full heating and cooling cycle under concentric axial compressive monotonic loading with a rate of 0.1 mm/min. The test results revealed that for both confined and unconfined specimens, the temperature effect started to be pronounced beyond 400°C and the maximum reduction in the mechanical properties of 60% of the unheated specimens were detected at a temperature of 800°C. The overall structural behavior of the confined specimens experienced less deterioration rate and found to be more ductile when the spacing of the lateral steel reinforcement was reduced for all temperature values resulting in higher load carrying capacity and less deformations. Increasing the yield strength of the lateral steel reinforcement resulted in negligible effect for temperatures less than 300°C and a small reduction in the axial capacity beyond that. Also, increasing the concrete compressive strength resulted in faster deterioration rate of the specimens' peak capacity at elevated temperatures.

Vieira *et al.* [43] conducted an experimental research towards achieving better prediction of the mechanical properties of concrete made of recycled aggregate after being exposed to elevated temperatures. The compressive strength, tensile strength and modulus of elasticity were evaluated for various concrete mixes using the appropriate standard test after bringing the heated specimens back to room temperature. The authors concluded that the residual mechanical performance of the concrete made of recycled aggregate is similar to the normal concrete despite the differences in porosity and thermal properties between them.

Dimia *et al.* [44] numerically investigated the influence of the cooling stage on the behavior of the structural system due to the exposure of the reinforced concrete columns

to natural fire. The main focus of this study was on the columns geometrical properties as well as the duration of the fire event. All columns were subjected to fire from three sides and were fully modeled using SAFIR finite element software to determine the temperature distribution in certain sections. The thermal properties of steel were assumed to be fully reversible after cooling whereas the residual thermal expansion and shrinkage were taken into consideration for concrete by assuming its thermal conductivity after cooling was the same as the value reached at the highest temperature during heating. The results of the proposed model showed that the structure remains in risk of collapse throughout the cooling period even after distinguishing the fire due to the continuous heat transfer in the internal parts of the section. According to the authors, this conclusion can be generalized for all solid reinforced concrete columns and is more pronounced in axially loaded columns with low slenderness ratio and exposed to short fire durations.

2.7 Concrete Jacketing of Reinforced Concrete Members

2.7.1 Jacketing of Undamaged Reinforced Concrete Members

Several studies were conducted to understand the influence of concrete jacketing on the mechanical behavior of various RC elements. For instance, an experimental study by Cheong and MacAlevey [45] was carried out to investigate the behavior of retrofitted RC beams by RC jacketing. The experimental program was divided into two phases by testing plain concrete prisms with different interface angles in shear and testing retrofitted RC beams with fully and partially roughened interfacial surfaces in bending. The tested beams were either simply supported or continuous and subjected to two point loads. It was noticed that the jacketed beams behaved in a similar manner to their monolithic counterparts in terms of the ductility, cracking and deflection behaviors. Also, due to the observed little difference in the performance of the fully roughened and partially roughened jacketed beams, it was suggested that roughening the surfaces with conventional impact tools does not have significant enhancement to the overall behavior of the retrofitted RC beams.

Altun[46] performed an experimental study to examine the influence of RC jacketing on the mechanical performance of simply supported RC beams considering the load-displacement behavior, ultimate load, ductility and toughness. The study was conducted by applying flexural load to nine RC beams that vary in their cross-sectional area but having a fixed span length of 2 meters. Then, the four sides of these beams were trimmed, roughened and cleaned off by a strong water jet to remove all the dust and fine materials in order to form a strong bond with the later applied 10 cm thick RC jacket. The test results revealed that the behavior of the jacketed RC beams is similar to the corresponding ordinary ones throughout the testing range where flexural cracks kept growing in size until failure occurred.

Júlio *et al.* [47] conducted a research in order to better understand the structural performance of jacketed RC columns with different interface treatments. The columns used in the experimental program were 1.35 meters long and having square cross-sectional area of 200 mm breadth and RC jacket thickness of 35 mm. The experimental measurements were verified by a proposed analytical model assuming either a complete non-adherence or perfect bonding between the original RC column and the surrounding jacket. It was concluded that for undamaged and undeteriorated columns, the interfacial preparation method resulted in insignificant variation in the columns mechanical behavior compared to their monolithic counterparts as long as the surfaces are well roughened.

In another study, Vadoros and Dritsos [48] investigated the significance of surface preparation of deteriorated concrete columns before applying the new concrete jacketing. The surface treatment was assessed based on the degree of surface roughening and the effect of steel dowels placement. All jacketed specimens had 250 mm x 250 mm core cross-sectional area and 75 mm thick reinforced concrete jacket confining all the four sides. The columns were subjected to a constant 800 kN compressive axial load in addition to a horizontal cyclic loading applied at their upper side. The authors observed a similar failure mechanism for all of the jacketed specimens characterized by the propagation of horizontal cracks above the foundation followed by sequential order of concrete cover spalling, stirrups opening and bars buckling. The results revealed that strength and stiffness of the jacketed columns are less of their monolithic counterparts

unless both good surface roughening and sufficient dowels placements are taken into account. The energy dissipation of the jacketed specimens was more pronounced than the monolithic specimens as a result of the interface friction and dowel action contributions.

In 2007, Santos *et al.* performed pull-off tests and slant shear tests in an attempt to assess the interfacial behavior of jacketed concrete specimens quantitatively as an alternative of the current qualitative methods. The pull-off tests were conducted on concrete cubes of 200 mm side length whereas the slant shear tests were carried out using prismatic specimens having dimensions of 200 x 200 x 400 mm. By observing the results, it was shown that sandblasting provides better performance in terms of both shear and tensile bond strengths compared to some other surface treatment methods such as wire-brushing, water jetting and chipping. Also, it was suggested that the use of sandblasting can eliminate the need for applying epoxy resins at the treated surfaces. The authors introduced certain parameters, such as the peak height and valley depth along the surface, which can be evaluated experimentally to describe the bond strength and interfacial behavior of the jacketed concrete member.

In 2007, Martinola *et al.* conducted a study in an attempt to understand the behavior of RC beams when jacketed with high performance fiber reinforced cementitious composites (HPFRCC) which are characterized by their tensile hardening behavior. The experimental work was carried out by testing one control and two jacketed beams each having a clear span of 4.35 m and cross-sectional dimensions of 300 mm x 500 mm under two-point loading set up. The compressive strength of all beams was 25 MPa and the jacketing material was 40 mm thick and made of HPFRCC having compressive strength of 176 MPa. In order to ensure full bond between the new and old concrete materials, sandblasting was performed on the beams' sides before casting applying the jacketing material. Preliminary investigation was carried out on smaller specimens and the no slippage assumption was verified. The results showed that stiffness and cracking load both increased substantially and the peak load was observed to be 2.5 times higher than the unstrengthened RC beam. As a result of the considerably higher stiffness, the midspan deflection at service load was decreased by just over 91% from 6 mm to 0.5

mm. The failure of the jacketed beams was brittle and characterized by yielding of steel reinforcement rather than crushing at the concrete face.

Shehata *et al.* [49] underwent both experimental and analytical studies in an attempt to understand the behavior of RC beams retrofitted with partial jacketing using shear connectors. The research program was carried out by testing eight 4.5 meters long beams having rectangular cross-sectional dimensions of 150 mm x 400 mm with varying amount of original and added reinforcement. The side surfaces of all beams were roughened and expansion bolts were fixed along the entire span before applying the trapezoidal shape RC jacket. The results showed that when using expansion bolts with sufficient shear strength, increasing the steel reinforcement ratio in the jackets caused a substantial increase in both the rigidity and strength of the retrofitted beams. It was also recommended to ignore the concrete contribution in providing shear strength to the interface and to keep the expansion bolts close to the jacket main and shear reinforcement.

An experimental study was carried out by Wang and Hsu [50] to investigate the behavior of beam-column connections without horizontal shear studs and the possible enhancement these connections would attain under seismic loading when retrofitted with reinforced concrete jackets. By retrofitting and testing seven beam-column connections, it was noticed that the new concrete should be anchored to the old one by means of dowels in order to eliminate any possible slippage during cyclic loading conditions and hence to improve the connections performance. The shear strength of the jacketed connections was found to be more influenced by the compressive load acting on the columns than the slippage at the interface between the old concrete and its surrounding jacket.

Tsonos[51] compared the performance of shotcrete and cast-in-place concrete jacketing in retrofitting damaged reinforced concrete columns as well as beam-column connections. For both strengthening techniques, jacketing was executed from four sides for some specimens and from two sides only for the remaining ones in an attempt to model the different constructions in practice. The experimental program was carried out on five columns and beam-column connections by applying a reversed cyclic lateral

loading in one direction for the specimens. By examining the results, the authors concluded that the performance of all retrofitted elements under seismic loading scenarios was more satisfactory than the undamaged unrepaired ones in terms of ductility and energy absorption. It was also observed that both retrofitting arrangements contributed to increasing the connections ductility and generating flexural hinges in the attached beams leading to a substantial enhancement in their seismic loading resistance.

2.7.2 Jacketing of Fire-Damaged Reinforced Concrete Members

When a building is exposed to elevated temperatures, the following step is to perform an instant and detailed assessment on the structural and non-structural elements. The inspection must start immediately after the building is accessible for engineers and before the debris are cleared away. This initial appraisal is essential to determine the cause of the fire and to estimate its severity and the maximum temperature reached. Rehabilitation of a fire-damaged structure is preferable to demolition and constructing a new one due to the earlier settlement of the occupants and the significant cost savings that can be made. Experience revealed that reinforced concrete members can almost always be repaired provided that a suitable repair technique is selected.

Studies related to the performance of jacketed reinforced concrete members after being exposed to elevated temperatures are very limited in the literature. One of the first attempts in this research field was carried out by Lin *et al.* [52] by investigating the mechanical behavior of RC columns after being repaired from severe fire damage. The repair technique was conducted by removing the damaged concrete surface and replacing it with new concrete material especially designed to provide higher strength and more durability than the original concrete in order to compensate for the potential loss in the deteriorated concrete core. Full bond between the new concrete cover and the exposed core was maintained by roughening the surfaces prior to concrete casting. The experimental program was performed by first exposing eleven columns to heat flow according to BS476 temperature curve and then testing them under eccentric axial loading conditions. The main parameters investigated in this study were the columns' gross cross-sectional area, longitudinal steel reinforcement yield strength, fire duration and the location of the applied concentrated load. The load-curvature curves were plotted

for undamaged, damaged unrepaired and damaged repaired columns. The results revealed that full or even higher strength regain can be obtained by replacing the outer deteriorated concrete layers with a concrete of higher strength and durability. Surface roughening and preparation was found to be of significant importance in order to avoid premature failure of the repaired columns resulting from spalling of the new concrete cover. The authors provided and recommended the use of an analytical approach, which was verified in view of the experimental results, for future investigations.

Haddad *et al.* [53] investigated experimentally the influence of applying high strength fiber reinforced concrete (FRC) jackets on the flexural performance of fire damaged RC beams. The experimental program was carried out by testing fourteen simply supported T-beams having a span of 1400 mm under two-point loading system until failure. The beams were first heated for 2.5 hours to a maximum temperature of 600°C and left to cool down before treating their surfaces and applying the FRC jackets at the web's sides and flange's bottom. These jackets were prepared using four different types of fibers; namely: brass coated steel (BCS), hooked steel (HS), glass (G) and high performance polypropylene (HPP). The load deflection curves for the undamaged specimens, fire damaged specimens and retrofitted specimens revealed that the ultimate load capacity, ductility, toughness and stiffness were significantly improved by applying the FRC jackets to the damaged beams. The degree of improvement depends on the type and proportions of the fibers used in the jacketing material. For instance, the ultimate load was increased from 86.29 kN for the fire damaged specimen to 103.3 kN for the GFRC and 121.6 kN for the HBCSFRC jacketed specimens indicating an overall flexural capacity improvement ranging from 19.7% to 40.9%, respectively. The ultimate carrying capacity of the retrofitted beams was pronounced and even exceeded the flexural capacity of the undamaged beams when BCSFRC or HBCSFRC jacketing materials were used. The cracking pattern for the jacketed beams was similar to the undamaged ones where flexural cracks initiated at the beam mid-span and propagating towards the compression face of the beam until concrete crushing. However, the cracking load for the beams was increased by applying the jackets due to the fibers influence on increasing the concrete tensile strength and regaining part or all of the flexural capacity of the undamaged specimen. The authors recommended the use of high strength steel FRC jackets as a

repair technique for fire damaged concrete beams since it provides it provides the highest displacement ductility ratio improvement of 112%, the highest stiffness enhancement of 220% and almost full flexural capacity regain relative to the undamaged beam specimen.

Greepala and Nimityongskul [54] examined experimentally the structural performance of ferrocement jackets when exposed to fire scenarios with a maximum temperature of 1060°C for short duration of 3 hours and long duration of 63 hours. The main objective of the experimental program was to investigate the influence of both the wire mesh volume fraction and mortar thickness on the mechanical properties of the ferrocement panels. The geometry of the ferrocement specimens was 200 mm x 240 mm x 25 mm and they were prepared from hydraulic cement mortar reinforced with multiple layers of steel wire mesh. The specimens were heated in electric furnace for the specified period of time and then left to cool down to room temperature before being tested in flexure. The results revealed that retrofitting the fire damaged RC members with ferrocement jackets would cause a substantial regain in flexural capacity of those members and enhance their resistance against other possible fire events. Also, it was concluded that the influence of wire mesh assemblies on the flexural performance of the ferrocement panels were more pronounced under normal conditions and became almost negligible at elevated temperatures. The effect of mortar covering on the specimens' carrying capacity and toughness was found to be insignificant in all fire exposure conditions. The visual inspection of the fire damaged specimens showed that increasing the wire mesh volume fraction beyond 0.54% or reducing the mortar covering to less than 2 mm resulted in more severe cracking and damage to the ferrocement jackets. The authors recommended the use of ferrocement jacketing with proper wire mesh arrangements as a superior alternative to its plain mortar or concrete cover counterparts currently used in practice.

Leonardi *et al.* [55] conducted an analytical study to evaluate the performance of fire damaged reinforced concrete beams and columns when retrofitted with high performance fiber reinforced concrete (HPFRC) jackets with steel microfibers content of 2.5%, length of 15 mm and diameter of 0.18 mm. It was assumed that the surfaces of fire damaged concrete element were treated and roughened using sandblasting and thus slippage between the old concrete and the jacketing material can be ignored. The first phase of the

analytical program was conducted on a beam having a cross-sectional area of 300x500 mm and steel reinforcement ratio of 0.6%. The second phase was concerned with modeling concrete column with the same cross-sectional area and properties of the beam. The concrete material was modeled according to Kent and Park method whereas steel behavior was modeled based on the elastic hardening law. The heat transfer mechanism within the reinforced concrete elements was described by Fourier's equation for the non-steady conditions in terms of the thermal conductivity (λ), specific heat (c) and material density (ρ) as shown in Equation 28.

$$\lambda \left(\frac{\partial^2 T}{\partial x^2} + \frac{\partial^2 T}{\partial y^2} + \frac{\partial^2 T}{\partial z^2} \right) - \rho c \frac{\partial T}{\partial t} = 0 \quad (28)$$

The beams were assumed to be exposed to elevated temperatures from three sides only and the upper side was considered to be in adiabatic conditions; whereas the columns were assumed to be subjected to fire from all four sides. The load carrying capacities of the modeled beam and column decreased substantially as expected due to the decrease in their mechanical properties at elevated temperatures. The beams were repaired using 40 mm thick jacket along the three sides exposed to fire; whereas the jacketing in columns was applied on all four sides. The concrete core was modeled based on the reduced mechanical properties after being exposed to fire while the surrounding jacketing material was modeled considering the actual undamaged conditions. The current provisions recommended by different design codes require that the fire resistance for the repaired structure to be at least equal to the fire resistance of the undamaged one. Thus, the capacity of the repaired beams and columns was assessed for four conditions; namely: undamaged, fire damaged, repaired and repaired fire damaged. The corresponding moment-fire duration curves for beams and interaction diagrams for columns were presented for all conditions. The authors strongly recommend the use of HPFRC jacketing as a retrofitting technique for fire damaged members as it provides higher strength capacity compared to the undamaged members under the normal conditions and provide fire resistance that satisfies the current provisions when exposed again to similar fire scenarios.

Recently, Guo *et al.* [56] proposed an analytical calculation method to evaluate the capacity of jacketed RC columns subjected to fire scenarios under eccentric loading conditions. The residual mechanical properties of both concrete and steel were calculated at different temperatures using any of the provided models in literature. Spalling and consequently potential reduction in cross-sectional area of the columns was ignored in the analysis. A reduction factor was then introduced by dividing the residual property by its original counterpart prior to fire exposure for each grid element within the cross-section. The strain and stress distributions resulting from the eccentric loading were obtained from sectional analysis of the proposed columns. The steel reinforcement ratio and bars cross-sectional area were chosen so as to eliminate failure of the original column prior to jacketing application. The interaction between the new concrete jacketing and the confined concrete core was determined by comparing the stress state in concrete jacketing to the tensile strength in steel reinforcement bars. The method suggested that columns failure can be modeled as transformed section with known stress-strain distribution assuming full bond between the new and old concrete.

2.8 Summary and Conclusions

This chapter summarized the commonly used design procedure related to fire adopted in Canada. It also discussed the concept of standard fire and described the finite difference procedure implemented to perform thermal analysis in reinforced concrete members. Then, a discussion of the residual mechanical properties and stress-strain relationship of both concrete and steel reinforcement in addition to the interfacial behavior between them was first presented. The chapter proceeded by discussing jacketing as an efficient strengthening and/or repair technique for enhancing the properties of different reinforced concrete members before and after being exposed to elevated temperatures. The results obtained from those researches revealed that with proper surface treatment and under well controlled conditions, the retrofitted members could regain their full or even more of their original strength provided that better concrete quality than the original one is used as a repair material.

2.9 References

- [1] National Building Code of Canada (NBCC). National Research Council (NRC), 2015, Vol. 1, Canada.
- [2] Lie., T.T., "A Method for Assessing the Fire Resistance of Laminated Timber Beams and Columns," *Canadian Journal of Civil Engineering*, 1977, Vol. 2, No. 2, pp. 161-169.
- [3] Thomas, P.H., Heselden, A.J.M., and Law, M., "Fully-Developed Compartment Fires; Two Kinds of Behaviour," *Fire Research Technical Paper No. 18*, H.M. Stationery Office, London.
- [4] ISO 834. "Fire Resistance Tests, Elements of Building Construction", International Organization for Standardization, 2014, London, UK.
- [5] ASTM. "Standard Methods of Fire Test of Building Construction and Materials, Test Method E119-01", American Society for Testing and Materials, 2001, West Conshohocken, PA, USA.
- [6] Harmathy T.Z., Allen L.W. "Thermal properties of selected masonry unit concretes," *ACI Journal Proceedings*, 1973, Vol. 70, No. 2, pp. 132-42.
- [7] Gao, W.Y., Dai J.G. and Teng, J.G. "Simple Method for Predicting Temperatures in Reinforced Concrete Beams Exposed to a Standard Fire," *Advances in Structural Engineering*, 2014, Vol. 17, No. 4, pp. 573-589.
- [8] Dusenberre, G. M. "Heat Transfer Calculation by Finite Differences," International Textbook Company, Scranton, PA, 1961, 293 pp.
- [9] Lie, T.T., ed., "Structural Fire Protection," *ASCE Manuals and Reports on Engineering Practice No. 78*, New York, 1992, 241 pp.
- [10] Blundell, S. and Blundell, K., "Concepts in Modern Physics," Oxford University Press, 2006, pp 247.

- [11] Incropera, F.P. and DeWitt, D.P., "Fundamentals of Heat and Mass Transfer," 1990, 3rd Edition, John Wiley & Sons, pp. 28.
- [12] Trinks, W. and Mawhinney, M.W., "Industrial Furnaces," Carnegie Inst. Technology, 1961, Wiley, New York, N.Y.
- [13] Schneider, U. "Properties of Materials at High Temperatures -- Concrete," RILEM 44-PHT, 1985, University of Kassel, Kassel.
- [14] Hertz, K.D. "Concrete Strength for Fire Safety Design", Magazine of Concrete Research, 2005, Vol. 57, No. 8, pp. 445-453.
- [15] Franssen, J.M. and Kodur, V. "Residual Load Bearing Capacity of Structures Exposed to Fire," Proceedings of the 2001 Structures Congress and Exposition, 2004, Vol. 109, Washington, DC, pp. 1-12.
- [16] Khoury, G. "Effect of Fire on Concrete and Concrete Structures," Progress in Structural Engineering and Materials, 2000, Vol. 2, No. 4, pp. 429-447.
- [17] International Code Council (ICC), "ICC performance code for buildings and facilities," 2001, Falls Church, VA.
- [18] Bingol, A.F. and Gul, R. "Effect of elevated temperatures and cooling regimes on normal strength concrete," *Fire and materials*, 2009, Vol. 33, pp. 79-88.
- [19] Izabela, H., "Colour Change in Heated Concrete," *Fire Technology*, Springer, 2014, Vol. 50, pp. 945-958.
- [20] Bessy, G.E., "The Visible Changes in Concrete or Mortar Exposed to High Temperatures," Investigations on Building Fires, Part 2, National Building Studies, 1950, Technical Paper, No. 4, HMSO, London, pp. 6-18.
- [21] Short, N.R., Purkiss, J.A. and Guise, S.E., "Assessment of Fire Damaged Concrete Using Colour Image Analysis," *Construction and Building Materials*, Elsevier, 2001, Vol. 15, pp. 9-15.

- [22] Phan, L.T. and Carino, N.J., "Review of Mechanical Properties of HSC at Elevated Temperature," *Journal of Materials in Civil Engineering*, 1998, V. 10, No. 1, pp. 58-64.
- [23] Abrams M. "Compressive strength of concrete at temperatures to 1600°F," *ACI Special Publication*, 1971, SP25: 33–58.
- [24] Jau, W.C. and Huang, K.L. "A study of reinforced concrete corner columns after fire," *Cement and Concrete Composites*, 2008, Vol. 30, No. 7, pp. 622-638.
- [25] Felicetti, F., Gambarova, P.G., Rosati, G.P., Corsi, F. and Giannuzzi, G. "Residual Mechanical Properties of High Strength Concretes Subjected to High Temperature Cycles", *Proceedings, 4th International Symposium on Utilization of High Strength/High Performance Concrete*, 1996, Paris, France, pp. 579-588.
- [26] Chang, Y.F., Chen, Y.H., Sheu, M.S. and Yao, G.C. "Residual Stress-Strain Relationship for Concrete after Exposure to High Temperatures," *Cement and Concrete Research*, 2006, Vol. 36, pp. 1999-2005.
- [27] CSA. "Design of concrete structures (CAN/CSA A23.3-14)," *Cement Association of Canada*, 2014, Ottawa, ON.
- [28] Neves, I.C., Rodrigues, P.C. and Loureiro, A.D.P. "Mechanical properties of reinforced and prestressed steels after heating," *Journal of Materials in Civil Engineering*, 1996, Vol. 8, No. 4, pp. 189-194.
- [29] Malhotra, H.L., "Design of Fire Resisting Structures," *Chapman and Hall*, 1982, New York, pp. 67-78.
- [29] Bhadeshia, H. and Honeycombe, R. "Steels: Microstructure and Properties," 3rd edition, *Butterworth-Heinemann*, 2006, ISBN 9780080462929, 360 pp.
- [30] Kodur, V.K.R., Raut, N.K., Mao, X.Y. and Khaliq, W. "Simplified approach for evaluating residual strength of fire-exposed reinforced concrete columns," *Materials and Structures*, Springer, 2013, Vol. 46, pp. 2059-2075.

- [31] Qiang, X., Bijlaard, F. and Kolstein, H. "Post-fire mechanical properties of high strength structural steels S460 and S690," *Engineering Structures*, Elsevier, 2012, Vol. 35, pp. 1-10.
- [32] Youssef, M.A. and Moftah, M. "General Stress-Strain Relationship for Concrete at Elevated Temperatures," *Engineering Structures*, Elsevier, 2007, Vol. 29, pp. 2618-2634.
- [33] Poon, C., Azhar, S., Anson, M. and Wong, Y. "Strength and durability recovery of fire-damaged concrete after post-fire curing," *Cement and Concrete Research*, Pergamon, 2001, Vol. 31, pp. 1307-1318.
- [34] Tsai, W.T. "Uniaxial Compressional stress-strain relation of concrete," *Journal of Structural Engineering*, 1988, Vol. 114, No. 9, pp. 2133-2136.
- [35] Zega, C.J. and Maio, A.A. "Recycled concrete exposed to high temperatures," *Magazine of Concrete Research*, 2006, Vol. 58, pp. 675-682.
- [36] Xiao, J., and Zang, C. "Fire damage and residual strengths of recycled aggregate concrete," *Key Engineering Materials*, 2007, Vols. 348-349, pp. 937-940.
- [37] Belkacem, T., Hocine, C., Hacène, H. and Resheidat, M. "Effects of Cooling Condition on Residuals Properties of High-Performance Concrete at High Temperature," *ICCBT*, A-11, pp. 135-142.
- [38] Klingsch, E., Frangi, A. and Fontana, M. "Experimental Analysis of Concrete Strength at High Temperatures and after Cooling," *Czech Technical University Publishing House, Acta Polytechnica*, 2009, Vol. 49, No. 1, pp. 34-38.
- [39] Tanacan, T., Ersoy, H.Y. and Arpacıoğlu, U. "Effect of high temperature and cooling conditions on aerated concrete properties," *Construction and Building Materials*, Elsevier, 2009, Vol. 23, pp. 1240-1248.
- [40] Wu, B., Li, Y. and Chen, S. "Effect of Heating and Cooling on Axially Restrained RC Columns with Special-Shaped Cross Section," *Fire Technology*, Springer, 2010, Vol. 46, pp. 231-249.

- [41] Liu, G., Song, Y. and Qu, F. "Post-fire cyclic behavior of reinforced concrete shear walls," *Journal of Central South University of Technology*, Springer, 2010, Vol. 17, pp. 1103-1108.
- [42] Sharma, U.K., Zaidi, K.A., Bhargava, P. and Bhandari, N.M. "Residual Strength and Deformation Characteristics of Confined Concrete Subjected to Elevated Temperature," *Proceedings of the 9th US National and 10th Canadian Conference on Earthquake Engineering*, 2010, Toronto, Ontario, Canada, 2178-2187.
- [43] Vieira, J.P.B., Correia, J.R. and Brito, J. "Post-fire residual mechanical properties of concrete made with recycled concrete coarse aggregates," *Cement and Concrete Research*, Elsevier, 2011, Vol. 41, pp. 533-541.
- [44] Dimia, M.S., Guenfoud, M., Gernay, T. and Franssen J. "Collapse of concrete columns during and after the cooling phase of a fire," *Journal of Fire Protection Engineering*, SAGE, 2011, Vol. 21, No. 4, pp. 245-263.
- [45] Cheong, H.K. and MacAlevey, N. "Experimental behavior of jacketed reinforced concrete beams," *Journal of structural engineering*, ASCE, 2000, pp. 692-699.
- [46] Altun, F. "An experimental study of the jacketed reinforced-concrete beams under bending," *Construction and Building Materials*, Elsevier, 2004, Vol. 18, pp. 611-618.
- [47] Júlio, E.N.B.S., Branco, F.A.B. and Silva, V.D. "Reinforced Concrete Jacketing - Interface Influence on Monotonic Loading Response," *ACI Structural Journal*, 2005, Vol. 12, No. 2, pp. 252-257.
- [48] Vandoros, K.G. and Dritsos, S.E. "Interface treatment in shotcrete jacketing of reinforced concrete columns to improve seismic performance," *Structural Engineering and Mechanics*, 2006, Vol. 23, No. 1, pp. 43-61.
- [49] Shehata, I., Shehata, L., Santos, E. and Simoes, M. "Strengthening of reinforced concrete beams in flexure by partial jacketing," *Materials and Structures*, 2009, Vol. 42, pp. 495-504.

- [50] Wang, Y. and Hsu, K. "Shear Strength of RC Jacketed Interior Beam-Column Joints without Horizontal Shear Reinforcement," *ACI Structural Journal*, Vol. 106, No. 2, pp. 222-232.
- [51] Tsonos, A.G. "Performance enhancement of R/C building columns and beam-column joints through shotcrete jacketing," *Engineering Structures*, Elsevier, 2010, Vol. 32, pp. 726-740.
- [52] Lin, C., Chen, S. and Yang, C. "Repair of Fire-Damaged Reinforced Concrete Columns," *ACI Structural Journal*, 1995, Vol. 92, No.4, pp. 406-411.
- [53] Haddad, R.H., Shannag, M.J. and Hamad, R.J. "Repair of Heat-Damaged Reinforced Concrete T-Beams Using FRC Jackets," *Magazine of Concrete Research*, 2007, Vol. 59, No. 3, pp. 223-231.
- [54] Greepala, V. and Nimityongskul, P. "Influence of Heating Envelope on Structural Fire Integrity of Ferrocement Jackets," *Fire Technology*, Springer, 2009, Vol. 45, pp. 385-404.
- [55] Leonardi, A., Meda, A. and Rinaldi, Z. "Fire-Damaged R/C Members Repair with High-Performance Fiber-Reinforced Jacket," *Strain - International Journal for Experimental Mechanics*, Blackwell Publishing Ltd., 2010, Vol. 47, No. 2, pp. 28-35.
- [56] Guo, J., Lu, Y. and Li, P. "Calculation Method Investigation on Jacketing Reinforcement of RC Eccentric Compressive Column Subjected to Fire," *Applied Mechanics and Materials*, Trans Tech Publications, Vols. 166-169, pp. 1548-1553.

Chapter 3

3 ANALYSIS OF REINFORCED CONCRETE BEAMS STRENGTHENED USING CONCRETE JACKETS

There are several reasons that necessitate rehabilitating a Reinforced Concrete (RC) structure, such as new safety requirements, a change of structure occupancy, an incorrect design calculations and/or degradation of materials with time. Flexural strengthening of RC beams results in increasing their capacity and stiffness to accommodate certain design requirements. One of the most commonly used strengthening techniques for RC beams involves the application of RC jackets with different configurations. The added concrete layers are usually reinforced with longitudinal steel bars, stirrups, welded wire mesh or various kinds of fibrous materials. The behavior of RC members strengthened with RC jackets was investigated experimentally by many researchers [1-10].

Composite beams have been used in construction since time immemorial in the form of layered timber planks glued or packed together with ropes to create one entity. The efficiency of such structural elements relies chiefly on the ability of the sliding surfaces to transfer the generated shear stresses [11]. The 1966 Canadian [12] and American [13] standards included provisions for the concrete-to-concrete interfacial behavior in view of shear-friction theory. According to this theory, the horizontal shear strength along the interface depends on four main parameters; namely, the concrete-compressive strength, the vertical-pressure component at the interface, the ratio of transverse reinforcement crossing the interface, and the roughness of the underlying-concrete surface [14]. In many design practices, full bond between the existing and the added concrete layers in jacketed RC beams is assumed. The accuracy of this assumption depends on the loading type, the interface-shear-plane area, the surface roughness and the layout of the attached concrete jacket. However, in typical constructions, a relative slip is expected between the new and old concrete layers, which may result in separation of the two surfaces [15] and will influence the capacity and stiffness of a jacketed beam.

The following sections summarize the proposed calculation algorithm for estimating the behavior of RC beams jacketed with concrete. The material and interfacial mechanical behaviors are estimated from relevant models found in literature. Subsequently, the developed algorithm is validated in view of relevant experimental studies. The model is utilized to investigate the effects of interfacial friction coefficient, material properties and geometrical characteristics on the flexural behavior of the jacketed beams. Slip modification factors are proposed to allow engineers to estimate the critical design variables.

3.1 Material Models

Scott *et al.*'s model [16] is adopted to model the concrete in compression as it provides a robust yet simple expression to describe its stress-strain behavior. Concrete is assumed to fail when the crushing strain reaches a value of 0.0035 [12]. Concrete is assumed to carry tensile stresses up to the cracking point beyond which the tensile capacity of concrete drops to zero.

The steel reinforcement monotonic stress-strain relationship is expressed according to the model reported by Karthik and Mander [17] in view of the general formula proposed by Ramberg and Osgood [18]. It conveniently combines the initial elastic response, yield plateau and strain hardening stages in a single rigorous form to model the actual behavior of steel bars. The value of the strain hardening strain (ε_{sh}) is set equal to the yield strain (ε_y) and the strain hardening modulus (E_{sh}) is taken as 1% of the Young's modulus of elasticity (E_s).

3.2 Typical Strain and Stress Distributions in Jacketed RC Beams

Simply supported beams jacketed from one side and three sides are considered in the analysis. The concrete jacket in both cases extends between the two supports along the entire beam. The cross-sectional view of the 1-side jacketed beam is shown in Fig. 3-1(a) in which h_c is the height of the existing section, b_c is the interface width, h_j is the

thickness of the attached concrete jacket, d_c is the effective depth of the tension core reinforcement, d'_c is the effective depth of the compression core reinforcement, $A_{s,c}$ is the area of the tension core reinforcement, $A'_{s,c}$ is the area of the compression core reinforcement, and $A_{s,J}$ is the area of the tension jacket reinforcement.

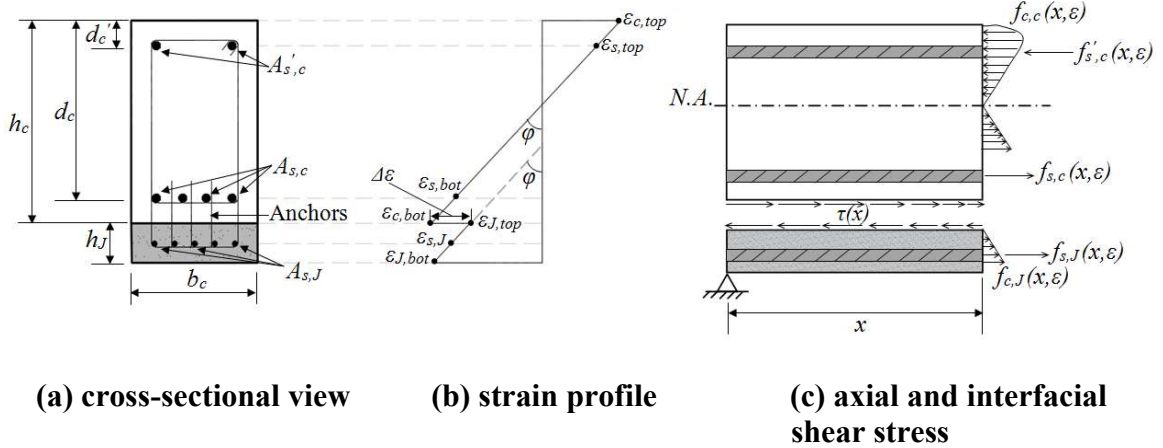


Figure 3-1: Geometrical properties, strains and stresses of 1-side jacketed beam

The corresponding strain profile is illustrated in Fig. 3-1(b) where $\varepsilon_{c,top}$ and $\varepsilon_{c,bot}$ are the strains at the top and bottom fibers of the original beam; $\varepsilon_{J,top}$ and $\varepsilon_{J,bot}$ are the strains at the top and bottom fibers of the attached concrete jacket; $\varepsilon_{s,top}$, $\varepsilon_{s,bot}$ and $\varepsilon_{s,J}$ are the strains developed in the top core reinforcement, bottom core reinforcement and jacket reinforcement, respectively. $\Delta\varepsilon$ is the slip strain, which represents the drop in strain at the interface caused by the relative slip between the two surfaces. The resulting stress distribution at an arbitrary section located at a distance of (x) from the support is shown in Fig. 3-1(c). In this figure, $f_{c,c}$ and $f_{c,J}$ represent the stress distribution in the concrete core and jacket, respectively; $f'_{s,c}$, $f_{s,c}$ and $f_{s,J}$ represent the stress generated in the core top reinforcement, core bottom reinforcement and jacket reinforcement, respectively; and $\tau(x)$ is the shear stress distribution along the interface from the support to the section under consideration. If the beam is jacketed from three sides, only the effect of slip along the horizontal interface is taken into account. The inaccuracy that may be caused by this

assumption is minor and can be ignored [19] as slip becomes less remarkable closer to the neutral axis. For the 3-sides jacketing scheme, an additional term must be added to the stress distribution shown in Fig. 3-1(c) to account for the compressive stress acting on the two vertical sides of the jacket.

3.3 Interfacial Shear Stress (τ) and Slip (S) Relationship

Interfacial shear-slip models are generally expressed as the summation of concrete contribution (i.e. adhesion, aggregate interlock and friction) and dowel action owing to any transverse reinforcement crossing the interface. The model proposed by Tassios and Vintzeleou [22] to determine the concrete contribution (v_c) in transferring the shear along a contact plane is adopted. The frictional force generated between the two substrates depends on the surface roughness and the applied normal pressure due to the reinforcing bars crossing the interface as depicted in Fig. 3-2. As the relative slip (S) between the existing concrete layer and the attached jacket increases, some overriding deformations occur due to the uneven surfaces causing them to move apart from each other. This lateral movement generates pullout forces in the vertical steel bars that in turn produce compressive forces on the concrete to maintain equilibrium along the interface. The steel bars (dowels) also provide horizontal force components that contribute directly to the interfacial shear resistance.

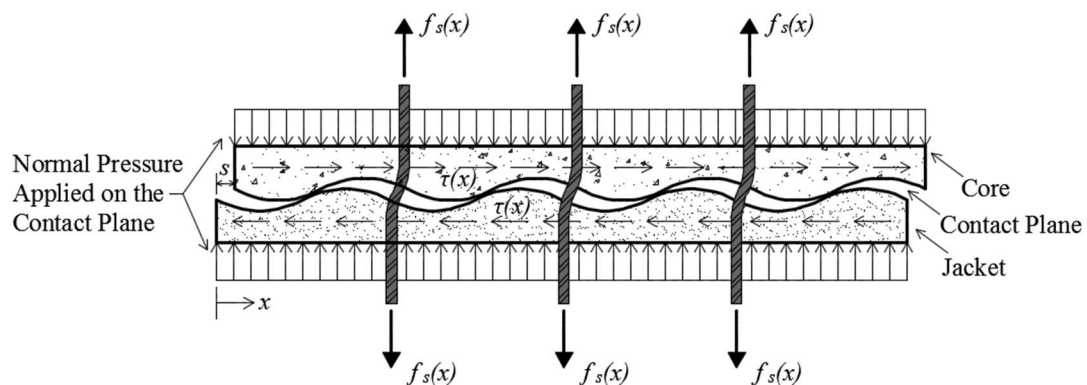


Figure 3-2: Interfacial slip model

Tassios and Vintzeleou [22] empirical model is presented in terms of the lateral slip (S), ultimate slip value at the onset of frictional mechanism failure (S_{cu}) and ultimate frictional capacity of the interface (v_{cu}) as expressed by Equations 1 and 2.

$$v_c(S) = \begin{cases} 1.14(v_{cu}) \left(\frac{S}{S_{cu}}\right)^{\left(\frac{1}{3}\right)} & , \left(\frac{S}{S_{cu}}\right) \leq 0.5 \\ (v_{cu}) \left[0.81 + 0.19\left(\frac{S}{S_{cu}}\right)\right] & , \left(\frac{S}{S_{cu}}\right) > 0.5 \end{cases} \quad (1)$$

$$v_{cu} = \mu(f_c'^2 \rho_s f_s)^{\left(\frac{1}{3}\right)} \quad (2)$$

where μ is the coefficient of friction at the interface, ρ_s is the reinforcement ratio of the bars crossing the interface and f_s is the corresponding tensile stress developed in these bars as given in Equation 3.

$$f_s = \left(\frac{0.3 S^{\left(\frac{2}{3}\right)} E_s f_c'}{D_b}\right) \leq f_y \quad (3)$$

The resultant dowel force (V_D) is expressed as a function of the lateral slip between the two concrete surfaces, studs' diameter (D_b) and the ultimate dowel force (V_{Du}) given by Equations 4 and 5.

$$S = \begin{cases} 0.012 \left(\frac{V_D(S)}{V_{Du}}\right) & , S \leq 0.006D_b \\ 0.006D_b + 0.088D_b \left[\left(\frac{V_D(S)}{V_{Du}}\right)^4 - 0.5\left(\frac{V_D(S)}{V_{Du}}\right)^3\right] & , \frac{V_D(S)}{V_{Du}} \geq 0.5 \end{cases} \quad (4)$$

$$V_{Du} = 1.3 D_b^2 \sqrt{f_c' f_y} \quad (5)$$

3.4 Interfacial Shear Stress (τ) and Slip Strain ($\Delta\varepsilon$) Relationships

The interfacial shear stress distribution is assumed to vary as a cubic function in the form of Equation 6. This assumption was validated through performing a numerical analysis aiming at defining the shape of the shear stress distribution along the interface [15].

$$\tau = A x^3 + B \quad (6)$$

Slip, and consequently shear stress, reach their maximum value at the support and fade away as they approach the maximum bending moment section (i.e. beam mid-span). The proportion of the average shear stress (τ_{avg}) distribution from support to mid-span relative to its maximum value (τ_{max}) are related by a factor γ_1 (i.e. $\gamma_1 = \tau_{avg}/\tau_{max}$). The average slip strain ($\Delta\varepsilon_{avg}$) is defined as a proportion of its maximum value ($\Delta\varepsilon_{max}$) by a factor of γ_2 (i.e. $\gamma_2 = \Delta\varepsilon_{avg}/\Delta\varepsilon_{max}$). The maximum slip (S_{max}) is determined as the product of the distance from support to mid-span section ($L/2$) and the average slip strain ($\Delta\varepsilon_{avg}$) along that same distance. At any applied load increment, the average value of interfacial shear stress (τ_{avg}) can be obtained by assuming a direct relationship with the maximum slip strain ($\Delta\varepsilon_{max}$) value located at the beam mid-span [5, 11, 12]. From the above discussion, average shear stress can be expressed in terms of the factors γ_1 and γ_2 according to Equation 7.

$$\tau_{avg} = \gamma_1 \tau_{max} = \gamma_1 [k_s S_{max}] = \gamma_1 \left[k_s \left(\Delta\varepsilon_{avg} \frac{L}{2} \right) \right] = \gamma_1 \left[k_s \left(\gamma_2 \Delta\varepsilon_{max} \frac{L}{2} \right) \right] \quad (7)$$

The global interfacial slip coefficient (K) is defined by Equation 8.

$$K = k_s \gamma \left(\frac{L}{2} \right) \quad (8)$$

where k_s is the secant interfacial stiffness (N/mm³) and γ is the product of the factors γ_1 and γ_2 . By combining Equations 7 and 8, τ_{avg} can be expressed by Equation 9.

$$\tau_{avg} = K \Delta\varepsilon_{max} \quad (9)$$

To evaluate the coefficients (A) and (B) in Equation 6, two boundary conditions are determined. The first one is assigning the interfacial shear stress (τ) a value of zero at the beam mid-span and the other one is setting the average shear stress resulting from the distribution provided by Equation 6 as τ_{avg} defined in Equation 9. Solving Equation 6 for the coefficients (A) and (B) and integrating it with respect to (x) provides the corresponding interfacial shear force (F_τ) at any section at a distance (x) from the support as expressed by Equation 10.

$$F_\tau = (b) \left[\left(\frac{4 \tau_{avg}}{3} \right) (x) - \left(\frac{\tau_{avg}}{3 \left(\frac{L}{2} \right)^3} \right) (x^4) \right] \quad (10)$$

3.5 Proposed Calculation Algorithm

The main objectives of the proposed calculation algorithm are to predict the slip distribution along the interface and to determine the moment-curvature ($M-\phi$) relationship at different segments along the jacketed beam. The proposed model considers the full non-linear characteristic of the jacketed RC beams taking into account both the elastic and post-yield behaviors. This allows the determination of the capacity and deformation behavior of ductile members rather than limiting the analysis to brittle [19] or linear elastic sections [20,21]. The influence of interfacial slip on the flexural behavior of the jacketed beams is modeled by modifying Tsioulou and Dritsos [15] procedure that was derived based on Eurocode [23] expressions. According to their model, the beam is considered as one entity and integrations are performed to estimate the slip and shear stress distributions along the interface. The effect of slip would thus be reflected through obtaining a $M-\phi$ diagram that describes the flexural behavior of any section along the beam. In the current proposed method, the beam is divided into multiple segments, Fig. 3-3, and a unique $M-\phi$ diagram is obtained for each segment using sectional analysis technique [24].

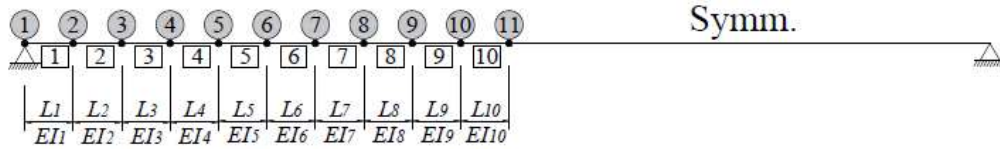


Figure 3-3: Definition of jacketed beam segments

Each point on the $M-\phi$ diagrams (at each segment) can be obtained through an iterative procedure to incorporate the slip strain ($\Delta\varepsilon$) distribution in the analysis at each beam segment. The kinematic and compatibility conditions are considered in view of the corresponding material stress-strain relationships. Assumptions that are made in the developed procedure are:

- 1) Plane sections remain plane after deformation, implying that shear deformations are small relative to bending deformations.
- 2) Perfect bond exists between steel reinforcement and the surrounding concrete material. Thus, strain in both concrete and steel bars at the same location is identical.
- 3) Failure criterion of the composite beam is defined by crushing of the extreme compression fiber as it reaches the concrete ultimate strain (ε_{cu}) of 0.0035 [12] provided that shear failure and rupture of steel bars are forestalled.
- 4) The original RC beam and the added concrete layer are considered to deform by the same curvature throughout the beam length, as usually carried out in mechanics of materials of composite sections [15,19].

The proposed calculation algorithm comprises two main stages. In the first one, the beam is divided into a number of segments having a maximum length of 50 mm each which was found to enhance the accuracy based on a preliminary sensitivity analysis as illustrated in Fig. 3-3. Then, an iterative sectional analysis procedure is performed at different load increments at the mid-span section only to obtain the maximum slip strain ($\Delta\varepsilon_{max}$) at that section and the corresponding slip strain ($\Delta\varepsilon$) and slip (S) at all other beam segments. In the second stage, sectional analysis is conducted directly at the other sections taking into account the $\Delta\varepsilon$ evaluated from the first analysis phase for each beam segment. Details about the developed method are given below.

3.5.1 Iterations at Mid-Span Section

Combining the sectional analysis method [24] with the interfacial slip model [22] at different segments along a jacketed beam provides the base for the developed algorithm as illustrated in the flowcharts in Figs. 3-4 through 3-6. An iterative sectional analysis is carried out at the beam mid-span section to determine the maximum slip strain ($\Delta\epsilon_{max}$) value at various load increments up to failure.

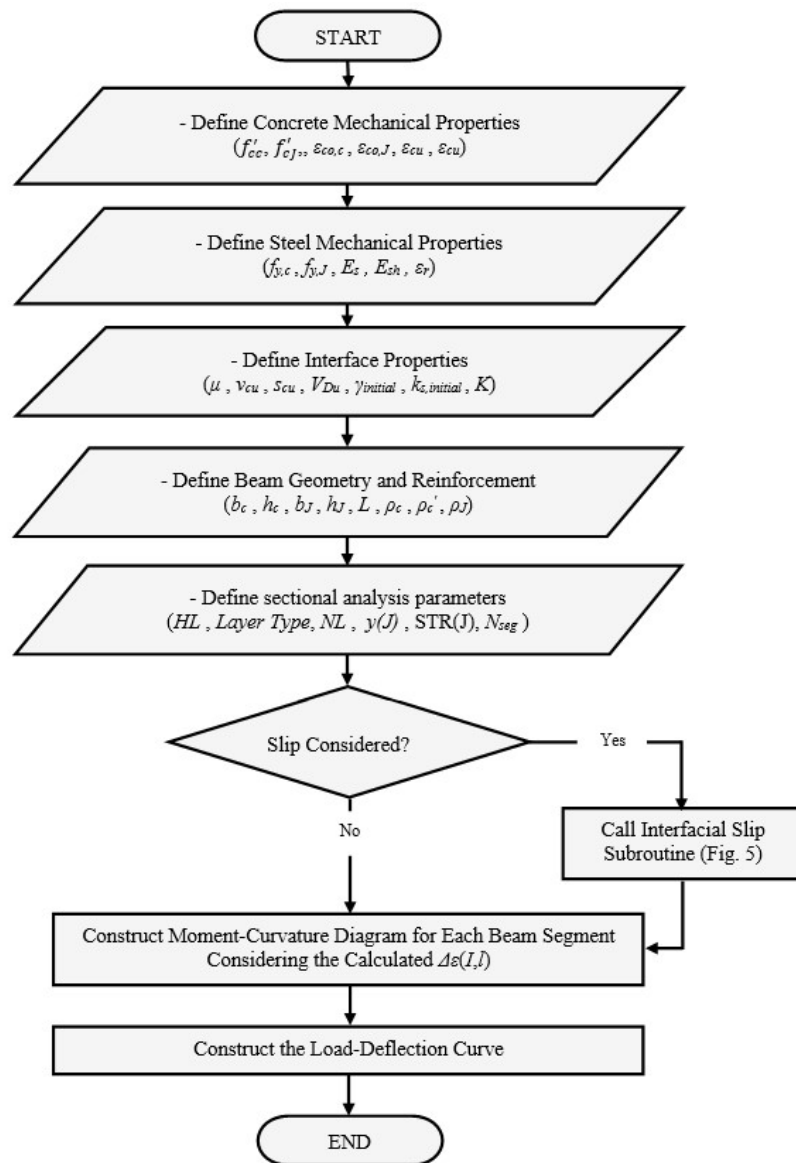


Figure 3-4: Flowchart showing the calculation algorithm to analyze jacketed beams

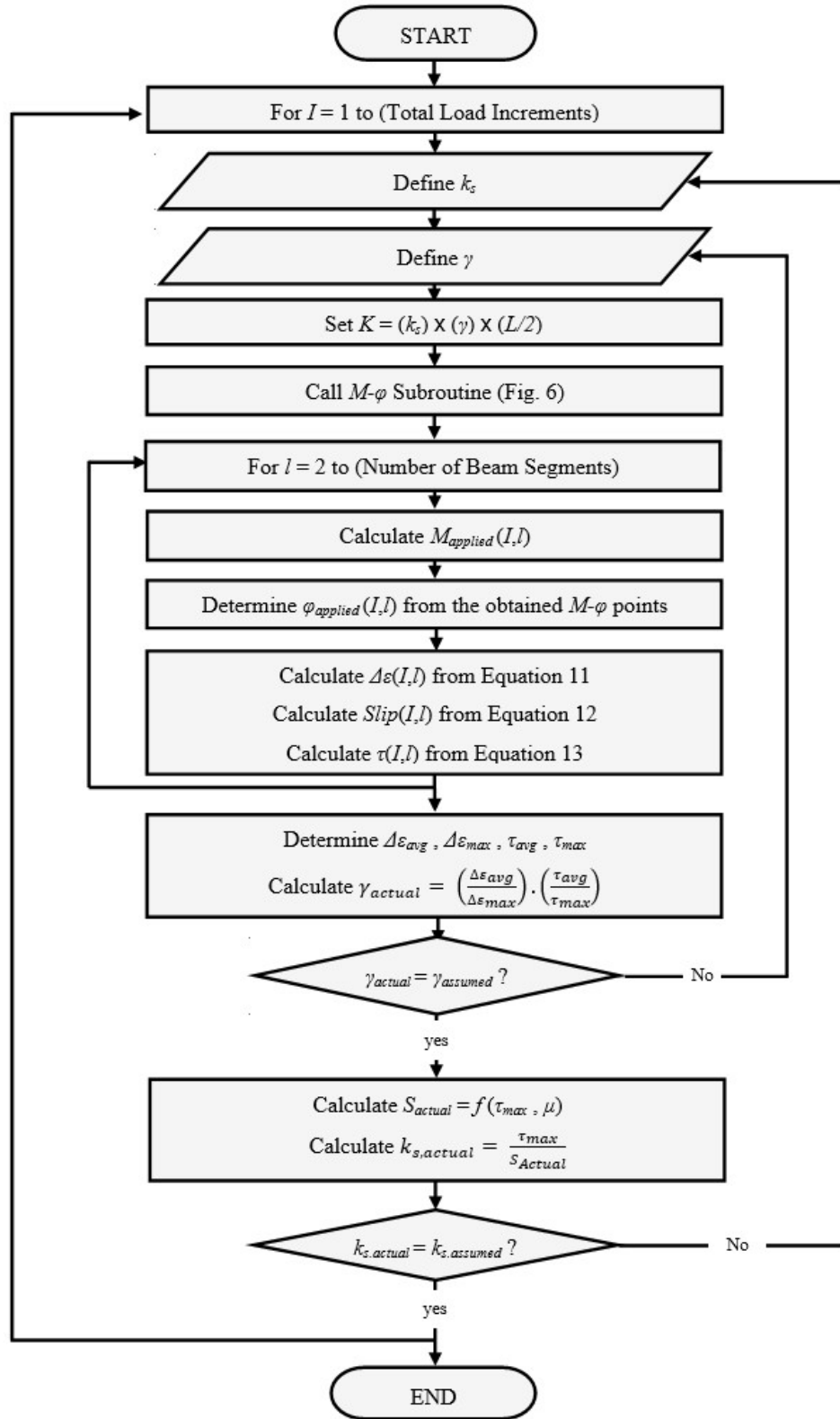


Figure 3-5: Interfacial slip calculation subroutine

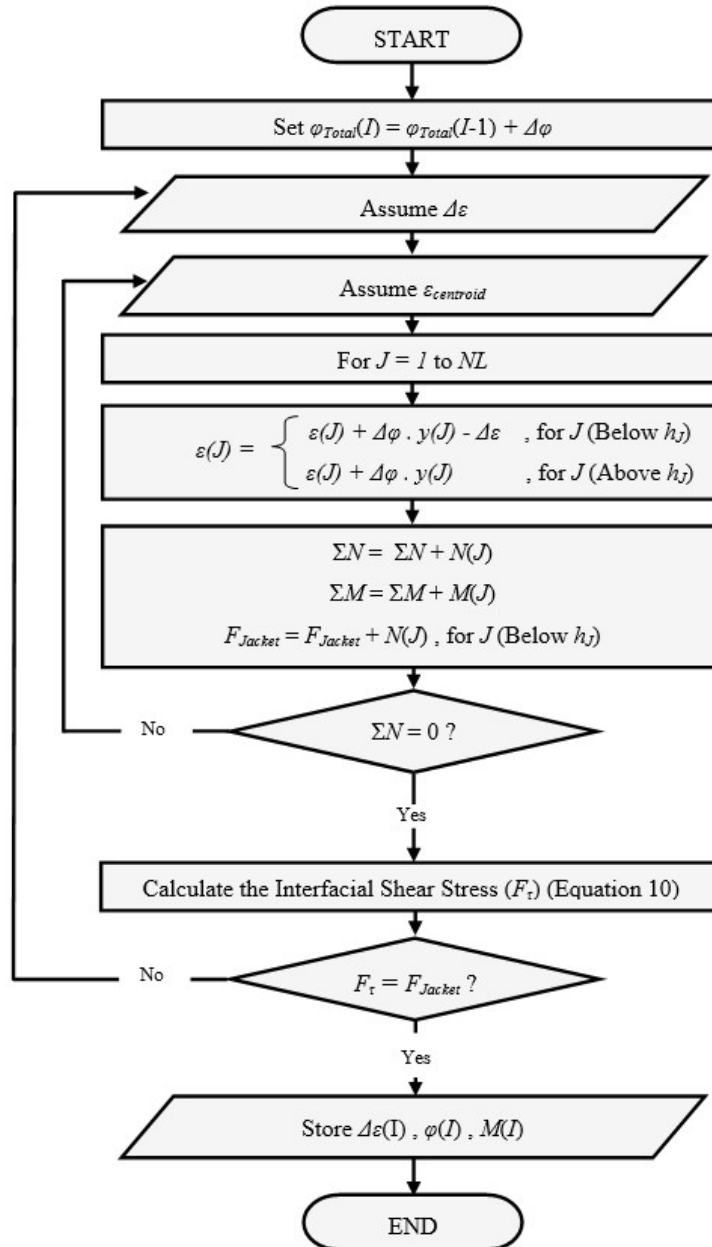


Figure 3-6: Moment-curvature (M-φ) subroutine

The composite section is first divided into multiple discrete strips having a maximum height of 2 mm for better accuracy. At every load step, an incremental curvature ($\Delta\phi$) is applied and the strain at each strip in both the concrete core and the jacket is calculated based on its location from the centroid of the jacketed section. Each curvature increment comprises the following steps:

- 1) Assume a value of the secant interfacial stiffness (k_s).
- 2) Assume a value of the shear stress distribution factor (γ) shown in Equation 8.
- 3) Calculate the global interfacial slip coefficient (K) defined by Equation 8.
- 4) For the total curvature (φ) of the current step, apply two equilibrium conditions at the mid-span section; namely, equilibrium between the internal forces at the section, and equilibrium between the resultant axial forces at one side of the interface and the resultant shear force (F_τ) acting along the interface. The interfacial shear force can be obtained from Equation 10. The outcomes of this step are the moment (M) and maximum slip strain ($\Delta\varepsilon_{max}$) at beam mid-span section corresponding to the current curvature value (φ).
- 5) Determine the load value (P), which produces a moment equal to the value obtained from step 4 at the beam mid-span section. This load is then used to determine the bending moment distribution along the beam. For each beam segment, Fig. 3-3, an average bending moment value is considered.
- 6) Determine the slip strain ($\Delta\varepsilon$) at each beam segment from Equation 11 in which i is the load step number, j is the segment number and m is the load step number that produces a bending moment in the mid-span segment equals to the moment applied at segment j .

$$\Delta\varepsilon_{(i,j)} = \Delta\varepsilon_{(m,1)} \left(\frac{x_j}{(L/2)} \right) \quad (11)$$

- 7) Once the slip strain ($\Delta\varepsilon$) distribution along the interface is established, both the slip (S) and the shear stress (τ) distributions are obtained using the developed equations 12 and 13, respectively.

$$S_{(i,j)} = \sum_{n=1}^{n=j} [(\Delta\varepsilon_{(i,n)})(x_j)] \quad (12)$$

$$\tau_{(i,j)} = k_s S_{(i,j)} \quad (13)$$

- 8) Calculate the shear stress distribution factor (γ), shown in Equation 8, and compare it to the initially assumed value. The analysis continues if they are equal, otherwise the whole procedure is repeated with the new calculated value.
- 9) Determine the secant interfacial stiffness (k_s) value from Tassios and Vintzeleou [22] shear stress-slip model in terms of τ_{max} and compare it to the previously assumed value. The analysis continues if they are equal, otherwise the whole procedure is repeated with the new obtained value.

3.5.2 Obtaining Moment-Curvature Relationship at Other Beam Segments

Having obtained the slip strain ($\Delta\varepsilon$) at each beam segment, a unique $M-\phi$ diagram is determined using sectional analysis method. Then, deflection at the mid-span point of the simply supported beam is determined using the moment-area method. If the beams were subjected to initial loading prior to jacketing, then a preliminary sectional analysis on the unjacketed sections has to be carried out first to obtain the resulting $M-\phi$ curve and strain profile at each beam segment. These diagrams will then be included as an input in the jacketed beam calculation algorithm to obtain the full behavior of the beam at different loading stages before and after jacketing. The calculation algorithm according to the aforementioned procedure and the flow charts in Figs. 3-4 through 3-6 is illustrated in the Appendix considering beam B-3 in Table 3-1.

Table 3-1: Geometry of the Discussed Jacketed Beams

Section	L (m)	b_c (mm)	h_c (mm)	h_J (mm)	Studied Variables
B-1	3	200	300	100	h_J, f'_c, f_y
B-2	3	200	300	150	h_J
B-3	3	200	300	200	b_c, h_c, h_J, L
B-5	3	200	450	150	$\Delta\varepsilon, S, \tau, L_p$
B-6	3	200	450	200	h_c
B-9	3	200	600	200	h_c
B-12	3	300	300	200	b_c
B-21	3	400	300	200	b_c
B-30	4	200	300	200	L
B-57	5	200	300	200	L

3.6 Validation

The capability of the present model to predict the flexural behavior of jacketed RC beams is validated in view of the experimental results obtained by Chalioris and Pourzitidis [1], Chalioris *et al.* [2], Martinola *et al.* [3], Hussein *et al.* [4] and Shehata *et al.* [5]. The geometrical mechanical properties of the examined specimens are detailed in Table 3-2. In general, the proposed model is found to be in a very good agreement with the experimental results as shown in Table 3-2 and Figs. 3-7 through 3-9.

Table 3-2: Description of the examined experimental studies

Reference	Beam	Jacketing Scheme	Geometrical Properties (mm)				Mechanical Properties (MPa)		Percent Error (%)		
			L	b_c	h_c	h_J	f'_c/f'_{cJ}	f_y	Yield	Ultimate	Stiffness
Chalioris and Pourzitidis [1]	B2-J	3 Sides	1400	125	200	25	28.2/42.8	250/φ5 580/φ8	2.9	3.6	4.1
	B4-J	3 Sides	1400	125	200	25	23.4/40.0	250/φ5 580/φ8	7.6	7.5	5.3
Chalioris <i>et al.</i> [2]	B1-M	3 Sides	1400	125	200	25	25.6/40.1	255/φ5 570/φ8	13.4	8.6	19.2
Martinola <i>et al.</i> [3]	HPFRC	3 Sides	4350	300	500	40	22/147	560	4.3	1.7	4.1
Hussein <i>et al.</i> [4]	B-U-0	1 Side	1500	200	200	50	25/111	437	5.5	3.4	3.4
	B-U-1	1 Side	1500	200	200	50	25/111	437	6.5	4.7	5.3
	B-U-2	1 Side	1500	200	200	50	25/111	437	3.5	2.2	6.2
Shehata <i>et al.</i> [5]	V2A	1 Side	4000	150	400	150	38.6/32	500	3.7	4.3	7.3
	V3A	1 Side	4000	150	400	150	39.2/32	500	1.9	2.4	5.9

3.6.1 Chalioris and Pourzitidis [1]

The influence of applying self-compacting concrete (SCC) jackets on the flexural behavior of RC beams was investigated by Chalioris and Pourzitidis [1]. The experimental program commenced by applying monotonic two point concentrated loads on the RC beams to cause some cracks. The load was then removed and a self-compacting concrete (SCC) jacket was applied from three sides to strengthen the cracked

beams. The load-deflection curves for beams B2-J and B4-J were obtained analytically and compared to the experimental results as shown in Figs. 3-7(a) and 3-7(b), respectively. The capability of the model to capture the full deformation behavior is proved by the small error in the yield load, ultimate load and elastic stiffness as indicated in Table 3-2. The slight variation from the experimental results may be attributed to the difference between material properties and friction coefficient used in the analytical model from the actual values.

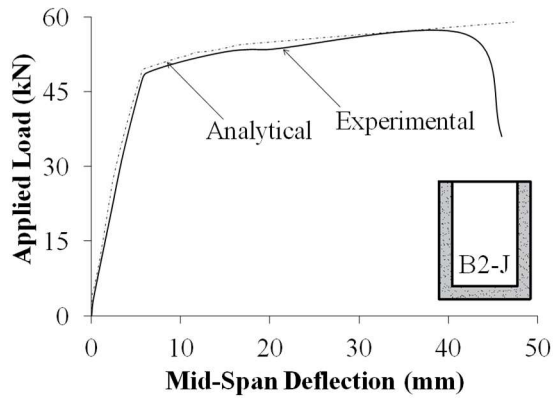
3.6.2 Chalioris *et al.* [2]

In another relevant study, Chalioris *et al.* [2] further investigated the flexural performance of simply supported RC beams jacketed with SCC jackets from three sides. Beam B1-M having the properties shown in Table 3-2 is considered for validation. A comparison between the experimental and analytical moment-deflection relationship of the examined beam is shown in Fig. 3-7(c). Again, the model is found to well predict the actual deformation behavior at different load values. The error associated with yield and ultimate loads does not exceed 7.6% as indicated in Table 3-2. The relatively high stiffness obtained from the analytical model can be justified by the presence of initial cracks in the original beam before jacketing. The detected error may be attributed to the difference in the material models and constitutive relationships that are adopted in the analytical model from the actual behavior of both concrete and steel bars.

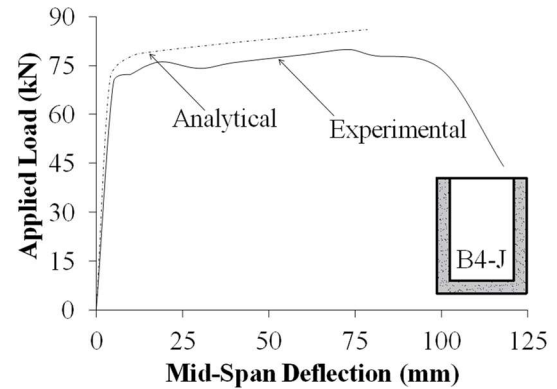
3.6.3 Martinola *et al.* [3]

The flexural behavior of simply supported beams jacketed with high performance fiber reinforced concrete was investigated experimentally by Martinola *et al.* [3]. The jacket material was cast of self-leveling mortar with embedded steel microfibers having a diameter of 0.18 mm and length of 12 mm. The actual material stress-strain behavior was obtained by conducting a direct tensile test on dog-bone specimens and two-point bending tests on unreinforced prisms. The beams were subjected to a displacement controlled load until crushing of concrete occurred. The resulting load-deflection is shown in Fig. 3-7(d) along with the analytically obtained ones assuming a partially composite action. The sudden drop after reaching the peak point is justified by the full

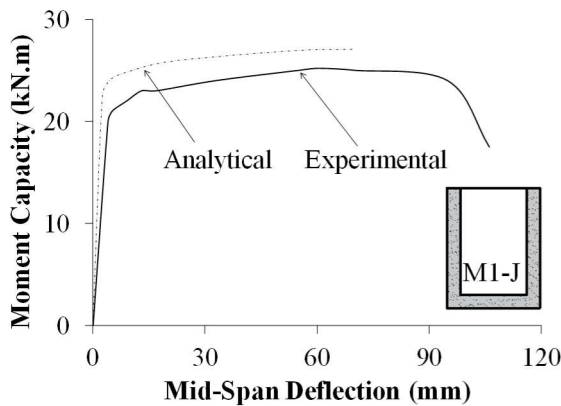
cracking of the jacketing material. As illustrated in Table 3-2, there is an excellent agreement between the analytical and experimental results in the ultimate capacity, yield load and elastic stiffness. This good agreement is obtained as a result of using the actual concrete and steel material properties, which were measured and reported before performing the full-scale experimental program [3].



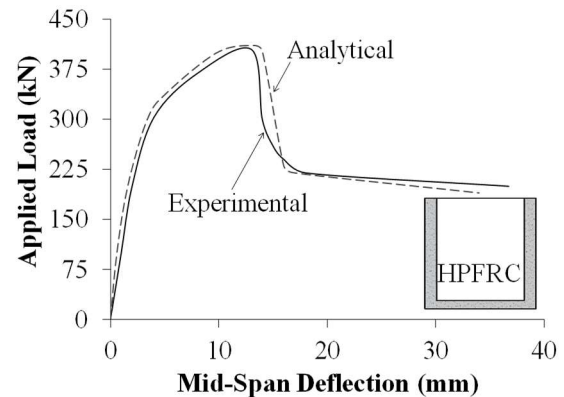
(a) Beam B2-J (Chalioris and Pourzitidis [1])



(b) Beam B4-J (Chalioris and Pourzitidis [1])



(c) Beam B1-M (Chalioris *et al.* [2])



(d) HPFRC (Martinola *et al.* [3])

Figure 3-7: Validation of the proposed analytical model

3.6.4 Hussein *et al.* [4]

The work carried out by Hussein *et al.* [4] examined the effectiveness of providing ultrahigh performance strain hardening cementitious composite (UHP-SHCC) layer with or without a small amount of steel reinforcement. The role of the steel reinforcement is to counteract the stiffness degradation of UHP-SHCC strengthening layer, caused by cracking, and consequently eliminates the observed early strain localization. The overall deformation behavior of beams B-U-0, B-U-1 and B-U-2 are investigated analytically and compared to the experimental results as indicated in Fig. 3-8. The load-deflection curves obtained analytically considering slip effect matches the experimental curves with small percent error in both the elastic and inelastic regions as indicated in Table 3-2. The actual stress-strain relationship of the material reported in the experimental study are used in the analytical model. In addition, a comprehensive description of the surface treatment conditions is provided in the experimental study, which resulted in accurately selecting the value of friction coefficient. These main reasons resulted in minimizing the difference between the experimental and analytical results.

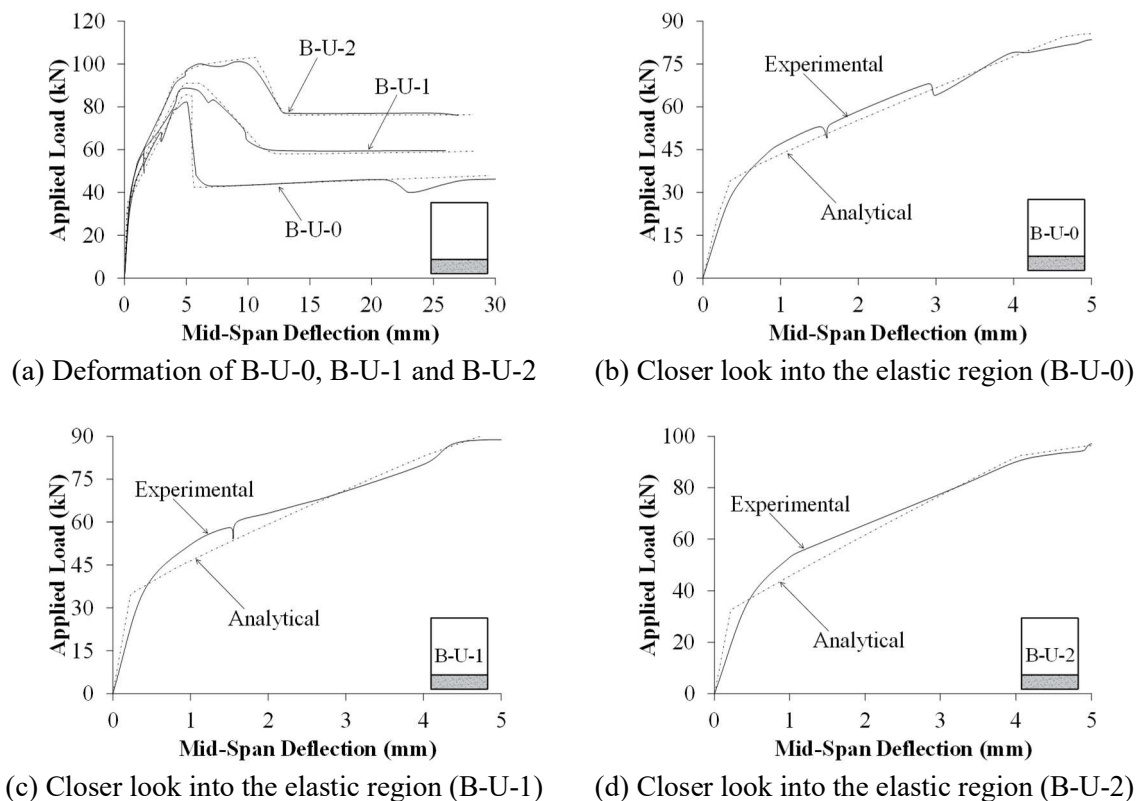
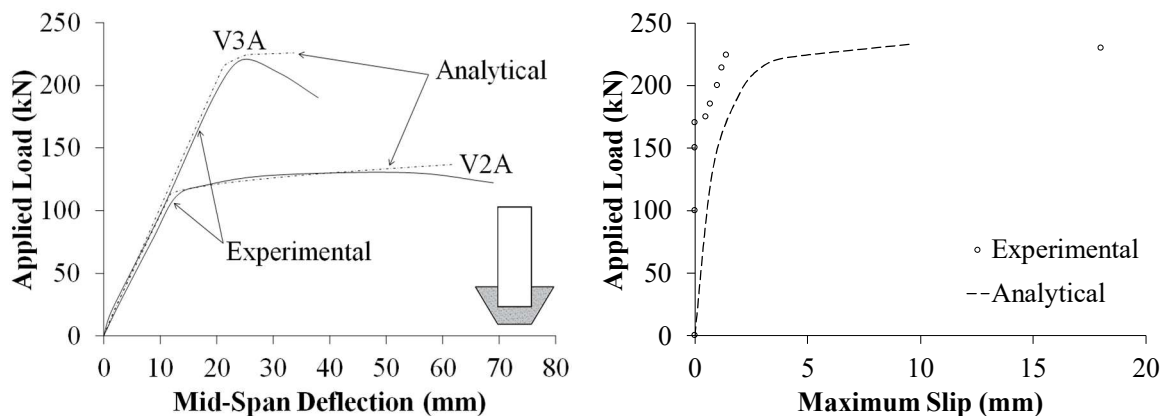


Figure 3-8: Validation of the analytical model (Hussein *et al.* [4])

3.6.5 Shehata *et al.* [5]

Shehata *et al.* [5] studied the influence of various jacketing configurations on the load-deflection and slip behaviors of RC jacketed beams. Beams V2A and V3A are considered in the validation as they vary in the amount of original main steel and the percentage of the added steel in the jacket for flexural strengthening. The beams were loaded at their mid-span by means of controlled hydraulic jack. The experimental study started by loading the unjacketed beams until the strains in their flexural steel reached a value close to 2%. The beams were then unloaded, jacketed and then tested until crushing of concrete took place. A Very good agreement between the analytical and experimental load-deflection curves are shown in Fig. 3-9(a) for beams V2A and V3A. The maximum error in the elastic flexural stiffness and capacity in both beams is small as shown in Table 3-2. The maximum slip recorded at different loading stages for beam V3A was recorded experimentally and compared to the analytical results as shown in Fig. 3-9(b). The slip in the analytical model commences at the onset of load but with an acceptable difference from the actual slip.



(a) Load-deflection curve of V2A and V3A

(b) Maximum slip of V3A

Figure 3-9: Validation of the analytical model (Shehata *et al.* [5])

3.7 Parametric Study

The main parameters are the concrete compressive strength (f'_c), steel yield strength (f_y), coefficient of friction at the interface (μ), existing beam depth (h_c), concrete jacket thickness (h_j), beam width (b_c) and beam span (L). The values of the chosen parameters are set based on the practical considerations in the design of typical RC buildings. The mechanical properties for concrete are defined in terms of concrete compressive strength as 25 MPa, 30 MPa and 35 MPa; and defined for steel in terms of yield strength as 300 MPa, 400 MPa and 500 MPa. In practice, concrete jacket is made from similar or stronger materials than the original beam. Thus, the mechanical properties of both the concrete core and the attached jacket are assumed to be the same in the analysis. The coefficient of friction is assumed to range between 0.4 for smooth concrete surface and 1.4 for intentionally highly roughened concrete in increments of 0.2. The beams' cross-sectional dimensions are defined with reference to the unjacketed beam height (300 mm, 450 mm and 600 mm), jacket thickness (100 mm, 150 mm and 200 mm), unjacketed beam width (200 mm, 300 mm and 400 mm), and span (3 m, 4 m and 5 m). The main steel reinforcement in the concrete core is set as 0.01 and 0.02. The amount of jacket reinforcement is decided based on the maximum practical spacing for 10M bars placed in one layer to resist flexural loads according to CSA A23.3-14 [12]. The compression steel reinforcement is fixed at 2- ϕ 6mm bars in all beams. Two jacketing schemes are adopted in the analysis. In the first one, the beams are jacketed at their soffits only; whereas in the second configuration, the beams are jacketed from three sides forming a U-shape. Therefore, for each jacketing scheme, a total of 10,206 cases are considered in the analysis. The following discussion refers to the beam sections in Table 3-1 for the cases involving $f'_c = 30$ MPa, $f_y = 400$ MPa and $\mu = 0.4$ unless otherwise specified.

3.8 Flexural Behavior of the Jacketed Beams

3.8.1 Effect of Beam Width (b_c)

The effect of varying beam width (b_c) on the $M-\phi$ relationship for simply supported beam jacketed from 1 side and 3 sides is shown in Fig. 3-10. Beams B-3, B-12 and B-21 are

considered for comparison. Increasing b_c increases the beam's elastic stiffness and capacity.

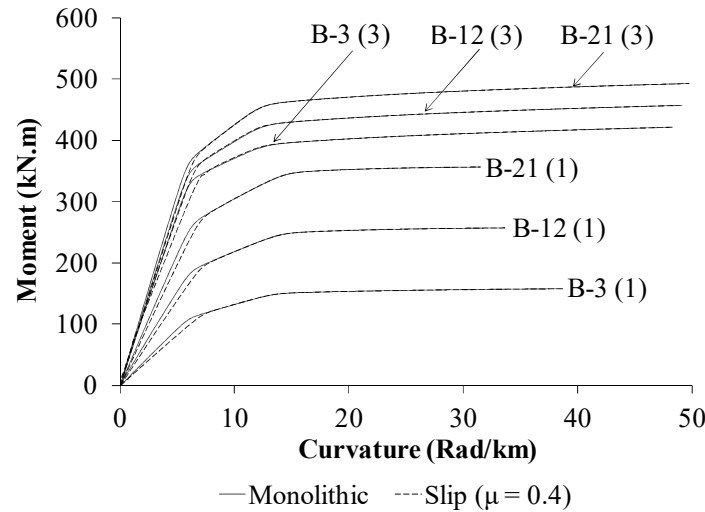


Figure 3-10: Effect of varying b_c on the $M-\phi$ relationship

The two sudden changes in the slope indicate the jacket reinforcement yielding followed by core steel bars yielding. The elastic stiffness decreases when slip is considered and the extent of this reduction has an inverse relationship with the beam width. Increasing the beam width increases the contact surface between the concrete core and the attached jacket. The relative slip between the two surfaces results in a strain reduction ($\Delta\varepsilon$) in the jacket layer that delays the onset of jacket reinforcement yielding. Once jacket yielding is reached, the $M-\phi$ behavior becomes identical to the one obtained assuming a full composite section. The behavior of the beam jacketed from 3 sides exhibits the same behavior of the one jacketed from 1 side. However, the extent of stiffness reduction is less significant due to the larger contact area provided by the U-shape jacket.

When slip is considered in the analysis, the $M-\phi$ diagram varies at each segment in the beam as discussed previously. The load-deflection curve has an advantage in capturing the full behavior along the entire beam span making it easier to track the overall flexural behavior as shown in Fig. 3-11.

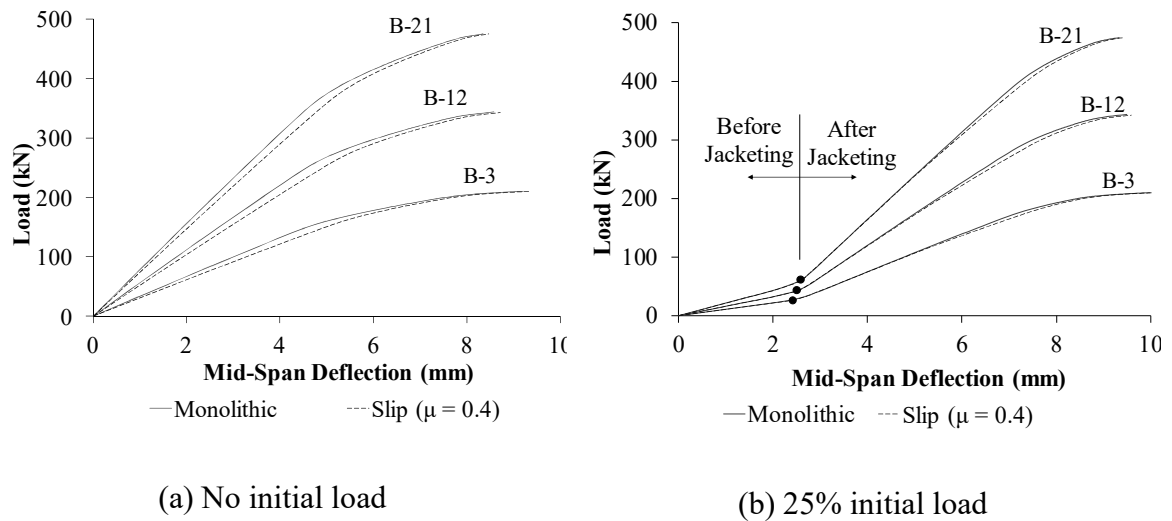


Figure 3-11: Effect of varying b_c on the $P-\Delta$ relationship jacketed along one side

For initially unloaded one-side jacketed beams, increasing the beam width is found to increase its capacity by about 25% as illustrated in Fig. 3-11(a). Any increase in core width for beams jacketed from one side results in a more significant increase in the capacity compared to the beams jacketed from three sides. Also, the overall drop in the initial flexural stiffness decreases as the core width increases for the examined range. The stiffness reduction is more pronounced in the beams jacketed from three sides since larger total jacket width is considered in the analysis. The load-deflection curves for the beams jacketed from one side and initially subjected to 25% of their unjacketed capacities are presented in Fig. 3-11(b). Adding extra reinforced concrete layer in the jacket results in a significant increase in the elastic stiffness by more than 50%. All beams failed by concrete crushing at the same ultimate load regardless of the initial load they were subjected to prior to jacketing. Initially loaded beams experience more ductility as the additional jacket steel bars were unstressed at the moment the partial interaction between the core and the jacket commenced. The influence of slip on reducing the flexural stiffness of the jacketed beams becomes less pronounced when jacketing takes place at higher initial loads. This is caused by the relatively low stresses within the jacket compared to the ones generated in the existing beam due to the initial load.

In the subsequent discussions, influence of slip on the moment-curvature and load-deflection relationships has a similar trend to the curves shown in Figs. 3-10 and 3-11 but with different magnitudes, respectively. Thus, repetition of the specific curves for each parameter is not shown but can be understood in view of Figs. 3-10 and 3-11.

3.8.2 Effect of Jacket Thickness (h_j)

Increasing jacket thickness has a direct impact on both the yield and ultimate capacities of the strengthened beams owing to the increase in cross-sectional area and lever arm to the steel bars within the jacket. This rise is more pronounced in beams jacketed from three sides since part of the jacket extends above the neutral axis and contributes more in resisting the compressive stresses. Using the U-shape jacket increases the flexural ductility up to 18% for the considered range of jacket thicknesses. Doubling the jacket thickness from 100 mm to 200 mm results in increasing the capacity by just over 15% when the beam is jacketed from its soffit and by around 53% when it is jacketed from three sides. In all sections, larger drop in the elastic stiffness is observed as the jacket thickness increases. However, the reduction becomes less significant and almost constant if the beam is jacketed from three sides. For initially loaded beams, adding the reinforced concrete layers at a later stage results in increased overall ductility while maintaining the same ultimate capacity. Also, the load-deflection curves considering the interfacial slip tend to approach the ones obtained assuming monolithic sections for the same aforementioned reasons.

3.8.3 Effect of Existing Beam Height (h_c)

The variation of concrete core height is discussed in view of beams B-3, B-6 and B-9. Cross-sectional height plays a major role in increasing the concrete area subjected to compression. It also increases the lever arm of not only the jacket steel reinforcement, but also the main core steel bars. This results in a significant increase in both the elastic stiffness and the ultimate strength while reducing ductility. By doubling the core height from 300 mm to 600 mm, the initial stiffness increase by about four folds and approximately three times for the beams jacketed from one side and three sides, respectively. The stiffness reduction due to slip is found to decrease slightly as the

concrete core height increases for both jacketing configurations. For initially loaded beams, the flexural behavior of the jacketed beams approaches the monolithic assumption as the initial load increases. Therefore, slip influence can be ignored if jacketing takes place while the beam is subjected to a significant percentage of its ultimate capacity.

3.8.4 Effect of Beam Span (L)

The effect of changing the span on the flexural behavior of jacketed beams is presented in view of beams B-3, B-30 and B-57. If a monolithic interaction is assumed, then the beams' flexural behavior depends merely on the section geometry and does not vary regardless of the span. However, if partial interaction is considered in the analysis, then the span length becomes a major parameter in determining the actual $M-\phi$ behavior of the jacketed beams. Increasing the beam span results in a consequent reduction in the ultimate capacity but a significant increase in ductility. As the span increases, the contact area between the concrete core and the attached jacket also increases resulting in higher interfacial frictional forces and consequently lower relative displacement between the two surfaces. Increasing the span from 3 m to 5 m results in a drop of the initial stiffness by about 40% and 60% for the beams jacketed at their soffit and three sides, respectively. It is worth mentioning that increasing the span becomes more significant as the jacket width increases. This causes the beams surrounded by jacket from three surfaces to exhibit less initial stiffness reduction relative to the ones jacketed from one side only. Also, the stiffness reduction rate decreases as the span increases as indicated by the 13%, 8% and 5% drop in initial stiffness for the one-side jacketed beams B-3, B-30 and B-57, respectively. The same observation is shown for the other jacketing scheme but to a less extent as indicated by the 9%, 6% and 4% reduction in initial stiffness for the same beams, respectively. Applying the jacket once the existing beam reaches 25% or 50% of its ultimate capacity reduces the influence of interfacial slip on the flexural behavior of the jacketed beams.

All of the examined beams experience flexural mode of failure as sufficient stirrups are provided to eliminate premature shear failure. Moment-shear interaction along the span is examined in view of Russo *et al.* [25] proposed expressions for M_u/M_{fl} , where M_u is the flexural capacity including shear influence and M_{fl} is the pure flexural capacity. For all of

the examined beams, it was found that decreasing the shear span to depth ratio (L_s/d) results in a more pronounced reduction in flexural capacity. For instance, a drop of about 19% and 27% in the flexural capacity of beam B-3 subjected to a mid-span concentrated load and uniform load, respectively. On the other hand, the change in capacity in beam B-57 is less significant due to the longer span. The same conclusion was obtained by Chalioris and Pourzitidis [1] who experimentally examined the behavior of jacketed RC beams with various L_s/d ratios.

3.8.5 Effect of Concrete Compressive Strength (f'_c)

Increasing the concrete compressive strength increases the stiffness and capacity of the jacketed beams for both 1 side and 3 sides jacketing configurations. However, its influence is found to be more pronounced in the latter case. This is justified by the greater area of concrete subjected to compression that results in higher stiffness and capacity. Considering beam B-1, a 12% increase in capacity for the U-shape jacketed beam is shown compared to the 5% for the other jacketing scheme. In addition, flexural ductility is shown to have a direct relationship with concrete compressive strength and jacketing scheme. For the same concrete grade, ductility is more remarkable when the beam is jacketed from three-sides. Furthermore, slip reduction rate within the elastic range decreases as the compressive strength increases because of the larger surface friction provided at the interface corresponding to the stronger concrete. This explains the 11% and 5% drop in the initial stiffness for the beam cast of concrete grades 25 MPa and 35 MPa, respectively.

3.8.6 Effect of Steel Yield Strength (f_y)

An inverse relationship between the steel grade and the ductility of the entire beam is detected due to the fact that the ductility of steel bars decreases as their ultimate strength increases. For the same steel grade, it is found that the ultimate curvatures the beams reached are almost the same regardless of the jacketing scheme. The initial stiffness for all beams with the same jacketing configuration is identical since all steel bars share the same elastic stiffness. The stress in all steel bars is related to the modulus of elasticity within the elastic region and thus follows a linear pattern. Variation in the reduction of

the initial stiffness between the beams reinforced with steel bars of different grades is not substantial. This observation is explained by knowing that once the steel bars in both the jacket and the core have been yielded, the resistance becomes almost identical to the beam behaving monolithically. Thus, the main reduction in stiffness is witnessed in the elastic zone.

3.9 Interfacial Slip Behavior

The partial interaction between the existing concrete beam and the attached jacket is better understood in view of the slip strain, slip and horizontal shear distribution along the interface. The following discussion is presented in view of beam B-5 whose geometrical properties are shown in Table 3-1 with $f'_c = 30$ MPa and $f_y = 400$ MPa. Two values of friction coefficient are considered to account for smooth surfaces ($\mu = 0.4$) and intentionally roughened surfaces with sandblasting ($\mu = 1.0$).

3.9.1 Slip Strain ($\Delta\varepsilon$) Distribution

The slip strain distribution along half the beam span at different load levels for the first jacketing scheme are illustrated in view of Figs. 3-12(a) and 3-12(b) for smooth and rough surfaces, respectively.

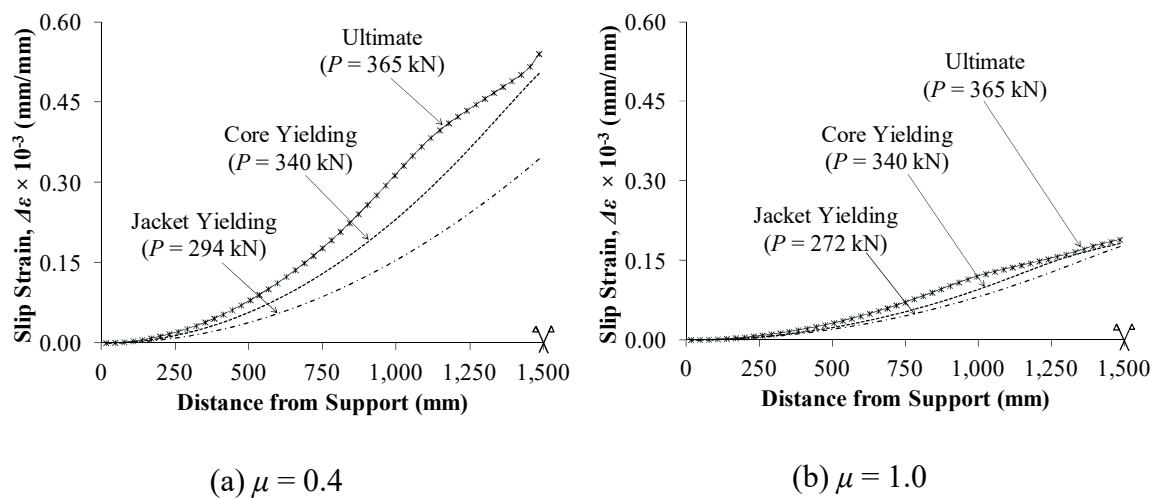


Figure 3-12: Slip strain ($\Delta\varepsilon$) distribution along beam B-5 jacketed along one side

The shown loading values cover the beam onset of jacket yielding, core yielding and ultimate load reached before failure. The slip strain takes its maximum value at mid-span and diminishes as it approaches the supports. The increase in slip strain when the beam is undergoing elastic deformation is proportional to the value of the applied load. This rate of increase changes as yielding of jacket steel reinforcement initiates at beam segments close to the mid-span. This is justified by the reduction in flexural stiffness caused by yielding of these steel bars at these segments. As the load further increases, the slip strain keeps increasing but with a decreasing rate in the segments that exceeded the core yielding point. For the remaining segment that are still behaving elastically, the increasing rate of the slip strain remains almost constant until concrete crushes at the mid-span section. Figs. 3-12(a) and 3-12(b) show that as the friction coefficient increases, the slip strain at any segment decreases under the same applied load. This is true because the rougher the surfaces, the higher resistance to relative sliding they will exhibit, and consequently the lower slip strain they will possess. Thus, as the friction coefficient increases, the interfacial behavior approaches the monolithic action assuming full bond between the core and the added concrete layers. The loading values at jacket yield, core yield and ultimate of the three-side jacketed beams are higher than the ones obtained from the former jacketing case due to the larger available concrete area that counteracts the compressive stresses. Despite of these higher loads, the slip strain values along the entire beam are shown to be less than the ones obtained from one side jacketing for the same friction coefficient. This is explained by the larger contact area available between the existing beam and the surrounding jacket that causes a higher increase in frictional resistance that counteracts the relative movement between the two substrates. Hence, increasing the contact area through adopting the U-shape jacket is found to shift the interfacial behavior of the jacketed beams closer to the monolithic action.

3.9.2 Slip (S) Distribution

The slip distribution along the interface for the beam jacketed from one side is presented in Figs. 3-13(a) and 3-13(b) for friction coefficient of 0.4 and 1.0, respectively. Due to geometrical and loading symmetry, the distribution is presented along one half the span

only. Slip is shown to approach its maximum value at the supports and decreases gradually towards the beam mid-span.

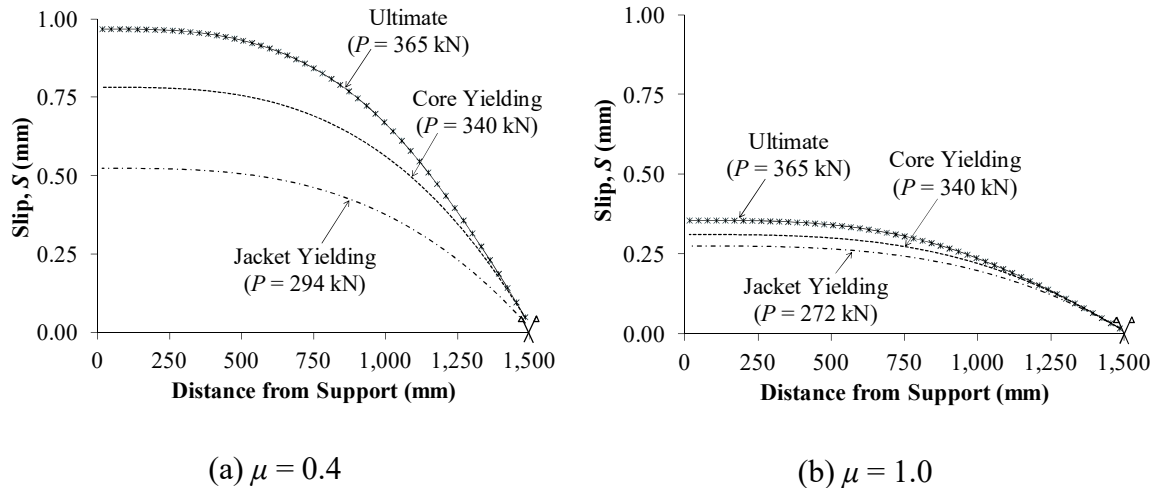


Figure 3-13: Slip distribution (S) along beam B-5 jacketed from one side

The rate of slip increase is constant from the instance the beam is loaded until the steel reinforcement within the jacket are yielded. Beyond this point, the slip rate keeps increasing with an increasing rate due to the yielding of the segments adjacent to the mid-span where the maximum moment is present. Although the beam failure occurred at a load of 365 kN for both friction coefficients, the maximum slip reached considering smooth surfaces is about 62% less than the one obtained for the rougher surfaces. Extending the concrete layers around the sides of the beam to form a U-shape results in higher contact area and lower slip values along the interface for the smooth and rough surfaces, respectively. The reduction in maximum slip by increasing the surface roughness is found to be just over 59% which is very close to the value obtained for the former case. Since the stiffness reduction is directly related to the relative movement activated between the two surfaces, the beams jacketed from three sides exhibit less stiffness reduction than the ones jacketed from one side under the same surface treatment.

3.9.3 Interfacial Shear Stress (τ) Distribution

The horizontal shear stress distribution along the interface is directly related to the slip distribution through the stiffness coefficient (k_s). As the slip increases, the secant stiffness

coefficient decreases and consequently the calculated shear stress increases but with a decreasing rate as indicated in Figs. 3-14(a) and 3-14(b) for smooth and rough surfaces, respectively.

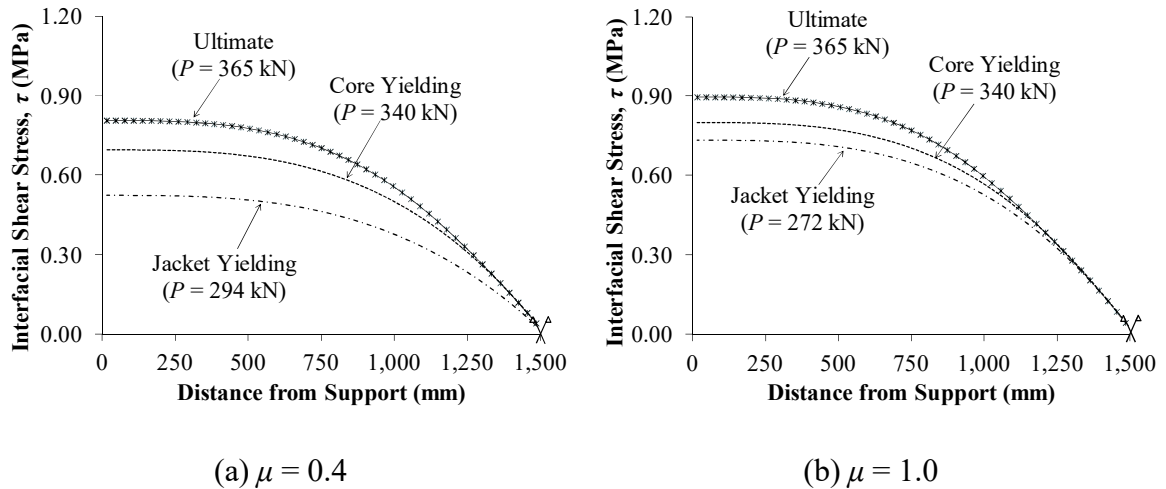


Figure 3-14: Interfacial shear stress distribution (τ) along beam B-5 from one side

Adopting the U-shape jacketing scheme increases the interfacial stiffness coefficient resulting in higher horizontal shear stress resistance for the same slip value. For instance, the maximum slip at ultimate obtained at $\mu = 0.4$ for the first case is 0.96 mm and for the second case is 0.45 mm. However, the corresponding interfacial shear stress is found to be 0.76 MPa and 1.25 MPa for the same cases. This indicates that the stiffness coefficient is about 0.8 N/mm for the one side jacketing scheme and 2.8 N/mm for the U-shape jacketing configuration at the same load level. This interfacial stiffness variation is justified by the larger contact area and the higher frictional resistance between the two surfaces offered by the three sides jacketing compared to the one side jacketing scheme. Another observation shows that increasing the friction coefficient from 0.4 to 1.0 results in a consequent increase in the maximum slip at ultimate by about 16% for the first case and by 7% for the second case. This increase results from the increased interfacial frictional resistance provided by the rougher surface treatment and hence the higher friction coefficient.

3.9.4 Plastic Hinge Region

The formation of a plastic hinge has a detectable influence on the deformation behavior of the examined jacketed beams. The length of the plastic hinge zone (L_p) is defined by the extent of reinforcement yielding within the concrete jacket. The nonlinear material behavior and slip along the interface requires detailed analysis of the jacketed beams. Figure 3-15(a) illustrates the curvature distribution from the support to the mid-span of beam B-5 corresponding to the ultimate load.

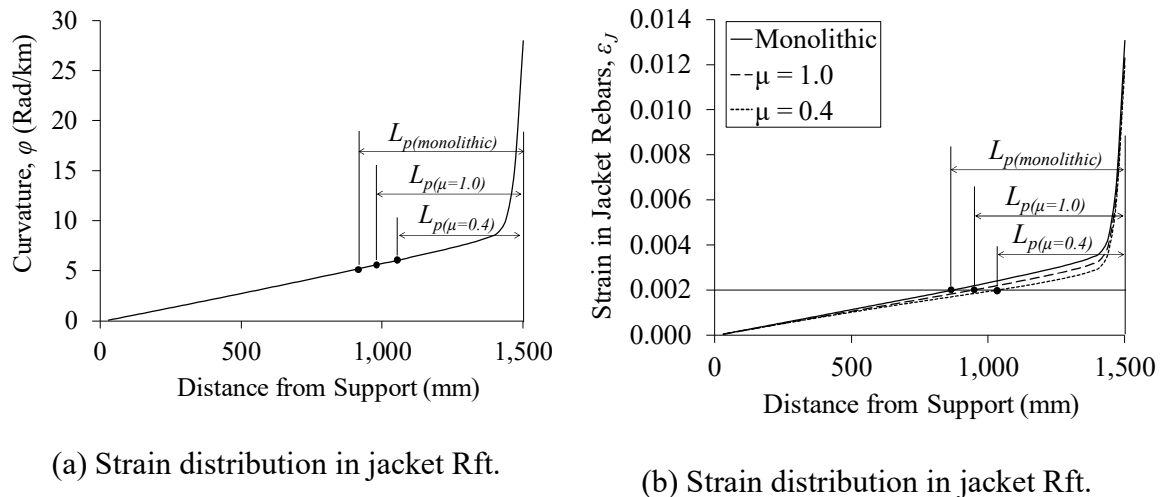


Figure 3-15: Interfacial shear stress distribution (τ) along beam B-5 from one side

It is shown that decreasing the friction coefficient results in reducing the length of the developed plastic hinge. Considering a monolithic interaction between the original beam and the attached jacket, the plastic hinge is found to extend a distance of 582 mm toward each side from the mid-span. Reducing the friction coefficient to 1.0 and 0.4 results in a consequent reduction of 10.6% and 21.1%, respectively. This change in behavior is attributed to the stress redistribution that result from the sudden drop in strain at the interface ($\Delta\epsilon$) depending on the friction between the two surfaces. For a smaller friction coefficient, $\Delta\epsilon$ increases causing the strain in the jacket reinforcement to be less than the developed strain in its monolithic counterpart. Fig. 3-15(b) provides further clarification of this observation through plotting the distribution of the strain in the jacket bars from support to the mid-span at ultimate load. The distance from the mid-span to the point on the curve corresponding to yield strain ($\epsilon_y = 0.002$) represents the plastic hinge region

along half the beam span. This zone represents the location where the tensile jacket reinforcement has attained or exceeded its yield value. For the same applied load, decreasing the coefficient of friction reduces the generated strains in the steel bars and consequently results in decreasing the extent of the plastic hinge region. The sudden increase in the curvature and strain distribution in Fig. 3-15 reflects the onset of yielding of the core reinforcement.

3.10 Proposed Expressions for the Monolithic Factors

The influence of interfacial slip on the flexural behavior of jacketed RC beams is found to have a reduction in their stiffness especially prior to reaching the core yielding point. Assuming monolithic action in the design of jacketed sections may result in serviceability issues related to excessive deflection and undesirable cracks formation. Including the influence of slip in the analysis is tedious and requires a sequence of nested iterations that may not be convenient for design engineers. Therefore, based on the analytical results conducted on the 20,412 beam specimens, some expressions are developed to plot the actual load-deflection curve of the jacketed beams including slip effects. The difference in load-deflection behavior between a typical monolithic and partially composite jacketed beams not subjected to initial load prior to strengthening is illustrated in Fig. 3-16(a). The same information is detailed in Fig. 3-16(b) but taking into consideration the presence of initial load on the overall flexural behavior.

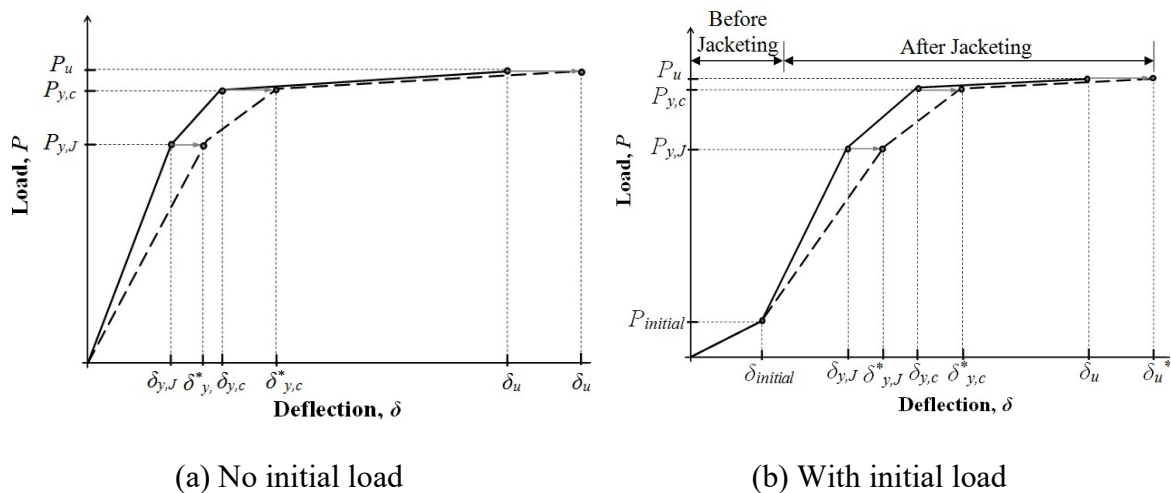


Figure 3-16: Stiffness reduction model for a typical jacketed beam

The main parameters defining these curves are the jacket yield load ($P_{y,J}$) and the corresponding deflections assuming monolithic ($\delta_{y,J}$) and partially composite ($\delta_{y,J}^*$) actions; core yield load ($P_{y,c}$) and the corresponding deflections assuming monolithic ($\delta_{y,c}$) and partially composite ($\delta_{y,c}^*$) actions; and ultimate load (P_u) and the corresponding deflections assuming monolithic (δ_u) and partially composite (δ_u^*) actions. For the initially loaded beams scenario, two additional terms are introduced that define the both the load ($P_{initial}$) and the deflection ($\delta_{initial}$) corresponding to the initial loading value at the onset of jacketing. According to Fig. 3-16, the monolithic trilinear load-deflection curve of the jacketed beam can be first plotted at three points defined by the jacket yield, core yield and ultimate. Then, the stiffness of each line is reduced indirectly by multiplying the jacket yield deflection, core yield deflection and ultimate deflection by the jacket yield monolithic factor ($\alpha_{y,J}$), core yield monolithic factor ($\alpha_{y,c}$) and ultimate monolithic factor (α_u), respectively. Expressions of the aforementioned factors are derived through performing a non-linear regression analysis on the data points and given in Equations 14 and 15 in terms of the material mechanical properties, interfacial friction coefficient and the jacketed beam geometrical dimensions.

$$\alpha_i = (A_1 \xi^2 + A_2 \xi + A_3) \times [A_4 \exp(A_5 \mu)] \geq 1.0 \quad (14)$$

$$\begin{aligned} \xi = C_1 + C_2 \rho + C_3 f'_c + C_4 f_y + C_5 L + C_6 b_c + C_7 h_c + C_8 h_J + C_9 \frac{\rho f_y}{f'_c} + C_{10} \frac{h_J}{h_c} + C_{11} \frac{b_c}{L} \\ + C_{12} \rho b_c h_c \end{aligned} \quad (15)$$

Where μ is the coefficient of friction, ρ is the steel reinforcement ratio, f'_c is the concrete compressive strength (MPa), f_y is the steel yield strength (MPa), L is the beam span (m), b_c is the original cross-sectional width (m), h_c is the original cross-sectional height (m), h_J is the jacket thickness (m). The coefficients $(A_i)_{i=1,2,3,4,5}$ and $(C_i)_{i=1,2,3,4,5,6,7,8,9,10,11,12}$ for each monolithic factor (i.e. $\alpha_{y,J}$, $\alpha_{y,c}$ and α_u) are given in Table 3-3 as a function of the jacketing scheme.

Table 3-3: Coefficients Used to Calculate $\alpha_{y,J}$, $\alpha_{y,c}$ and α_u in Equations 14 and 15

	Jacketing Scheme					
	One-Side (Bottom)			Three-Sides (U Shape)		
	$\alpha_{y,J}$	$\alpha_{y,c}$	α_u	$\alpha_{y,J}$	$\alpha_{y,c}$	α_u
A_1	2.6899961649	36.96861446	41.981867551	4.438599382	75.725029793	82.439153754
A_2	- 5.134946995	- 73.83647068	- 83.92806393	- 8.333525868	- 151.3706306	- 164.8292489
A_3	3.479735767	37.870955816	42.948454867	4.9037982627	76.647175373	83.391236967
A_4	1.6286381500	1.9235439146	2.1064756518	2.3942208560	2.2535194858	1.9741828085
A_5	- 1.200125896	- 1.602941595	- 1.905764829	- 2.332570206	- 2.370423110	- 2.453134776
C_1	1.47472	1.03673	1.00242	1.15853	1.0183	1.00177
C_2	10.0270	0.17240	- 0.08430	2.58620	0.1083	0.06280
C_3	- 0.0005273	0.0003043	0.0004479	- 0.0002683	0.0001383	0.00018642
C_4	0.0000482	- 0.00001012	- 0.00001189	0.00001066	- 0.00000385	- 0.00000425
C_5	- 0.1175	- 0.01127	- 0.00881	- 0.03016	- 0.0056	- 0.00461
C_6	0.49459	0.04989	0.03798	- 0.01821	0.0241	0.02229
C_7	0.03576	0.00143	0.01821	- 0.01393	0.0004	0.0109
C_8	0.93104	0.0881	0.06117	0.35399	0.04704	0.02744
C_9	- 0.13484	0.03868	0.10403	- 0.03108	0.01634	0.045543
C_{10}	- 0.09899	0.005892	0.021324	- 0.04814	0.002406	0.01155
C_{11}	- 3.0016	- 0.29909	- 0.18542	- 0.4079	- 0.14899	- 0.10340
C_{12}	- 17.54	- 1.22	- 3.08	- 1.44	- 0.50	- 1.70

If the beams were subjected to initial loading before jacketing, then the monolithic factors should be reduced according to the expression given in Equation 16.

$$(\alpha_i)_{initial} = \alpha_i - \left(\frac{P_{initial}}{P_{u,unjacketed}} \right)^B (\alpha_i - 1.0) \geq 1.0 \quad (16)$$

Where the factor B is taken as 1.432, 0.921 and 0.426 for the jacket yield ($\alpha_{y,J}$), core yield ($\alpha_{y,c}$) and ultimate (α_u) monolithic factors, respectively.

The expectation function of the proposed monolithic factors is determined considering nonlinear regression analysis of the data. Figs. 3-17(a) and 3-17(b) presents the line of equality corresponding to $\alpha_{y,J}$, $\alpha_{y,c}$ and α_u for both the one-side and three-sides jacketing schemes. The line of equality plots for all factors reveal that the model provides a very good prediction of the actual behavior. The residuals for the three factors clearly shows a uniformly distributed pattern of the residuals about the mean. The presence of outliers is almost negligible which enhances the confidence of using the proposed expressions.

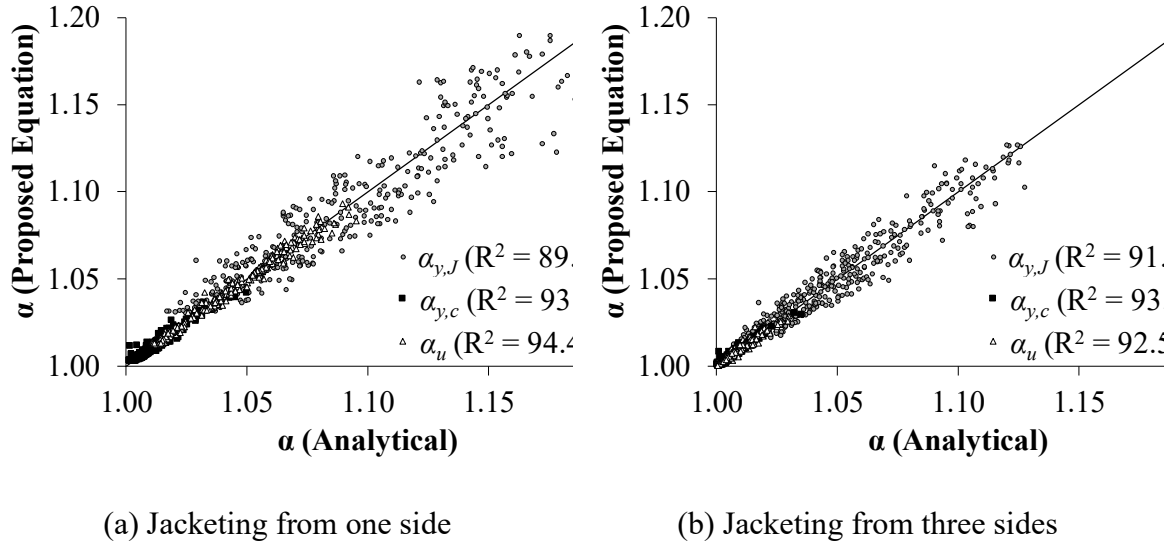


Figure 3-17: Statistical analysis for the proposed expressions for $\alpha_{y,J}$, $\alpha_{y,c}$ and α_u

3.11 Conclusions

An analytical procedure for predicting the flexural behavior of jacketed RC beams is presented in this chapter. The procedure introduces the influence of interfacial slip between the original substrate and the added concrete layer on the moment-curvature and load-deflection relationships. Sectional analysis methodology is extended in the current research to consider the nonlinear properties of both the core and jacket layers simultaneously. The model is validated against relevant experimental results in literature and found to have very good agreement in terms of load-deflection relationship and maximum interfacial slip. Although the proposed model is applicable for beams subjected to uniform loads, literature lacks experimental results related to such loading condition and additional experimental work is required for further validation. Several parameters including material mechanical properties, steel reinforcement ratio, surface treatment conditions, beam span and its cross-sectional dimensions are considered in a parametric study. The parametric analysis encompasses a total of 20,412 beams jacketed from either one side or three sides. Flexural mode of failure is observed in all of the examined specimens regardless of the considered friction coefficient. Investigation of the aforementioned parameters has led to a comprehensive assessment of their significance as well as full description of the developed slip and shear stress distribution. The effect of

moment-shear interaction and the development of plastic hinges in the jacketed beams were highlighted. The parametric study culminated in proposing slip modification factors that can be manipulated by engineers to accurately plot the load-deflection curves of jacketed RC beams taking into account slip impact.

3.12 Appendix

Sample calculation of the proposed analytical model and the flowcharts in Figs. 3-4 through 3-6 considering beam B-3 defined in Table 3-1.

1) Define the Inputs:

Concrete properties: $f'_{cc} = 30$ MPa, $f'_{cJ} = 30$ MPa, $\varepsilon_{co,c} = 0.002$, $\varepsilon_{co,J} = 0.002$, $\varepsilon_{cu} = 0.0035$

Steel properties: $f_{yc} = 400$ MPa, $f_{yJ} = 400$ MPa, $E_s = 200$ GPa, $E_{sh} = 2$ GPa, $\varepsilon_r = 0.2$

Beam geometry: $b_c = 200$ mm, $h_c = 300$ mm, $b_J = 200$ mm, $h_J = 200$ mm, $L = 3$ m

Reinforcement: $\rho_c = 0.5 \rho_{balance} = 0.5 \times 0.0263 = 0.01315$, $A_{s,J} = A_{bar} \times S_{max} = 100 \times 15.8 = 158$ mm

Sectional analysis parameters: $HL = 2$ mm, $NL = 250$, $N_{seg} = 60$

Slip coefficients: $\mu = 0.4$, $k_s = 1.0$ N/mm³ (Assumed), $\gamma = 0.3$ (Assumed), $K = 450$ MPa (Equation 8).

2) Calculate the (moment-curvature) and (moment-slip strain) curves at the mid-span section:

Sample point at load increment 5: $M_{max} = 3,906,586$ N.mm, $\varphi = 0.4 \times 10^{-6}$, $\Delta\varepsilon_{max} = 2.80 \times 10^{-5}$, $F_\tau = F_{Jacket}$

3) Calculate the (moment-curvature) and (moment-slip strain) curves at all other segments:

The moment distribution along the beam depends on the applied load. For this example, assume a concentrated load at beam mid-span. The load (P) points corresponding to all moment values in the $M_{max}-\varphi$ diagram obtained from step 2 are calculated as $P_{max} = 4 M_{max}/L = 4 \times 3,906,586/3000 = 5,208$ N. Then, the moment and the corresponding

curvature at each beam segment are determined. At the same load increment for beam segment number 10 located at a distance of 500 mm from mid-span:

$$M_{(5,10)} = 1,302,000 \text{ N.mm}, \varphi_{(5,10)} = 0.136 \times 10^{-6}, \Delta\varepsilon_{(5,10)} = 3.24 \times 10^{-6}$$

4) Calculate the maximum and average and maximum (slip strain) and (shear stress) along the beam:

$$\Delta\varepsilon_{max} = 2.80 \times 10^{-5}, \Delta\varepsilon_{avg} = 9.52 \times 10^{-6}, \tau_{max} = 0.0142 \text{ MPa}, \tau_{avg} = 0.0108 \text{ MPa}$$

5) Calculate γ_{actual} and compare it to $\gamma_{assumed}$:

$$\gamma_{actual} = (\Delta\varepsilon_{avg}/\Delta\varepsilon_{max}) \times (\tau_{avg}/\tau_{max}) = 0.258 < (\gamma_{assumed} = 0.3)$$

Therefore, repeat the same procedure until $\gamma_{actual} = \gamma_{assumed}$. After many iterations, the values of the parameters become: $\Delta\varepsilon_{max} = 3.10 \times 10^{-5}$, $\Delta\varepsilon_{avg} = 1.07 \times 10^{-5}$, $\tau_{max} = 0.0161$ MPa, $\tau_{avg} = 0.0122$ MPa

6) Calculate $k_{s,actual}$ and compare it to $k_{s,assumed}$:

$$k_{s,actual} = 3.33 \text{ N/mm}^3 > (k_{s,assumed} = 1.0 \text{ N/mm}^3)$$

Therefore, repeat the same procedure until $k_{s,actual} = k_{s,assumed}$. After many iterations, the values of the parameters become: $\Delta\varepsilon_{max} = 1.09 \times 10^{-5}$, $\Delta\varepsilon_{avg} = 3.76 \times 10^{-6}$, $\tau_{max} = 0.0188$ MPa, $\tau_{avg} = 0.0143$ MPa

7) Repeat steps 3 through 6 for all load increments in order to obtain both (moment-curvature) and (moment-slip strain) diagrams for each beam segment.

8) Construct the load-deflection curve using moment-area theorem with the knowledge of the moment-curvature diagram of each beam segment.

3.13 References

- [1] Chalioris, C.E. and Pourzitidis, C.N. “Rehabilitation of shear-damaged reinforced concrete beams using self-compacting concrete jacketing,” *International Scholarly Research Notices*, 2012; Article 816107, pp. 1-12.
- [2] Chalioris, C., Papadopoulos, C., Pourzitidis, N., Fotis, D. and Sideris K. “Application of a Reinforced Self-Compacting Concrete Jacket in Damaged Reinforced Concrete Beams under Monotonic and Repeated Loading,” *Journal of Engineering*, Hindawi, 2013, ID 912983, pp. 1-12.
- [3] Martinola, G., Meda, A., Plizzari, G. and Rinaldi, Z. “Strengthening and repair of RC beams with fiber reinforced concrete,” *Cement and Concrete Composites*, 2010, Vol. 32, No. 9, pp. 731-739.
- [4] Hussein, M., Kunieda, M. and Nakamura, H. “Strength and ductility of RC beams strengthened with steel-reinforced strain hardening cementitious composites,” *Cement and Concrete Composites*, 2012, Vol. 34, No. 9, pp. 1061-1066.
- [5] Shehata, I., Shehata, L., Santos, E., Simoes, M. “Strengthening of Reinforced Concrete Beams in Flexure by Partial Jacketing,” *Materials and Structures*, Springer, 2009, pp. 42, No. 4, pp. 495-504.
- [6] Meda, A., Plizzari, G., Rinaldi, Z. and Martinola, G. “Strengthening of R/C existing columns with high performance fiber reinforced concrete jacket,” *Concrete Repair, Rehabilitation and Retrofitting II*, Taylor and Francis Group, 2009, London, UK.
- [7] Ersoy, U., Tankut, T. and Suleiman, R. “Behavior of Jacketed Columns,” *ACI Structural Journal*, 1993, Vol. 90, No. 3, pp. 288-293.
- [8] Ilki, A., Demir, C., Bedirhanoglu, I. and Kumbasar, N. “Seismic retrofit of brittle and low strength RC columns using fiber reinforced polymer and cementitious composites,” *Advances in Structural Engineering*, 2009, Vol. 12, No. 3, pp. 325-347.

- [9] Bousias, S., Spathis, A. and, Fardis, M. “Seismic retrofitting of columns with lap-spliced smooth bars through FRP or concrete jackets,” *Journal of Earthquake Engineering*, 2007, Vol. 11, pp. 653-674.
- [10] Bousias, S., Spathis, A. and Fardis, M. “Seismic retrofitting of columns with lap-splices through CFRP jackets,” *13th World Conference on Earthquake Engineering*, 2004, Vancouver, B.C., Canada.
- [11] Santos, P. and Júlio, E. “A State-of-the-Art Review on Shear-Friction,” *Engineering Structures*, 2012, Vol. 45, pp. 435-448.
- [12] CSA. “Design of concrete structures (CAN/CSA A23.3-14),” *Cement Association of Canada*, 2014, Ottawa, ON.
- [13] ACI Committee 318, “Building code requirements for structural concrete and commentary (ACI 318-14),” *American Concrete Institute*, 2014, Farmington Hills, MI.
- [14] Zilch, K. and Reinecke, R. “Capacity of shear joints between high-strength precast elements and normal-strength cast-in-place decks,” *Proceedings of the International Symposium of High Performance Concrete*, 2000, Orlando, FL, pp. 551-560.
- [15] Tsioulou, O.T. and Dritsos, S.E. “A theoretical model to predict interface slip due to bending,” *Materials and Structures*, 2011, Vol. 44, pp. 825-843.
- [16] Scott, B. Park, R. and Priestley, M. “Stress-Strain Behavior of Concrete Confined by Overlapping Hoops at Low and High Strain Rates,” *Journal of the American Concrete Institute*, 1982, Vol. 79, No. 1, pp. 13-27.
- [17] Karthik, M. and Mander, J. “Stress-block parameters for unconfined and confined concrete based on a unified stress-strain model,” *Journal of Structural Engineering*, ASCE, 2011, Vol. 137, No. 2, pp. 270-273.
- [18] Ramberg, W. and Osgood, W.R. “Description of stress–strain curves by three parameters,” *Technical Note No. 902*, National Advisory Committee for Aeronautics, 1943, Washington DC.

- [19] Thermou, G.E., Pantazopoulou, S.J. and Elnashai, A.S. "Flexural behavior of brittle RC members rehabilitated with concrete jacketing," *Journal of Structural Engineering*, ASCE, 2007, Vol. 133, No. 10, pp. 1373-1384.
- [20] Gohnert, M. "Proposed Theory to Determine the Horizontal Shear between Composite Precast and In-Situ Concrete," *Cement and Concrete Composites*, Elsevier, 2000, Vol. 22, No. 6, pp. 469-476.
- [21] Abdelouahed, T. "Improved Theoretical Solution for Interfacial Stresses in Concrete Beams Strengthened with FRP Plate," *International Journal of Solids and Structures*, Elsevier, 2006, Vol. 43, No. 14-15, pp. 4154-4174.
- [22] Tassios, T. and Vintzeleou, E. "Concrete-to-Concrete Friction," *Journal of Structural Engineering*, ASCE, 1987, Vol. 113, No. 4, pp. 832-849.
- [23] Eurocode2, "Design of concrete structures- part 1.1: general rules and rules for buildings," European Committee for Standardization (CEN), 2004, Brussels, Belgium.
- [24] Youssef, M.A. and Rahman, M. "Simplified seismic modeling of reinforced concrete flexural members," *Magazine of Concrete Research*, 2007, Vol. 59, No. 9, pp. 639-649.
- [25] Russo, G., Zingone, G. and Puleri, G. "Flexure-Shear Interaction Model for Longitudinally Reinforced Beams," *ACI Structural Journal*, 1991, Vol. 88, No. 1, pp. 60-68.

Chapter 4

4 ANALYSIS OF CONTINUOUS REINFORCED CONCRETE BEAMS STRENGTHENED USING CONCRETE JACKETS

The need to strengthen Reinforced Concrete (RC) structure emerges from various reasons such as new safety requirements, a change of structure occupancy, an incorrect design calculations and/or degradation of materials with time. Jacketing is one of the widely spread procedures to strengthen and repair RC beams. It comprises the addition of concrete layers that are usually reinforced with longitudinal steel bars, stirrups, welded wire mesh or various kinds of fibrous materials.

In the current practice, monolithic action is assumed between the original beam and the attached jacket. This implies that the internal stresses developed in both substrates due to the applied loads are distributed among them assuming infinite interfacial slip stiffness. This assumption may result in higher estimates of stiffness and/or capacity depending on the geometrical properties and interfacial surface treatment. The actual behavior of typical jacketed beams is partially composite in which the interfacial slip stiffness can take any value between (0) and (∞) depending on the frictional resistance between the surfaces and the presence of steel anchors connecting the two substrates [1]. This implies that the analysis of jacketed beams in this case requires a knowledge of the nonlinear behavior of the interface as well as the nonlinear properties of both concrete and the embedded steel bars at each loading step along the beam.

Literature is ample with experimental programs and numerical investigations that have been performed to address the influence of jacketing schemes, geometrical characteristics, mechanical properties and interfacial treatment on the flexural behavior of determinate jacketed RC structural members. For instance, Altun [2] and Bousias *et al.* [3] examined the effect of RC jacketing on the mechanical performance of statically-determinate RC beams considering the load-displacement behavior, ultimate load, ductility and toughness. Other researchers [1, 4] investigated the significance of surface preparation of concrete members before applying the new concrete jacket. The use of

fiber reinforced cementitious composites as an alternative to adding steel reinforcement within the jacket has been addressed by other studies [5 – 10]. In addition, the impact of using shear studs to further attach the existing beam with the additional concrete layers has been investigated by Shehata *et al.* [11]. Furthermore, the influence of varying the method of applying the jacket on site, such as shotcrete or cast-in-place concrete, have been considered by many researchers [12, 13, 14].

Experimental and numerical studies related to strengthening indeterminate RC beams using concrete jackets is scarce in literature. At the time of writing, the only available relevant experimental work was performed by Cheong and MacAlevey [15]. The rather extensive use of indeterminate RC beams in building structures and bridges requires further research regarding the influence of partial composite action their flexural performance.

4.1 Objectives and Scope of Work

The purpose of this chapter is to propose a simplified method to capture the influence of interfacial slip on the moment-curvature and load-deflection relationships of jacketed continuous RC beams. This is achieved by performing nonlinear analysis in view of the material properties and interfacial behavior. A calculation algorithm is proposed to determine the slip distribution along the beam length and to obtain the corresponding moment-curvature diagram at both the sagging and hogging moment regions. This analysis procedure is sensitive to the bending moment distribution along the beam; therefore, the concept of moment redistribution in indeterminate beams is illustrated and considered in the analysis. After validating the model with reference to related experimental work, a parametric study is performed and the flexural behavior of the strengthened beams is discussed in light of the moment-curvature relationships. Finally, slip modification factors are proposed to allow engineers to adjust the monolithic moment-curvature diagram at both the sagging and hogging moment zones in continuous beams by considering slip effect.

4.2 Concrete Material Model

Scott *et al.* [16] model, Equation 1, provides a robust yet simple expression to describe the stress-strain behavior of normal strength concrete in compression. The tangential Young's modulus of concrete is taken as the first derivative of the concrete stress (f_c) with respect to concrete strain (ε_c). The tensile behavior of concrete is predominantly brittle. It is assumed to carry tensile stresses up to the cracking point beyond which the tensile capacity of concrete drops to zero.

$$f_c = \begin{cases} f'_c \left[2.0 \left(\frac{\varepsilon_c}{\varepsilon_o} \right) - \left(\frac{\varepsilon_c}{\varepsilon_o} \right)^2 \right] & , 0 \leq \varepsilon_c \leq \varepsilon_o \\ f'_c [1 - Z(\varepsilon_c - \varepsilon_o)] & , \varepsilon_c > \varepsilon_o \text{ and } f_c > 0.2f'_c \\ 0.2f'_c & , \varepsilon_c > \varepsilon_o \text{ and } f_c \leq 0.2f'_c \end{cases} \quad (1)$$

where the slope of the strain softening branch (Z) is given by Equation 2 in terms of the concrete compressive strength and the corresponding peak strain.

$$Z = \frac{0.5}{\left[\frac{3.0 + 0.29f'_c}{145f'_c - 1000} \right] - \varepsilon_o} \quad (2)$$

4.3 Steel Material Model

The steel reinforcement monotonic stress-strain relationship can be expressed using Equations 3 and 4, which conveniently combine the initial elastic response, yield plateau and strain hardening stages in a rigorous form [17, 18].

$$f_s = \frac{E_s \varepsilon_s}{\left[1 + \left(\frac{E_s \varepsilon_s}{f_y} \right)^{20} \right]^{0.05}} + (f_{su} - f_y) \left[1 - \frac{(\varepsilon_u - \varepsilon_s)^P}{\{(\varepsilon_u - \varepsilon_{sh})^{20P} + (\varepsilon_u - \varepsilon_s)^{20P}\}^{0.05}} \right] \quad (3)$$

$$P = \frac{E_{sh}(\varepsilon_u - \varepsilon_{sh})}{(f_u - f_y)} \quad (4)$$

where f_s and ε_s are steel stress and strain, respectively; E_s and E_{sh} are the elastic modulus and strain hardening modulus, respectively; f_y and f_u are the yield and ultimate strengths,

respectively; ε_s and ε_{sh} are strain hardening and ultimate strains, respectively. The value of ε_{sh} is set equal to ε_y and E_{sh} is taken as 1% of E_s in the analysis.

4.4 Interfacial Shear Stress (τ) and Slip (S) Relationship

The shear transfer mechanism is activated by the frictional resistance between the contact surfaces and the axial forces developed in the anchors crossing the interface. The former mechanism represents the concrete contribution; whereas the second case represents the influence of dowel action. The concrete contribution (v_c) is determined in view of Tassios and Vintzeleou [1] empirical model as a function of the lateral slip (S), ultimate slip value at the onset of frictional mechanism failure (S_{cu}) and ultimate frictional capacity of the interface (v_{cu}) as expressed by Equations 5 and 6. This model was derived considering various grades of concrete and a wide variety of surface roughness conditions that vary between smooth and highly roughened interfaces. The model proposed was adopted and validated by other researchers, such as Thermou *et al.* [19], considering relevant experimental studies.

$$v_c(S) = \begin{cases} 1.14(v_{cu}) \left(\frac{S}{S_{cu}}\right)^{\frac{1}{3}} & , \left(\frac{S}{S_{cu}}\right) \leq 0.5 \\ (v_{cu}) \left[0.81 + 0.19 \left(\frac{S}{S_{cu}}\right)\right] & , \left(\frac{S}{S_{cu}}\right) > 0.5 \end{cases} \quad (5)$$

$$v_{cu} = \mu(f_c'^2 \rho_s f_s)^{\frac{1}{3}} \quad (6)$$

where μ is the coefficient of shear friction at the interface, ρ_s is the steel reinforcement ratio of the steel bars crossing the interface and f_s is the corresponding tensile stress developed in these bars as given in Equation 7.

$$f_s = \left(\frac{0.3 S^{\frac{2}{3}} E_s f_c'}{D_b} \right) \leq f_y \quad (7)$$

The resultant dowel force (V_D) is expressed as a function of the lateral slip between the two concrete surfaces, stud diameter (D_b) and ultimate dowel force (V_{Du}) as given by Equations 8 and 9 [19].

$$S = \begin{cases} 0.012 \left(\frac{V_D(S)}{V_{Du}} \right) & , S \leq 0.006D_b \\ 0.006D_b + 0.088D_b \left[\left(\frac{V_D(S)}{V_{Du}} \right)^4 - 0.5 \left(\frac{V_D(S)}{V_{Du}} \right)^3 \right] & , \frac{V_D(S)}{V_{Du}} \geq 0.5 \end{cases} \quad (8)$$

$$V_{Du} = 1.3 D_b^2 \sqrt{f'_c f_y} \quad (9)$$

Therefore, the overall interfacial shear stress (τ) corresponding to any slip (S) value can be obtained as the summation of concrete contribution (Equations 6 and 7) and dowel action contribution (Equations 8 and 9) for given material properties and interfacial roughness.

4.5 Assumptions

Assumptions considered in the current study encompasses the following:

- 1) Plane sections remain plane after deformation, implying that shear deformations are small relative to bending deformations.
- 2) Perfect bond exists between steel reinforcement and the surrounding concrete material. Thus, strain in both concrete and steel bars at the same location is identical.
- 3) The failure criterion of the composite beam is defined by crushing of the extreme compression fiber at a concrete ultimate strain (ϵ_{cu}) of 0.0035 [20].
- 4) The original RC beam and the added concrete layer are considered to deform by the same curvature through the beam length [19, 21].
- 5) The interfacial shear stress distribution within each region is assumed to vary as a cubic function with the distance from the zero moment section [21].

4.6 Typical Jacketed Section

The developed model is applicable to analyze symmetric continuous RC beams subjected to either uniform or concentrate loads. Fig. 4-1 shows the geometry and reinforcement details of a typical continuous beam that will be used for discussion throughout the chapter. The main steel reinforcement in the positive and negative moment regions are assumed to be 20% and 40% of the balanced steel reinforcement ratio, respectively. The compression steel reinforcement is 2-10M bars. The amount of jacket reinforcement is assumed as 10M bars placed in one layer at the maximum spacing provided by CSA 23.3-14 [20]. One half of the core and jacket steel bars from the hogging moment region are assumed to extend throughout the beam.

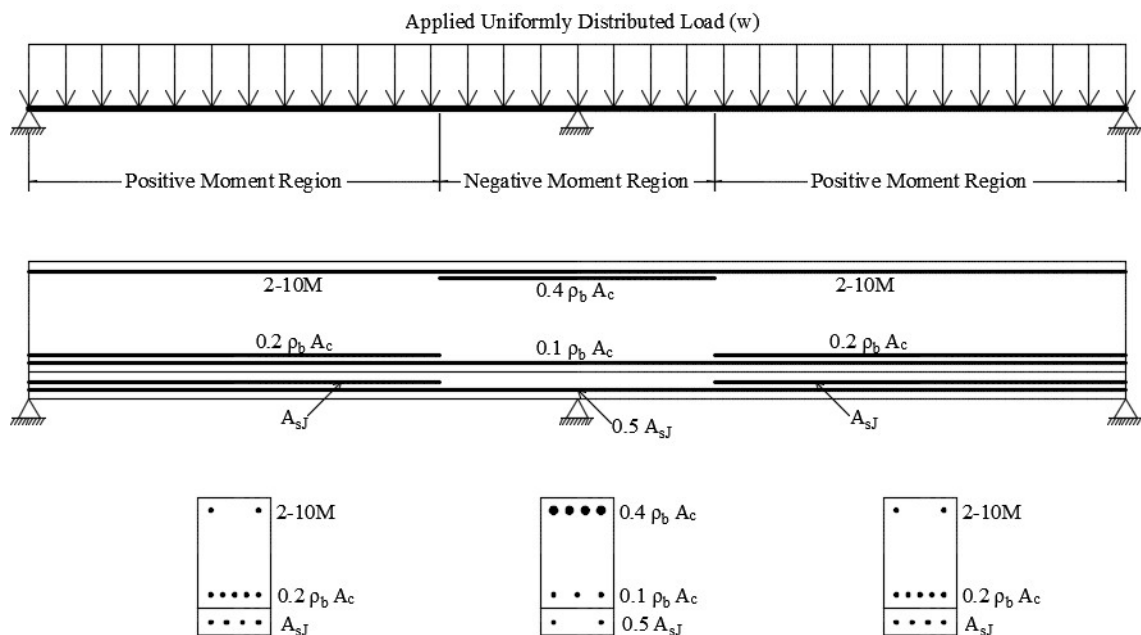


Figure 4-1: Continuous beam loading scheme and reinforcement configuration

Geometry and loading scheme of the continuous beam are assumed to be symmetric about the intermediate support. Thus, one span of the beam can be modeled as a propped cantilever as shown in Fig. 4-2(a). This span is assumed to be composed of several members rigidly connected at their ends as illustrated in Fig. 4-2(b). Each segment has a defined length (L_i) and a distinct flexural rigidity (EI_i). The segment length is set at about

50 mm, which was found to enhance the accuracy based on a preliminary sensitivity analysis.

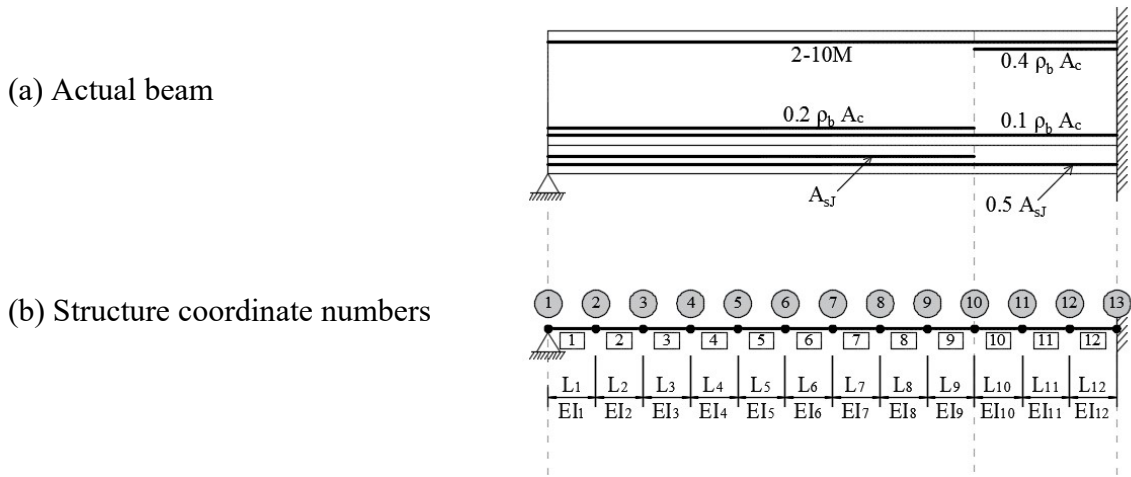


Figure 4-2: Propped cantilever analytical model

The expected trends of the moment-curvature diagrams in both the positive and negative moment regions are shown in Fig. 4-3. The trend for the positive moment section is characterized by three points; namely, the yielding of jacket reinforcement, yielding of the core reinforcement and crushing of concrete. The trend of the negative moment section is defined by yielding of the core reinforcement and crushing of concrete.

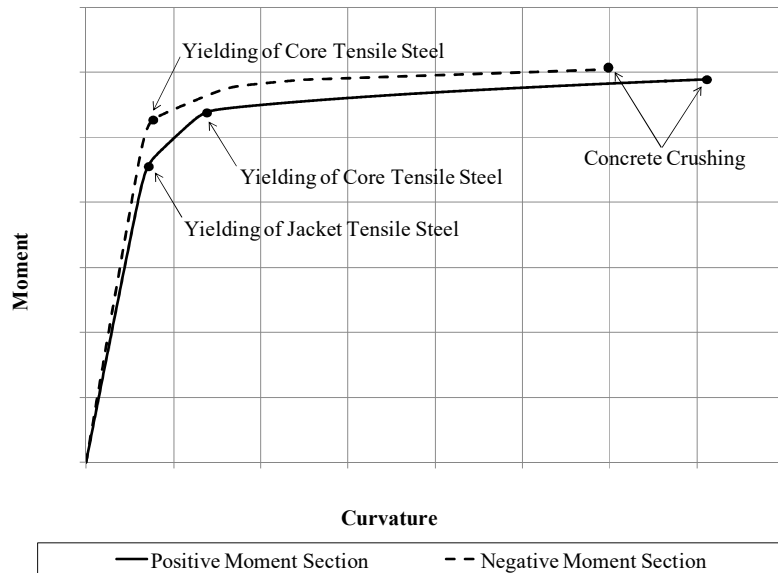


Figure 4-3: Moment-curvature diagrams for positive and negative moment sections

4.7 Proposed Calculation Algorithm

The primary challenges for the proposed calculation algorithm are prediction of the slip distribution along the interface and determination of the moment-curvature relationships for the beam segments shown in Fig. 4-2. Alhadid and Youssef [22] have proposed a calculation algorithm to determine these relationships in jacketed RC simply supported beams considering slip effect. A summary of the procedure is provided in section 4-1 of this chapter along with the new proposed changes to analyze continuous beams. Sectional analysis procedure to determine the equilibrium conditions is described in section 4-2. The influence of moment redistribution becomes substantial in the prediction of slip distribution along continuous beams and is discussed in section 4-3. An equivalent curvature distribution is then obtained based on the load-deflection relationship of the actual curvature distribution considering slip effect as illustrated in section 4-4.

Slip, and consequently shear stress, reach their maximum value at the point of zero moment and fade away as they approach the maximum bending moment section. In continuous RC beams, each span can be divided into positive and negative moment zones as indicated in Fig. 4-4. To obtain the complete slip distribution along the span, the analysis procedure is carried out individually for each of the two zones. Assuming a propped cantilever model for each span, the analyzed segment within the positive moment zone is taken from the pinned support to the point of maximum bending; whereas, for the negative moment zone, this segment is taken from the point of contraflexure to the point of maximum negative bending moment at the fixed end.

The proposed analysis method comprises two main stages. In the first one, an iterative sectional analysis procedure is performed at different load levels only at the maximum sagging and hogging moment sections. This results in determining the maximum slip strain ($\Delta\varepsilon_{max}$) at these locations and the corresponding slip strain ($\Delta\varepsilon$) and slip (S) at the other segments along the span. In the second stage, sectional analysis is conducted directly at the remaining segments taking into account the $\Delta\varepsilon$ distribution evaluated from the first analysis step for each segment. The slip distribution is obtained while satisfying the equilibrium and compatibility conditions at each segment. Details about the mentioned steps are given below.

(a) propped cantilever idealization

(b) bending moment diagram showing the point of zero moment

(c) bending moment diagram showing the point of zero moment

(d) anticipated deflection shape of the propped cantilever

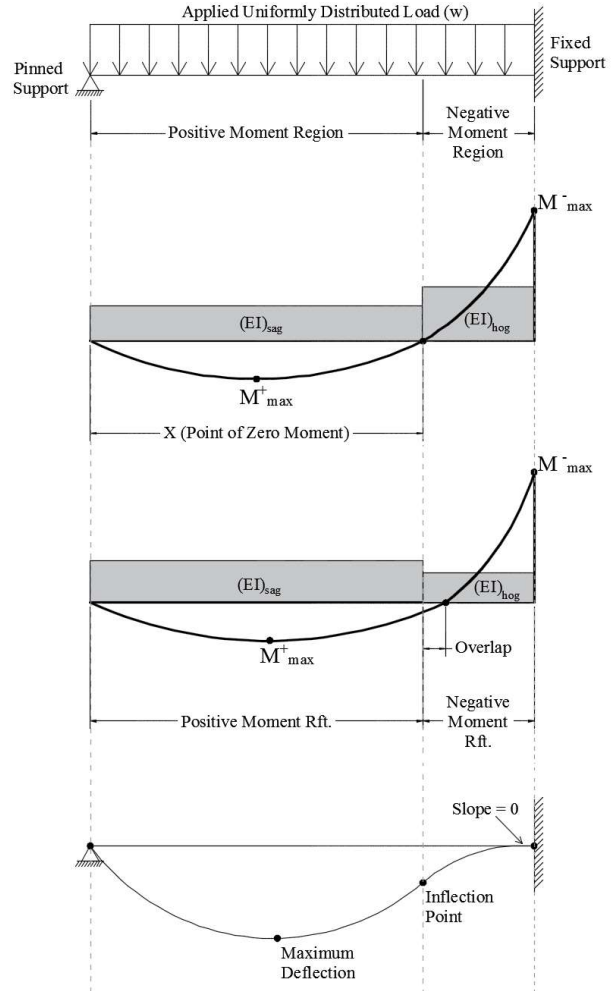


Figure 4-4: Bending moment and deflection profile of the propped cantilever model

4.7.1 Moment-Curvature at Maximum Moment Sections

For each moment zone, the average value of interfacial shear stress (τ_{avg}) at any load level can be calculated assuming a direct relationship with the maximum slip strain ($\Delta\epsilon_{max}$) located at the maximum moment section [21, 23, 24]. Therefore, the average shear stress can be given according to the expression ($\tau_{avg} = \gamma_1 \gamma_2 k_s \Delta\epsilon_{max} L'$) in terms of the secant interfacial stiffness, k_s (N/mm³); the ratios ($\gamma_1 = \tau_{avg} / \tau_{max}$) and ($\gamma_2 = \Delta\epsilon_{avg} / \Delta\epsilon_{max}$); the average slip strain ($\Delta\epsilon_{avg}$) from point of zero moment to maximum positive or negative moment; and the corresponding length, L' (m) [22].

For each of the two moment zones, the analysis procedure to determine interfacial slip distribution is carried out at each applied load level (i.e. assumed applied curvature value) until failure occurs. Firstly, initial values of the secant interfacial stiffness (k_s) and the shear stress distribution ratios (γ_1 and γ_2) are assumed. Then, for the total curvature (ϕ) value of the current load increment, two equilibrium conditions are applied at the maximum moment sections: (1) equilibrium between the internal forces; and (2) equilibrium between the resultant axial forces at one side of the interface and the resultant shear force acting along the interface. Hence, the moment (M) and maximum slip strain ($\Delta\varepsilon_{max}$) at the maximum moment sections corresponding to the current curvature value (ϕ) are obtained. After that, bending moment diagram is constructed along the span assuming uniform load and considering the obtained maximum moment values. Next, the slip strain ($\Delta\varepsilon$) distribution is determined along the span with respect to the location of each segment as shown in the proposed Equation 10.

$$\Delta\varepsilon_{(i,j)} = \Delta\varepsilon_{(m,1)} \left(\frac{x_j}{L} \right) \quad (10)$$

Where i is the load step number, j is the segment number and m is the load step number that produces a bending moment in the mid-span segment equals to the moment applied at segment j . Once the slip strain ($\Delta\varepsilon$) distribution along the interface is established, both the slip (S) and the shear stress (τ) in each segment is obtained from Equations 11 and 12, respectively.

$$S_{(i,j)} = \sum_{n=1}^{n=j} [(\Delta\varepsilon_{(i,n)})(x_j)] \quad (11)$$

$$\tau_{(i,j)} = k_s S_{(i,j)} \quad (12)$$

Having obtained the slip distribution for both moment zones, continuity conditions is checked at the point of contraflexure to ensure it is satisfied by calculating the error between the obtained slip (S) from the sagging moment zone and the hogging moment zone. The procedure is repeated if the error is more than 1% by adjusting the slip strain ($\Delta\varepsilon$) at all segments and repeating the analysis to check equilibrium and compatibility

conditions. Finally, based on the obtained slip and shear stress distributions, the secant interfacial stiffness (k_s) and the shear stress distribution ratios (γ_1 and γ_2) are calculated and compared to the initially assumed values. The analysis continues if they are equal with a tolerance of 1%, otherwise the whole procedure is repeated with the new calculated values. A detailed description of this calculation procedure considering simply supported beams is provided by Alhadid and Youssef [22].

If the beams are subjected to initial loading prior to jacketing, then a preliminary sectional analysis on the unjacketed sections has to be carried out first to obtain the resulting moment-curvature curve and strain profile at each beam segment. These diagrams are then included as an input in the jacketed beam calculation algorithm to obtain the full behavior of the beam at different loading stages before and after jacketing.

4.7.2 Sectional Analysis in Jacketed Sections

The sectional analysis procedure [25] is implemented to analyze the jacketed sections. The upper limit for the height of each layer is taken as 0.5 mm. At every loading step, an incremental curvature is applied and the strain at each strip in both the concrete core and the jacket is calculated based on its location from the centroid (y_i) of the jacketed section. The kinematic and compatibility conditions are considered in view of the corresponding material stress-strain relationships and Equation 13, which relates the incremental applied moment (ΔM) and axial load (ΔP) to the incremental curvature ($\Delta\phi$) and axial strain ($\Delta\varepsilon_a$) by a defined stiffness matrix. In this equation, n represents the number of discrete layers, E_i is the elastic modulus of layer i , A_i is the area of layer i , subscript (c) represents concrete core and subscript (J) represents concrete jacket.

$$\begin{pmatrix} \Delta M \\ \Delta P \end{pmatrix} = \begin{pmatrix} \sum_{i=1}^n (E_{i,c} A_{i,c} + E_{i,J} A_{i,J}) y_i^2 & -\sum_{i=1}^n (E_{i,c} A_{i,c} + E_{i,J} A_{i,J}) y_i \\ -\sum_{i=1}^n (E_{i,c} A_{i,c} + E_{i,J} A_{i,J}) y_i & \sum_{i=1}^n (E_{i,c} A_{i,c} + E_{i,J} A_{i,J}) \end{pmatrix} \begin{pmatrix} \Delta\phi \\ \Delta\varepsilon_a \end{pmatrix} \quad (13)$$

4.7.3 Moment Redistribution in Continuous Beams

Matrix stiffness analysis is carried out to account for moment redistribution caused by the difference in stiffness between the hogging and sagging moment zones. Fig. 4-5

represents an arbitrary element of the propped cantilever model subjected to external static uniformly distributed load.

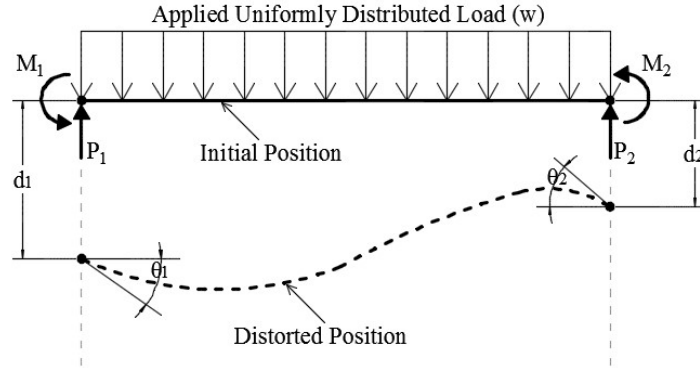


Figure 4-5: Element forces and displacements

The distorted shape of the element can be described in terms of a translational displacement (d_i) and in-plane rotation (θ_i) at its ends. The element stiffness is used in Equation 14 to express the joint internal forces (i.e. P_i and M_i) as functions of the corresponding displacements (i.e. d_i and θ_i) and fixed-end forces due to the applied loads (i.e. p_i and m_i) [26].

$$\begin{bmatrix} P_i - p_i \\ M_i - m_i \\ P_{i+1} - p_{i+1} \\ M_{i+1} - m_{i+1} \end{bmatrix} = (EI)_{i,j} \begin{bmatrix} \frac{12}{L_i^3} & \frac{6}{L_i^2} & -\frac{12}{L_i^3} & \frac{6}{L_i^2} \\ \frac{6}{L_i^2} & 4 & -6 & 2 \\ -\frac{12}{L_i^3} & -6 & \frac{12}{L_i^3} & -6 \\ \frac{6}{L_i^2} & 2 & -6 & 4 \\ \frac{12}{L_i^3} & \frac{6}{L_i^2} & -\frac{12}{L_i^3} & \frac{6}{L_i^2} \\ \frac{6}{L_i^2} & 4 & -6 & 2 \\ -\frac{12}{L_i^3} & -6 & \frac{12}{L_i^3} & -6 \\ \frac{6}{L_i^2} & 2 & -6 & 4 \end{bmatrix} \begin{bmatrix} d_i \\ \theta_i \\ d_{i+1} \\ \theta_{i+1} \end{bmatrix} \quad (14)$$

Once the stiffness matrix for each element is completed, a global stiffness matrix is constructed. The global displacement vector is then obtained by multiplying the inverse of the global stiffness matrix with the global load vector.

The proposed method modifies the matrix analysis procedure by incorporating the influence of slip. The moment-curvature diagram for each section is first calculated while accounting for slip as explained in section 8-1. The secant stiffness is then evaluated for a given moment. For each loading step, the relationship in Equation 14 is carried out for each segment (i) considering the secant flexural stiffness (j) obtained from the corresponding moment-curvature diagram at the specified load level. The equilibrium and compatibility conditions obtained from the matrix structural analysis and the slip calculation algorithm must be verified simultaneously. Hence, nested iterations are required for each load step to satisfy equilibrium and continuity for each segment along the beam.

The moment redistribution along the beam is dictated by the flexural stiffness ratio between the hogging and sagging moment regions [27]. Fig. 4-3 shows the moment-curvature relationships for the positive and negative moment sections of an arbitrary continuous beam. Because of the higher initial stiffness of the negative moment section, the point of zero moment is shifted away from the intermediate support towards the mid-span. A sketch of the bending moment diagram and the flexural rigidities within the elastic loading stage for both the hogging and sagging regions are illustrated in Fig. 4-4(b). In this case, the flexural rigidity is constant within each region but vary between the positive and negative zones. The boundaries of the sagging and hogging moment zones are determined through iteration. The length of each region is first assumed and the corresponding stiffness is assigned. Bending moment diagram is obtained based on the stiffness distribution along the span. The resulting point of zero moment is used to adjust the boundary between the two zones and consequently alters their length and assigned stiffness. Iterations are performed until the resulting length of each zone becomes identical to the assumed value. The reinforcement defining both the positive and negative sections is then determined based on the obtained length of each zone.

Once the negative moment section yields, its secant stiffness will decrease gradually with the applied load until it equates the positive moment section stiffness. In this case, the bending moment diagram obtained from stiffness analysis will be identical to that obtained from elastic structural analysis. As the load keeps increasing, the hogging-to-

sagging stiffness ratio further decreases resulting in a shift of the point of zero moment towards the intermediate support as more proportion of the additional load is carried by the sagging moment region. However, since the length of each element, and consequently the reinforcement, is assumed to be fixed up to failure, part of the assumed hogging moment region will start to resist small amount of positive moment as shown in Fig. 4-4(c). The influence of this overlap is insignificant since the moment values adjacent to the point of contraflexure are relatively low. Failure of the beam is activated by crushing of the extreme concrete fibers at the intermediate support where the maximum moment is anticipated. The anticipated load-deflection curve of the modeled propped cantilever is presented in Fig. 4-4(d). It shows both the point of maximum deflection and the inflection point that is determined at the initial loading steps and fixed throughout the analysis.

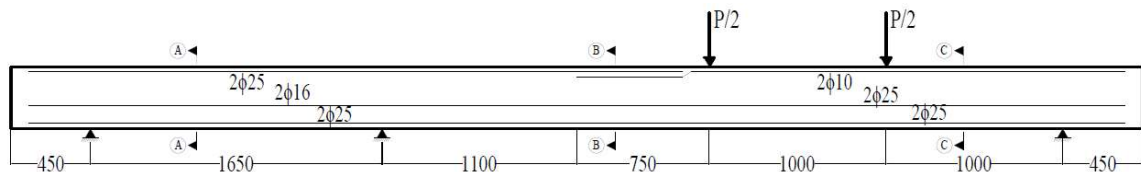
4.7.4 Load-Deflection Relationship and Equivalent Curvature Distribution

Once the slip effect is incorporated in a unique moment-curvature diagram for each segment, the widely used area-moment method is carried out to determine the deflection at distance of 0.4215 of the span away from the edge support. This distance defines the location of maximum deflection for symmetric typical continuous beam supporting a uniformly distributed load [27].

Having obtained the load-deflection curve of the jacketed beam including slip effect, the actual curvature distribution of the propped cantilever is determined at different loading steps for each segment. These values are obtained from the corresponding moment-curvature diagram and take into account the partial composite action according to the jacketing scheme used. After that, positive (φ_{eq}^+) and negative (φ_{eq}^-) equivalent curvatures are obtained by assuming the curvature distribution along the beam simulating the monolithic behavior of jacketed beams. Therefore, at each loading value, and consequently deflection, equivalent maximum positive and negative curvatures corresponding to the applied moment can be obtained. Hence, equivalent moment-curvature curve can be obtained for the jacketed beam including slip effect. The load-deflection curve can be determined at any point using the moment-area theorem and the anticipated deflection shape.

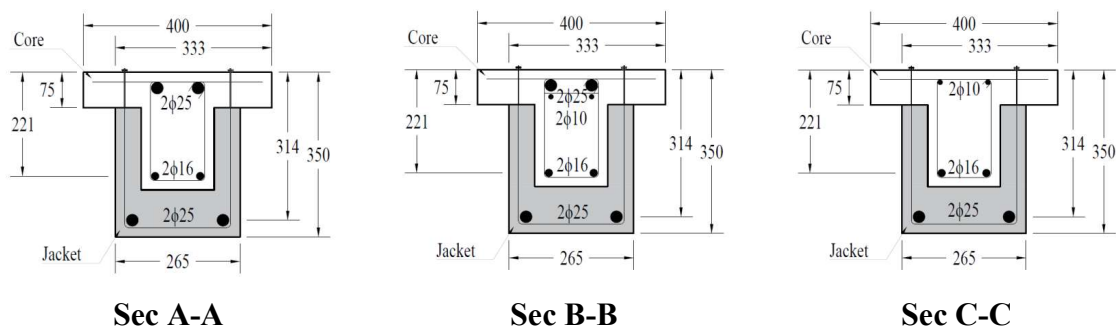
4.8 Validation

The capability of the proposed model to capture the flexural behavior of simply supported jacketed RC beams was previously validated [22]. Other than the study performed by Cheong and MacAlevey [15], experimental studies investigating the flexural behavior of continuous jacketed RC beams are lacked. Fig. 4-6 shows the longitudinal and cross-sectional views of the jacketed continuous beam. Initially, the T-section concrete core was cast according to the cross-sectional dimensions and reinforcement distribution shown. After 28 days of curing, the surfaces to be in contact with the jacketing material were roughened prior to applying the jacket. The concrete compressive strength was reported as 30 MPa for the core and 60 MPa for the jacketing material. The tensile yield strength for bars $\Phi 16$, $\Phi 25$, $\Phi 6$, $\Phi 10$ and $\Phi 8$ were 583 MPa, 567 MPa, 290 MPa, 321 MPa and 407 MPa, respectively. The tensile ultimate strength for the same sequence of bar were 652 MPa, 670 MPa, 394 MPa, 424 MPa and 477 MPa, respectively. The jacketed beam was subjected to two-point loading scheme at one span only as shown in Fig. 4-6(a).



Note: Stirrups are $\phi 6$ spaced at 115 mm along the beam

(a) jacketed beam longitudinal view and location of the applied loads



(b) cross-sectional views.

Figure 4-6: Longitudinal and cross-sectional views of the beams tested experimentally by Cheong and MacAlevey [15].

The proposed calculation method is carried out to determine the flexural behavior of the jacketed continuous beam in terms of the load-deflection curve at the center of the loaded span. The load-deflection curves assuming monolithic and partially composite behaviors are then plotted and compared with the ones obtained experimentally by Cheong and MacAlevey [15]. Fig. 4-7 shows that the percent errors in initial stiffness between the experimental results and the proposed analytical ones are 7.9% and 2.9% assuming both monolithic and partial interaction, respectively.

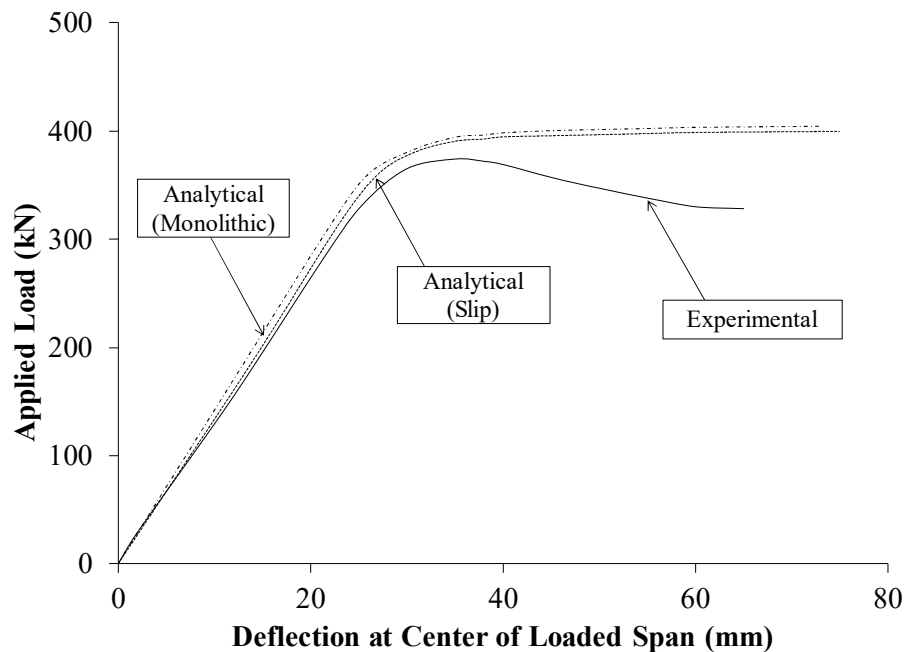


Figure 4-7: Validation of the proposed model

Cheong and MacAlevey [15] reported that a slip between the concrete core and the surrounding jacket was detected without presenting any more data about the slip distribution along the interface. The relatively close variations in the flexural stiffness in the elastic range indicates that the proposed model is capable of predicting the load-deflection behavior prior to steel yielding. Introducing the slip effect in the analysis further improves the predictions by lowering the stiffness to approach the experimental trend. The value of friction coefficient chosen in the analysis is 0.8 to account for surface treatment using electric chisel used in the experiment (i.e. roughened surface) [28]. Regarding the ultimate load, the percent error between the experimental and proposed

analytical results is 6.2% and 3.8% by ignoring and including the slip effect, respectively. Cheong and MacAlevey [15] reported that the observed failure is brittle caused by the excessive tensile stresses at the narrow bearing supports, which was not accounted for in the proposed model.

4.9 Parametric Study

A parametric study is carried out to investigate the influence of different design parameters on the performance of jacketed continuous RC beams. The concrete compressive strength is taken as 25 MPa, 30 MPa and 35 MPa; and the steel yield strength is taken as 300 MPa, 400 MPa and 500 MPa. For each of the analyzed sections, the mechanical properties are assumed to be the same for the concrete core and its jacket. The coefficient of friction ranges according to ACI [28] between 0.4 for smooth concrete surface to 1.4 for intentionally highly roughened concrete in increments of 0.2. The beams' cross-sectional dimensions are defined with reference to the existing beam height (300 mm, 450 mm and 600 mm), jacket thickness (100 mm, 150 mm and 200 mm), existing beam width (200 mm, 300 mm and 400 mm), and beam span (3 m, 4 m and 5 m). The steel reinforcement distribution along the beam is shown in Fig. 4-1 in which the balanced steel reinforcement ratio is determined with regard to A23.3 [20]. The total reinforcement ratio in all leads to a ductile behavior. Jacketing from one side at the soffit of all beams is adopted in the analysis. Each section is analyzed 63 times to account for the considered variables. Therefore, a total of 5,103 different cases are considered in the current parametric study.

4.10 Moment-Curvature Behavior

The following discussion refers to the beam sections whose geometrical and mechanical properties are listed in Table 4-1. These sections are considered to examine the influence of slip on flexural behavior of jacketed RC beams due to the variation of jacket thickness, beam width, beam height, span, concrete compressive strength and steel grade. The effect of each parameter is investigated by three sections that are labeled in Table 4-1.

Table 4-1: Geometry of the discussed jacketed beams

Section	Studied Parameters	Span (m)	b_c (mm)	h_c (mm)	h_J (mm)	f'_c (MPa)	f_y (MPa)
B-1	h_J, f'_c, f_y	3	200	300	100	30	400
B-2	h_J	3	200	300	150	30	400
B-3	$h_J, b_c, h_c, \text{Span}$	3	200	300	200	30	400
B-4	h_c	3	200	450	200	30	400
B-5	h_c	3	200	600	200	30	400
B-6	b_c	3	300	300	200	30	400
B-7	b_c	3	400	300	200	30	400
B-8	Span	4	200	300	200	30	400
B-9	Span	5	200	300	200	30	400
B-10	f'_c	3	200	300	100	25	400
B-11	f'_c	3	200	300	100	35	400
B-12	f_y	3	200	300	100	30	300
B-13	f_y	3	200	300	100	30	500
B-14	$\Delta\varepsilon, S, \tau$	3	200	450	150	30	300

Figs. 4-8 and 4-9 show the initial stiffness values for each section assuming full and partial composite actions (assuming a friction coefficient of 0.4) under both sagging and hogging moments, respectively. The reduction in initial stiffness caused by slip is indicated as a percentage in the corresponding figures.

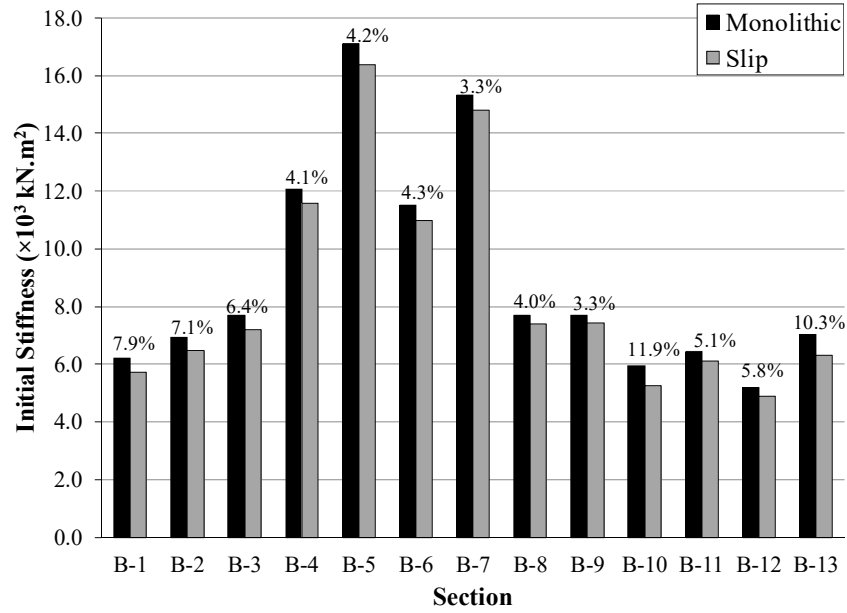


Figure 4-8: Percent difference of initial stiffness by including and neglecting slip effect (sagging)

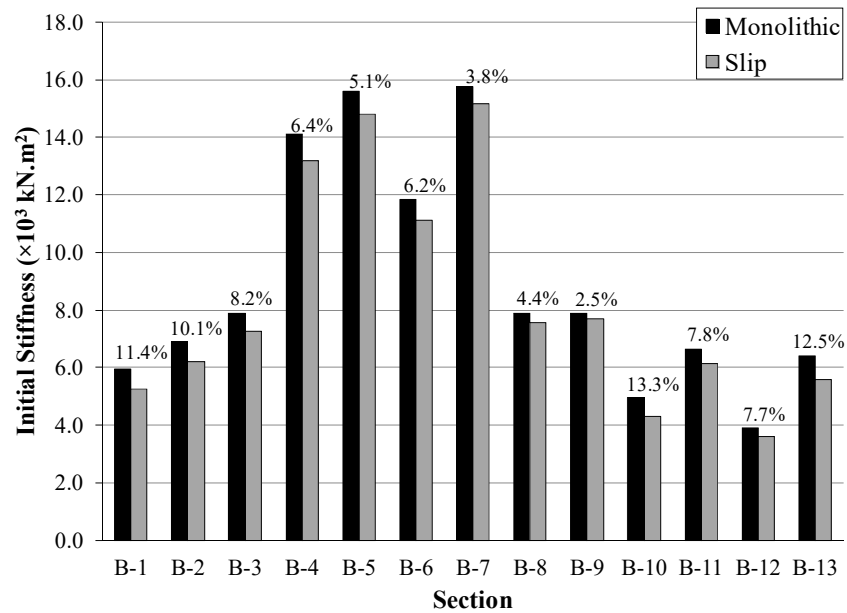


Figure 4-9: Percent difference of initial stiffness by including and neglecting slip effect (hogging)

Fig. 4-10 describes the variation of the reduction rate in stiffness (as percentage) due the variation of each of the aforementioned parameters. Reference to Table 4-1 and Figs. 4-8, 4-9 and 4-10 should be considered throughout the following discussion.

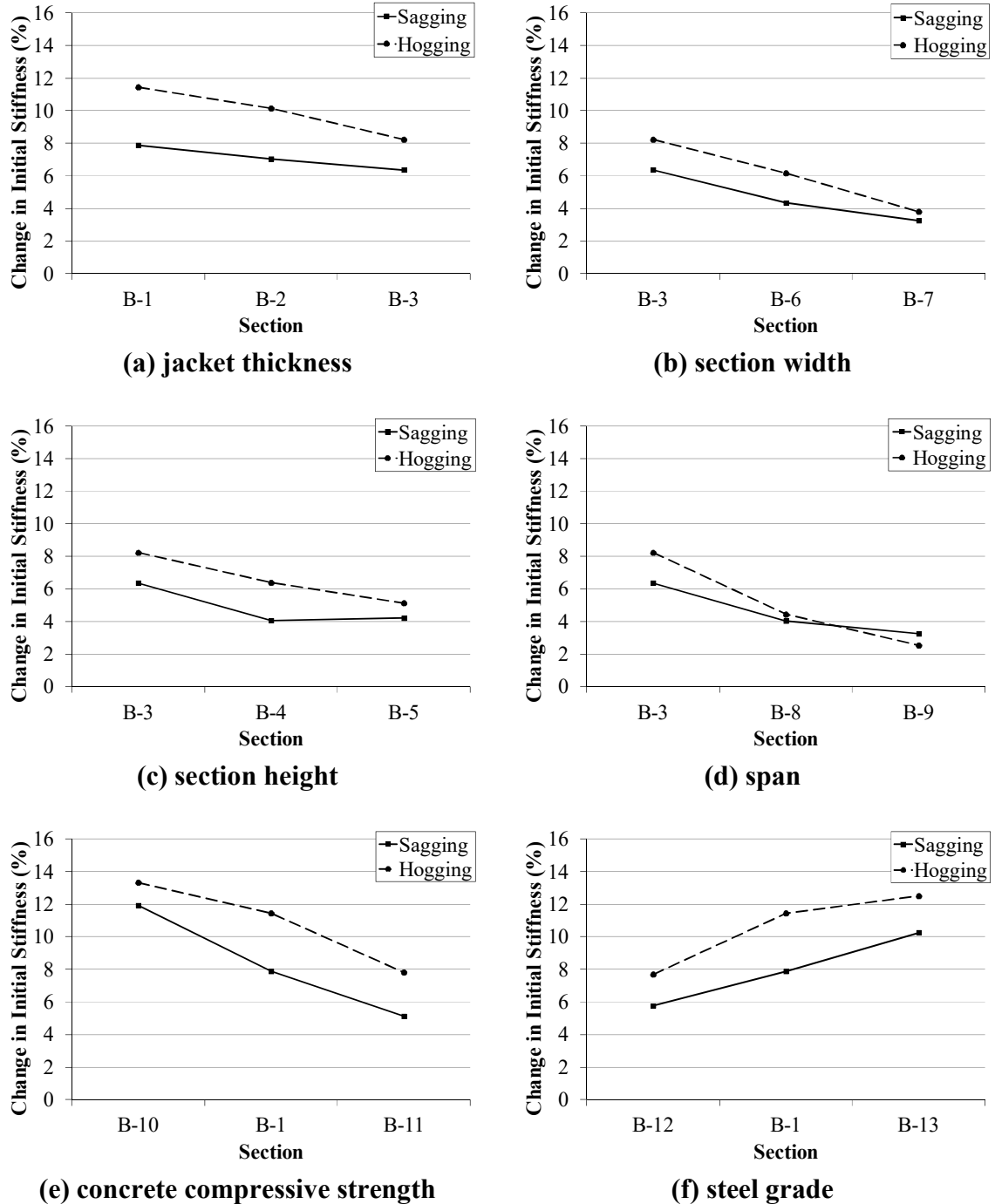


Figure 4-10: Variation of sagging and hogging initial stiffness with various parameters

4.10.1 Effect of Jacket Thickness (h_j)

Beams B-1, B-2 and B-3 are considered for comparison. Figs. 4-11 and 4-12 illustrate the influence of varying the jacket thickness on the flexural behavior of continuous beams in view of the moment-curvature relationships along the sagging and hogging moment regions, respectively. The flexural behavior in the sagging moment region is characterized by yielding of jacket reinforcement ensued by yielding of core reinforcement and a yielding plateau until failure by concrete crushing. Regarding the hogging moment region, the yielding plateau occurs immediately after yielding of the tension steel bars located in the original beam. The same behavior is found for the remaining parameters and, therefore, only the stiffness values are included in the discussion.

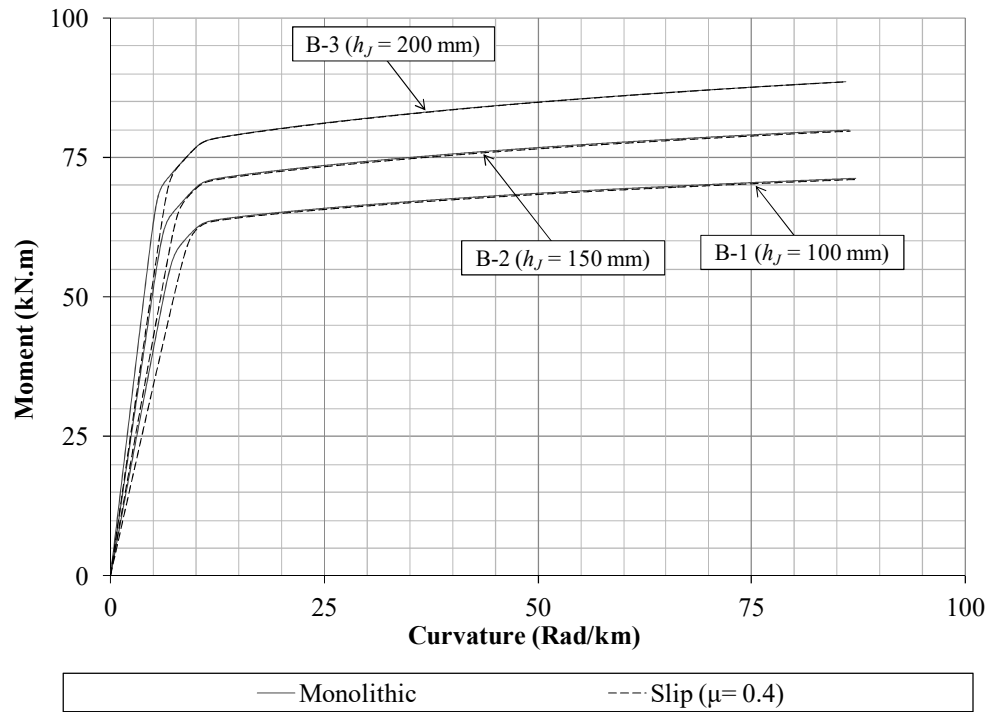


Figure 4-11: Effect of varying h_j on the $M-\phi$ relationship (sagging)

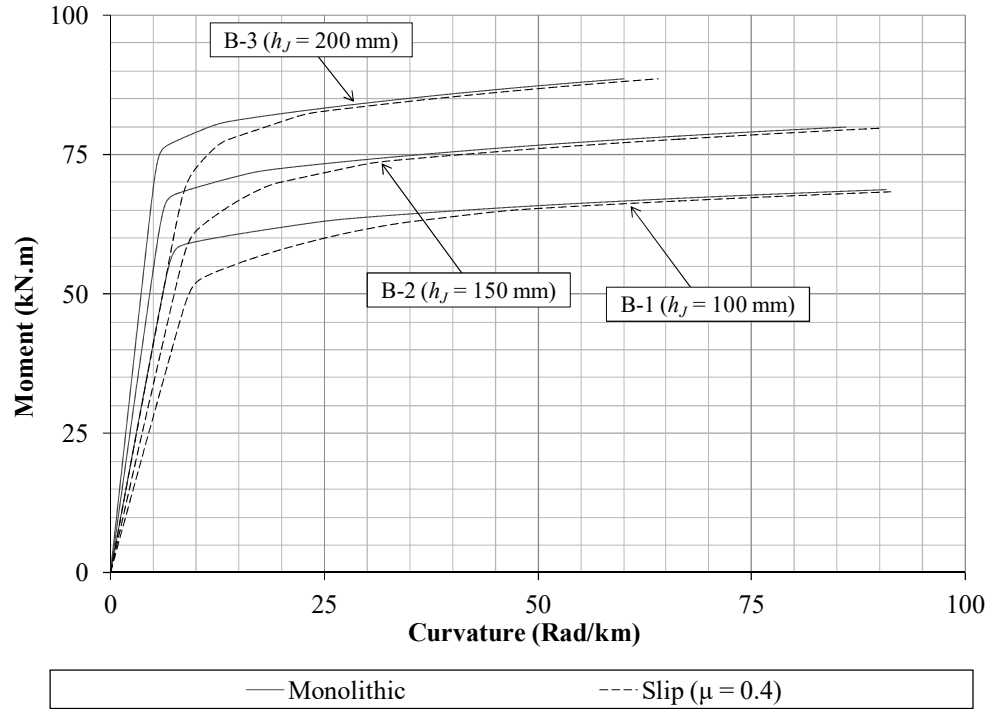


Figure 4-12: Effect of varying h_J on the $M-\phi$ relationship (hogging)

The stiffness reduction rate in both the sagging and hogging moment zones slightly decreases with increasing the jacket thickness. The ductility increase is insignificant when slip is considered for the sagging moment region indicating that the compressive strains at the extreme compression fibers reach the concrete crushing strain value at the same curvature. This happens since the axial stress in the jacketing layer assuming both monolithic and partially composite actions become identical beyond the yielding point of the jacket steel bars regardless of the slip strain. However, in the hogging moment region, as the jacket thickness increases, the contribution of the concrete material and the compression steel bars located in the jacket layer becomes more prevalent relative to the entire section. Therefore, slip strain reduces the generated compressive stresses within the jacket layer at the same curvature value. This results in delaying the concrete crushing and consequently increasing the ductility as the jacket height increases relative to the monolithic beams.

4.10.2 Effect of Beam Width (b_c)

Increasing the beam width results in a consequent increase in both the initial stiffness and capacity with minor influence on the flexural ductility. Regarding the slip influence, increasing the beam width results in decreasing the reduction rate of the initial stiffness in both sections. This is justified by the larger contact area between the concrete core and the jacket that is provided by the additional beam width. Two main differences arise from changing the location of the contact surface with respect to the neutral axis. When the interface is located at the tension side (i.e. sagging moment section), the reduction in the elastic stiffness is relatively smaller than the case of hogging moment. This variation in stiffness reduction is attributed to the contribution of both concrete and steel in determining the slip strain ($\Delta\varepsilon$) at each section. For the sagging moment region, the bending stresses at the tension side are resisted by both the core steel bars and the jacket steel bars especially after concrete cracking takes place. This means that the steel in the jacketing layer sustains part of the generated tensile stresses and the remaining part is resisted by the steel bars in the original beam. Thus, the slip strain required to achieve equilibrium at any section along the jacketed beam is governed by a portion of the total tensile stress generated at a given applied load. A different situation is observed along the hogging moment region where the jacketing layer is at the compression side. In this case, the entire concrete material is utilized along with the jacket steel bars to resist the same applied load. This indicates that a larger portion of bending is carried by the jacket part causing an increase in the slip strain required to achieve equilibrium at any segment along the hogging moment region. The other difference that prevails from changing the location of the interface with respect to the neutral axis is the point which the moment-curvature curves ignoring and including slip effects follow the same path. For the sagging moment region, the major difference in the moment-curvature diagram is within the elastic region before yielding of the jacket steel bars. This is justified by knowing that the axial force at any section is determined by the jacket steel bars. So, once these bars yield, the tensile forces in the jacket steel bars becomes almost constant and any increase depends on the strain hardening modulus. Thus, after jacket yielding is reached, the influence of slip strain becomes negligible in changing the behavior of the moment-curvature diagram compared to its monolithic counterpart. Regarding the hogging moment region, yielding

point is dictated by the tensile steel reinforcement in the concrete core. Therefore, the yielding point considering slip occurs at a larger curvature value compared to the monolithic case. Since the tensile stresses in the jacketing layer are governed by the compression behavior of both the concrete material and the embedded jacket steel bars, the influence of slip strain remains considerable in reducing the moment carrying capacity at a given curvature. As the load increases, the effect of slip strain diminishes until the moment-curvature behavior of the partially composite section becomes identical to the monolithic one.

4.10.3 Effect of Existing Beam Depth (h_c)

In both the sagging and hogging moment cases, increasing the existing section height increases both the elastic stiffness and capacity of the jacketed beams. This is justified by the larger concrete material available in the compression side and the longer lever arm the tension steel bars have. The ductility, on the other hand, decreases as the section height increases and becomes even more pronounced if the interface is at the compression side. This drop in ductility is related to the higher stresses developed in the tension steel bars as the original beam height rises at any curvature level. Therefore, at the same applied bending moment, this higher stress at the tension steel bars is translated into higher compressive stresses at the compression face of the jacketed beam causing the concrete to reach its crushing strain at lower curvature values. Regarding the slip influence on the flexural behavior of these beams, the initial stiffness reduction rate decreases as the original section height increases for both the sagging and hogging moment cases. This decrease is a result of the higher slip strain required to equilibrate the axial force within the jacket with the horizontal shear force along the interface.

4.10.4 Effect of Beam Span (L)

The moment-curvature curve assuming monolithic interaction between the core and the jacket are identical regardless of the span as they depend merely on the cross-sectional properties. However, including the slip effect activates the partially composite action and consequently the horizontal shear distribution along the interface becomes a major player in determining the flexural behavior of any section along the beam. In both the sagging

and hogging moment cases, as the span increases, the elastic stiffness reduction rate decreases proportionally. This observation is justified by the higher contact area provided by the larger span and consequently the increased frictional forces along the jacketed beam. For the positive moment section, the partially composite flexural behavior becomes identical to the monolithic counterpart once jacket steel bars yield. This happens due to the small variation in the axial stresses governed by the strain hardening modulus of jacket steel bars after yielding occurs. Thus, at the same curvature value, the stress in these steel bars is almost identical to the ones in the monolithic case. Although it still exists, the influence of slip strain diminishes even more at higher loading values due to the higher contribution of compression concrete and tension core steel bars while the stresses in the jacket steel bars remain almost constant. Regarding the hogging moment region, the variation between the partially composite scenario and monolithic behaviors persists within a portion of the inelastic region. This occurs since the jacketing layer is governed by the compressive stresses developed in concrete and the embedded steel bars rather than the tensile stresses generated merely in the steel bars. Thus, even after yielding of the section takes place, the axial force within the jacket at any section remains different from the monolithic case due to the influence of slip strain which decreases the jacket stresses at any curvature value. At higher loading values, the slip strain becomes less pronounced relative to the higher curvature values and consequently its influence becomes less substantial.

4.10.5 Effect of Concrete Compressive Strength (f'_c)

Increasing the concrete compressive strength results in a consequent increase in the beam capacity as it resists higher stresses for the same peak strain value. Also, increasing the concrete grade rises the concrete modulus resulting in a higher elastic stiffness value. Regarding the slip effect, increasing the concrete compressive strength decreases the stiffness reduction rate indirectly through increasing the friction between the two surfaces. This is inferred by examining the change in flexural behavior when slip is considered in both the sagging and hogging moment regions.

4.10.6 Effect of Steel Grade (f_y)

Increasing the steel yield strength has a negligible influence on the initial stiffness of the jacketed beams but a substantial enhancement to its capacity. The main reduction in stiffness will be in the elastic zone in which the steel elastic modulus plays the major role. Considering slip in the analysis shows that as the steel grade increases, the drop in flexural stiffness also increases for both the sagging and hogging moment sections. This happens since the steel bars with higher grade within the jacket resist larger axial forces before yielding and consequently result in higher shear stresses to achieve equilibrium. These higher stresses result in larger slip and consequently larger slip strain that reduces the flexural stiffness of the jacketed beams.

4.11 Interfacial Slip Behavior

The influence of interfacial slip between the concrete core and the underlying jacket layer is investigated in view of the slip strain ($\Delta\varepsilon$), slip (S) and interfacial shear stress (τ) distribution along the continuous beams under different loading values. Beam B-14 in Table 4-1 is considered for the following discussion. The coefficient of friction between the two surfaces is taken as 0.4 and 1.0 which represent untreated surfaces and intentionally roughened surfaces, respectively. Figs. 4-13 through 4-18 represent the distribution along one span only of the continuous beam.

4.11.1 Slip Strain ($\Delta\varepsilon$) Distribution

Figs. 4-13 and 4-14 illustrate the slip strain distribution from the edge support towards the intermediate support for coefficient of friction of 0.4 and 1.0, respectively. Four loading values representing the elastic range, onset of jacket yielding, onset of core yielding and maximum capacity of the section at the intermediate support at the onset of concrete crushing. Both figures show the same trend in which the slip strain at any section increases with the applied load except at the points of zero moment (i.e. the edge support and the point of contraflexure). This increase corresponds to the rise in the axial stresses within the jacket layer to maintain the equilibrium condition with the interfacial shear along the contact plane.

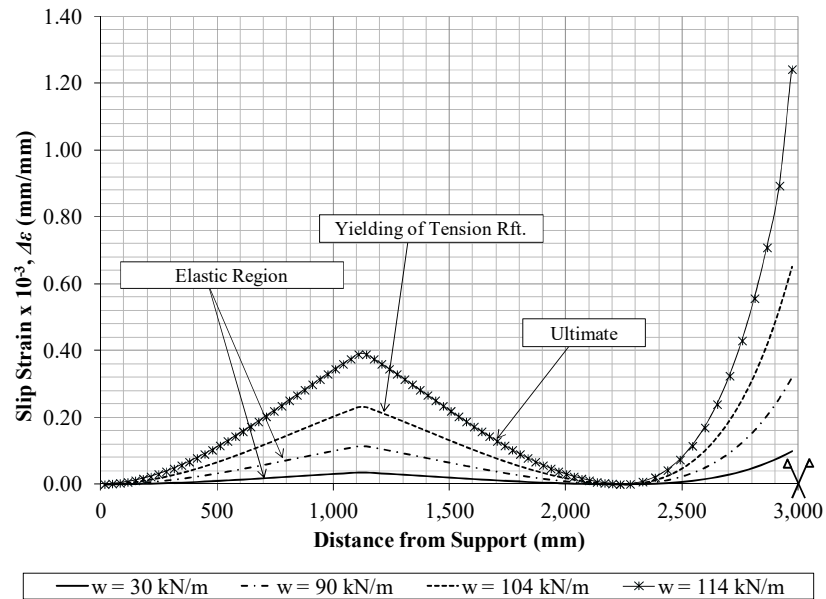


Figure 4-13: Slip strain ($\Delta\varepsilon$) distribution along beam B-5 ($\mu = 0.4$)

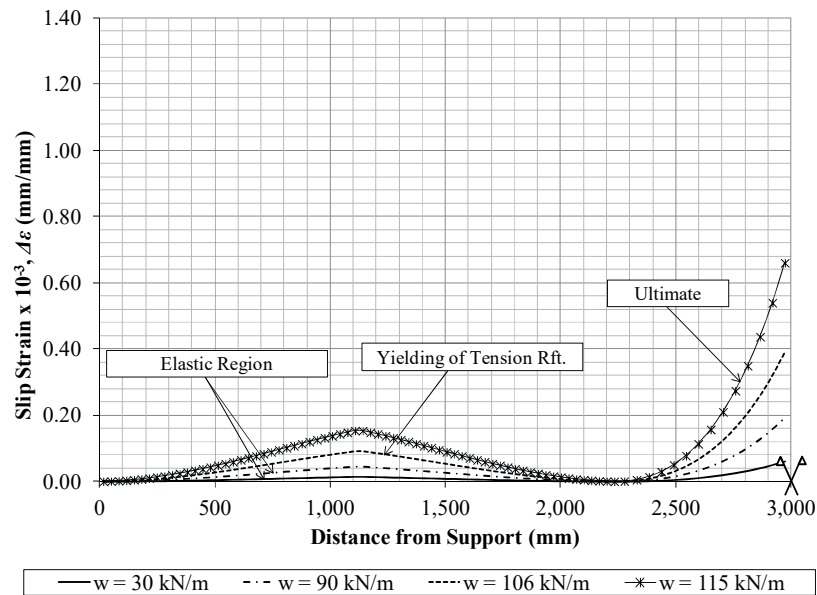


Figure 4-14: Slip strain ($\Delta\varepsilon$) distribution along beam B-5 ($\mu = 1.0$)

The maximum slip strain reaches the peak value at two points corresponding to the maximum positive bending moment and the maximum negative bending moment

sections. The slip strain is always higher at the intermediate support than the maximum positive moment for two main reasons. The first one is that the sagging moment region extends along a larger distance than the hogging moment zone resulting in a larger contact area and friction resistance and consequently less slip strain in the former case. Also, the slip strain is proportional to the bending moment that develop axial stresses within the jacket. Since the negative moment at the middle support is always larger than the maximum positive moment at any loading value, the slip strain follows the same trend and becomes higher at the intermediate support. By comparing the curves in Fig. 4-13 for $\mu = 0.4$ to their counterparts in Fig. 4-14 for $\mu = 1.0$, higher slip strain values at any given load are observed in the former case. This difference occurs due to the lower interfacial stiffness as the friction coefficient decreases. Thus, for the same axial stresses in the jacket, higher slip strain is required to achieve equilibrium with the interfacial shear stress. By roughening the concrete surface prior to jacketing, the slip strain at the maximum positive moment section drops from about 0.39 to 0.16 indicating a ratio of 58.9%. This drop at the maximum negative moment section is shown to be from 1.25 to 0.66 with a ratio of 47.2%. The slip strain increasing rate rises at higher loading values compared to the elastic region in both the hogging and sagging moment regions. For the maximum positive moment section, increasing the uniformly applied load from 30 kN/m to 90 kN/m along the beam results in a consequent increase of the slip strain by just 0.07×10^{-3} for the untreated surface and by just 0.03×10^{-3} for the roughened surface. After yielding occurs, increasing the load by about 10 kN/m results in an increase of 0.16×10^{-3} and 0.08×10^{-3} for the smooth and rough surfaces, respectively. The same observation applies for the maximum negative moment section but with different increasing rate. This is explained by the larger curvature the beam undergoes within the yielding plateau corresponding to any variation in the applied load relative to the elastic range.

4.11.2 Slip (S) Distribution

The slip distribution along the interface considering both smooth and rough surfaces are shown in Figs. 4-15 and 4-16, respectively.

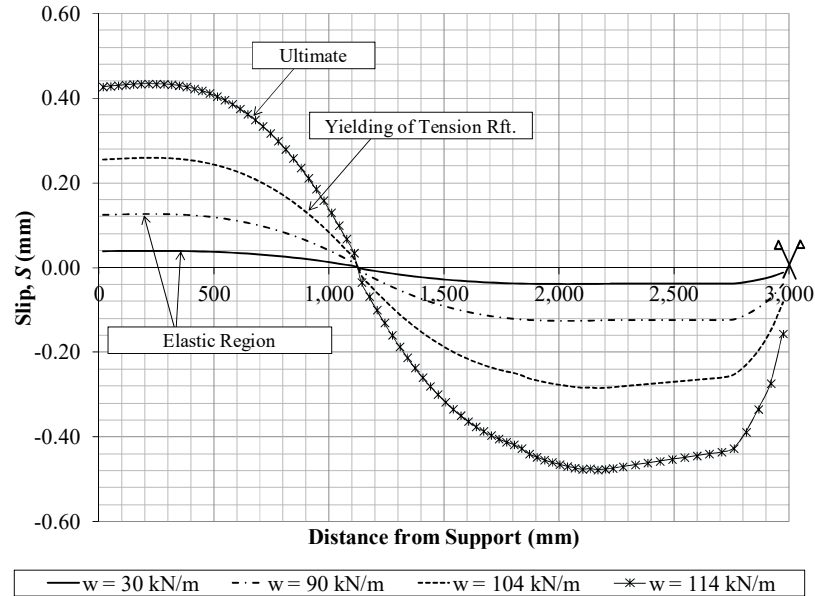


Figure 4-15: Slip distribution along beam B-5 ($\mu = 0.4$)

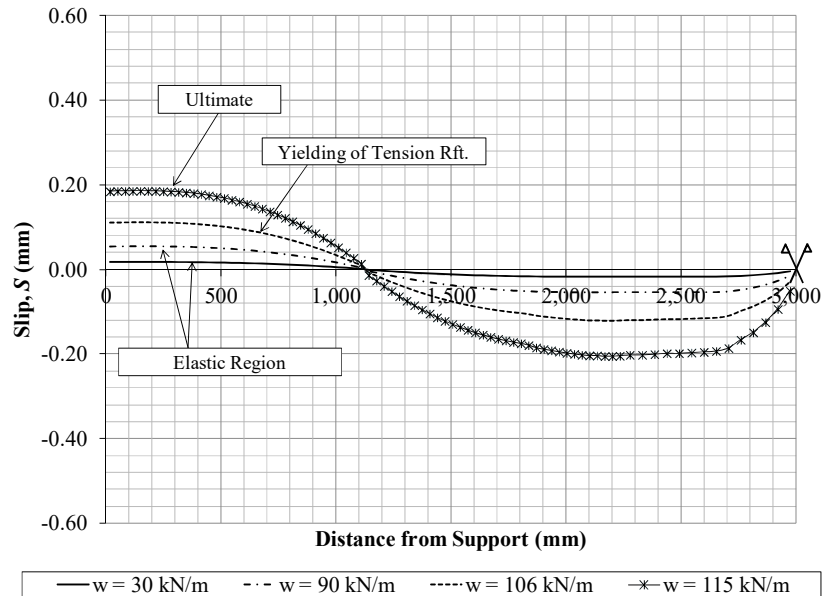


Figure 4-16: Slip distribution along beam B-5 ($\mu = 1.0$)

As shown in these figures, the maximum slip values are obtained at the edge support and the point of contraflexure that both correspond to the sections of zero moments. On the contrary, relative slip between the two surfaces becomes negligible at the locations of maximum positive and negative moments. The same figures also show that slip values at

sections closer to the edge support are slightly less than those near the middle support. This reduction is due to concrete cracking in the sagging moment region that takes place during the initial loading stage. When the concrete jacket is cracked, only the jacket reinforcement contributes in resisting the generated axial force resulting in lower level of shear stresses transferred along the interface.

In the hogging moment region, both concrete and the jacket steel bars are active and resist the bending moment in terms of compressive stresses. This results in larger contribution of the jacket and consequently higher shear stress to be transferred along the interface as translated by the higher slip values. The slip increasing rate after the first yielding point is higher than the rate before yielding for both kinds of surface treatment. For example, increasing the applied load within the elastic region from 30 kN/m to 90 kN/m results in a consequent increase in the maximum slip at the edge support from 0.04 mm to just over 0.12 mm for the untreated surface case. However, after the yielding point is reached, increasing the load by just 10 kN/m results in extra relative sliding between the two surfaces of about 0.18 mm. The same observations are shown for the roughened surface case. This higher rate of slip rise is justified by the higher curvature the beam exhibits after reaching the yielding point for the same amount of load compared to the elastic range. Consequently, the slip strain ($\Delta\varepsilon$) at the yielded segments increases resulting in a larger increase in slip. By examining both figures, the slip values considering smooth surfaces are higher than the ones obtained assuming roughened surfaces at any section for the same loading level. For example, the slip at the edge support for the former case is 138.9% higher than the second case at the ultimate loading value. This is justified by the higher frictional resistance and consequently the higher interfacial stiffness as the original beam surface is roughened. It is worth mentioning that at the ultimate load, the slip value at any section is less than the failure value defined in the slip model of about 2 mm.

4.11.3 Interfacial Shear Stress (τ) Distribution

Figs. 4-17 and 4-18 detail the horizontal shear stress distribution along the interface between the concrete core and the attached jacket layer considering untreated and roughened surfaces, respectively.

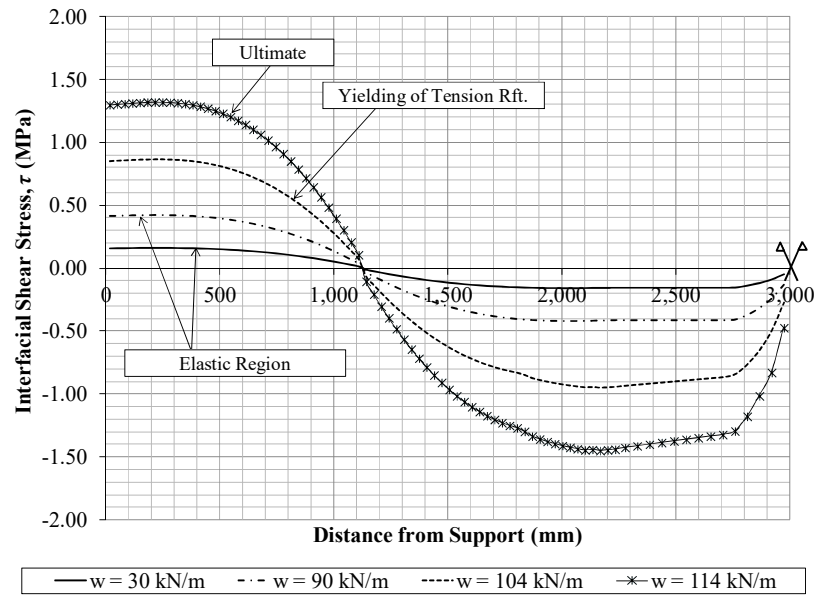


Figure 4-17: Interfacial shear stress distribution along beam B-5 ($\mu = 0.4$)

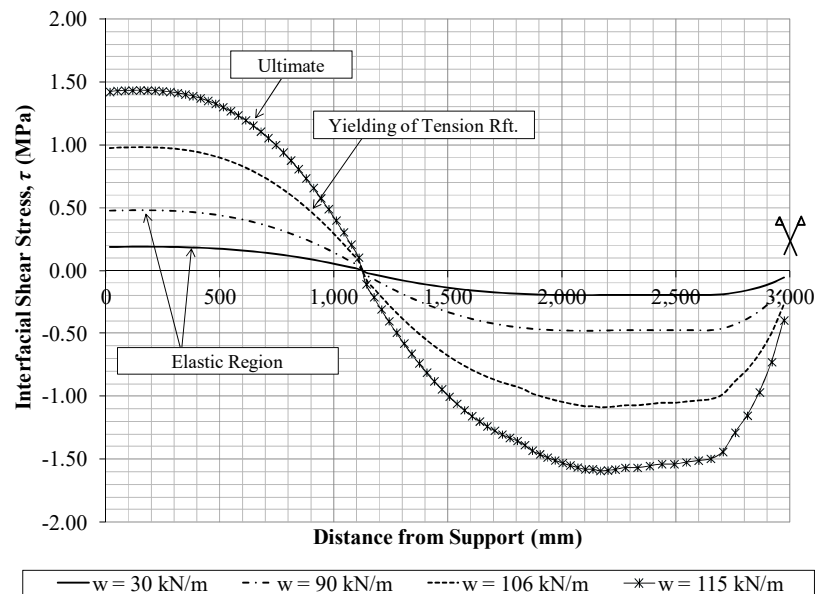


Figure 4-18: Interfacial shear stress distribution along beam B-5 ($\mu = 1.0$)

As shown in both figures, the distribution follows a third order parabolic function as initially assumed. The shear values are then determined by carrying out both sectional and longitudinal analyses to satisfy the equilibrium, compatibility and constitutive conditions. Also, the figures demonstrate the direct relationship that relate the interfacial

shear stress (τ) to the slip (S) at any section through the interfacial stiffness (k_s). Since the shear-slip model at the interface is non-linear, the secant interfacial stiffness varies depending on the slip value. For the smooth connection, the interfacial shear to slip ratio at the edge support is obtained as 3.4 N/mm^3 for all distributions up to the yield point and 2.9 N/mm^3 at ultimate. The same conclusion is drawn by comparing the curves in the second figure but with the secant interfacial stiffness of 9.1 N/mm^3 up to the yield point and 7.7 N/mm^3 at ultimate at the same section. As expected, the interfacial stiffness at any given load is higher when the original beam surface is roughened compared to the untreated case. Although the slip distribution along the interface is different for both cases, the interfacial shear stress distribution is almost identical. This is justified by the variation of the interfacial stiffness between both cases that result in equilibrium between the axial force in the jacketing layer and the horizontal shear force at any segment along the interface. The same observations are shown in the hogging moment region.

4.12 Proposed Expressions for the Effective Stiffness

Having developed and verified an analytical procedure to analyze jacketed continuous RC beams considering the influence of interfacial slip, a parametric study including 5,103 specimens was carried out to determine the contribution of various parameters on the flexural behavior of such beams. These parameters encompass the beams' geometrical properties, mechanical properties and interfacial behavior between the core and the RC jacket. The outcomes showed that ignoring the relative slip between the two substrates may overestimate the flexural stiffness causing serviceability issues such as larger deflections and unexpected cracking. Therefore, the influence of slip should be considered when designing such jacketed beams. Including the influence of slip in the analysis is tedious and requires a sequence of nested iterations that may not be convenient for design engineers. Here comes the importance of providing the engineers with expressions that improves the accuracy of their designs with less time and effort. The extent of flexural stiffness reduction as well as the point at which both the monolithic and partially composite curves becomes almost identical differ between the sagging and hogging moment regions. Therefore, different expressions are provided to adjust the

monolithic moment-curvature diagram of each region by considering the slip effect. Equations 15 through 18 provide the expressions for α_y and α_u that represent the yield monolithic factor and ultimate monolithic factor for the hogging moment section, respectively. Equations 19 and 20 presents the yield monolithic factor (α_y) for the sagging moment section.

$$\alpha_y^{-ve} = (\xi_y^{-ve}) + \left[22.6645 (\xi_y^{-ve})^2 - 46.3178 (\xi_y^{-ve}) + 23.6573 \right] \quad (15)$$

$$\begin{aligned} \xi_y^{-ve} = & 1.15545 - 2.661 \times 10^{-4} f'_c + 3.229 \times 10^{-5} f_y - 1.266 \times 10^{-5} L + 3.30 \\ & \times 10^{-7} b_c^2 - 2.811 \times 10^{-4} b_c - 1.704 \times 10^{-5} h_c + 5.22 \times 10^{-6} \frac{h_j^2}{b_c} \\ & - 1.57 \times 10^{-5} h_j - 0.037306 \mu \geq 1.0 \end{aligned} \quad (16)$$

$$\alpha_u^{-ve} = (\xi_u^{-ve}) + [1.4756 \exp (138.9291 \xi_u^{-ve})] \quad (17)$$

$$\begin{aligned} \xi_u^{-ve} = & 1.11070 - 1.108 \times 10^{-4} f'_c + 3.459 \times 10^{-5} f_y - 1.018 \times 10^{-5} L + 1.90 \\ & \times 10^{-7} b_c^2 - 1.784 \times 10^{-4} b_c - 8.39 \times 10^{-6} h_c + 2.857 \times 10^{-5} \frac{h_j^2}{b_c} \\ & - 9.06 \times 10^{-6} h_j - 0.033465 \mu \geq 1.0 \end{aligned} \quad (18)$$

$$\alpha_y^{+ve} = (\xi_y^{+ve}) + \left[20.3463 (\xi_y^{+ve})^2 - 41.0203 (\xi_y^{+ve}) + 20.6732 \right] \quad (19)$$

$$\begin{aligned} \xi_y^{+ve} = & 1.11354 - 1.108 \times 10^{-4} f'_c + 3.459 \times 10^{-5} f_y - 1.018 \times 10^{-5} L + 2.20 \\ & \times 10^{-7} b_c^2 - 2.043 \times 10^{-4} b_c - 8.39 \times 10^{-6} h_c - 2.190 \times 10^{-5} h_j \\ & - 0.033465 \mu \geq 1.0 \end{aligned} \quad (20)$$

Where f'_c is the concrete compressive strength in MPa; f_y is the steel yield strength in MPa; L is the beam span in mm; b_c is the section width in mm; h_c is the section height in mm; h_j is the jacket thickness in mm and μ is the coefficient of friction between the

original beam and the attached jacket. If the beams were subjected to initial loading before jacketing, then the monolithic factors should be reduced according to the expressions given in Equations 21, 22 and 23 for hogging ultimate monolithic factor, hogging yield monolithic factor and sagging yield monolithic factor, respectively.

$$(\alpha_y^{-ve})_{initial} = \alpha_y^{-ve} - \left(\frac{M_{initial}}{M_{u,unjacketed}} \right)^{1.327} (\alpha_y^{-ve} - 1.0) \geq 1.0 \quad (21)$$

$$(\alpha_u^{-v})_{initial} = \alpha_u^{-v} - \left(\frac{M_{initial}}{M_{u,unjacketed}} \right)^{0.849} (\alpha_u^{-v} - 1.0) \geq 1.0 \quad (22)$$

$$(\alpha_y^{+ve})_{initial} = \alpha_y^{+ve} - \left(\frac{M_{initial}}{M_{u,unjacketed}} \right)^{1.113} (\alpha_y^{+ve} - 1.0) \geq 1.0 \quad (23)$$

Where $M_{initial}$ is the maximum applied moment during jacketing and $M_{u,unjacketed}$ is the flexural capacity of the unjacketed section. In these expressions, the section subjected to maximum negative moment is considered to determine the hogging moment, while the section subjected to maximum positive moment is used in evaluating the sagging moment. Figs. 4-19(a) and 4-19(b) detail the variation in a typical equivalent moment-curvature diagrams assuming monolithic and partially composite sections without and with initially applied load, respectively.

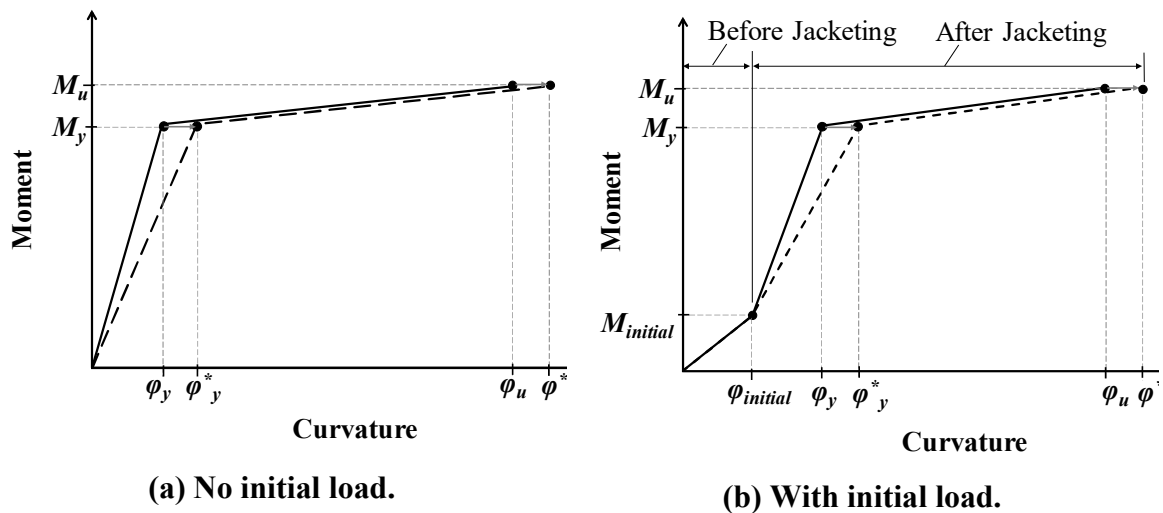


Figure 4-19: Typical moment-curvature diagram for jacketed beams.

The main parameters defining the curves in Fig. 4-19 are the yield moment (M_y) and the corresponding equivalent curvature assuming monolithic (ϕ_y) and partially composite (ϕ_y^*) actions; and ultimate moment (M_u) and the corresponding equivalent curvature assuming monolithic (ϕ_u) and partially composite (ϕ_u^*) actions. For the initially loaded beams, two additional terms are introduced that define the both the moment ($M_{initial}$) and the equivalent curvature ($\phi_{initial}$) corresponding to the initial loading value at the onset of jacketing as indicated in Fig. 4-19(b).

The proposed design procedure is summarized in the following three steps to obtain the actual load-deflection curve considering the sliding between the two surfaces:

- 1) Plot the moment-curvature diagram for the sections representing both the sagging and hogging moment regions assuming monolithic interaction between the original beam and the attached jacket. The hogging moment-curvature diagram is assumed bilinear and can be plotted by evaluating the yield and ultimate points. Regarding the sagging moment section, only the yield point is required since concrete crushing usually occurs at the negative moment section in continuous beams subjected to static loads.
- 2) Modify these moment-curvature diagrams in view of Fig. 4-19(a) and Equations 15 through 20 for beams not subjected to initial load during jacketing. If the beam was subjected to initial loading prior to jacketing, then modify the moment-curvature diagrams in view of Fig. 4-19(b) and Equations 21 through 23 taking into account the initial applied load level and the monolithic factors for unloaded beams obtained from Equations 15 through 20.
- 3) Use the equivalent moment-curvature diagrams obtained at the sagging and hogging moment regions along with the moment-area theorem to obtain the load-deflection diagram at any point along the beam.

The expectation function of the proposed monolithic factors is determined considering nonlinear regression analysis of the data. Figs. 4-20(a), 4-20(b) and 4-20(c) present the line of equality corresponding to α_y^{-ve} , α_u^{-ve} and α_y^{+ve} without initial loading, respectively.

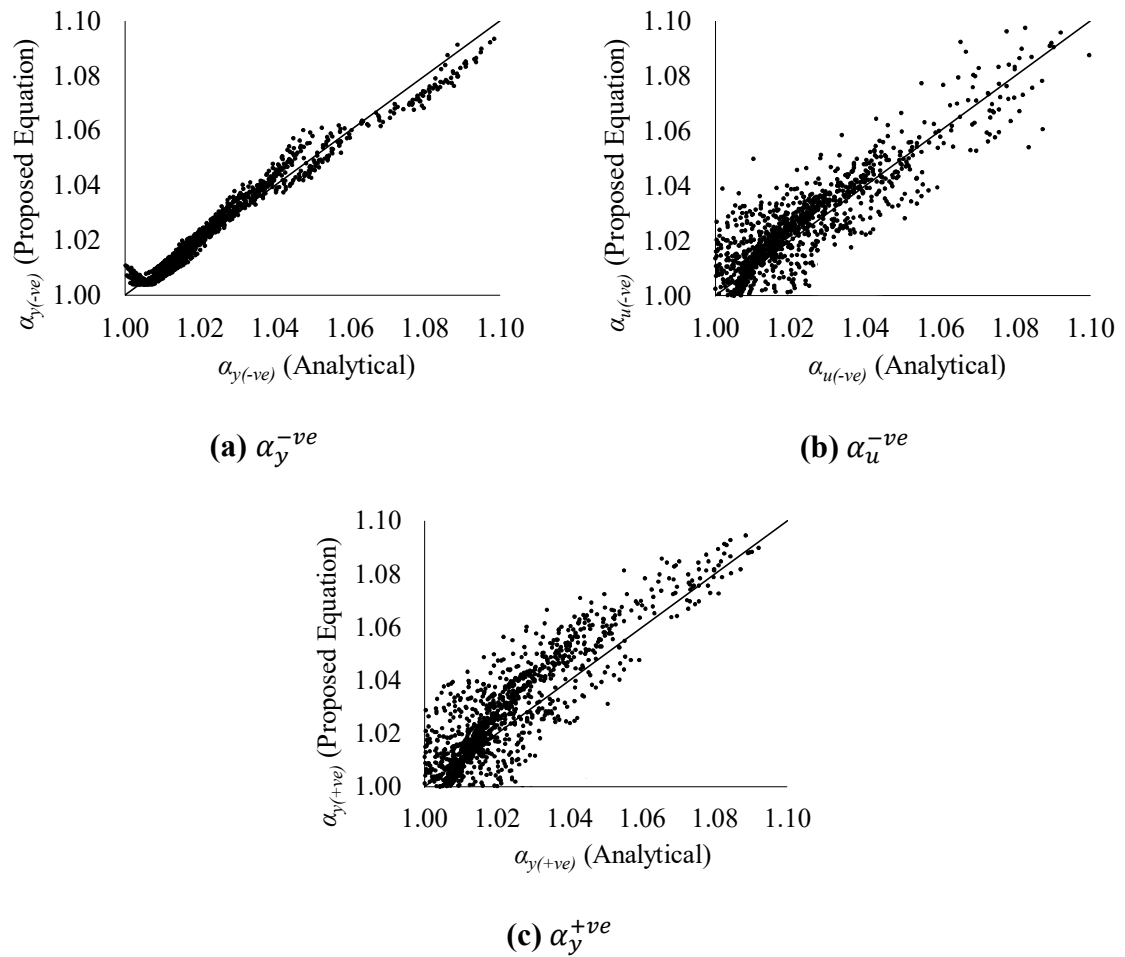


Figure 4-20: Statistical analysis for the proposed expressions

The line of equality plots for all factors reveal that the model provides a very good prediction of the actual behavior. Residual analysis for the three factors clearly shows a normally distributed pattern of the residuals about the mean. The small positive value of mean indicates that the proposed expressions tend to slightly round up the actual factor resulting in higher stiffness reduction and therefore more conservative estimates. Similar statistical analysis is carried out for the factors when initial load level is considered and a very good agreement is also found.

4.13 Summary and Conclusions

An investigation of the influence of RC jackets on the flexural behavior of continuous RC beams is presented. A parametric study including 5103 symmetric continuous beams subjected to uniformly distributed loads is carried out. The jacket is applied from one side at the soffit of all beams. Different parameters including the geometrical properties (i.e. original beam width, original beam depth, jacket thickness and beam span); mechanical properties (i.e. concrete compressive strength and steel yield strength); and surface treatment (i.e. interfacial friction coefficient) are investigated. An analytical modeling program encompassing sectional and interfacial analyses are developed taking into account that constitutive, compatibility and equilibrium conditions are satisfied. The results reported experimentally is used to verify the accuracy of the analytical model. The influence of each parameter is discussed in details in view of the moment-curvature diagrams of selected beams. The parametric study reveals that including the slip influence in the analysis results in a considerable stiffness reduction that should be considered in the analysis and design of jacketed sections. Also, a minor drop in the capacity of the jacketed beams is observed. The failure mode of the jacketed beams including slip effect is shown to be identical to that observed for their monolithic counterparts. For the beams considered in the analysis, ductile failure mode characterized by yielding of tension steel bars followed by concrete crushing at the extreme compression fiber is detected. Slip failure between the concrete core and the surrounding jacket is not observed for all of the analyzed cases. The effect of each of the studied parameters on the moment-curvature relationship is similar for both the hogging and sagging moment regions but shown to be more pronounced in the former zone. A design procedure and stiffness monolithic factors are introduced in terms of the studied parameters to obtain the flexural behavior of the continuous RC beams.

4.14 References

- [1] Tassios, T., Vintzeleou, E. "Concrete-to-Concrete Friction," *Journal of Structural Engineering*, ASCE, 1987, Vol. 113, No. 4, pp. 832-849.
- [2] Altun, F. "An experimental study of the jacketed reinforced-concrete beams under bending," *Construction and Building Materials*, 2004, Vol. 18, No. 8, pp. 611-618.
- [3] Bousias, S., Spathis, A. and Fardis, M. "Seismic retrofitting of columns with lap-spliced smooth bars through FRP or concrete jackets," *Journal of Earthquake Engineering*, 2007, Vol. 11, pp. 653-674.
- [4] Santos, P. and Júlio, E. "A State-of-the-Art Review on Shear-Friction," *Engineering Structures*, 2012, Vol. 45, pp. 435-448.
- [5] Martinola, G., Meda, A., Plizzari, G.A. and Zinaldi, Z. "An Application of High Performance Fiber Reinforced Cementitious Composites for RC Beam Strengthening," *Fracture Mechanics of Concrete and Structures - High Performance Concrete*, Taylor and Francis Group, 2007, pp. 1541-1548.
- [6] Shimoyama, Y., Uzawa, M. "Properties and application of ductal," *Journal of the Taiheiyo Cement Corporation*, 2002, Vol. 142, pp. 55-62.
- [7] Vicenzino, E., Culhman, G., Perry, V., Zakariasen, D. and Chow, T. "The first use of UHPFRC in thin precast roof shell for LRT Canadian station," *PCI Journal*, September-October, 2005.
- [8] Li, V.C. "From Micromechanics to Structural Engineering - the design of cementitious composites for civil engineering applications," *Doboku Gakkai Rombun-Hokokushu/Proceedings of the Japan Society of Civil Engineers*, 1993, Vol. 471, No. 1-24, pp. 1-12.

- [9] Rossi, P. "High Performance multimodal fiber reinforced fiber reinforced cement composite (HPMFRCC): the LPC experience," *ACI Materials Journal*, 1997, Vol. 94, No. 6, pp. 478-483.
- [10] Meda, A., Minelli, F., Plizzari, G.A. and Riva, P. "Shear behavior of steel fiber reinforced concrete beams," *Materials and Structures*, 2005, Vol. 38, No. 3, pp. 343-351.
- [11] Shehata, I., Shehata, L., Santos, E. and Simoes, M. "Strengthening of Reinforced Concrete Beams in Flexure by Partial Jacketing," *Materials and Structures*, 2009, Vol. 42, No. 4, pp. 495-504.
- [12] Tsonos, A.D.G. "Performance enhancement of R/C building columns and beam-column joints through shotcrete jacketing," *Engineering Structures*, 2010, Vol. 32, pp. 726-740.
- [13] Hamilton, C., Pardoen, G., Navalpakkam, S. and Kanzasjy, R. "Reinforced concrete bridge column performance enhancement through shotcrete jacketing," *ACI Structural Journal*, 2004, Vol. 101, No. 3, pp. 332-340.
- [14] Souza, R.H.F. and Appleton, J. "Flexural Behavior of Strengthened Reinforced Concrete Beams," *Materials and Structures*, 1997, Vol. 30, pp. 154-159.
- [15] Cheong, H.K. and MacAlevey, N. "Experimental Behavior of Jacketed Reinforced Concrete Beams," *Journal of Structural Engineering – ASCE*, 2000, Vol. 126, No. 6, pp. 692-699.
- [16] Scott, B.D., Park, R. and Priestley, M.J.N. "Stress-Strain Behavior of Concrete Confined by Overlapping Hoops at Low and High Strain Rates," *Journal of the American Concrete Institute*, 1982, Vol. 79, No. 1, pp. 13-27.
- [17] Karthik, M.M and Mander, J.B. "Stress-block parameters for unconfined and confined concrete based on a unified stress-strain model," *Journal of Structural Engineering – ASCE*, 2011, Vol. 137, No. 2, pp. 270-273.

- [18] Ramberg, W. and Osgood, W.R. "Description of stress-strain curves by three parameters," Technical Note No. 902, National Advisory Committee for Aeronautics, 1943, Washington DC.
- [19] Thermou, G.E., Pantazopoulou, S.J. and Elnashai, A.S. "Flexural behavior of brittle RC members rehabilitated with concrete jacketing," *Journal of Structural Engineering*, ASCE, 2007, Vol. 133, No. 10, pp. 1373-1384.
- [20] CSA. "Design of concrete structures (CAN/CSA A23.3-14)," Cement Association of Canada, 2014, Ottawa, ON.
- [21] Tsioulou, O.T. and Dritsos, S.E. "A theoretical model to predict interface slip due to bending," *Materials and Structures*, 2011, Vol. 44, pp. 825-843.
- [22] Alhadid, M.M. and Youssef, M.A. "Analysis of reinforced concrete beams strengthened using concrete jackets," *Engineering Structures*, Elsevier, 2017, Vol. 132, pp. 172-187.
- [23] Kotsira, E., Dritsos, S., Pilakoutas, K. "Effectiveness of techniques for flexural repair and strengthening of RC members," *Proceedings of the 5th international conference on Structural faults and repair*, 1993, Edinburgh, UK, pp. 235-243.
- [24] Saiidi, M., Vrontinos, S. and Douglas, B. "Model for the response of reinforced concrete beams strengthened by concrete overlays," *ACI Structural Journal*, 1990, Vol. 87, No. 6, pp. 687-695.
- [25] Youssef, M.A. and Rahman, M. "Simplified seismic modeling of reinforced concrete flexural members," *Magazine of Concrete Research*, 2007, Vol. 59, No. 9, pp. 639-649.
- [26] Kassimali, A. "Matrix Analysis of Structures," Thomson-Engineering, 2nd ed., 2011, 640 pp.
- [27] Oehlers, D.J., Haskett, M., Mohamed, M.S. and Griffith, M.C. "Moment Redistribution in Reinforced Concrete Beams," *Proceedings of the Institution of Civil Engineers, Structures and Buildings* 163, June 2010, pp. 165-176.

[28] ACI Committee 318. "Building code requirements for structural concrete and commentary (ACI 318-14)," American Concrete Institute, 2014, Farmington Hills, MI.

Chapter 5

5 SIMPLIFIED APPROACH TO ASSESS THE CAPACITY OF FIRE-DAMAGED REINFORCED CONCRETE BEAMS

Concrete is considered as one of the most highly efficient materials to withstand elevated temperatures and to provide protection from fire [1]. North American building codes [2-4] address fire-structure interaction in view of prescriptive methods that specify fire-resistance rating and minimum cross-sectional dimensions. Although performance-based approach has been widely used by engineers to analyze and design structural members under various load conditions, its adoption is still in its infancy when fire loads are considered. Objective-based design is already introduced in the National Building Code of Canada (NBCC) to design the structural components to achieve specified performance levels under various loading and fire exposure scenarios. The recommended guidelines are considered as an alternative of the prescriptive design provisions for the fire design of building structures.

Analysis and design of RC beams at room temperature has been performed using the concept of stress-block parameters proposed by Kazinczy [5] and Whitney [6]. In this approach, a fictitious rectangular stress block possessing the same resultant force and point of application with the actual compressive stress distribution is utilized. The flexural capacity of RC beams subjected to either sagging or hogging moments is barely affected by the chosen constitutive relationship of concrete or by the assumed simplification [5-7]. Both ACI [8] and CSA [9] permit the calculation of beams' flexural capacity based on the equivalent stress-block parameters at ambient conditions.

A simplified method to evaluate these parameters for RC beams during fire exposure was previously introduced by El-Fitiany and Youssef [10]. The aim of this chapter is to propose and validate a procedure to determine the residual stress-block parameters that can be used in calculating the post-fire flexural capacity of RC beams. The analysis procedure starts by performing heat transfer analysis to determine the maximum temperature distribution after a full heating-cooling cycle. Then, sectional analysis

considering material residual mechanical properties is conducted to plot the moment-curvature ($M-\phi$) relationship of the damaged beams. The validated method is implemented to carry out a parametric study to investigate the influence of fire duration, cross-sectional dimensions and material mechanical properties on the maximum potential temperature distribution and residual capacity of fire-damaged RC beams.

Determination of the residual flexural capacity of RC beams is not practical in design offices due to the complexity associated with performing comprehensive thermal and structural analyses. Analysis of RC beams at ambient conditions considering the stress-block concept is widely implemented by engineers. This study aims at manipulating this concept to provide engineers with simplified tools that will assist them during the preliminary design phase in predicting the maximum temperature reached and to evaluate the residual capacity of beams subjected to extreme standard fire scenarios. The outcome of this research provides a solid basis for objective-based design considering natural fire.

5.1 Assumptions

The proposed analytical model is performed considering the following assumptions: (1) a cross section remains plane after fire exposure. This assumption was previously validated for exposure temperatures up to 1200°C [10], (2) perfect bond exists between steel reinforcement and the surrounding concrete material, (3) spalling of concrete is neglected in the analysis as normal strength concrete is assumed, (4) two dimensional heat transfer analysis is considered along the member length, (5) influence of concrete tensile cracks on heat flow is neglected in heat transfer analysis, (6) geometrical nonlinearity is not considered.

5.2 Heat Transfer Analysis

At each time step during the heating-cooling cycle, temperature distribution is determined within the cross-section in view of the finite difference method detailed by Dusenberre [11] and Lie [12]. The calculation procedure commences by meshing the section into

interior square elements and boundary triangular elements. The temperature is represented for each square element by its center and for each triangular element by the hypotenuse mid-point. Temperature in steel bars is considered equal to the temperature of the adjacent concrete elements due to the relatively high thermal conductivity of steel. Heat analysis is carried out in time steps considering ASTM E119 [13] standard fire during the heating phase. During the cooling stage, ISO 834 [14] recommendations are adopted since the ASEM E119 lacks a descending branch. At any given time, the temperature in each element is calculated by solving heat balance equations based on the temperature reached in the previous time increment. Thermal properties (i.e. specific heat, emissivity and thermal conductivity) proposed by Lie [12] are considered in the heat transfer analysis. These properties are assumed to be irreversible and do not restore their initial values after cooling [15-17]. Thus, during the cooling phase, thermal properties are considered to maintain a constant value corresponding to the maximum temperature reached in concrete. This assumption is valid for temperatures above 100oC when most of the moisture is evaporated and its influence on temperature distribution becomes negligible [15].

5.3 Materials Residual Behavior

The permanent concrete damage caused by fire exposure occurs due to the irreversible chemical and physical processes in both the heating and cooling phases of a fire cycle. The general form of Tsai model [18] is adopted to represent the compressive stress-strain relationship of concrete. The residual mechanical properties of concrete are obtained using the models proposed by Chang *et al.* [19] which agree with experimental studies by others [20-25]. Generally, concrete exhibits a continuous reduction in its residual strength for a period of time after fire due to thermal incompatibility, internal crack development and dehydration reactions. Exposing concrete to elevated temperature reduces its residual compressive strength (f_{cR}') and increases its strain at peak stress (ϵ_{oR}) causing the material to soften. The permanent increase in ϵ_{oR} is attributed to the cracks developed during the heating-cooling cycle resulting from the thermal incompatibility between the cement matrix and the embedded aggregates. The original compressive strength of concrete was

shown to have a substantial impact on ε_{oR} when the temperature exceeds 200°C [19] or 250°C [26].

The crushing strain (ε_{cu}) of concrete at failure is taken as 0.0035 at ambient conditions [9]. Unfortunately, few information is available in the literature regarding the residual crushing strain (ε_{cuR}). In this study, the value of ε_{cuR} is proposed as the summation of ε_{cu} and the difference between ε_{oR} and its counterpart at ambient conditions (ε_o), Equation 1.

$$\varepsilon_{cuR} = \varepsilon_{cu} + (\varepsilon_{oR} - \varepsilon_o) \quad (1)$$

The proposed equation is found to agree well with the experimental data obtained by Felicetti *et al.* [26] especially at temperatures beyond 350°C.

Regarding steel constitutive relationship, the model used by Karthik and Mander [27] is adopted as it conveniently combines the initial elastic response, yield plateau and strain hardening stages in a rigorous form. A complete heating-cooling cycle does not alter the intrinsic shape of steel stress-strain curve including the well-defined yielding plateau and strain hardening behavior [28]. The models proposed by Qiang *et al.* [29] is adopted to determine the residual yield strength and modulus of elasticity for steel bars with grade higher than 460 MPa (66.72 ksi). For mild steel, the residual yield strength (f_{yR}), Equation 2, is proposed and validated in this study in view of relevant experimental data [25,30]. An approximate relationship showing the same trend was also obtained by Kodur *et al.* [31].

$$\frac{f_{yR}}{f_y} = \begin{cases} (-1.855 \times 10^{-5}) T_{max} + 0.993 & , T_{max} \leq 500 \text{ } ^\circ\text{C} \\ (8.237 \times 10^{-7}) T_{max}^2 - (1.809 \times 10^{-3}) T_{max} + 1.682 & , T_{max} > 500 \text{ } ^\circ\text{C} \end{cases} \quad (2)$$

The residual Young's modulus of mild steel is not affected by the heating-cooling cycle at all temperature levels and can be taken equal to its original value before fire [25,30,32].

5.4 Strength Analysis

Having determined the maximum temperature reached and the residual properties of each layer along the cross-section, an iterative sectional analysis procedure [33] is carried out to determine the residual $M-\phi$ relationship. At every loading step, the curvature is increased incrementally until failure occurs. The kinematic and compatibility conditions are considered in view of the corresponding residual mechanical properties and constitutive relationships of both concrete and steel. To maintain the high accuracy while reducing the computation time, a sensitivity analysis was performed and the maximum layer height is chosen as not to exceed 2 mm. The failure criterion of the RC element is defined by crushing of concrete once the strain in any of the sectional layers reaches ϵ_{cuR} given in Equation 1.

Fig. 5-1a illustrates the development of residual strain components along a typical beam cross section. The residual free thermal strain (ϵ_R) represents the irreversible part of the free thermal expansion that occurred during fire. During cooling, thermal strain is partially restored by a rate of $8 \times 10^{-6}/^\circ\text{C}$ [34] from the maximum temperature reached, while ϵ_R for steel is set to zero. Residual stress-induced strain ($\epsilon_{\sigma i}$) distribution, Fig. 5-1b, is determined as the difference between an equivalent strain (ϵ_{eq}) and ϵ_R .

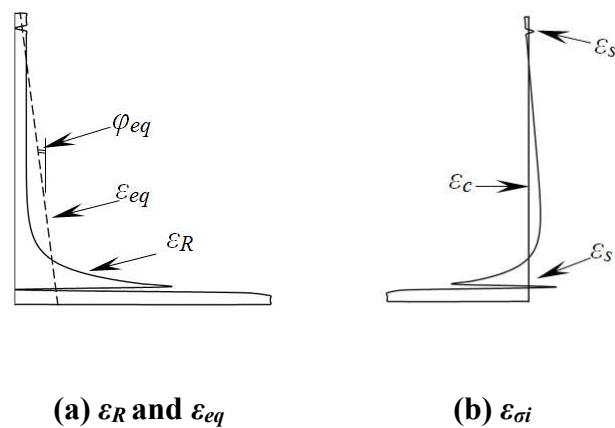


Figure 5-1: Development of strain components along the beam cross-section

Residual stresses are induced in fire-damaged members for two main reasons:

- 1) Thermal strain is partially reversible in concrete and fully reversible in steel bars [34]. Hence, concrete tends to remain partially expanded while steel bars tend to restore their initial length after fire. The internal stresses required to achieve equilibrium due to the variation in behavior between concrete and the embedded steel bars is explicitly considered in this study.
- 2) Thermal strain distribution along section height is nonlinear as it follows the nonlinear temperature profile. Therefore, internal stresses are developed to maintain the plane section assumption. An iteration process is performed in this study by changing the ε_{eq} and φ_{eq} while checking the equilibrium condition of $\varepsilon_{\sigma i}$ distribution. Once equilibrium is achieved, $\varepsilon_{\sigma i}$ are applied as initial strains in the concrete and steel layers. Similar approaches to calculate the equivalent thermal distribution of RC members during and after fire were previously developed by El-Fitiany and Youssef [10] and Alhadid and Youssef [35].

5.5 Validation

The capability of the presented model to predict the structural performance of fire-damaged RC members is validated in view of the experimental results obtained by Kodur *et al.* [36] and Haddad *et al.* [37].

5.5.1 Kodur *et al.* [36]

The experimental program encompassed testing rectangular RC beams having cross-sectional dimensions of 406×254 mm (15.8×10 in.) and an overall length of 3.96 m (13.0 ft). The validation is performed considering beam BB1 made with normal weight concrete having a compressive strength (f'_c) of 58.2 MPa (8.44 ksi) at the time of testing. The beam was reinforced with 3Φ19 mm (#6) and 2Φ13 mm (#4) steel bars at the tension and compression sides, respectively. Shear reinforcement was provided using Φ6 mm (#2) stirrups with a spacing of 150 mm (5.90 in.). The yield strength (f_y) of the flexural and shear reinforcement is 420 MPa (60.92 ksi) and 280 MPa (40.61 ksi), respectively.

The test commenced by placing the beam on two supports 3.66 m (12.0 ft) apart and subjecting it to two point loads of 50 kN (11.24 kip) each located 1.4 m (4.59 ft) from the supports. A portion of the beam having a length of 2.44 m was placed inside a furnace resulting in the time-temperature curve described by Kodur *et al.* [36]. After 24 hours, the load-deflection behavior of the fire-exposed beam was determined by increasing the two-point loads until concrete crushing occurred. Since the beam was loaded during the test, Terro model [38] was adopted to account for the transient strain (ϵ_{tr}) at each concrete layer subjected to an initial compressive stress. A comparison between the experimental load-deflection curve and the one obtained by the proposed model show a very good match with an error of 6.99%, 3.53% and 8.16% for the ultimate capacity, yield load and initial stiffness as illustrated in Fig. 5-2(a), respectively. The 50% secant stiffness obtained from the proposed model is found to be 22.63% higher than the one obtained experimentally. One reason for the higher values determined by the model is the minor surface spalling in beam BB1 that occurred during the test and not accounted for in the analysis. In addition, restraining beam BB1 throughout the heating period could alter $\epsilon_{\sigma i}$ resulting in decreasing the residual stiffness in the fire-damaged beam [15]. Regarding maximum deflection, the proposed model produced a lower value than the experimental one. This may be attributed to the assumption that the analytical analysis terminates once any of the concrete layers reaches crushing strain, which may not be the case if the experimental test continues beyond this point as indicated by the drop in the load-deflection curve at the end.

5.5.2 Haddad *et al.* [37]

The control beam had a width of 250 mm (9.84 in.), height of 100 mm (3.94 in.) and a total length of 1.5 m (4.92 ft) with a concrete cover of 25 mm (0.98 in.). The compressive strength of the normal weight concrete was 65 MPa (9.43 ksi). The reinforcement consisted of 3 Φ 14 mm (0.55 in.) main steel bars and 2 Φ 10 mm (0.39 in.) top steel bars having a yield strength of 620 MPa (89.92 ksi). The beams were confined with Φ 8 mm (0.31 in.) stirrups with a spacing of 50 mm (1.96 in.) near the supports and 90 mm (3.54 in.) towards the mid-span. The beam was exposed to a controlled prolonged heating and cooling cycle using an electric furnace. The unrestrained simply supported beams were

then subjected to a two-point loading scheme with a loading rate of 20 N/s (4.5 lb/s) until failure. There was no spalling in the tested beams during heat exposure and the loss in strength was due to material degradation. A comparison of the measured and predicted load-deflection curves at the beam mid-span is plotted in Fig. 5-2(b). The results agree well with the experimental data as indicated by the small error of 5.2% difference in capacity and 4.1% in initial flexural stiffness. The difference in ductility between the experimental and analytical results may be attributed to the strain hardening assumption in the steel model, and to the assumed residual crushing strain at which the analysis is terminated. Also, the shift in the load-deflection curve of 4.6 mm (0.25 in.) is justified by the residual thermal expansion that was considered in the analytical model.

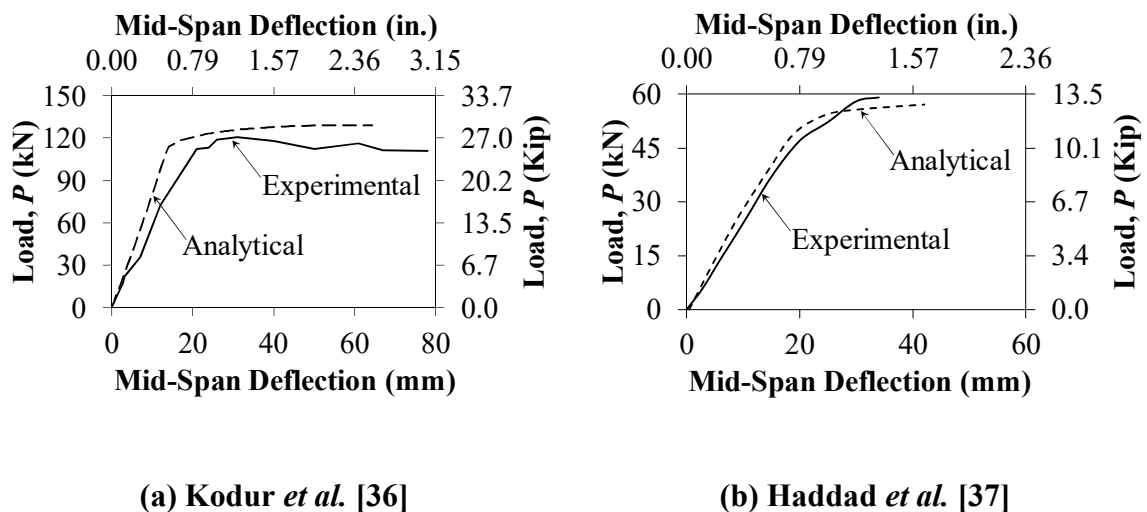


Figure 5-2: Validation of the proposed model in view of load-deflection relationship

5.6 Parametric Investigation and Discussion

An extensive parametric study is carried out to determine the influence of a complete heating-cooling cycle on the stress-block parameters (i.e. α_l and β_l) of rectangular RC sections exposed to fire from three sides and subjected to either sagging or hogging moments. The main parameters are the concrete compressive strength (f'_c), steel yield

strength (f_y), beam height (h_c), beam width (b_c), tensile reinforcement ratio (ρ) and fire duration (t_{hot}). The values of the chosen parameters are set based on the practical considerations in the design of typical RC buildings and duration of typical fire incidents. The mechanical properties for concrete are defined in terms of f_c' as 25, 30 and 35 MPa (3.63, 4.35 and 5.07 ksi) and defined for steel in terms of f_y as 300, 400 and 500 MPa (43.51, 58.01 and 72.51 ksi). The chosen widths and heights of the analyzed beams range from 200 to 500 mm (7.87 to 19.69 in.) and from 400 to 700 mm (15.75 to 27.57 in.) with an increment of 100 mm (3.94 in.), respectively. The tension steel reinforcement ratio is taken as 0.5%, 1.0%, 1.5% and 2.0% which are found to cause the desired ductile mode of failure in the tested beams. Compression steel reinforcement are not considered in the analysis for simplicity. Concrete cover is taken as 30 mm (1.18 in.). The considered sections are subjected to ASTM E119 [13] heating phase followed by an ISO 834 [14] cooling phase. Each section is analyzed five times to account for fire durations (t_{hot}) of 0.5, 1.0, 1.5, 2.0 and 2.5 hrs before cooling. Therefore, a total of 2880 different cases are considered in the analysis.

5.6.1 Influence of Fire Duration

The influence of increasing the maximum fire duration (t_{max}) on the residual flexural behavior is examined in view of a 300×500 mm (11.81×19.69 in.) RC beam having f_c' of 30 MPa (4.35 ksi), f_y of 400 MPa (58.01 ksi) and ρ of 1.0%. The variation in $M-\phi$ relationship with the temperature at the end of the heating phase (t_{hot}) is illustrated in Figs. 5-3(a) and 5-3(b) for beams subjected to sagging and hogging moments, respectively. Prolonged exposure to fire results in material strength degradation and softening. These alterations adversely affect the stiffness and capacity of the fire-damaged sections depending on the location of the compression block relative to the fire.

Beams subjected to hogging moment experience larger drop in stiffness than those subjected to sagging moment for all fire durations as indicated in Figs. 5-3 and 5-4(a). In both cases, fire is applied from the bottom and the two vertical sides. Compression zone in the sagging moment sections is located away from heat concentration region resulting in less deterioration of concrete. Tension steel bars, which are located near the beam's soffit, are subjected to relatively high temperatures. However, this has negligible impact

on the overall flexural stiffness reduction due to the full recovery of the elastic stiffness of mild steel bars after fire exposure [25,30,32]. In the case of high strength steel bars, fire effect on stiffness reduction is negligible for temperatures up to 600°C [29]. Regarding flexural capacity, the permanent strength reductions in the hogging moment sections are found to be higher than those for beams subjected to sagging moments. This can be attributed to the higher decrease in concrete compressive strength in the former case.

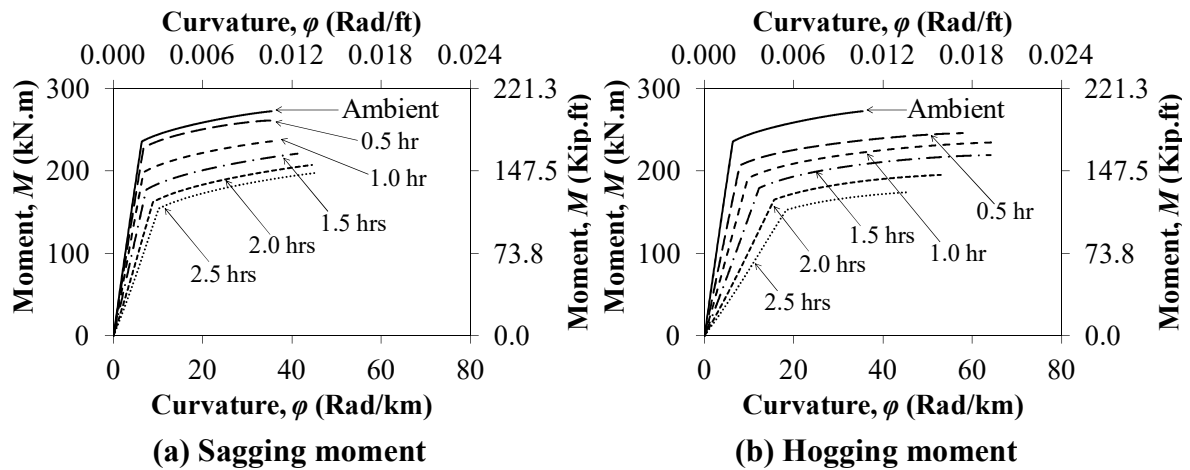


Figure 5-3: Effect of fire duration on M - ϕ relationship

Another observation is that the residual ductility of beams subjected to sagging moment increases with fire duration; whereas no clear relationship can be drawn for the hogging moment case. The reason lies in the increase of residual crushing strain (ϵ_{cuR}), Equation 1, with the rise in the temperature of concrete layers. Average temperature distribution becomes almost constant at the top concrete layers since heat flow in that region is governed by the two vertical sides only as indicated in Fig. 5-5(a).

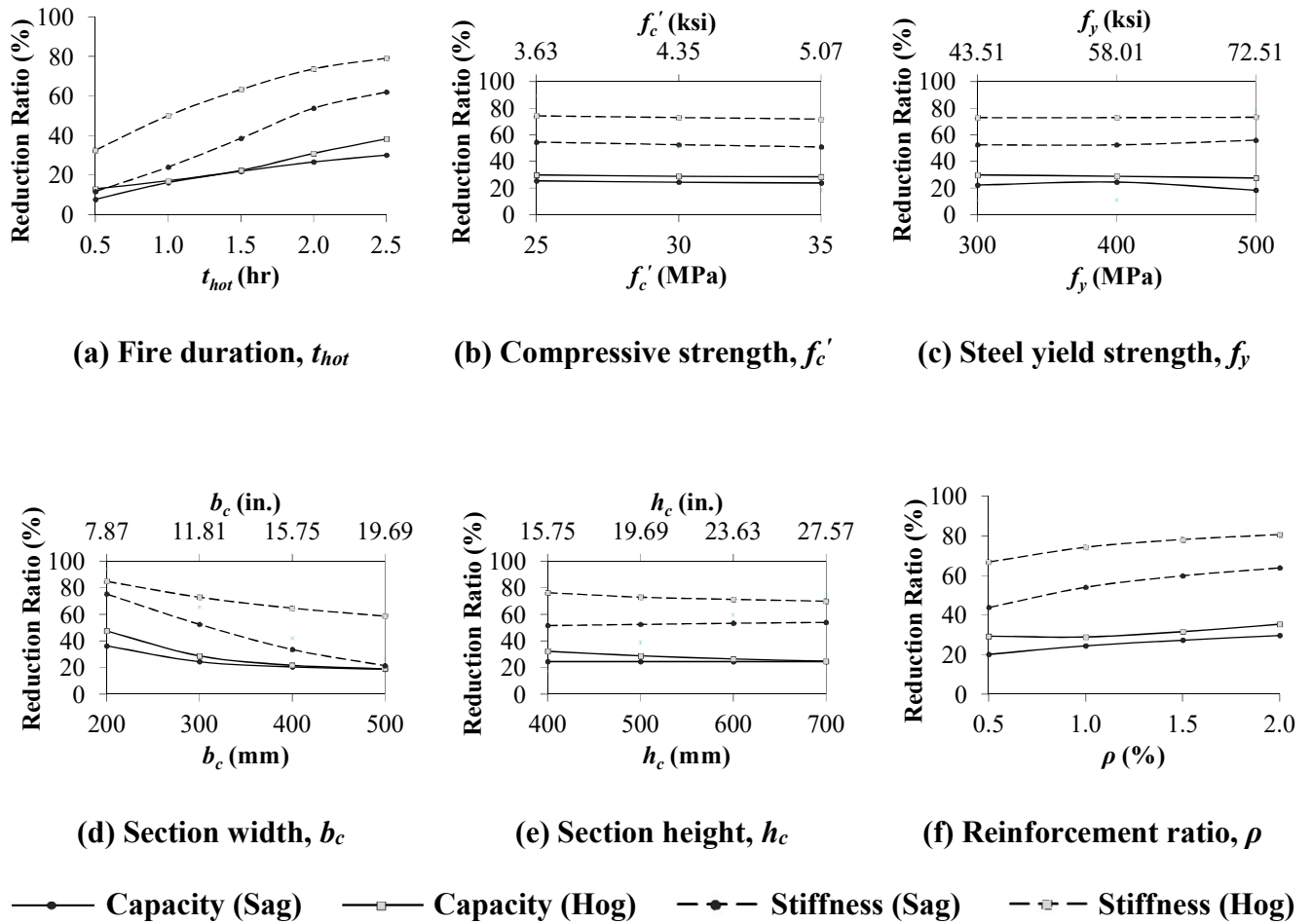


Figure 5-4: Influence of the parameters on the reduction ratios of capacity and stiffness

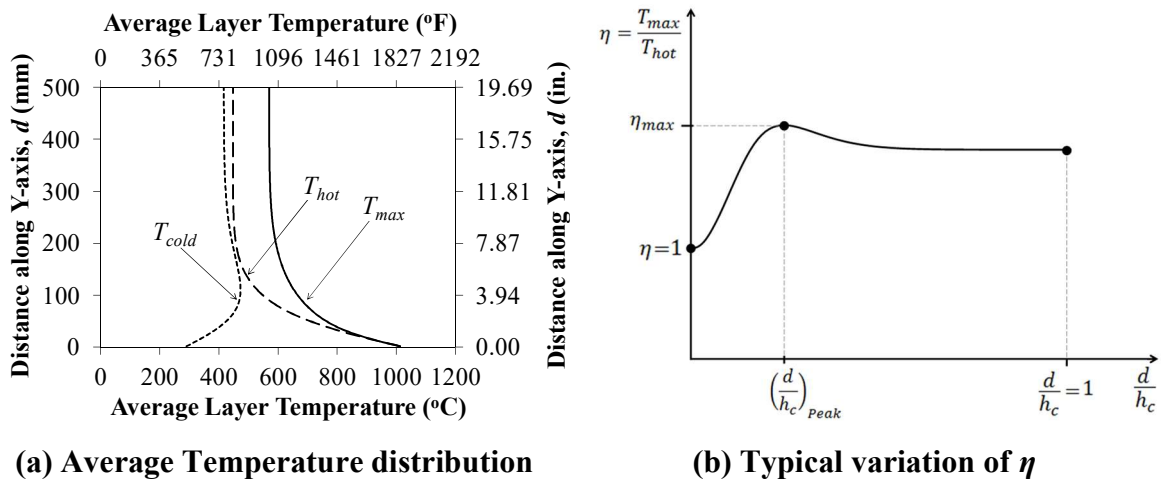


Figure 5-5: Temperature distribution and variation of η

Near the beam bottom face, significant variation in temperature exists between the concrete layers as the heat transfer from all three sides is predominant. For sagging moment sections, ε_{cuR} takes the same value at the upper concrete layers forcing the failure to always occur at the extreme top compression fiber. However, for hogging moment sections, ε_{cuR} takes its maximum value at the bottom concrete layer and decreases in the upper layers that experience lower temperatures. In this case, crushing of concrete does not necessarily occur at the extreme bottom compression fiber. Hence, ductility is governed by the location of the first concrete layer that reached a strain value equal to its corresponding ε_{cuR} .

The influence of the mechanical and geometrical properties on the $M-\phi$ relationship of fire-damaged beams have a similar trend to the curves shown in Figs. 5-3(a) and 5-3(b) but with different magnitudes. Thus, repetition of the specific $M-\phi$ curves for each parameter is not shown but can be understood in view of Figs. 5-4(b) through 5-4(f) in the subsequent discussion.

5.6.2 Influence of Mechanical Properties

The considered sections have the same geometric properties of the aforementioned beam and subjected to fire for 2 hrs. The influence of each parameter on the residual capacity and stiffness is investigated by changing it while fixing all other parameters.

Increasing f'_c from 25 MPa to 35 MPa results in negligible variation in residual capacity and minor reduction in elastic stiffness for both the sagging and hogging moment cases. The reduction in both capacity and elastic stiffness is found to be higher in the hogging moment sections than their counterparts in the sagging moment sections. This occurs because of the higher strength degradation of concrete in the former case as the compression zone is located closer to the bottom surface where higher temperature values exist.

Regarding steel grade, stiffness of sagging moment beams reinforced with mild steel bars (i.e. grade 300 and 400) remains constant but decreases slightly when high strength steel bars (i.e. grade 500) are used as shown in Fig. 5-4(c). This is justified by knowing that

the elastic modulus is fully regained for mild steel but partially regained for high strength steel. Stiffness reduction for high strength steel is barely noticeable for the hogging moment case as the steel bars did not experience significant increase in temperature due to their location near the top side of the section. The capacity obtained for both cases is governed by the residual yield strength that is significantly recovered in all sections causing the reduction in capacities to be almost identical.

5.6.3 Influence of Geometrical Properties

The reduction in residual capacity of both sagging and hogging moment sections decreases by increasing b_c as indicated in Fig. 5-4(d). This is attributed to the additional concrete cover provided by the larger width causing hindrance of heat transfer from the beam sides towards its core. Hence, internal concrete fibers experience lower temperatures and consequently higher residual compressive strength than the inner elements of beams with smaller width. Hogging moment sections experience higher reduction in capacity since concrete subjected to compression is exposed directly to heat from three sides. However, for wide beam sections (i.e. $b_c \geq 500$ mm), influence of heat transfer from the two vertical sides on temperature distribution becomes insignificant. Regarding the elastic stiffness, percent reduction takes its maximum value for beams with small widths and decreases as the width increases. Since the concrete subjected to compression is exposed to higher temperatures in the hogging moment sections than sagging moment sections, residual stiffness for the studied widths is found to be larger for the latter case. The difference becomes more pronounced for beams with larger width as the additional concrete alleviates the temperature rise in the upper concrete core (i.e. heat flow from two sides) more than lower concrete (i.e. heat flow from three sides).

Regarding section height, Fig. 5-4(e) shows it has negligible influence on both elastic stiffness and capacity of the sagging moment sections and minor influence the hogging moment sections. The increase in residual flexural stiffness and strength is attributed to the larger area of concrete under compression caused by increasing the section height. Since concrete in the bottom zone is exposed to heat from three sides, increasing the compression area decreases the average concrete temperature by considering more

concrete fibers away from the beam soffit. This results in higher residual compressive strength and consequently greater residual stiffness and capacity.

Increasing the tensile reinforcement results in greater reduction in stiffness and strength as shown in Fig. 5-4(f). This is attributed to the larger steel area being affected by the reduction in steel mechanical properties at any given temperature.

5.7 Maximum temperature distribution along the cross-section

Temperature distributions at the end of the heating phase (T_{hot}), at the end of the cooling phase (T_{cold}) and at peak values (T_{max}) along the cross-section of the considered beam are illustrated in Fig. 5-5(a) for ASTM E119 [13] fire exposure of 2.5 hrs and ISO 834 [14] cooling duration of 4.07 hrs. Concrete fibers adjacent to the beam soffit reach their maximum temperature at the end of the heating phase as heat flow direction during the cooling stage within this zone is predominant towards the atmosphere. The difference between T_{max} and T_{hot} becomes more pronounced at the upper concrete layers due to the significant inward heat transfer resulting from temperature gradient between the inner and outer concrete elements. Typical variation of the ratio between T_{max} to T_{hot} (designated by η in this study) along the cross-section with respect to the normalized distance from the bottom surface along the vertical axis (d/h_c) is illustrated in Fig. 5-5(b). At the beam soffit (i.e. $d/h_c = 0$), T_{max} possesses the same value as T_{hot} . Then, the ratio increases dramatically until reaching its peak value of η_{max} corresponding to $(d/h_c)_{peak}$ beyond which the ratio decreases slightly before it stabilizes at almost a constant value. Regarding the end of the cooling period, heat flow takes place from the heated concrete core towards the surrounding colder environment resulting in the lowest average temperature value near the beam soffit as shown in Fig. 5-5(a).

5.8 Stress distribution within the compression zone

The variation of stress distribution within the compression area is illustrated in Figs. 5-6(a) and 5-6(b) for sagging and hogging moment cases of the considered section, respectively.

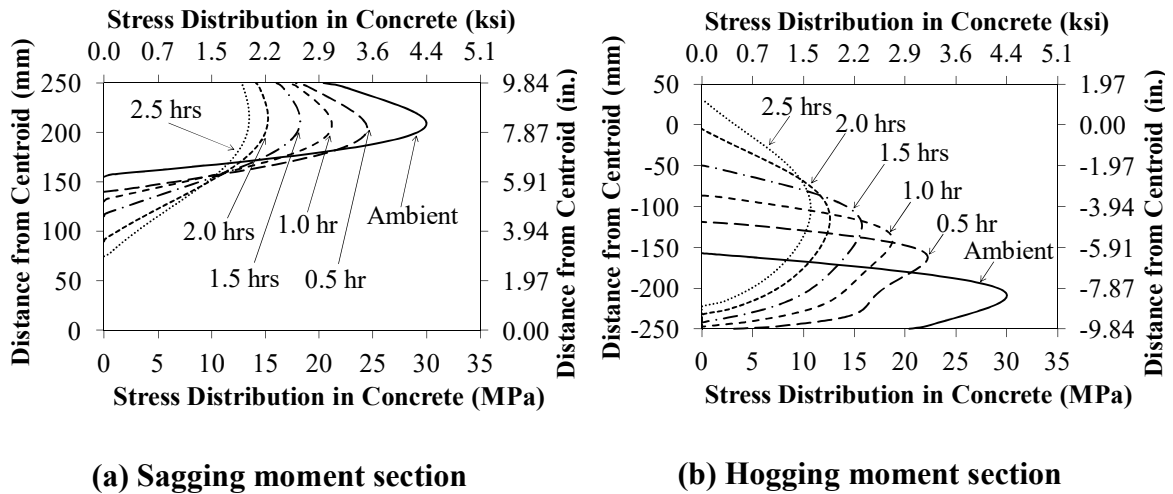


Figure 5-6: Stress distribution of the examined RC beam

Stress distributions at ambient conditions for both sagging and hogging moment cases are identical and extend from the neutral axis towards the extreme compression fibers taking the shape of the considered concrete constitutive relationship [18]. Concrete subjected to elevated temperature becomes softer as indicated by the drop in its residual compressive strength (f_{CR}) and the increase in both residual peak (ϵ_{oR}) and crushing (ϵ_{cuR}) strains, respectively. Under a standard fire scenario, temperature distribution along a cross-section heated from three sides takes its maximum value near the soffit and decreases gradually at the upper layers until uniform distribution is achieved as shown in Fig. 5-5(a). This indicates that for the sagging moment section, the layers close to the top unexposed surface are influenced by the same temperature level and consequently their residual mechanical properties are identical. Therefore, crushing of concrete occurs always at the extreme compression fiber at a strain value of ϵ_{cuR} . Thus, the shape of stress distribution will take the same shape of the stress-strain curve considering the residual mechanical properties. However, for hogging moment sections, temperature variation is highly nonlinear, Fig. 5-5(a), resulting in a significant variation in ϵ_{cuR} between the

concrete layer in the compression region. The layers that reach higher temperature values experience higher ε_{cuR} than the layers with lower temperatures. Hence, crushing of concrete does not necessarily occur at the extreme compression fiber and can happen at the layer where mechanical strain reaches its corresponding ε_{cuR} first. This justifies the variation of stress distribution within the compression zone from the shape of the stress-strain curve considered. For fire durations above 1.0 hr, the stress close to the soffit is negligible since the residual strength of these concrete layers approach zero and becomes useless in resisting the applied stresses. This explains the wider extension of the compression zone in hogging moment compared to sagging moment sections.

Two stress-block parameters are introduced to define the dimensions of the equivalent rectangular block; namely α_l and β_l . The first parameter (α_l) defines the ratio of average stress in rectangular compression stress-block to the concrete compressive strength; whereas the latter one (β_l) represents the ratio of the rectangular compression stress-block depth to the distance between the extreme compression fiber and the neutral axis. Once these parameters are determined, equilibrium between tension and compression forces is performed to determine the distance from the neutral axis to the extreme compression fiber in addition to the corresponding flexural capacity of the section (M_r). In a typical $M-\phi$ diagram, attention should be made not to confuse between the ultimate moment (M_r) and the moment corresponding to the maximum curvature (M_f). Stress-block parameters are determined at the section corresponding to the ultimate moment (M_r); and the corresponding strain at extreme compression fiber is defined as ε_{max} which may not be equal to the crushing strain (ε_{cu}). The concept of equivalent stress block is extended in this research to account for the changes in concrete and steel mechanical properties and constitutive relationships owing to exposing the RC sections to a complete heating-cooling cycle.

5.9 Proposed Simplified Method

Temperature distribution and the corresponding material deterioration has to be considered thoroughly during both the heating and cooling phases. This study proposes a

method in view of the validated parametric study to determine the residual capacity of fire-damaged determinate RC beams subjected to either sagging or hogging moments. The procedure encompasses two steps:

- 1) Determination of maximum temperature distribution along the vertical axis of a beam cross-section after a full heating-cooling cycle.
- 2) Evaluation of post-fire flexural capacity (M_r) considering the residual stress-block parameters (α_{IR} and β_{IR}), residual compressive strength (f'_{CR}) and residual concrete strain at maximum moment (ε_{max}). The following subsections illustrate these steps for both the sagging and hogging moment cases.

5.9.1 Evaluation of the Maximum Temperature (T_{max}) Distribution in Concrete

The first stage in the proposed procedure is to determine T_{max} distribution along the cross-section of the fire-exposed beam as shown in Fig. 5-5(a). Various studies [39-41] have been performed to determine temperature distribution at the end of the heating phase (T_{hot}) in concrete sections exposed to a standard fire. However, published studies lack the availability of a method to predict T_{max} distribution along the cross-section. Thus, a procedure is proposed in this study to convert the T_{hot} distribution into T_{max} distribution through proposing a factor (η) as a function of the distance from the bottom surface along the vertical axis (d), heating phase duration (t_{hot}) and beam cross-sectional dimensions.

The proposed procedure commences by using Gao *et al.* method [39] to determine T_{hot} distribution along the cross-section due to its simplicity and accuracy compared to other methods. The next step is to evaluate $(d/h_c)_{peak}$, defined in Fig. 5-5(b), using the proposed Equation 3 that is developed by performing regression analysis from the parametric investigation.

$$\left(\frac{d}{h_c}\right)_{Peak} = \begin{cases} \frac{(56.25 t_{hot} + 65.0)}{h_c} & , 0.5 \text{ hr} \leq t_{hot} \leq 1.5 \text{ hr} \\ \frac{(7.584 t_{hot} + 14.713)}{h_c} \times f(b_c) & , 1.5 \text{ hr} < t_{hot} \leq 2.5 \text{ hr} \end{cases} \quad (3)$$

where $f(b_c)$ is a function given by Equations 4 based on fire duration at the end of the heating phases (t_{hot}) in hrs., section height (h_c) in mm and section width (b_c) in mm, respectively.

$$f(b_c) = -1.632 \times 10^{-8} b_c^4 + 2.285 \times 10^{-5} b_c^3 - 1.159 \times 10^{-2} b_c^2 + 2.514 b_c - 190.263 \quad (4)$$

If the duration of fire exposure (t_{hot}) is between 2.0 and 2.5 hours, then $(d/h_c)_{peak}$ obtained from Equation 3 should be multiplied by the factor (ω) given in Equation 5.

$$\omega = 1.0 - 0.16 e^{(11.51293 - 0.057565 b_c)} \quad (5)$$

The following step encompasses the calculation of the factor (η) which represents the ratio between T_{max} and T_{hot} as proposed in Equations 6 and 7 for $(d/h_c) \leq (d/h_c)_{peak}$ and $(d/h_c) > (d/h_c)_{peak}$, respectively.

$$\eta = \frac{T_{max}}{T_{hot}} = (a_1 b_c^2 + a_2 b_c + a_3) d^3 + (b_1 b_c^2 + b_2 b_c + b_3) d^2 + (c_1 b_c^2 + c_2 b_c + c_3) d + d_1 b_c^2 + d_2 b_c + d_3 \geq 1.0 \quad (6)$$

$$\eta = \frac{T_{max}}{T_{hot}} = e_1 b_c^3 + e_2 b_c^2 + e_3 b_c + e_4 + \exp[(f_1 b_c^2 + f_2 b_c + f_3) d] \geq 1.0 \quad (7)$$

where d is the distance from beam soffit to the point of interest along the vertical axis (mm) and b_c is the cross-sectional width (mm). The coefficients $a_{i(i=1,2,3)}$, $b_{i(i=1,2,3)}$, $c_{i(i=1,2,3)}$ and $d_{i(i=1,2,3)}$ are determined from the parametric study results through performing least-square regression analysis; whereas the coefficients $e_{i(i=1,2,3,4)}$ and $f_{i(i=1,2,3)}$ are obtained by performing nonlinear regression. The values of the aforementioned parameters are given in Table 5-1 as a function of fire duration at the end of the heating phase (t_{hot}).

Table 5-1: Coefficients for Equations 6 through 7

Coefficient	$t_{hot} = 0.5$ hr	$t_{hot} = 1.0$ hr	$t_{hot} = 1.5$ hr	$t_{hot} = 2.0$ hr	$t_{hot} = 2.5$ hr
a_1	1.183×10^{-11}	6.271×10^{-12}	4.225×10^{-12}	-1.622×10^{-12}	-1.871×10^{-12}
a_2	-1.310×10^{-8}	-6.307×10^{-9}	-4.066×10^{-9}	6.471×10^{-10}	1.005×10^{-9}
a_3	6.146×10^{-7}	6.491×10^{-7}	5.283×10^{-7}	-1.912×10^{-7}	-2.228×10^{-7}
b_1	-1.663×10^{-9}	-1.108×10^{-9}	-9.107×10^{-10}	3.226×10^{-10}	4.686×10^{-10}
b_2	1.987×10^{-6}	1.183×10^{-6}	9.194×10^{-7}	-6.259×10^{-8}	-2.168×10^{-7}
b_3	-1.848×10^{-4}	-1.460×10^{-4}	-1.351×10^{-4}	1.788×10^{-5}	4.134×10^{-5}
c_1	3.260×10^{-8}	2.675×10^{-8}	2.945×10^{-8}	-3.169×10^{-8}	-4.114×10^{-8}
c_2	-4.062×10^{-5}	-3.069×10^{-5}	-3.039×10^{-5}	1.691×10^{-5}	2.543×10^{-5}
c_3	1.393×10^{-2}	7.839×10^{-3}	7.310×10^{-3}	-6.519×10^{-4}	-2.671×10^{-3}
d_1	-1.463×10^{-7}	-1.227×10^{-7}	-1.915×10^{-7}	3.998×10^{-7}	5.190×10^{-7}
d_2	1.918×10^{-4}	1.592×10^{-4}	2.022×10^{-4}	-2.462×10^{-4}	-3.442×10^{-4}
d_3	9.394×10^{-1}	9.525×10^{-1}	9.455×10^{-1}	1.018	1.039
e_1	1.194×10^{-8}	5.388×10^{-9}	7.583×10^{-9}	5.504×10^{-9}	-2.517×10^{-10}
e_2	-1.518×10^{-5}	-8.291×10^{-6}	-1.084×10^{-5}	-8.717×10^{-6}	-1.912×10^{-6}
e_3	6.012×10^{-3}	4.078×10^{-3}	5.248×10^{-3}	4.800×10^{-3}	2.197×10^{-3}
e_4	8.809×10^{-1}	7.999×10^{-1}	5.513×10^{-1}	5.321×10^{-1}	7.872×10^{-1}
f_1	-1.176×10^{-7}	-1.315×10^{-7}	-1.859×10^{-7}	-1.436×10^{-7}	-1.154×10^{-7}
f_2	1.256×10^{-4}	1.394×10^{-4}	1.839×10^{-4}	1.507×10^{-4}	1.297×10^{-4}
f_3	-4.184×10^{-2}	-4.699×10^{-2}	-5.616×10^{-2}	-4.947×10^{-2}	-4.657×10^{-2}

For time intervals other than the ones shown in Table 5-1, linear interpolation should be performed considering two values of η . An excellent agreement between the analytical results and Equations 1 through 7 are found as evidenced by the high coefficients of determinations with a minimum value of 91.3% and a maximum value of 96.1%. This excellent match makes the proposed model reliable in determining the maximum temperature distribution (T_{max}) considering the entire heating-cooling cycle.

5.9.2 Evaluation of the maximum temperature (T_{max}) in steel bars

The method proposed by Wickstrom [40] is recommended to determine T_{hot} in steel bars as it predicts the temperature at specific points in terms of the horizontal and vertical coordinates. Due to the high thermal conductivity of steel, its temperature is assumed to be identical to concrete at the same point. According to the results of the conducted parametric study, the maximum temperature (T_{max}) reached in steel bars is higher than the value obtained at the end of the heating phase (T_{hot}). Based on regression analysis, Equation 8 is proposed to determine T_{max} developed in top and bottom steel bars depending on their location.

$$\frac{T_{max}}{T_{hot}} = \begin{cases} (-0.108 y + 2.4) \left[\left(\frac{x}{b_c} \right)^2 - \left(\frac{x}{b_c} \right) \right] - 0.0063 y + 1.19 \geq 1, Bottom \\ (5.96 \times 10^{-4} b_c^2 - 0.44 b_c + 44.18) \left[\left(\frac{x}{b_c} \right)^2 - \left(\frac{x}{b_c} \right) \right] - 4.20 \geq 1, Top \end{cases} \quad (8)$$

where T_{hot} is the bar temperature at the end of the heating stage ($^{\circ}\text{C}$), x is the horizontal distance from the edge of the cross-section (mm), y is the vertical distance measured from the beam soffit (mm) and b_c is the section width (mm). For bars at the bottom side, Equation 8 is applicable if the vertical distance (y) is less than 100 mm.

5.9.3 Evaluation of the residual stress-block parameters (α_{1R} and β_{1R})

For a rectangular compressive zone, the residual resultant compressive force (C_{cR}) is calculated by Equation 9 and represents the volume of the equivalent fictitious stress-block.

$$C_{cR} = \alpha_{1R} f'_{cR} \beta_{1R} c b_c \quad (9)$$

The stress-block parameters (α_{1R} and β_{1R}) corresponding to fire-damaged sections can be obtained from the proposed Equations 10 and 11, respectively.

$$\alpha_{1R} = V_1 + V_2 f'_c + V_3 f_y + V_4 b_c + V_5 h_c + V_6 \rho_c + V_7 t_{hot} \quad (10)$$

$$\beta_{1R} = Z_1 + Z_2 f'_c + Z_3 f_y + Z b_c + Z_5 h_c + Z_6 \rho_c + Z_7 t_{hot} \quad (11)$$

These functions are determined using least-square regression analysis based on the results obtained from the extensive parametric study. In these equations, the units of the mechanical properties, cross-sectional dimensions and fire duration are MPa, m and hr, respectively. The coefficients $V_{i(i=1,2,3,4,5,6,7)}$ and $Z_{i(i=1,2,3,4,5,6,7)}$ are given in terms of fire duration in Table 5-2 for both the sagging and hogging moment cases. A comparison between the calculated values of α_{1R} and β_{1R} with the analytically obtained ones is conducted in view of Figs. 5-7(a) and 5-7(b), respectively. Similar comparison is carried out to determine the accuracy of the proposed model for the hogging moment case. The

proposed equations are found to be in a very good agreement with the analytical results taking into account the simplicity of its application.

Table 5-2: Coefficients for Equations 10 and 11

Moment <i>t_{hot} (hr)</i>	Sagging			Hogging			
	0.5 to 1.8	1.8 to 2.2	2.2 to 2.5	0.5 to 0.8	0.8 to 1.2	1.2 to 2.2	2.2 to 2.5
V_1	9.75×10^{-1}	1.00	1.05	8.33×10^{-1}	7.72×10^{-1}	6.98×10^{-1}	4.18×10^{-1}
V_2	-3.40×10^{-3}	-2.76×10^{-3}	-2.87×10^{-3}	-2.71×10^{-3}	-3.16×10^{-3}	-4.16×10^{-3}	-5.01×10^{-3}
V_3	6.40×10^{-5}	4.90×10^{-5}	5.60×10^{-5}	7.60×10^{-5}	1.09×10^{-4}	1.71×10^{-4}	1.89×10^{-4}
V_4	-1.02×10^{-4}	-4.90×10^{-5}	-1.23×10^{-4}	-1.00×10^{-4}	-5.50×10^{-5}	1.68×10^{-4}	3.29×10^{-4}
V_5	7.00×10^{-6}	-3.30×10^{-5}	-7.40×10^{-5}	2.30×10^{-5}	8.40×10^{-5}	1.77×10^{-4}	2.51×10^{-4}
V_6	1.35	1.25	2.39	1.77	3.79	6.54	7.52
V_7	2.04×10^{-2}	0.00	0.00	0.00	0.00	-7.87×10^{-2}	0.00
Z_1	8.66×10^{-1}	7.00×10^{-1}	7.16×10^{-1}	1.11	1.13	1.10	1.07
Z_2	-1.04×10^{-3}	-1.75×10^{-3}	-1.91×10^{-3}	-4.03×10^{-4}	-2.35×10^{-4}	-8.08×10^{-4}	-9.97×10^{-4}
Z_3	-7.80×10^{-5}	-4.70×10^{-5}	-4.40×10^{-5}	-1.55×10^{-4}	-1.64×10^{-4}	-1.39×10^{-4}	-1.11×10^{-4}
Z_4	2.50×10^{-4}	3.87×10^{-4}	3.13×10^{-4}	1.17×10^{-4}	2.83×10^{-4}	4.67×10^{-4}	4.79×10^{-4}
Z_5	-1.10×10^{-5}	1.80×10^{-5}	2.80×10^{-5}	-8.40×10^{-5}	-1.17×10^{-4}	-1.24×10^{-4}	-1.50×10^{-4}
Z_6	-1.64	-1.11	-1.15	-4.41	-5.33	-4.63	-3.79
Z_7	-4.98×10^{-2}	0.00	0.00	0.00	0.00	-2.10×10^{-2}	0.00

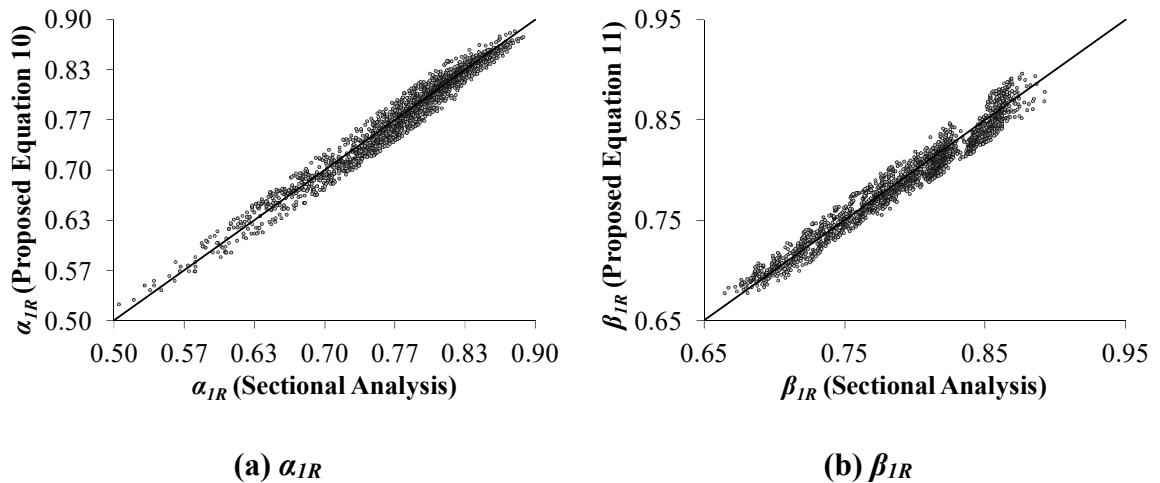


Figure 5-7: Validation of α_{IR} and β_{IR} for the sagging moment case

5.9.4 Evaluation of the residual concrete compressive strength (f_{cR}')

Due to the variation of T_{max} along the depth of the compression zone, the residual compressive strength (f_{cR}') in Equation 9 has to be calculated by integrating the temperature-dependent f_{cR}' function [19] with respect to the stress-block depth. Carrying out this integration is complicated and not practical in design offices since temperature varies with the section depth according to the regression models proposed in this study and the ones proposed by Gao *et al.* [39]. Therefore, another least-square linear regression analysis is performed in the current work to determine an average f_{cR}' that represents the residual concrete strength within the compression zone of a typical sagging moment section as proposed in Equation 12.

$$\frac{f_{cR}'}{f_c'} = \frac{(-0.84t_{hot} - 1.46)b_c^2}{10^6} + \frac{(2.58t_{hot}^{0.4682})b_c}{10^3} - 0.08973t_{hot}^3 + 0.4617t_{hot}^2 - 1.129t_{hot} + 0.878 \quad (12)$$

where t_{hot} and b_c are given in hr and mm, respectively.

The compression zone within the hogging moment section experiences chaotic temperature distribution due to its vicinity from the three fire exposed surfaces simultaneously. Therefore, the average residual concrete strength within this region becomes more sensitive to the variation of all parameters. By performing regression analysis based on the results of hogging moment sections, Equations 13 and 14 are proposed to calculate f_{cR}' for $b_c = 200$ mm (7.87 in.) and $b_c \geq 300$ mm (11.81 in.), respectively.

$$\frac{f_{cR}'}{f_c'} = -1.28 + \frac{1.68}{\sqrt{t_{hot}}} + \frac{0.00308f_y}{f_c'} + 0.000128h_c + 0.773\rho^{0.1} - \frac{0.00275b_c}{t_{hot}} \quad (13)$$

$$\frac{f_{cR}'}{f_c'} = -1.74 + \frac{0.65}{\sqrt{t_{hot}}} + \frac{0.00661f_y}{f_c'} + 0.028\sqrt{b_c} + 0.000223h_c + 1.57\rho^{0.1} - \frac{0.000306b_c}{t_{hot}} \quad (14)$$

The parameters defining the equations are t_{hot} (hr), f_y (MPa), f_c' (MPa), h_c (mm), b_c (mm) and ρ (dimensionless). An excellent agreement between the outcomes of these equations and the results obtained from the analytical model are found.

5.9.5 Evaluation of the residual maximum strain at extreme compression fiber (ε_{maxR})

The results of the conducted parametric study reveal that the ultimate moment (M_r) is identical to the failure moment (M_f) for all specimens except for sections with reinforcement ratios ($\rho = 1.5\%$ or 2.0%), yield strengths ($f_y = 400$ MPa and 500 MPa) and fire durations ($t_{hot} = 0.5, 1.0$ and 1.5 hours). This means that the residual maximum strain (ε_{maxR}) corresponding to M_r can be calculated directly from Equation 1 in terms of T_{max} obtained at the extreme compression fiber except for the aforementioned sections. In the latter case, ε_{cuR} obtained from Equation 1 should be multiplied by the factor given in Equation 15 to get the corresponding ε_{maxR} .

$$\frac{\varepsilon_{maxR}}{\varepsilon_{cuR}} = (c_1 b_c^2 + c_2 b_c + c_3) h_c + c_4 f_c' + c_5 \geq 1.0 \quad (15)$$

Concrete compressive strength (f_c') is given in MPa and the coefficients $c_{i(i=1,2,3,4,5)}$ are given in Table 5-3 in terms of ρ, f_y (MPa) and t_{hot} (hr). This factor is proposed based on regression analysis with a high coefficient of determination (R^2) of 94.2%.

Table 5-3: Coefficients for Equations 15

Yield Strength	c_i	$t_{hot} = 0.5$ hr		$t_{hot} = 1.0$ hr		$t_{hot} = 1.5$ hr	
		$\rho = 1.5\%$	$\rho = 2.0\%$	$\rho = 1.5\%$	$\rho = 2.0\%$	$\rho = 1.5\%$	$\rho = 2.0\%$
400 MPa (58.0 ksi)	c_1	0.00	3.54×10^{-9}	0.00	-9.27×10^{-10}	0.00	0.00
	c_2	0.00	-2.94×10^{-6}	0.00	2.00×10^{-9}	0.00	0.00
	c_3	0.00	5.75×10^{-4}	0.00	1.45×10^{-4}	0.00	0.00
	c_4	0.00	1.48×10^{-4}	0.00	-2.30×10^{-4}	0.00	0.00
	c_5	1.00	8.73×10^{-1}	1.00	9.50×10^{-1}	1.00	1.00
500 MPa (72.5 ksi)	c_1	3.33×10^{-9}	2.61×10^{-9}	1.04×10^{-9}	1.36×10^{-9}	-2.07×10^{-9}	-1.20×10^{-9}
	c_2	-2.78×10^{-6}	-2.36×10^{-6}	-1.54×10^{-6}	-1.72×10^{-6}	8.43×10^{-7}	1.81×10^{-7}
	c_3	5.44×10^{-4}	4.93×10^{-4}	4.17×10^{-4}	4.23×10^{-4}	3.00×10^{-6}	9.8×10^{-5}
	c_4	-1.46×10^{-4}	-1.74×10^{-2}	-5.40×10^{-4}	-1.22×10^{-2}	-4.77×10^{-4}	-8.18×10^{-3}
	c_5	8.73×10^{-1}	1.40	9.33×10^{-1}	1.29	9.66×10^{-1}	1.20

Regarding the hogging moment section, ε_{maxR} cannot be determined using the same procedure because crushing of concrete does not necessarily occur at the extreme

compression fiber as mentioned in the discussion of Fig. 5-6. Therefore, another regression analysis is carried out to determine the value of ε_{maxR} corresponding directly to the extreme compression fiber as shown in Equation 16.

$$\varepsilon_{maxR} = c_1 f'_c + c_2 f_y + c_3 b_c^2 + c_4 b_c + c_5 h_c + c_6 \ln(\rho) + c_7 \quad (16)$$

The geometrical parameters and mechanical properties are given in mm and MPa, respectively. The coefficients $c_{i(i=1,2,3,4,5,6,7)}$ are given in Table 5-4 in terms of fire duration (t_{hot}) in hr. The value of ε_{maxR} obtained from Equation 16 is found to be with very good agreement with sectional analysis results as indicated by the coefficient of determination (R^2) of 90.8%.

Table 5-4: Coefficients for Equations 16

c_i	$t_{hot} = 0.5$ hr	$t_{hot} = 1.0$ hr	$t_{hot} = 1.5$ hr	$t_{hot} = 2.0$ hr	$t_{hot} = 2.5$ hr
c_1	1.810×10^{-6}	-3.614×10^{-5}	-9.464×10^{-5}	-1.410×10^{-4}	-1.620×10^{-4}
c_2	-6.530×10^{-6}	-7.570×10^{-6}	-6.120×10^{-6}	-4.040×10^{-6}	-2.720×10^{-6}
c_3	1.922×10^{-8}	2.483×10^{-8}	1.506×10^{-8}	-6.353×10^{-9}	-1.303×10^{-8}
c_4	-1.869×10^{-5}	-2.648×10^{-5}	-1.951×10^{-5}	-1.473×10^{-6}	5.225×10^{-6}
c_5	-4.401×10^{-6}	-5.606×10^{-6}	-4.419×10^{-6}	-2.899×10^{-6}	-2.141×10^{-6}
c_6	-2.460×10^{-3}	-2.997×10^{-3}	-2.263×10^{-3}	-1.314×10^{-3}	-8.084×10^{-4}
c_7	4.530×10^{-3}	8.816×10^{-3}	1.315×10^{-2}	1.469×10^{-2}	1.561×10^{-2}

5.9.6 Evaluation of the residual flexural capacity (M_r)

Having determined the average residual compressive strength (f'_{cR}) corresponding to the equivalent stress block parameters (α_{IR} and β_{IR}), the residual compression force (C_c) in concrete can be calculated from Equation 9 in terms of the compression zone depth (c). The strain profile is established by assigning a strain of ε_{maxR} at the extreme compression fiber. Considering the residual properties of the steel bars (f_{yR} and E_{sR}), equilibrium condition in the section is applied and the residual moment of resistance (M_r) is calculated. In order to verify the applicability of the proposed method, the flexural capacity of the beam section discussed in Fig. 5-3 was calculated for both the sagging and hogging moments cases under all fire durations. A comparison between the predicted results and sectional analysis showed a very good agreement as indicated by average

errors of 1.4% and 3.7% and maximum errors of 2.3% and 4.4% for the sagging and hogging moment sections, respectively.

5.10 Summary and Conclusions

An analytical procedure for predicting the flexural capacity of fire-damaged RC beams is presented in this chapter. The procedure encompasses a thermal analysis to determine the heat flow and temperature distribution within the section followed by sectional analysis considering the residual mechanical properties and constitutive relationships of both concrete and steel. The proposed model is validated against related experimental results and found to be in very good agreement. An extensive parametric study is then conducted on 2880 sections varying in their geometrical and mechanical properties as well as the fire exposure duration under either sagging or hogging moments. The effects of these variations on the flexural behavior of the fire-damaged beams is discussed in view of the resulting $M-\phi$ relationships. A method is proposed to determine the maximum temperature distribution within a fire-damaged section and the corresponding residual stress-block parameters (α_{IR} and β_{IR}). The simplified proposed method allows engineers to determine the residual flexural capacity of fire-damaged RC beams made of normal weight concrete and subjected to either sagging or hogging moments for various fire durations.

5.11 References

- [1] Khoury, G. “Effect of Fire on Concrete and Concrete Structures,” *Progress in Structural Engineering and Materials*, 2000, Vol. 2, No. 4, pp. 429-447.
- [2] International Code Council (ICC). “ICC performance code for buildings and facilities,” 2001, Falls Church, VA.
- [3] National Fire Protection Association (NFPA). “NFPA 5000, Building construction and safety code,” 2002, Quincy, MA.
- [4] National Research Council Canada (NRCC). “National Building Code of Canada,” Associate Committee on the National Building Code, 2015, Ottawa, ON, 708 pp.
- [5] Kazinczy, G.V. “Die Plastizität des Eisenbetons,” *Beton und Eisen*, 1933, Vol. 32, No. 5, pp. 74-80.
- [6] Whitney, C.S. “Plastic Theory in Reinforced Concrete Design,” *Transactions, ASCE*, 1942, Vol. 107, pp. 251-326.
- [7] Popovics, S. “A Review of Stress-Strain Relationships for Concrete,” *ACI Journal*, 1970, Vol. 67, No. 3, pp. 243-248.
- [8] ACI Committee 318. “Building Code Requirements for Structural Concrete (ACI 318-08) and Commentary,” American Concrete Institute, 2008, Farmington Hills, MI, 473 pp.
- [9] Cement Association of Canada (CSA). “Design of Concrete Structures (CAN/ CSA A23.3-14),” 3rd ed., 2014, Ottawa, ON, 297 pp.
- [10] El-Fitiany, S. and Youssef, M.A. “Stress-Block Parameters for Reinforced Concrete Beams During Fire Events,” *ACI Special Publication*, 2011, Vol. 279, pp. 1-40.

- [11] Dusenberre, G. M. "Heat Transfer Calculation by Finite Differences," International Textbook Company, 1961, Scranton, PA, 293 pp.
- [12] Lie, T.T., ed. "Structural Fire Protection," ASCE Manuals and Reports on Engineering Practice No. 78, 1992, New York, 241 pp.
- [13] ASTM Committee E05. "Standard Methods of Fire Tests of Building Construction and Materials (ASTM E119)," American Society for Testing and Materials, 2016, Philadelphia, PA, 35 pp.
- [14] International Standard Organizations. "Fire-Resistance Tests - Elements of Building Construction (ISO 834-11)," 2014, 53 pp.
- [15] Schneider, U. "Concrete at High Temperatures - A General Review," Fire Safety Journal, Vol. 13, No. 1, 1988, pp. 55-68.
- [16] Hertz, K.D. "Concrete Strength for Fire Safety Design," Magazine of Concrete Research, 2005, Vol. 57, No. 8, pp. 445-453.
- [17] Franssen, J.M. and Kodur, V. "Residual Load Bearing Capacity of Structures Exposed to Fire," Proceedings of the 2001 Structures Congress and Exposition, 2004, Vol. 109, Washington, DC, pp. 1-12.
- [18] Tsai, W.T. "Uniaxial Compressional Stress-Strain Relation of Concrete," Journal of Structural Engineering, 1988, Vol. 114, No. 9, pp. 2133-2136.
- [19] Chang, Y.F., Chen, Y.H., Sheu, M.S. and Yao, G.C. "Residual Stress-Strain Relationship for Concrete after Exposure to High Temperatures," Cement and Concrete Research, 2006, Vol. 36, No. 10, pp. 1999-2005.
- [20] Abrams, M. "Compressive strength of concrete at temperatures to 1600°F," ACI Special Publication, SP25, 1971, pp. 33-58.

- [21] Phan, L.T. and Carino, N. J. "Review of Mechanical Properties of HSC at Elevated Temperatures," *Journal of Materials in Civil Engineering*, 1998, Vol. 10, No. 1, pp. 58-64.
- [22] Xiao, J. and König, G. "Study on Concrete at High Temperature in China - an Overview," *Fire Safety Journal*, 2004, Vol. 39, No. 1, pp. 89-103.
- [23] Lie, T.T., Lin, T.D., Allen, D.E. and Abrams, M.S. "Fire Resistance of Reinforced Concrete Columns," National Research Council Canada, Division of Building Research, NRCC 23065, 1984, Ottawa, ON, Canada, Paper 1166.
- [24] Felicetti, R., Gambarova, P.G., Silva, M. and Vimercati, M. "Thermal Diffusivity and Residual Strength of HPLWC Exposed to High Temperature," *Proceeding of the Sixth International Symposium on Utilization of HSC/HPC*, Leipzig, Germany, 2002, Vol.2, pp. 935-948.
- [25] Felicetti, R. and Gambarova, P.G. "Effects of High Temperature on the Residual Compressive Strength of High Strength Siliceous Concretes," *ACI Material Journal*, 1998, Vol. 95, No. 4, pp. 395-406.
- [26] Felicetti, R., Gambarova, P.G. and Bamonte, P. "Thermal and Mechanical Properties of Light-Weight Concrete Exposed to High Temperature," *Fire and Materials*, 2013, Vol. 37, No. 3, pp. 200-216.
- [27] Karthik, M. and Mander, J. "Stress-Block Parameters for Unconfined and Confined Concrete Based on a Unified Stress-Strain Model," *Journal of Structural Engineering*, 2011, Vol. 137, No. 2, pp. 270-273.
- [28] Edwards, W.T. and Gamble, W.L. "Strength of Grade 60 Reinforcing Bars After Exposure to Fire Temperatures," *Concrete International*, 1986, Vol., No. 10, pp. 17-19.
- [29] Qiang, X., Bijlaard, F.S.K. and Kolstein, H. "Post-Fire Mechanical Properties of High Strength Structural Steels S460 and S690," *Engineering Structures*, 2012, Vol. 35, pp. 1-10.

- [30] Neves, I.C., Rodrigues, J.P.C. and Loureiro A.D.P. "Mechanical properties of reinforcing and prestressing steels after heating," *Journal of Materials in Civil Engineering*, 1996, Vol. 8, No. 4, pp. 189-194.
- [31] Kodur, V.K.R., Raut, N.K., Mao, X.Y. and Khaliq, W. "Simplified Approach for Evaluating Residual Strength of Fire-Exposed Reinforced Concrete Columns," *Materials and Structures*, 2013, Vol. 46, No. 12, pp. 2059-2075.
- [32] Malhotra, H.L. "Design of Fire-Resisting Structures," Bishopbriggs and Glasgow, Surrey University Press, 1982, 226 pp.
- [33] Youssef, M.A. and Rahman M. "Simplified Seismic Modeling of Reinforced Concrete Flexural Members," *Magazine of Concrete Research*, 2007, Vol. 59, No. 9, pp. 639-649.
- [34] Guo, Z. and Shi, X., "Experimental and Calculation of Reinforced Concrete at Elevated Temperatures," 1st Ed., Butterworth-Heinemann, 2011, Oxford, UK, 336 pp.
- [35] Alhadid, M.M.A. and Youssef M.A. "Residual Axial Behavior of Fire-Damaged Reinforced Concrete Columns," *Proceedings of the Fifth International Structural Specialty Conference on Resilient Infrastructure*, CSCE, 1-4 June, 2016, London, ON, STR-898.
- [36] Kodur, V.K.R., Dwaikat, M.B. and Fike, R.S. "An Approach for Evaluating the Residual Strength of Fire-Exposed RC Beams," *Magazine of Concrete Research*, 2010, Vol. 62, No. 7, pp. 479-488.
- [37] Haddad, R.H., Shannag, M.J. and Moh'd, A. "Repair of Heat-Damaged RC Shallow Beams Using Advanced Composites," *Materials and Structures*, 2008, Vol. 41, No. 2, pp. 287-299.
- [38] Terro, M.J. "Numerical Modeling of the Behavior of Concrete Structures in Fire," *ACI Structural Journal*, 1998, Vol. 95, No. 2, pp. 183-193.

[39] Gao, W.Y., Dai, J.G. and Teng J.G. “Simple Method for Predicting Temperatures in Reinforced Concrete Beams Exposed to a Standard Fire,” *Advances in Structural Engineering*, 2014, Vol. 17, No. 4, pp. 573-589.

[40] Wickström, U. “A Very Simple Method for Estimating Temperature in Fire Exposed Concrete Structures,” *Proceeding of New Technology to Reduce Fire Losses and Costs*, Elsevier, 1986, New York.

[41] Abbasi, A. and Hogg, P.J., “A Model for Predicting the Properties of the Constituents of a Glass Fibre Rebar Reinforced Concrete Beam at Elevated Temperatures Simulating a Fire Test,” *Composites Part B: Engineering*, 2005, Vol. 36, No. 5, pp. 384-393.

Chapter 6

6 RESIDUAL AXIAL BEHAVIOR OF RESTRAINED REINFORCED CONCRETE COLUMNS DAMAGED BY A STANDARD FIRE

Reinforced concrete (RC) structures are widely used in construction as they possess superior performance index and provide high design flexibility [1]. The behavior of RC structures at ambient conditions is comprehensively addressed by various building codes and standards [2-4]. However, when these structures are exposed to fire incidents, the composing structural members experience various alterations in their capacity and deformation caused by material degradation, residual strains and stress redistribution [1,5,6]. Thus, analysis of RC structures after exposure to elevated temperatures becomes more complicated and require detailed examination due to the additional factors that govern their behavior. The mutual influence of mechanical and thermal stresses in addition to load-temperature history plays a key role in dictating the final state of the fire-exposed members [1,7]. In a relevant research [8], it was stated that "*Concrete has memory*" to indicate the significant influence of temperature-load interaction on the residual behavior of fire-exposed RC members.

Most concrete structures exposed to fire conditions are not fully deteriorated and their structural integrity and mechanical properties can be fully or partially restored. Many design codes and standards [9-12] adopt a prescriptive approach through providing data related to the anticipated fire resistance of various RC members based on their geometrical properties and fire exposure conditions. This approach is easy to implement but usually results in over-conservative sections that affect the cost of the structure. The prescriptive approach also overlooks the influence of temperature-load history despite its important role in determining the residual performance of the members. In practice, a preliminary assessment of the damaged members is performed immediately after being exposed to elevated temperatures by inspecting the building [13]. Both visual inspection and hammer tapping techniques are carried out to identify the maximum temperature reached, fire propagation route, residual strength of concrete, cracking schemes, color

changes and smoke characteristics [14]. After that, the structure is evaluated according to the relevant design code depending on the extent of damage and the affordability of the required work. Load-bearing members, such as columns, should maintain their structural integrity and sufficient capacity to withstand the applied load without exhibiting significant deformations associated with the deterioration in the material mechanical properties.

This study is an attempt to address an alternative procedure to the currently used prescriptive methods considering standard fire exposure. A model utilizing both heat transfer analysis and sectional analysis is developed to evaluate the residual axial behavior of rectangular and circular RC columns. Temperature-load history is explicitly considered in the analysis. The various strain components developed during and after fire are calculated and their influence on changing the residual performance of the damaged members under various restraining conditions is evaluated. The validity of the proposed model is assessed in view of relevant experimental results obtained from literature. The validated model is then utilized to perform a parametric study aiming at investigating the influence of mechanical properties, cross-sectional dimensions, fire exposure and support conditions on the residual performance of RC columns. A simplified procedure is then proposed to predict the residual axial capacity and stiffness of RC columns in typical frame structures. The outcomes of the current study provide a solid basis for a more comprehensive work that accounts for other fire types and exposure conditions.

6.1 Proposed Analytical Approach

Assessment of the post-fire behavior of RC columns in typical frame structures requires the consideration of not only the residual mechanical properties of the composing materials but also the temperature-load interaction before and during fire. Fig. 6-1 illustrates the influence of heating and loading history on the total strains (ϵ_t) induced in concrete. For instance, path 1 shows the case where the column supports a load that causes a mechanical strain $(\epsilon_m)_1$ before heat exposure. Heating this column induces a combination of thermal and transient strains $(\epsilon_{th})_1$. On the other hand, path 2 shows the

development of total strains under a successive application of temperature and load. In this case, the column experiences thermal strains (ϵ_{th}) followed by mechanical strains (ϵ_m) due to the loads applied on the fire-damaged member. Transient strains are not considered as the column is unloaded during heating. Although the column is supporting the same load level and is exposed to the same maximum temperature in both cases, the total strain differs significantly. In other loading and heating scenarios, the total strain can be somewhere in between the two previously mentioned extreme cases. Since the free thermal strain is partially irrecoverable and the transient strain is irreversible [7,15], detailed examination of the actual load-temperature path must be considered in the analysis. Guo and Shi [1] experimentally proved the variation in deformation behavior of RC columns when subjected to different heating-loading paths.

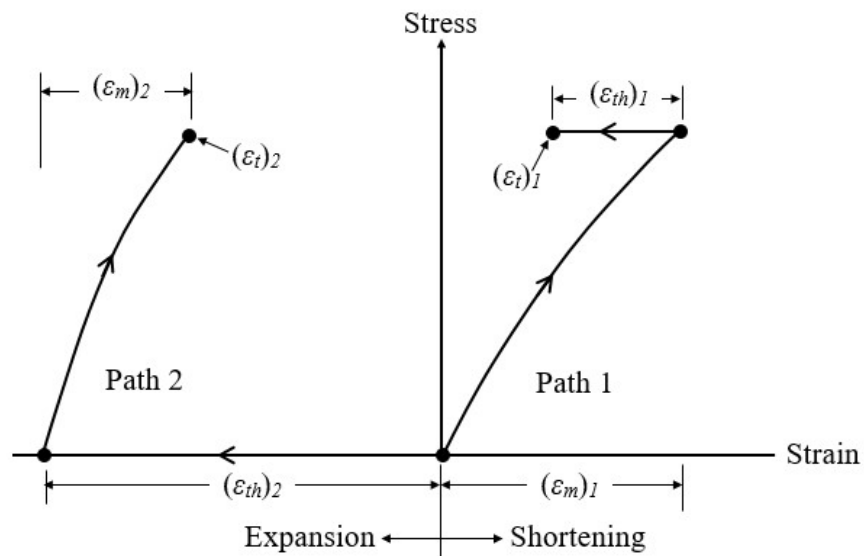


Figure 6-1: Influence of temperature-stress interaction on the concrete strains

The analytical approach, performed in this study, encompasses three main stages that describe the structural variations in the exposed member throughout the heating-cooling cycle. Firstly, the structural performance of the intact member is determined in terms of its capacity and stiffness considering the relevant material models at ambient conditions. The obtained structural characteristics act as a basis to calculate the initial axial load level

(λ) and to determine the extent of deterioration in the member after fire exposure. The second stage involves thermal and structural analyses of the exposed member during the heating and cooling cycles. Heat transfer analysis is carried out using the finite difference method in order to determine the maximum temperature distribution within the member depending on concrete thermal and physical properties. In Fig. 6-2, the residual properties of the member at the final stage (point 2) is highly dependent on the temperature-load path followed. Therefore, at each time increment, the change in the applied load level ($\Delta\sigma$) associated with the restraint conditions is considered. Both thermal and transient strains are calculated at each time increment as represented by the step function shown in Fig. 6-2.

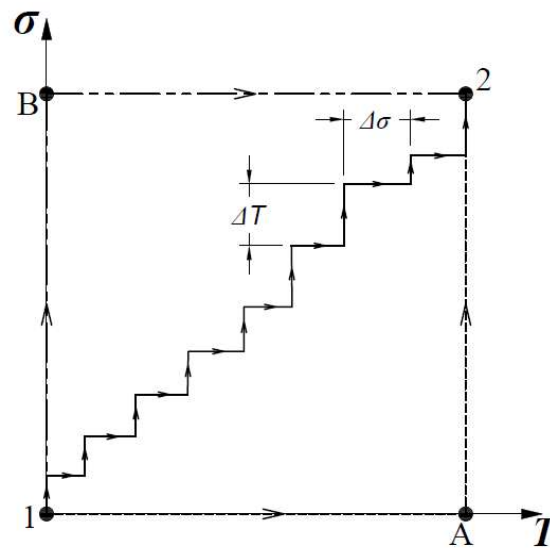


Figure 6-2: Temperature-stress interaction

The residual capacity of the member during fire is calculated based on the relevant material models to predict if failure occurs during fire exposure. The third analysis stage initiates after the member is completely cooled down to room temperature. In this stage, sectional analysis is carried out to determine the residual capacity and stiffness of the fire-damaged member depending on the recorded data including the maximum temperature reached and residual strain distribution. The analysis is performed by

applying uniform strain increments until failure occurs taking into account related post-fire mechanical properties and material models.

The current study focuses on the axial behavior of rectangular and circular RC members exposed to fire from all sides. The restraint condition is proposed to be determined by performing structural analysis of the entire frame, Fig. 6-3(a), with the aid of any commercially available software.

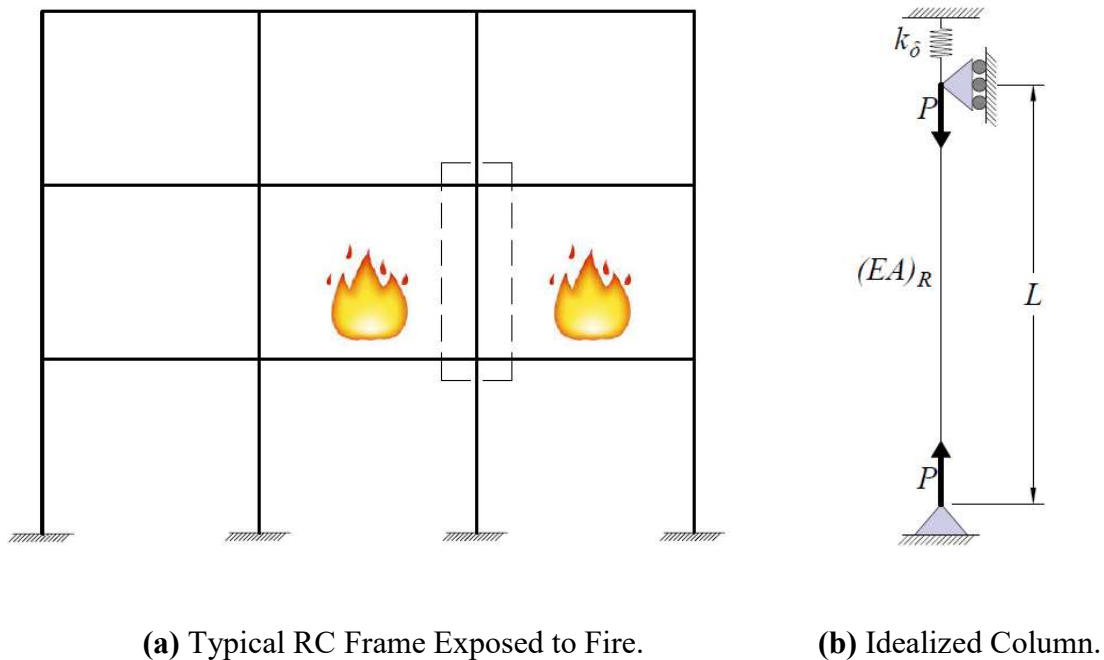


Figure 6-3: Isolation of Columns in Typical RC Frames

The first iteration is performed considering the mechanical properties of the section at ambient conditions. During fire exposure, the columns that are exposed to elevated temperatures experience reduction in their load bearing capacity and axial stiffness in addition to undergoing deformation depending on the temperature distribution within the member. The fire-exposed column can be isolated as shown in Fig. 6-3(b). A pin support is assigned to one end of the column, while the other end is attached to a roller support and a spring having an axial stiffness (k_δ) that represents the axial constraints provided by

the adjacent frame members. The value of k_δ can be obtained from any structural analysis program as discussed later in section 11. Springs are considered to resist the expansion tendency of the columns without affecting any possible contraction they may experience. When the column expands, the magnitude of the axial load acting on the column during fire encompasses the initial applied load (P_i) in addition to the restraining force that result from thermal expansion. The axial stiffness (EA) of the columns varies at each time step during fire which consequently affects the value of the additional restraining force. This mutual dependency is considered in the proposed model as will be discussed in the subsequent sections.

The proposed analysis of the fire-damaged RC members is carried out while making the following assumptions:

- 1) Cross sections remain plane before and after fire exposure. The validity of this assumption was validated for temperatures up to 1200°C [6].
- 2) Perfect bond exists between the steel reinforcement and the surrounding concrete material.
- 3) Spalling of concrete is not considered. This implies that the current work is limited to normal weight concrete.
- 4) Two dimensional heat transfer analysis is considered implying that heat flow is uniform along the member length.
- 5) Influence of concrete tensile cracks on heat flow is neglected in the heat transfer analysis.
- 6) Geometrical nonlinearity is not considered in the analysis.
- 7) Failure of the compression members is not governed by buckling.

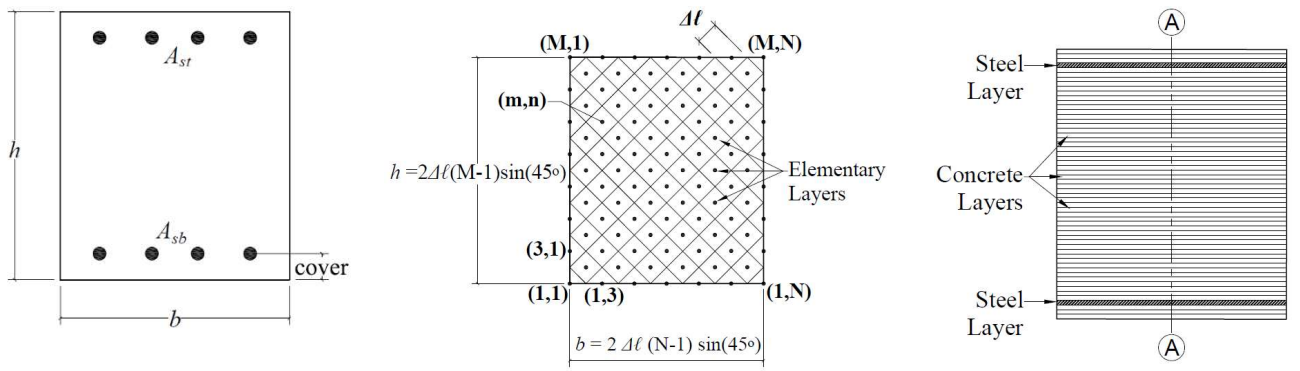
6.2 Definition of Cross-Sections

This study focuses on the residual axial behavior of fire-damaged RC rectangular and circular columns exposed to standard fire from all sides. The geometrical properties and reinforcement distribution of a typical cross-section considered in the analysis are defined

in Figs. 6-4(a) and 6-5(a) for rectangular and circular sections, respectively. Rectangular sections are defined in terms of section width (b), section height (h), top steel reinforcement (A_{st}) and bottom steel reinforcement (A_{sb}), whereas circular columns are defined in terms of cross-sectional diameter (D) and steel reinforcement (A_s) assumed to be uniformly distributed along the circumference. Table 6-1 details the mechanical and geometrical properties of selected rectangular and circular sections.

Table 6-1: Properties of the discussed rectangular and circular column sections

Rectangular Sections								Circular Sections						
Case	t (hr)	f_c' (MPa)	f_y (Mpa)	b (m)	h (m)	ρ	R_D	Case	t (hr)	f_c' (MPa)	f_y (Mpa)	D (mm)	ρ	R_D
R1	1.5	35	400	400	500	0.04	0.0	C1	1.5	35	400	500	0.04	0.0
R2	0.5	35	400	400	500	0.04	0.0	C2	0.5	35	400	500	0.04	0.0
R3	2.5	35	400	400	500	0.04	0.0	C3	2.5	35	400	500	0.04	0.0
R4	1.5	25	400	400	500	0.04	0.0	C4	1.5	25	400	500	0.04	0.0
R5	1.5	35	300	400	500	0.04	0.0	C5	1.5	35	300	500	0.04	0.0
R6	1.5	35	400	250	500	0.04	0.0	C6	1.5	35	400	310	0.04	0.0
R7	1.5	35	400	600	500	0.04	0.0	C7	1.5	35	400	400	0.04	0.0
R8	1.5	35	400	400	300	0.04	0.0	C8	1.5	35	400	780	0.04	0.0
R9	1.5	35	400	400	800	0.04	0.0	C9	1.5	35	400	500	0.02	0.0
R10	1.5	35	400	400	500	0.02	0.0	C10	1.5	35	400	500	0.04	0.5
R11	1.5	35	400	400	500	0.04	0.5	C11	1.5	35	400	500	0.04	1.0
R12	1.5	35	400	400	500	0.04	1.0							



(a) Typical Cross-Section. (b) Mesh for Heat Transfer Analysis. (c) Mesh for Strength Analysis.

Figure 6-4: Geometry and Meshing of Rectangular Sections

6.3 Thermal Analysis

Temperature distribution at any section along the member is determined based on the finite difference method described by Lie [16]. The physical and thermal properties of both concrete and steel are provided by Lie [16]. For each time increment, the temperature distribution within the section is obtained by solving the heat balance equations [16]. In the current study, the columns are exposed to an ASTM E119 [17] standard fire along their perimeter during the heating phase as given by Equation 1.

$$T_f - T_o = 750 [1 - e^{(-3.79553 \sqrt{t})}] + 170.41\sqrt{t} \quad (1)$$

where T_f is the fire temperature (°C), T_o is the room temperature (°C) and t is the time after the start of the fire (hr). During the cooling phase, temperature is assumed to decrease gradually according to ISO 834 [18] specifications, Equation 2, in terms of fire duration at the end of the heating phase (t_{hot}).

$$\Delta T = \begin{cases} -10.417 & , \quad t < 30 \text{ min} \\ -4.167 \left(3 - \frac{t_{hot}}{60}\right) & , \quad 30 \text{ min} \leq t < 120 \text{ min} \\ -4.167 & , \quad t \geq 120 \text{ min} \end{cases} \quad (2)$$

Concrete thermal properties are assumed to be irreversible and maintain a constant value corresponding to the maximum temperature reached [1,15]. A distinction in the meshing procedure between rectangular and circular column sections is illustrated in Figs. 6-4(b) and 6-5(b), respectively.

6.3.1 Rectangular Sections

The analysis procedure begins by dividing the cross section into $M \times N$ 45° inclined square elements as shown in Fig. 6-4(b). The point at the center of each internal element or on the hypotenuse of each boundary element represents the temperature of the entire element. Steel bars are considered as perfect conductors due to their high thermal conductivity and their temperature is assumed to be identical to the adjacent concrete elements. Heat energy is transferred from the outer elements toward the concrete core causing a subsequent increase in temperature depending on concrete thermal conductivity

and moisture content. The influence of moisture is considered by assuming that when an element reaches a temperature of 100°C , all the transferred heat causes evaporation of water particles instead of rising the element's temperature. Heat transfer equations between the elements throughout the cross-section are given by Lie [16].

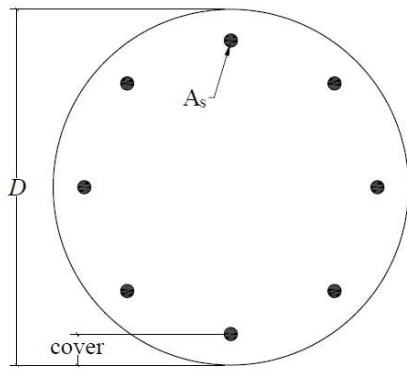
Having determined the temperature distribution within the cross-section, the section is divided into multiple horizontal layers each having a thickness of $\Delta\ell \sin(45^{\circ})$ as shown in Fig. 6-4(c). Average temperature is then calculated in each layer considering two methods that result in different temperature distribution along the cross-section. In the first one, the temperature of each horizontal layer is calculated as the algebraic average temperature of the square elements composing it. The other calculation procedure is performed by first calculating the residual compressive strength of each square element, and then evaluating the temperature which would result in the same average compressive strength in that layer. The first temperature distribution is utilized to calculate thermal and transient strains; whereas the second one is used in calculating the residual strength of each layer. The temperature of the steel layer is assumed to be similar to the temperature of the square mesh elements within which they are located. A similar procedure was performed and validated by El-Fitiany and Youssef [6].

6.3.2 Circular Sections

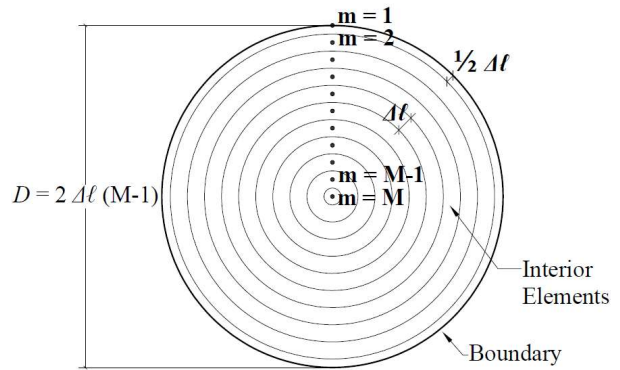
To determine the temperature within the circular cross-section along the RC columns, the area is first divided into M concentric layers as shown in Fig. 6-5(b). The change in temperature (T) in each layer circular layer is derived by solving the heat balance equations at each time increment assuming that the column is exposed to heat along its circumference as described by Lie [16]. The influence of steel bars and moisture contents is considered in the analysis in a similar manner to the rectangular sections.

In this study, a method is proposed and validated to transform the circular layers into equivalent horizontal layers that can be utilized in sectional analysis procedure. The procedure commences by dividing the semi-circular section into M horizontal layers (I) each corresponding to a unique circular layer (J) as indicated in Fig. 6-5(c). The upper and lower boundaries of any horizontal layer (I) are taken as the tangents to the two

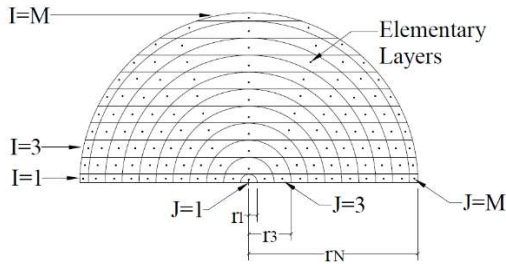
circular layers denoted by $(J = I)$ and $(J = I-1)$, respectively. The intersection between the horizontal and circular layers produce elementary layers whose temperatures represent the temperature of the circular element they are located in. The area (A) of each elementary layer is derived in terms of the radius of each circular layer (r) as given in Equation 3.



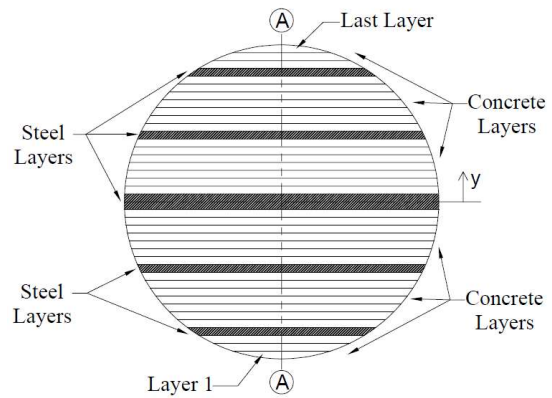
(a) Typical Cross-Section.



(b) Mesh for Heat Transfer Analysis.



(c) Proposed Mesh for Obtaining Average Layer Temperature.



(d) Mesh for Strength Analysis.

Figure 6-5: Geometry and Meshing of Circular Sections

$$A_{I,J} = \begin{cases} \frac{\pi r_1^2}{2} & , I = J = 1 \\ r_I^2 \times \frac{2\cos^{-1}\left(\frac{r_{I-1}}{r_I}\right) - \sin\left[2\cos^{-1}\left(\frac{r_{I-1}}{r_I}\right)\right]}{2} & , I = J \\ \frac{\pi r_J^2}{2} - r_J^2 \times \frac{2\cos^{-1}\left(\frac{r_I}{r_J}\right) - \sin\left[2\cos^{-1}\left(\frac{r_I}{r_J}\right)\right]}{2} - \sum_{1,1}^{I,J} A_{i,j} & , I \neq J \end{cases} \quad (3)$$

The temperature in each layer is calculated twice similar to the procedure performed in rectangular sections. However, in the first case, the weighted average is calculated for each layer instead of calculating the normal average. This requires the determination of the area and temperature of each small element composing the horizontal layer. In the second case, the average temperature that would result in the same weighted average of residual compressive strength is determined. The temperature of each steel layer is taken as the maximum temperature reached at a distance equal to the provided concrete cover since all bars are uniformly distributed parallel to the circumference.

For both rectangular and circular columns, temperature distribution within the section varies with the thermal properties of concrete and the cross-sectional dimensions. Figs. 6-6(a) and 6-6(b) illustrate the change in temperature at different points within sections R3 and C3 whose characteristics are detailed in Table 6-1.

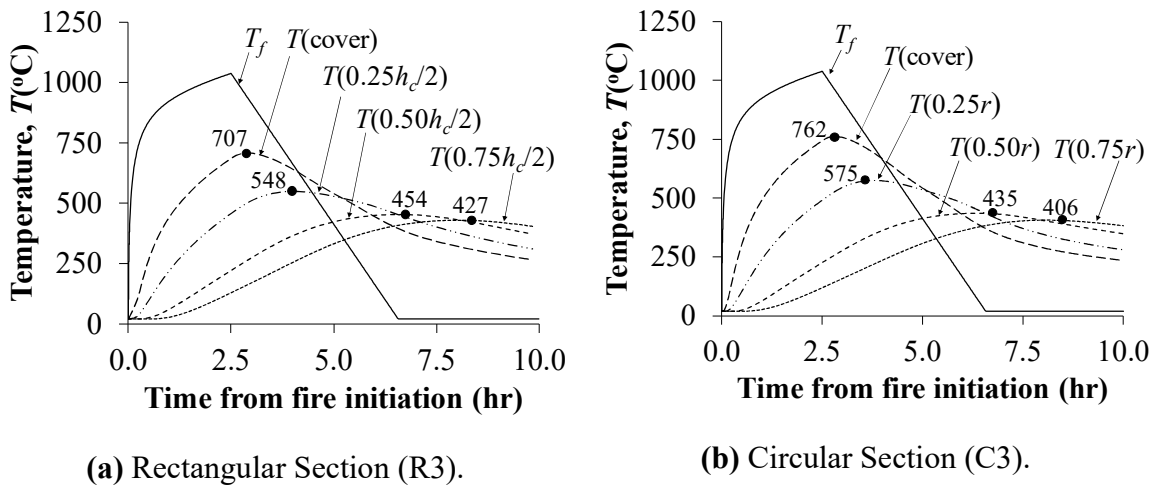


Figure 6-6: Temperature variation with time at different points along the cross-section

The location of each point is defined as the distance from the face of the column in terms of section height (h) for rectangular sections and radius (r) for circular sections. Two main observations can be drawn from these figures. Firstly, curves representing the points further away from the surface show continuous increase in temperature after the end of heating. This causes the maximum temperature in the interior elements to be reached during the cooling phase indicating that heat flow propagates not only to the atmosphere, but also to the inner colder portions of the member. The second observation shows that cooling continues for a considerable amount of time before heat flow starts to take one direction only toward the atmosphere. A distinction between the rectangular and circular sections is detected in terms of response to temperature variation. In the aforementioned two sections, concrete in column C3 located at a distance of up to $(0.5 r)$ respond faster to increase in temperature than that in rectangular sections located at the same distance. However, at a greater depth within the section, temperature variation becomes less pronounced in the circular section compared to its rectangular counterpart. This change in behavior is attributed to the more concrete area acts as a protecting cover for points closer to the core in section C3 compared to section R3. Temperature distributions within sections R3 and C3 corresponding to maximum temperature reached as well as the end of both the heating and cooling phases are shown in Figs. 6-7 and 6-8, respectively.

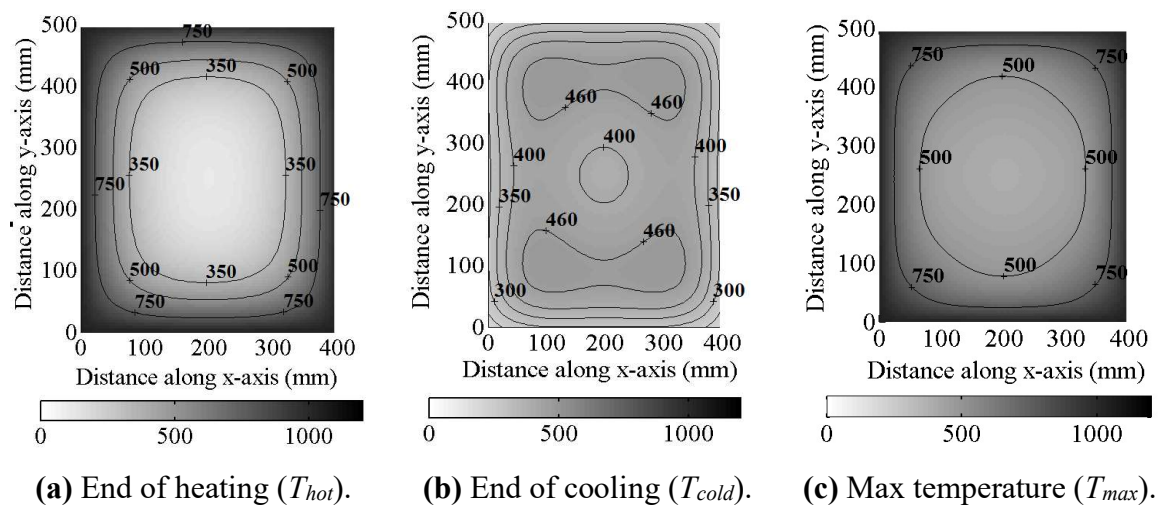


Figure 6-7: Temperature distribution within the rectangular cross-section of column (R3) at different time increments

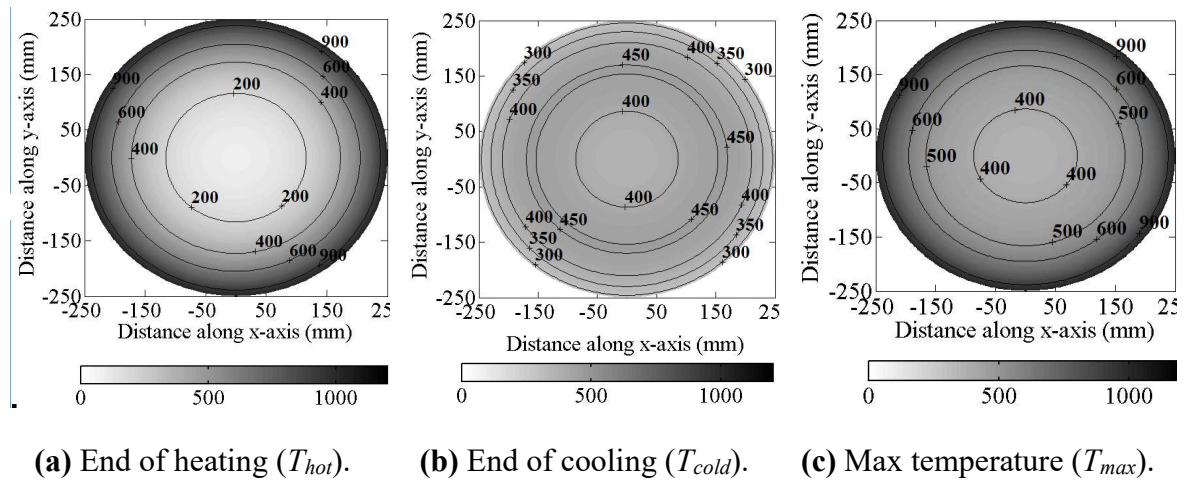


Figure 6-8: Temperature distribution within the circular cross-section of column (C3) at different time increments.

As indicated in Figs. 6-7(a) and 6-8(a), heat flow is initiated from the section perimeter towards the inner core resulting in the highest temperature rise near the exposed surfaces and the lowest values at the center point of section. During the gradual cooling phase, heat transfer takes place from the hot outer regions towards both the colder concrete zones and the surrounding air. This causes temperature to keep increasing in the interior concrete elements for a certain period of time beyond which heat transfer towards the atmosphere becomes predominant as shown in Figs. 6-7(b) and 6-8(b) for the rectangular and circular sections, respectively. The maximum temperature distribution attained at each point within the section throughout the heating-cooling cycle is illustrated in Figs. 6-7(c) and 6-8(c) for the same two sections, respectively. Maximum temperature distribution results in higher temperature values than that at the end of the heating phase. Hence, the residual mechanical properties and constitutive relationships of both concrete and steel are determined in the following sections based on the maximum temperature reached.

6.4 Material Models and Strain Components

The general form of Tsai [17] model is adopted in this study to represent the compressive stress-strain relationship of concrete at all stages. During fire, the reduced compressive strength due to fire (f'_{CT}) proposed by Hertz [15] is used; whereas, concrete strain at peak stress at elevated temperatures (ϵ_{oT}) is determined by Terro [20] formula. The post-fire mechanical properties are calculated based on the expressions provided by Chang *et al.* [21].

Regarding steel constitutive models, the model used by Karthik and Mander [22] is adopted for both ambient and post-fire conditions as it conveniently combines the initial elastic response, yield plateau and strain hardening stages in a rigorous form. At elevated temperatures, Lie [23] model is used as it implicitly includes the reduction in yield strength due to fire. The post-fire mechanical properties of steel are obtained from the expressions proposed and validated by Alhadid and Youssef [24].

Total strain in concrete (ϵ_t) is calculated as the summation of stress-related strain (ϵ_σ), free thermal strain (ϵ_{th}), creep strain (ϵ_{cr}), and transient strain (ϵ_{tr}). The tendency of the structural members to deform due to external applied loads is described in terms of the stress-related strain component. Free thermal strain of both concrete and steel bars is determined from Eurocode [4] proposed expressions. The residual free thermal strain (ϵ_{thR}) represents the irreversible part of the free expansion that occurred during fire. After a complete heating-cooling cycle, thermal strain is restored with a rate of $8 \times 10^{-6} / ^\circ\text{C}$ from the maximum temperature reached [1], while ϵ_{thR} for steel is set to zero. If the member is initially loaded or restrained, then transient strain is generated in concrete and maintains its maximum values after cooling [1]. The empirical model proposed by Terro [20] is adopted to calculate the transient creep strain as referred to by load induced thermal strain (ϵ_{LITS}). Regarding steel bars, the residual thermal strain is brought back to zero at the end of the cooling phase. Both transient and creep strain are not applicable for steel during and after fire. Detailed descriptions of the aforementioned material models and strain components during fire exposure are provided by Youssef and Moftah [5].

6.5 Strength Analysis

An iterative sectional analysis procedure is carried out to determine the residual P - ε behavior of the fire-damaged RC columns. The residual properties are determined in view of the temperature distribution obtained from thermal analysis. At every loading step, the axial strain is increased incrementally until reaching the total applied axial load. The kinematic and compatibility conditions are considered in view of the corresponding residual mechanical properties and stress-strain relationships of both concrete and steel. The strength analysis is performed by dividing the cross-section into multiple horizontal layers as shown in Figs. 6-4(c) and 6-5(d) for the rectangular and circular cross-sections, respectively. To maintain the high accuracy while reducing the computation time, a sensitivity analysis was performed and the maximum layer height is chosen as not to exceed 3 mm. The centroid of each concrete and steel layer is determined considering the appropriate geometrical expressions for both circular and rectangular sections. For concrete, temperature is obtained from the average distribution that would result in average compressive strength in each layer; whereas, the maximum temperature reached is used directly for steel layers corresponding to the exact location of steel bars. The failure criterion of the RC element is defined by crushing of concrete once the strain in any of the sectional layers reaches the residual ultimate strain (ε_{cuR}) proposed and validated by Alhadid and Youssef [24]. The restraining effect due to elevated temperature is considered in the analysis through calculating the axial restraint at each time increment depending on the assumed supporting condition. The axial force generated due to restraint is added to the initial applied load to determine the total axial load during fire exposure.

6.6 Equivalent Residual Strain

Residual stresses are induced in fire-damaged members for two main reasons:

(1) thermal strain in concrete is partially reversible, while transient strain is completely irreversible [1]. At equilibrium, unloaded fire-damaged concrete tends to remain either expanded or contracted depending on the temperature-load history. On the other hand,

thermal strain in steel is fully reversible. Hence, steel bars tend to restore their initial length after fire. The variation in behavior between concrete and the embedded steel bars generate internal stresses.

(2) both thermal and transient strain distributions along section height are nonlinear as they follow the nonlinear temperature profile. Therefore, internal stresses are developed in order to maintain the plane section assumption.

Figs. 6-9(a) through 6-9(d) illustrate the development of the strain components along section (A-A) of Fig. 6-4(c) for rectangular sections. The same analysis procedure is considered for circular sections while accounting for the modified location of the steel layers. The difference between the residual thermal strain (ϵ_{thR}) and the residual transient strain (ϵ_{trR}) is the total residual strain (ϵ_R), which can be either positive or negative depending on the temperature-load history and the magnitude of the developed transient strain. Due to the plane section assumption, the deformed section is represented by a uniform equivalent strain (ϵ_{eq}) along the cross-section. Residual stress-induced strain ($\epsilon_{\sigma i}$) distribution is determined as the difference between an equivalent strain (ϵ_{eq}) and the total residual strain (ϵ_R). An iteration process is performed to evaluate the uniformly distributed equivalent strain (ϵ_{eq}) that satisfies the equilibrium condition of $\epsilon_{\sigma i}$ distribution. The value of ϵ_{eq} is determined such that the total axial force in concrete and steel resulting from $\epsilon_{\sigma i}$ distribution is equal to zero.

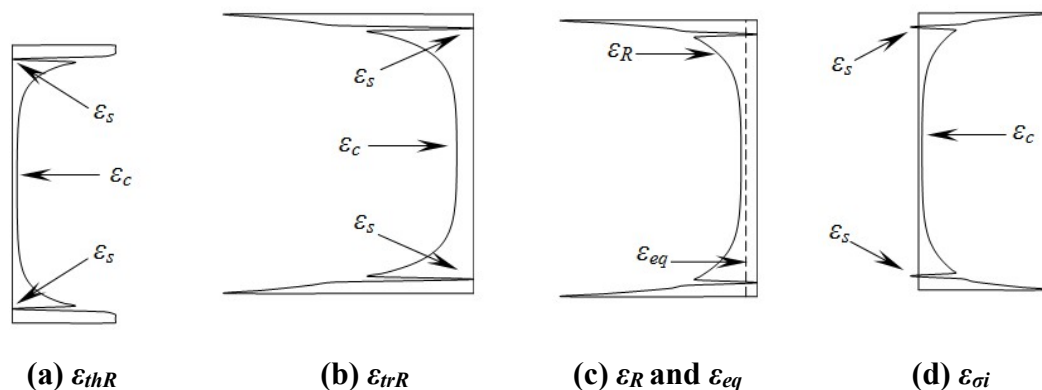


Figure 6-9: Development of various strain components along the cross-section

Once equilibrium is achieved, $\varepsilon_{\sigma i}$ are applied as initial strains in the concrete and steel layers; whereas, ε_{eq} results in shifting the $P-\varepsilon$ curve as illustrated in Figs. 6-10(a) and 6-10(b) for both rectangular and circular sections, respectively.

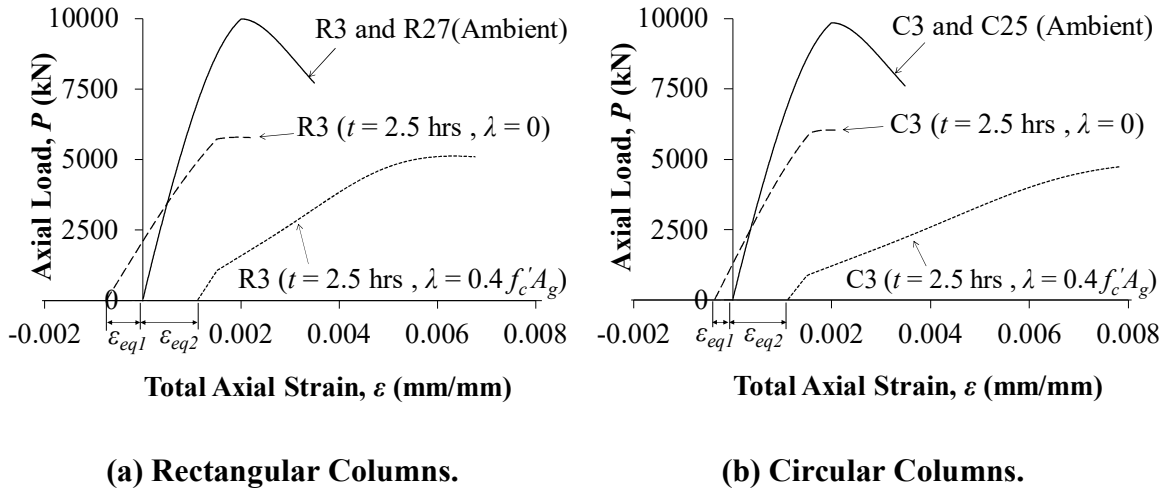


Figure 6-10: Influence of initial load level on the residual ($P-\varepsilon$) relationship

If the column is not initially loaded during fire exposure ($\lambda = 0$), then the residual equivalent strain (ε_{eq1}) is always negative causing the $P-\varepsilon$ curve to shift to the expansion side. However, by imposing an initial load to the column during the heating phase, transient strain component develops and counteracts the influence of thermal strain. If the applied load is large enough, the column experiences residual contraction instead of expansion after the cooling as indicated by the positive equivalent strain (ε_{eq2}). The change in stiffness is attributed to the elimination of the residual stress-induced strains. Restraining the column affects the magnitude of the generated transient strain especially if the column is not subjected to initial load. When the column is restrained, part of the equivalent strain (ε_{eq}) induces stresses within the section depending on the considered degree of restraint while maintaining the equilibrium condition. Strain profiles of columns R3 and C3 at various load levels are shown in Fig. 6-11.

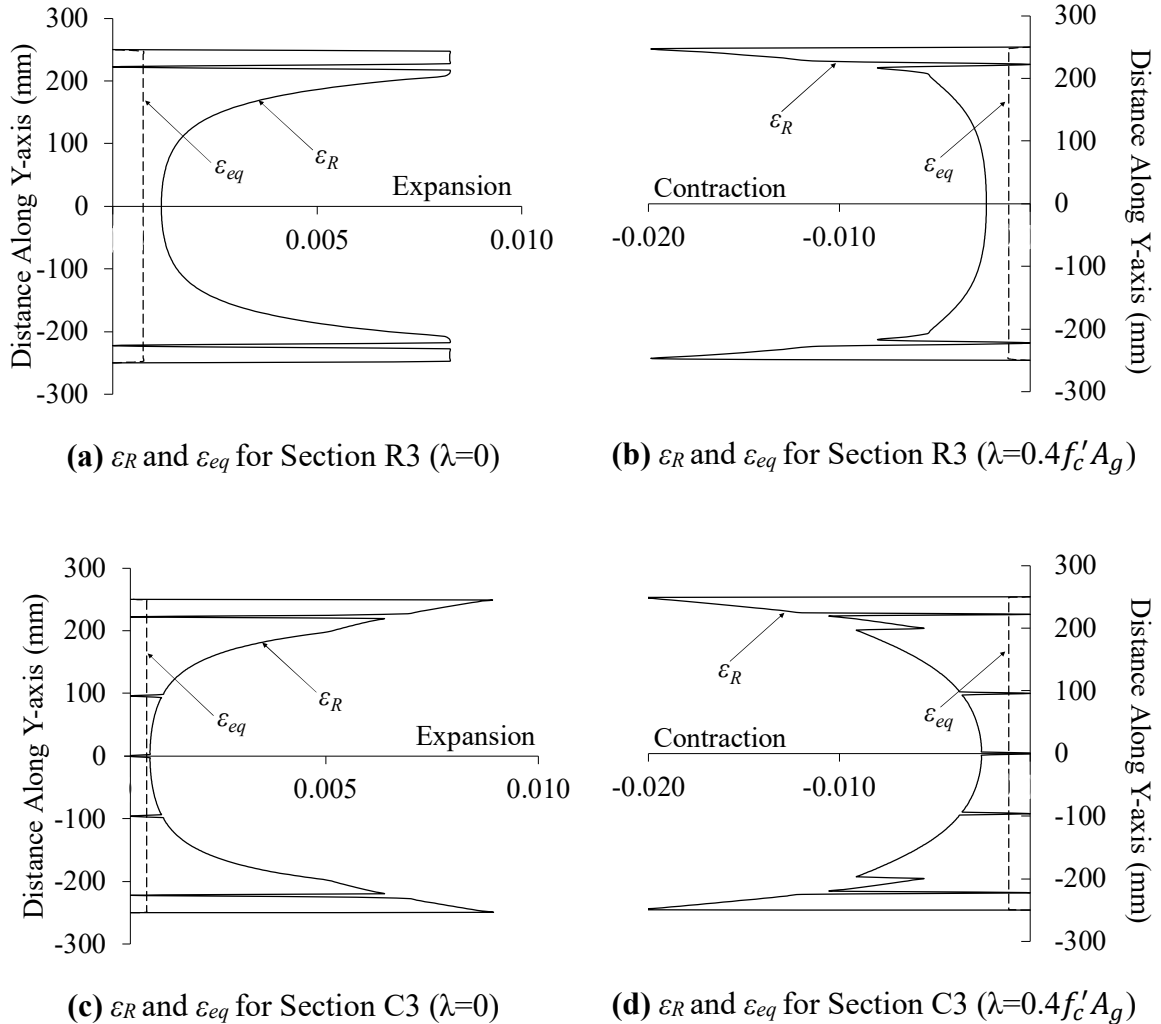
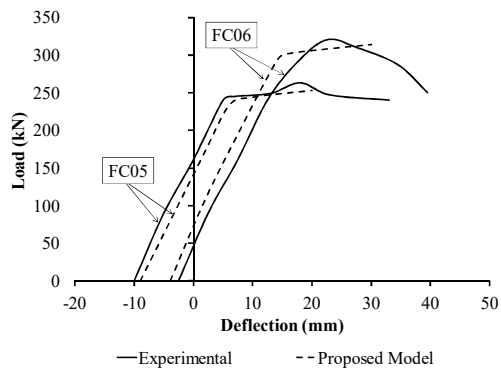
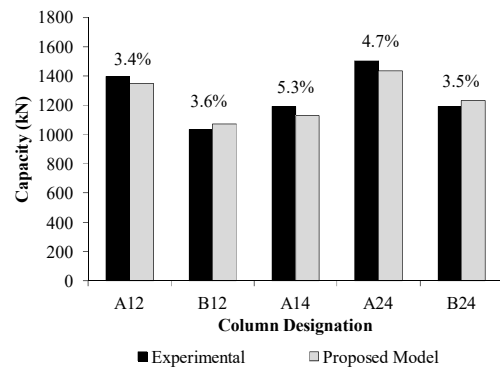


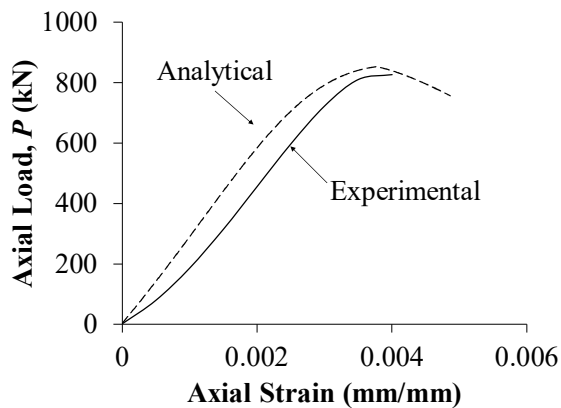
Figure 6-11: Residual and equivalent strains distribution along columns R3 and C3 cross-sections

6.7 Validation of the Proposed Analytical Model

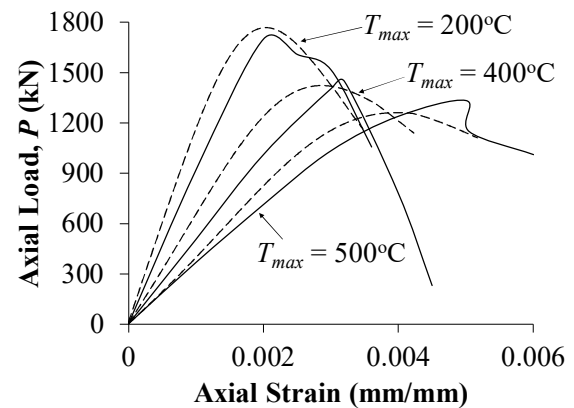
The capability of the present model to predict the post-fire structural performance of axially loaded RC members is validated in view of the experimental results obtained by Chen *et al.* [25], Jau and Huang [26], Yaqub and Bailey [27] and Elsanadedy *et al.* [28]. The validation is limited to structural members made of normal strength concrete where spalling does not occur.

(a) Chen *et al.* (2009)

(b) Jau and Huang (2008)



(c) Yaqub and and Bailey (2011)

(d) Elsanadedy *et al.* (2016)**Figure 6-12: Validation of the proposed analytical model with experimental data**

6.7.1 Chen *et al.* [25]

Chen *et al.* [25] carried out full-scale experiment to investigate the performance of RC columns after exposure to different fire conditions. The results obtained from the proposed analytical model are compared with the measured data of columns FC06 and FC05. These columns are exposed to ISO 834 (2014) standard fire curve from four sides for 2 hrs and 4 hrs, respectively. The tested columns have cross-sectional dimensions of

300 mm × 450 mm, concrete cover of 40 mm and overall length of 3.0 m. The concrete compressive strength at ambient conditions is 29.5 MPa. The longitudinal reinforcement consists of 4Φ19 mm and 4Φ16 mm steel bars having yield strengths of 476 MPa and 479 MPa, respectively. Both columns were subjected to an initial axial load of 797 kN prior to heat exposure. After 30 days from the fire test, the columns were subjected to the constant initial concentric load of 797 kN while another eccentric load is applied until failure. Fig. 6-12(a) shows the analytical and experimental load-deflection curves at the column mid-span due to the eccentric load about the y-axis. A very good agreement between both curves can be shown with a percent difference of 3.8% and 4.6% in the ultimate capacity of columns FC06 and FC05, respectively; and a percent difference of 6.3% and 5.4% in the 40% secant stiffness for the same two columns, respectively. This variation can be attributed to the sensitivity of the adopted thermal expansion model to the experimental conditions and concrete mix. Also, the heating-cooling cycle adopted in the model follows the ISO 834 [18] provisions which may be different from the actual relationship followed in lab.

6.7.2 Jau and Huang [26]

In another experimental study, Jau and Huang [26] investigated the residual behavior of initially loaded restrained RC columns subjected to heat from two adjacent sides. The cross-sectional dimensions of all columns are 300 mm × 450 mm with an overall length of 2.7 m. The concrete cover varies between 50 mm or 70 mm, whereas the steel reinforcement ratio varies between 1.8% and 3.0%. Normal strength concrete with compressive strength of 33.7 MPa and steel bars with yield strength of 475.8 MPa are used. The test setup allows the heat to flow through two adjacent surfaces only while the other two surfaces are insulated and not subjected to fire. The restrained columns are subjected to a 10% axial preloading of their ambient compressive strength during the 2 or 4 hrs fire test. After the columns naturally cooled down, the load is applied until failure occurs. Fig. 6-12(b) shows both the experimental and predicted residual capacity of columns A12, B12, A14, A24 and B24 whose detailed geometrical and mechanical properties are provided by Jau and Huang [26]. The proposed model is found to predict the capacity of the tested columns with high accuracy as indicated by the maximum

percent error of 5.3% depicted of column A14 shown in Fig. 6-12(b). Overall, the agreement between the experimental and analytical results is very good in terms of the predicting the ultimate residual capacity. This good agreement may be attributed to using the actual material properties and temperature-time curve, which were comprehensively described in the experimental program.

6.7.3 Yaqub and Bailey [27]

The influence of elevated temperature on the residual axial capacity, axial stiffness and stress-strain behavior of circular columns was experimentally investigated by Yaqub and Bailey [27]. All of the examined columns have a diameter of 200 mm and an overall length of 1000 mm. The concrete cover to the centroid of the steel bars was taken as 30 mm. The reinforcement consisted of 6 ϕ 10 mm Steel bars resulting in a reinforcement ratio of 1.5%. Normal weight concrete with compressive strength of 42.4 MPa and steel bars with yield strength of 570 MPa were used. The columns were exposed to a predefined heating-cooling cycle 9 months after casting until the entire cross-section reaches a uniform temperature of 500°C. After that, the columns were subjected to a displacement controlled uniaxial compression load until failure. Fig. 6-12(c) presents both the experimental and analytical axial load-deformation curves for the specimens exposed to a maximum temperature of 500°C. The proposed model is found to provide very good prediction of the experimental results as indicated by the 4.2% percent error. The incremental stiffness at service load is almost identical between the two curves. Also, the load-deformation behavior obtained from the proposed model is shown to be consistent with that obtained experimentally in terms of stiffness, peak and failure strain.s

6.7.4 Elsanadedy *et al.* [28]

The influence of elevated temperature on the residual axial capacity, axial stiffness and stress-strain behavior of circular columns was experimentally investigated by Elsanadedy *et al.* [28]. All of the examined columns have a diameter of 242 mm and an overall length of 900 mm. The concrete cover to the centroid of the steel bars was taken as 41 mm. The reinforcement consisted of 4 ϕ 10 Steel bars resulting in a reinforcement ratio of 0.68%. Normal weight concrete with compressive strength of 42 MPa and steel bars with

yield strength of 593 MPa were used. The columns were heated along the circumference under unstressed conditions according to the temperature path described by Elsanadedy *et al.* [28]. The columns were gradually cooled down inside the oven until reaching room temperature. After that, the columns were subjected to a displacement controlled uniaxial compression load until failure. Fig. 6-12(d) presents both the experimental and analytical axial load-deformation curves for the specimens exposed to a maximum temperature of 200°C, 400°C and 500°C. The capability of the proposed model to capture the residual capacity obtained experimentally is very good as indicated by the 4.7%, 3.7% and 6.5% percent errors, respectively. Also, the load-deformation behavior obtained from the proposed model is shown to be consistent with that obtained experimentally in terms of stiffness, peak strain and failure strain. The error between the model and experimental results can be attributed to the variation of heat rate, existence of residual surface cracks and initial misalignment in the column that are not accounted for in the model.

6.8 Parametric Study

The main parameters include the concrete compressive strength, f'_c (25 MPa and 35 MPa); steel yield strength, f_y (300 MPa and 400 MPa); fire duration, t (0.5 hr, 1.5 hrs and 2.5 hrs); initial load level, λ (0.0, $0.2 f'_c$, $0.4 f'_c$); axial restraint stiffness ratio, R_D (0.0, 0.5 and 1.0); and steel reinforcement ratio, ρ (0.02 and 0.04). The cross-sectional dimensions of the rectangular sections are defined in terms of member height, h (400 mm and 800 mm) and width, b (300 mm and 600 mm); whereas for circular sections, the geometrical properties are determined in terms of their diameter, D (350 mm and 650 mm). The members are exposed to fire along their perimeters according to ASTM E119 [17] standard fire curve followed by a cooling phase according to ISO 834 [18] recommendations. The influence of the considered factors on the post-fire behavior of both rectangular and circular RC axially loaded members is investigated in view of a parametric study. Based on these parameters, the analytical investigation consists of a total of 1728 different cases.

The effect of the aforementioned parameters on both the residual axial capacity and the residual 40% secant axial stiffness is illustrated in view of the members presented in

Table 6-1. The variation of the residual capacity and stiffness in terms of the different parameters at different initial load levels is presented Figs. 6-13 and 6-14 for both rectangular and circular sections, respectively.

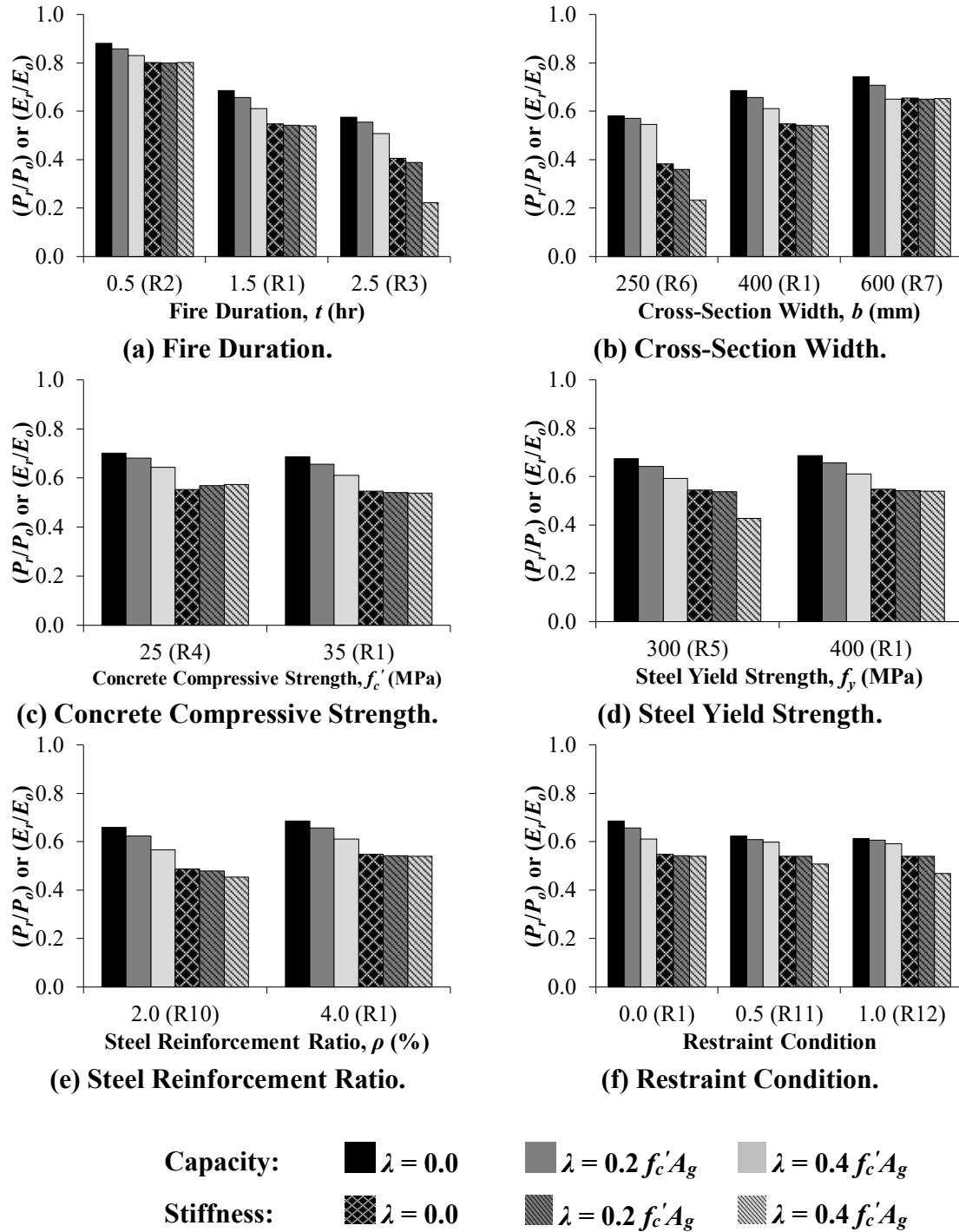


Figure 6-13: Influence of varying the examined parameters on the axial capacity and stiffness of rectangular columns

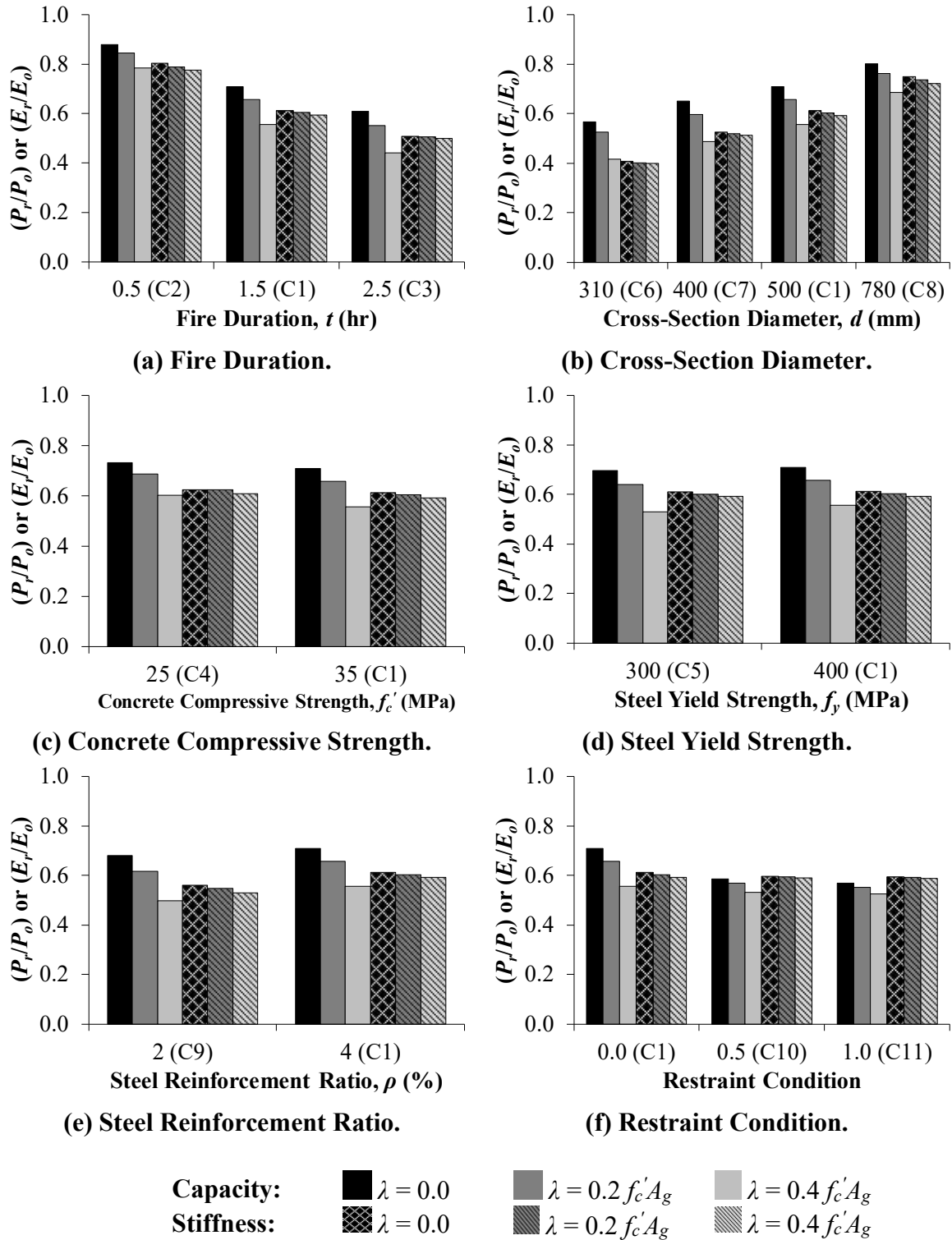


Figure 6-14: Influence of varying the examined parameters on the axial capacity and stiffness of circular columns

6.8.1 Effect of Fire Duration

Fire duration is found to have the most significant influence on reducing the post-fire capacity and stiffness of both rectangular and circular RC columns. The influence of increasing the fire duration on the residual flexural behavior is examined in view the rectangular sections (R1, R2 and R3) and the circular sections (C1, C2 and C3) as shown in Figs. 6-13(a) and 6-14(a), respectively. Prolonged exposure to fire results in material strength degradation and softening that adversely affect the stiffness and capacity of the fire-damaged section. The permanent strength and stiffness reductions in the circular columns are found to be slightly higher than those having rectangular sections. This can be attributed to the higher maximum temperature reached within the circular sections subjected to fire for the same fire duration as was previously described in Fig. 6-6. The additional deterioration in both concrete and steel residual mechanical properties caused by the longer duration of the heating-cooling cycle provides more time for heat to transfer to the inner elementary layers raising their temperatures.

6.8.2 Effect of Section Size

Increasing the cross-sectional dimensions of both rectangular and circular columns results in higher residual flexural strength and stiffness after fire as indicated in Figs. 6-13(b) and 6-14(b). This larger residual capacity is caused by the lower temperature increase within the larger member as it requires more heat energy to increase its temperature. This is attributed to the additional concrete cover provided by the larger sections causing hindrance of heat transfer from the column perimeter towards its core. Hence, internal concrete fibers experience lower temperatures and consequently higher residual compressive strength and stiffness than the inner elements of columns with smaller dimensions. For the same fire duration, concrete within the inner parts of the wider member experience lower increase in temperature and consequently more recovery after fire. The influence of strength recovery in steel bars is neglected since concrete cover is the same in all specimens causing the maximum temperature reached in all steel bars to be the same.

6.8.3 Effect of Mechanical Properties

Increasing the concrete compressive strength is found to have an insignificant inverse relationship on the reduction ratio of both capacity and stiffness for all load levels in the examined range as shown in Figs. 6-13(c) and 6-14(c) for rectangular and circular columns, respectively. The decreasing rate can be justified by the more reduction in compressive strength of the stronger concrete after fire. Hence, the reduction in concrete contribution within the compression zone becomes more pronounced and results in the observed larger decrease relative to the original capacity. The use of normal strength concrete infers that no spalling is encountered, which could otherwise significantly affect the residual capacity. The same observation can be drawn by varying the grade of the embedded steel bars from 300 MPa to 400 MPa as shown in Figs. 6-13(d) and 6-14(d) for rectangular and circular columns, respectively. This is attributed to the fact the steel bars restore a significant portion of their capacity and stiffness after fire as discussed previously.

6.8.4 Effect of Steel Reinforcement Ratio

Steel bars are located near the exposed surfaces of the columns and are subjected to relatively high temperatures. However, this has negligible impact on the overall axial capacity and stiffness reduction due to the significant recovery of mild steel bars after fire exposure [29-31]. Figs. 6-13(e) and 6-14(e) shows that increasing the reinforcement ratio results in insignificant increase in both residual capacity and stiffness the rectangular and circular columns, respectively. This is attributed to the higher impact of the larger steel area in replacing the fire-damaged concrete since recovery of steel bars is very significant as opposed to concrete.

6.8.5 Effect of Restraint Conditions

The influence of restraining the member against thermal expansion during heating is found to slightly decrease its post-fire stiffness and capacity as shown in Figs. 6-13(f) and 6-13(f) for both rectangular and circular columns, respectively. The reduction in residual properties is more pronounced when comparing the fully unrestrained sections with the restrained ones. However, the reduction seems to be almost identical for columns that are

fully restrained or 50% restrained. This is explained by the impact of transient strain in changing the deformation behavior of axially loaded members during fire exposure through alleviating the thermal expansion. As the stiffness of the supports provided by the adjacent frame members increases, more restraining forces are generated to counteract the tendency of the column to expand. This additional force results in transient creep strain which reduces the thermal strain and consequently decreases the amount of restraining force required to overcome the expansion. These two processes occur simultaneously and have negative influence on each other causing them to reduce the impact of restrains.

During fire exposure, the column's tendency to undergo thermal expansion increases with time causing the support to counteract this potential movement depending on the column's stiffness. Initially, the member's stiffness remains close to that at ambient conditions as the temperature increase within the member is relatively low. Thus, an increase in restraining force results in significant hindrance of the column's deformation as thermal strain component increases. However, after a certain period of time, temperature within the member becomes relatively high causing the stiffness degradation to become more pronounced. Thus, the forces required to resist the larger thermal expansion of the member drops. The axial force required to restrain the member keeps decreasing as a result of the continuous reduction in stiffness caused by elevated temperatures. Therefore, the change in the restraining load is characterized by a mild increase followed by a gradual decrease with time.

6.9 Proposed Simplified Expressions to Obtain Residual Axial Capacity and Stiffness

Prolonged exposure of RC columns to elevated temperatures according to a standard fire has a substantial influence on their axial capacity and deformation behavior. The residual structural performance of such columns relies on the geometrical characteristics, mechanical properties, initial load, restraint conditions and fire duration that should be appropriately accounted for in the analysis. Accurate determination of temperature

distribution and residual strain components developed within RC columns is tedious and requires detailed thermal and structural analyses that may not be convenient for design engineers. The proposed analytical model comprehensively addresses the influence of the aforementioned factors on determining the post-fire response of both rectangular and circular RC columns. Hence, based on the extensive parametric study conducted on the 1728 different cases, regression analysis is carried out to develop expressions for obtaining both the residual axial capacity and secant axial stiffness of fire-damaged rectangular and circular RC columns. These proposed expressions take into consideration the loading history, restraint conditions, fire duration, material strength and cross-sectional dimensions of the exposed members. The validity and accuracy of the proposed equations depend on the range of parameters considered in the parametric study. The proposed expressions provide a suitable approach for predicting the behavior of RC columns after exposure to an extreme standard fire scenario. This would be a valuable tool for both researchers and engineers to predict the post-fire performance of RC columns during the design phase.

6.9.1 Rectangular Sections

Linear multiple regression analysis is performed to propose an expression for both the residual capacity and axial stiffness ratios (ω) as given in Equation 4.

$$\omega = A_1 + A_2\lambda + A_3f'_c + A_4f_y + A_5\rho + A_6\frac{\rho f_y}{f'_c} + A_7b + A_8h \quad (4)$$

Where λ is the initial load level relative to ambient capacity, f'_c is the concrete compressive strength (MPa), f_y is the steel yield strength (MPa), ρ is steel reinforcement ratio, b is section width (m), h is section height (m). The coefficients $(A_i)_{i=1,2,3,4,5,6,7,8}$ are given in Table 6-2 in terms of the axial restraint ratio (R_D) and fire duration at the end of the heating phase (t) in hours. For values other than the listed t and R_D , linear interpolation of the upper and lower calculated ω should be performed. In Table 6-2, P_o and P_r are the axial capacities at ambient and post-fire conditions, respectively; EA_i and $(EA_i)_r$ are the initial axial stiffness at ambient and post-fire conditions, respectively; $EA_{0.4}$ and $(EA_{0.4})_r$ are the 40% axial stiffness at ambient and post-fire conditions, respectively;

and $EA_{0.8}$ and $(EA_{0.8})_r$ are the 80% axial stiffness at ambient and post-fire conditions, respectively.

Table 6-2: Coefficient of Equation 4 for rectangular sections

ω	A_i	$R_D = 0$ (Unrestrained)			$R_D = 0.5$ (Partially Restrained)			$R_D = 1$ (Fully Restrained)		
		$t = 0.5$ hr	$t = 1.5$ hrs	$t = 2.5$ hrs	$t = 0.5$ hr	$t = 1.5$ hrs	$t = 2.5$ hrs	$t = 0.5$ hr	$t = 1.5$ hrs	$t = 2.5$ hrs
$\frac{P_r}{P_o}$	A_1	6.90×10^{-1}	3.60×10^{-1}	2.06×10^{-1}	6.16×10^{-1}	3.28×10^{-1}	2.17×10^{-1}	5.96×10^{-1}	3.14×10^{-1}	2.18×10^{-1}
	A_2	-1.22×10^{-1}	-1.70×10^{-1}	-1.48×10^{-1}	-7.29×10^{-2}	-7.23×10^{-2}	-8.24×10^{-2}	-6.74×10^{-2}	-6.43×10^{-2}	-7.03×10^{-2}
	A_3	-7.09×10^{-4}	-1.28×10^{-3}	-1.58×10^{-3}	-1.08×10^{-3}	-1.97×10^{-3}	-2.16×10^{-3}	-1.16×10^{-3}	-1.94×10^{-3}	-2.26×10^{-3}
	A_4	5.01×10^{-5}	6.72×10^{-5}	7.83×10^{-5}	6.94×10^{-5}	8.57×10^{-5}	1.02×10^{-4}	7.58×10^{-5}	9.78×10^{-5}	1.04×10^{-4}
	A_5	1.31	1.90	2.34	1.82	2.46	3.05	2.09	2.65	3.17
	A_6	9.03×10^{-2}	1.16×10^{-1}	1.43×10^{-1}	1.14×10^{-1}	1.43×10^{-1}	1.41×10^{-1}	1.14×10^{-1}	1.42×10^{-1}	1.47×10^{-1}
	A_7	1.66×10^{-1}	3.45×10^{-1}	4.04×10^{-1}	1.54×10^{-1}	2.51×10^{-1}	3.00×10^{-1}	1.49×10^{-1}	2.37×10^{-1}	2.78×10^{-1}
	A_8	1.30×10^{-1}	2.23×10^{-1}	2.42×10^{-1}	1.78×10^{-1}	2.56×10^{-1}	2.43×10^{-1}	1.92×10^{-1}	2.61×10^{-1}	2.43×10^{-1}
$\frac{(EA_i)_r}{EA_i}$	A_1	5.36×10^{-1}	-1.38×10^{-1}	-3.18×10^{-1}	5.34×10^{-1}	-1.64×10^{-1}	-2.57×10^{-1}	5.32×10^{-1}	-2.41×10^{-1}	-2.75×10^{-1}
	A_2	-7.45×10^{-3}	-5.66×10^{-2}	-7.28×10^{-2}	-3.75×10^{-3}	-6.59×10^{-2}	-1.26×10^{-1}	-3.55×10^{-3}	-8.61×10^{-2}	-1.35×10^{-1}
	A_3	-3.90×10^{-4}	-2.01×10^{-3}	-3.58×10^{-3}	-4.00×10^{-4}	-3.97×10^{-3}	-2.77×10^{-3}	-3.56×10^{-4}	-2.69×10^{-3}	-4.56×10^{-3}
	A_4	-2.41×10^{-5}	1.79×10^{-4}	3.70×10^{-4}	-2.83×10^{-5}	3.14×10^{-4}	2.02×10^{-4}	-2.98×10^{-5}	2.99×10^{-4}	3.83×10^{-4}
	A_5	2.52	9.00	1.49×10^1	2.55	1.16×10^1	1.12×10^1	2.56	9.90	1.38×10^1
	A_6	4.68×10^{-2}	-1.37×10^{-1}	-3.52×10^{-1}	5.55×10^{-2}	-2.70×10^{-1}	-6.62×10^{-2}	5.88×10^{-2}	-3.94×10^{-2}	-2.54×10^{-1}
	A_7	2.11×10^{-1}	8.16×10^{-1}	7.84×10^{-1}	2.04×10^{-1}	8.70×10^{-1}	7.46×10^{-1}	2.01×10^{-1}	9.32×10^{-1}	7.42×10^{-1}
	A_8	1.64×10^{-1}	2.63×10^{-1}	2.56×10^{-1}	1.68×10^{-1}	2.49×10^{-1}	2.56×10^{-1}	1.69×10^{-1}	2.35×10^{-1}	2.59×10^{-1}
$\frac{(EA_{0.4})_r}{EA_{0.4}}$	A_1	5.74×10^{-1}	-1.53×10^{-1}	-2.88×10^{-1}	5.82×10^{-1}	-3.85×10^{-1}	-3.70×10^{-1}	5.81×10^{-1}	-4.48×10^{-1}	-4.43×10^{-1}
	A_2	1.37×10^{-3}	-1.58×10^{-1}	-3.34×10^{-1}	-5.76×10^{-4}	-1.49×10^{-1}	-3.58×10^{-1}	-1.15×10^{-3}	-1.38×10^{-1}	-3.08×10^{-1}
	A_3	-5.86×10^{-4}	8.44×10^{-4}	6.42×10^{-4}	-6.26×10^{-4}	1.16×10^{-3}	5.47×10^{-4}	-5.61×10^{-4}	1.94×10^{-3}	2.56×10^{-3}
	A_4	-1.88×10^{-5}	-4.47×10^{-5}	5.78×10^{-5}	-4.12×10^{-5}	1.41×10^{-4}	1.81×10^{-4}	-4.48×10^{-5}	1.61×10^{-4}	1.50×10^{-4}
	A_5	2.19	1.29	2.18	2.08	-1.56	6.68×10^{-1}	2.07	-3.09	-3.46
	A_6	7.94×10^{-2}	4.52×10^{-1}	4.49×10^{-1}	1.25×10^{-1}	7.39×10^{-1}	6.88×10^{-1}	1.33×10^{-1}	8.25×10^{-1}	1.06
	A_7	2.10×10^{-1}	9.25×10^{-1}	8.43×10^{-1}	1.89×10^{-1}	1.15	8.45×10^{-1}	1.83×10^{-1}	1.19	8.45×10^{-1}
	A_8	1.69×10^{-1}	2.78×10^{-1}	2.88×10^{-1}	1.77×10^{-1}	2.86×10^{-1}	2.83×10^{-1}	1.79×10^{-1}	2.97×10^{-1}	2.65×10^{-1}
$\frac{(EA_{0.8})_r}{EA_{0.8}}$	A_1	5.96×10^{-1}	-2.33×10^{-1}	-3.10×10^{-1}	5.11×10^{-1}	-4.88×10^{-1}	-4.27×10^{-1}	4.57×10^{-1}	-4.96×10^{-1}	-4.32×10^{-1}
	A_2	1.79×10^{-2}	-3.16×10^{-1}	-4.64×10^{-1}	-3.54×10^{-2}	-1.35×10^{-1}	-2.16×10^{-1}	-3.89×10^{-2}	-1.15×10^{-1}	-1.58×10^{-1}
	A_3	-8.59×10^{-4}	1.51×10^{-3}	1.54×10^{-3}	-1.37×10^{-3}	3.87×10^{-3}	3.30×10^{-3}	-1.11×10^{-3}	4.18×10^{-3}	3.29×10^{-3}
	A_4	2.76×10^{-5}	1.55×10^{-4}	1.06×10^{-4}	2.29×10^{-4}	2.43×10^{-4}	9.84×10^{-5}	3.04×10^{-4}	2.38×10^{-4}	8.56×10^{-5}
	A_5	1.88	-1.67	-9.57×10^{-1}	1.60	-8.52	-6.22	1.03	-8.62	-6.28
	A_6	1.44×10^{-1}	5.98×10^{-1}	5.20×10^{-1}	2.43×10^{-1}	9.97×10^{-1}	7.77×10^{-1}	3.07×10^{-1}	9.58×10^{-1}	7.35×10^{-1}
	A_7	2.03×10^{-1}	9.81×10^{-1}	8.88×10^{-1}	2.25×10^{-1}	1.09	8.52×10^{-1}	2.46×10^{-1}	1.08	8.43×10^{-1}
	A_8	1.72×10^{-1}	3.18×10^{-1}	3.08×10^{-1}	1.95×10^{-1}	3.54×10^{-1}	3.11×10^{-1}	2.03×10^{-1}	3.52×10^{-1}	3.04×10^{-1}

It is worth mentioning that although the rectangular column is exposed to fire from all sides, the coefficients of the section height (h) and section width (b) are different in Equation 4. This variation is attributed to the assumed reinforcement configuration where the steel bars lie in two opposite layers that are parallel to the section width as indicated in Fig. 6-4(a).

The equivalent residual strain (ε_{eq}) in rectangular axially loaded columns can be determined from the proposed Equation 5. The post-fire deformation of the columns is highly dependent on the state of stress during the heating-cooling cycle. Hence, the coefficients (E_i) _{$i=1,2,3,4,5,6,7,8$} in Equation 5 are presented in Table 6-3 in terms of the applied load level (λ) and the axial restraint ratio (R_D).

$$\varepsilon_{eq} = E_1 + E_2 t + E_3 f'_c + E_4 f_y + E_5 b + E_6 h + E_7 \rho + E_8 \frac{t^2}{\sqrt{b}} \quad (5)$$

Table 6-3: Coefficient of Equation 5 for rectangular sections

E_i	$R_D = 0$ (Unrestrained)			$R_D = 0.5$ (Partially Restrained)			$R_D = 1$ (Fully Restrained)		
	$\lambda = 0.0$	$\lambda = 0.2$	$\lambda = 0.4$	$\lambda = 0.0$	$\lambda = 0.2$	$\lambda = 0.4$	$\lambda = 0.0$	$\lambda = 0.2$	$\lambda = 0.4$
E_1	5.299×10^{-4}	-1.483×10^{-4}	-1.073×10^{-3}	-5.280×10^{-4}	-7.778×10^{-4}	-1.484×10^{-3}	-7.486×10^{-4}	-9.424×10^{-4}	-1.566×10^{-3}
E_2	4.439×10^{-5}	-3.225×10^{-4}	-6.560×10^{-4}	-1.070×10^{-3}	-1.017×10^{-3}	-9.664×10^{-4}	-1.082×10^{-3}	-1.084×10^{-3}	-1.085×10^{-3}
E_3	6.690×10^{-6}	-1.220×10^{-6}	-7.160×10^{-6}	-4.310×10^{-6}	-5.830×10^{-6}	-9.730×10^{-6}	-4.200×10^{-6}	-9.190×10^{-6}	-1.013×10^{-5}
E_4	-1.200×10^{-7}	0.000	4.900×10^{-7}	1.400×10^{-7}	1.600×10^{-7}	8.200×10^{-7}	1.800×10^{-7}	4.000×10^{-7}	7.600×10^{-7}
E_5	-6.677×10^{-4}	3.038×10^{-4}	1.275×10^{-3}	1.186×10^{-3}	1.400×10^{-3}	1.653×10^{-3}	1.374×10^{-3}	1.598×10^{-3}	1.860×10^{-3}
E_6	-1.894×10^{-4}	-4.567×10^{-5}	6.948×10^{-5}	-7.014×10^{-5}	3.920×10^{-6}	6.510×10^{-5}	-6.695×10^{-5}	-1.535×10^{-5}	2.000×10^{-5}
E_7	-1.537×10^{-2}	5.167×10^{-3}	3.015×10^{-2}	1.591×10^{-2}	1.970×10^{-2}	4.012×10^{-2}	1.969×10^{-2}	2.396×10^{-2}	4.320×10^{-2}
E_8	6.773×10^{-5}	6.273×10^{-5}	4.743×10^{-5}	2.206×10^{-4}	1.823×10^{-4}	1.205×10^{-4}	2.115×10^{-4}	1.868×10^{-4}	1.481×10^{-4}

The validity of the proposed Equations 4 and 5 is assessed by comparing the values obtained using the proposed equations and the results obtained from the analytical analysis. A comparison between the values predicted from Equation 4 and the results determined through performing detailed analytical analysis for all examined cases revealed a very good agreement as shown in Figs. 6-15(a) and 6-16(a) for both residual capacity and axial stiffness, respectively. Similar agreement between the analytical results and the values calculated from Equation 5 is shown in Fig. 6-17. The equality line denotes the location on the graph where the predictions from the proposed equations matches those obtained from the proposed analytical model. As shown in Figs. 6-15(a),

6-16(a) and 6-17, the data points are uniformly distributed in the vicinity of the equality line.

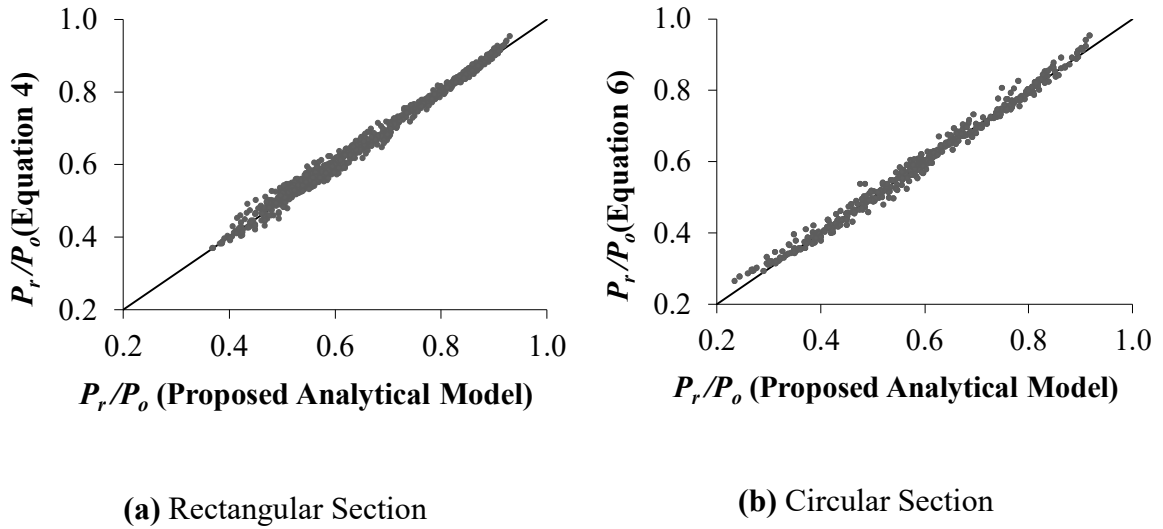


Figure 6-15: Validation of the proposed Equations 4 and 5 for residual capacity

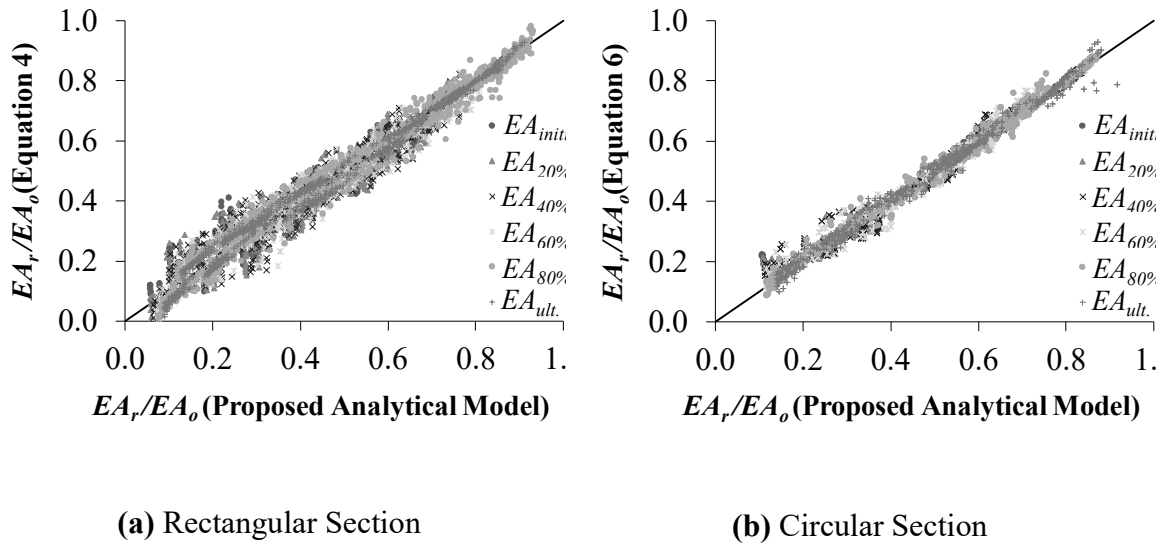


Figure 6-16: Validation of the proposed Equations 4 and 5 for residual axial stiffness

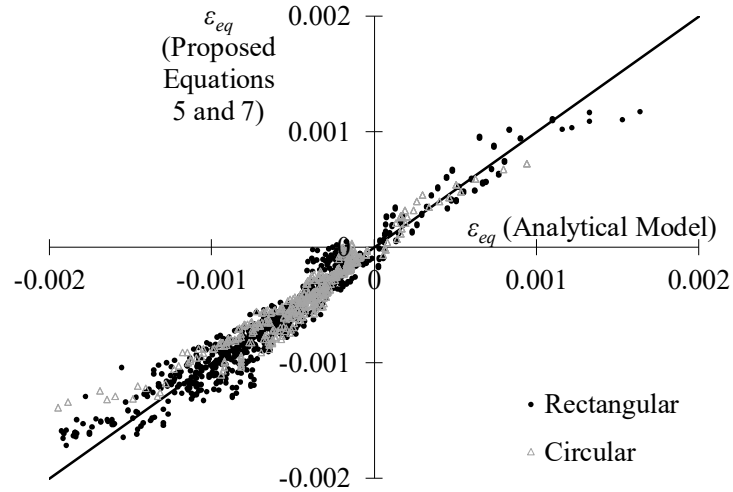


Figure 6-17: Validation of the proposed Equation 6 for equivalent residual strain

6.9.2 Circular Sections

Multiple linear regression analysis is also performed to propose similar expressions for the residual capacity and stiffness of axially loaded circular RC columns as shown in Equation 6.

$$\omega = B_1 + B_2\lambda + B_3f'_c + B_4f_y + B_5\rho + B_6\frac{\rho f_y}{f'_c} + B_7D \quad (6)$$

Where D is the diameter of the cross-section (m). The coefficients $(B_i)_{i=1,2,3,4,5,6,7}$ are given in Table 6-4 in a similar manner to the coefficients of the rectangular section.

Table 6-4: Coefficient of Equation 6 for circular sections

ω	B_i	$R_D = 0$ (Unrestrained)			$R_D = 0.5$ (Partially Restrained)			$R_D = 1$ (Fully Restrained)		
		$t = 0.5$ hr	$t = 1.5$ hrs	$t = 2.5$ hrs	$t = 0.5$ hr	$t = 1.5$ hrs	$t = 2.5$ hrs	$t = 0.5$ hr	$t = 1.5$ hrs	$t = 2.5$ hrs
$\frac{P_r}{P_o}$	B_1	6.70×10^{-1}	3.41×10^{-1}	1.96×10^{-1}	4.87×10^{-1}	1.74×10^{-1}	1.04×10^{-1}	4.41×10^{-1}	1.71×10^{-1}	4.63×10^{-2}
	B_2	-2.52×10^{-1}	-3.97×10^{-1}	-3.96×10^{-1}	-1.44×10^{-1}	-1.44×10^{-1}	-1.43×10^{-1}	-1.17×10^{-1}	-1.24×10^{-1}	-8.38×10^{-2}
	B_3	-1.76×10^{-3}	-1.91×10^{-3}	-1.86×10^{-3}	-1.77×10^{-3}	-2.32×10^{-3}	-2.40×10^{-3}	-1.92×10^{-3}	-2.62×10^{-3}	-7.54×10^{-4}
	B_4	5.55×10^{-6}	9.80×10^{-5}	1.05×10^{-4}	1.14×10^{-4}	1.28×10^{-4}	1.49×10^{-4}	1.25×10^{-4}	7.86×10^{-5}	1.02×10^{-4}
	B_5	5.75×10^{-1}	1.30	1.43	1.32	1.60	1.81	1.54	1.66	8.87×10^{-1}
	B_6	7.74×10^{-2}	8.00×10^{-2}	8.96×10^{-2}	7.71×10^{-2}	1.22×10^{-1}	1.06×10^{-1}	7.86×10^{-2}	1.37×10^{-1}	1.62×10^{-1}
	B_7	3.88×10^{-1}	6.00×10^{-1}	6.53×10^{-1}	4.62×10^{-1}	6.24×10^{-1}	5.74×10^{-1}	4.95×10^{-1}	6.32×10^{-1}	6.12×10^{-1}
$\frac{(EA_i)_r}{EA_i}$	B_1	4.51×10^{-1}	7.79×10^{-2}	-1.64×10^{-1}	4.14×10^{-1}	7.25×10^{-2}	-1.59×10^{-1}	4.00×10^{-1}	7.57×10^{-2}	-1.59×10^{-1}
	B_2	-5.91×10^{-2}	-4.15×10^{-2}	-6.81×10^{-2}	-3.41×10^{-2}	-1.79×10^{-2}	-4.96×10^{-2}	-2.83×10^{-2}	-1.56×10^{-2}	-5.38×10^{-2}
	B_3	1.38×10^{-4}	-2.76×10^{-4}	-1.75×10^{-3}	6.76×10^{-4}	-2.02×10^{-5}	-1.79×10^{-3}	9.26×10^{-4}	-7.20×10^{-6}	-3.19×10^{-3}
	B_4	-3.46×10^{-5}	-5.30×10^{-5}	1.60×10^{-4}	-4.79×10^{-5}	-7.07×10^{-5}	1.50×10^{-4}	-5.48×10^{-5}	-8.46×10^{-5}	2.40×10^{-4}
	B_5	1.33	2.41	4.78	1.40	2.41	4.78	1.41	2.42	5.64
	B_6	3.36×10^{-2}	5.16×10^{-2}	-5.01×10^{-2}	5.10×10^{-2}	7.11×10^{-2}	-4.03×10^{-2}	5.80×10^{-2}	7.49×10^{-2}	-9.85×10^{-2}
	B_7	4.98×10^{-1}	7.76×10^{-1}	9.21×10^{-1}	4.92×10^{-1}	7.42×10^{-1}	8.97×10^{-1}	4.94×10^{-1}	7.37×10^{-1}	9.04×10^{-1}
$\frac{(EA_{0.4})_r}{EA_{0.4}}$	B_1	4.95×10^{-1}	8.07×10^{-2}	-1.97×10^{-1}	4.42×10^{-1}	3.46×10^{-2}	-3.02×10^{-1}	4.23×10^{-1}	1.80×10^{-3}	-3.47×10^{-1}
	B_2	-7.98×10^{-2}	-7.01×10^{-2}	-1.66×10^{-1}	-3.87×10^{-2}	-5.52×10^{-2}	-1.28×10^{-1}	-3.26×10^{-2}	-5.93×10^{-2}	-1.04×10^{-1}
	B_3	4.74×10^{-5}	-1.17×10^{-3}	1.20×10^{-3}	8.94×10^{-4}	-1.66×10^{-3}	-3.48×10^{-4}	1.19×10^{-3}	-2.38×10^{-3}	2.62×10^{-4}
	B_4	-3.24×10^{-5}	3.93×10^{-5}	-6.58×10^{-5}	-7.04×10^{-5}	1.35×10^{-4}	1.55×10^{-4}	-7.71×10^{-5}	2.33×10^{-4}	1.32×10^{-4}
	B_5	1.31	3.24	1.31	1.33	4.32	3.06	1.37	5.19	2.26
	B_6	3.86×10^{-2}	1.76×10^{-2}	2.43×10^{-1}	6.98×10^{-2}	-1.77×10^{-2}	1.77×10^{-1}	7.61×10^{-2}	-6.54×10^{-2}	2.60×10^{-1}
	B_7	4.69×10^{-1}	7.98×10^{-1}	1.03	4.74×10^{-1}	7.77×10^{-1}	1.07	4.78×10^{-1}	7.91×10^{-1}	1.11
$\frac{(EA_{0.8})_r}{EA_{0.8}}$	B_1	5.44×10^{-1}	-1.01×10^{-2}	-2.63×10^{-1}	4.82×10^{-1}	-2.81×10^{-1}	-5.45×10^{-1}	4.53×10^{-1}	-3.12×10^{-1}	-5.66×10^{-1}
	B_2	-8.70×10^{-2}	-2.37×10^{-1}	-3.61×10^{-1}	-5.11×10^{-2}	-1.22×10^{-1}	-1.19×10^{-1}	-4.65×10^{-2}	-9.72×10^{-2}	-8.29×10^{-2}
	B_3	3.60×10^{-5}	9.20×10^{-5}	1.51×10^{-3}	3.15×10^{-4}	2.29×10^{-3}	3.44×10^{-3}	3.48×10^{-4}	2.34×10^{-3}	3.04×10^{-3}
	B_4	-4.74×10^{-5}	1.39×10^{-4}	8.88×10^{-5}	-7.26×10^{-5}	2.60×10^{-4}	2.96×10^{-4}	-5.30×10^{-5}	2.62×10^{-4}	3.22×10^{-4}
	B_5	1.22	1.16	-3.62×10^{-1}	1.55	-4.88×10^{-1}	-2.10	1.84	-5.61×10^{-1}	-1.37
	B_6	6.96×10^{-2}	2.09×10^{-1}	3.45×10^{-1}	1.00×10^{-1}	3.91×10^{-1}	4.48×10^{-1}	9.48×10^{-2}	3.92×10^{-1}	3.57×10^{-1}
	B_7	4.22×10^{-1}	9.14×10^{-1}	1.14	4.47×10^{-1}	1.06	1.25	4.60×10^{-1}	1.09	1.31

The equivalent residual strain can be calculated from the proposed Equation 7 with the aid of Table 6-5 that lists the values of the coefficients $(G_i)_{i=1,2,3,4,5,6,7}$.

$$\varepsilon_{eq} = G_1 + G_2 t + G_3 f'_c + G_4 f_y + G_5 D + G_6 \rho + G_7 \frac{t^2}{\sqrt{D}} \quad (7)$$

Table 6-5: Coefficient of Equation 7 for circular sections

G_i	$R_D = 0$ (Unrestrained)			$R_D = 0.5$ (Partially Restrained)			$R_D = 1$ (Fully Restrained)		
	$\lambda = 0.0$	$\lambda = 0.2$	$\lambda = 0.4$	$\lambda = 0.0$	$\lambda = 0.2$	$\lambda = 0.4$	$\lambda = 0.0$	$\lambda = 0.2$	$\lambda = 0.4$
G_1	4.737×10^{-4}	-1.801×10^{-4}	-1.001×10^{-3}	-5.995×10^{-4}	-7.763×10^{-4}	-1.284×10^{-3}	-7.533×10^{-4}	-1.043×10^{-3}	-1.312×10^{-3}
G_2	8.248×10^{-5}	-6.738×10^{-5}	-1.659×10^{-4}	-2.488×10^{-4}	-2.201×10^{-4}	-1.785×10^{-4}	-2.280×10^{-4}	-3.035×10^{-4}	-1.832×10^{-4}
G_3	4.990×10^{-6}	-8.300×10^{-7}	-4.260×10^{-6}	-2.060×10^{-6}	-3.210×10^{-6}	-5.340×10^{-6}	-2.700×10^{-6}	-2.750×10^{-6}	-6.830×10^{-6}
G_4	0.000	0.000	1.900×10^{-7}	1.000×10^{-7}	7.000×10^{-8}	3.100×10^{-7}	9.000×10^{-8}	-1.000×10^{-8}	2.700×10^{-7}
G_5	-9.168×10^{-4}	1.971×10^{-4}	1.356×10^{-3}	6.592×10^{-4}	9.238×10^{-4}	1.538×10^{-3}	8.597×10^{-4}	1.320×10^{-3}	1.587×10^{-3}
G_6	-2.942×10^{-3}	2.077×10^{-3}	6.942×10^{-3}	6.582×10^{-3}	7.195×10^{-3}	9.805×10^{-3}	6.999×10^{-3}	9.267×10^{-3}	1.085×10^{-2}
G_7	5.670×10^{-6}	9.000×10^{-7}	-7.870×10^{-6}	5.220×10^{-6}	1.520×10^{-6}	-5.670×10^{-6}	2.820×10^{-6}	7.840×10^{-6}	-5.270×10^{-6}

The line of equality plot reveals that the proposed expressions provide an excellent prediction of the capacity and stiffness compared to the results obtained from the analytical model as illustrated in Figs. 6-15(b) and 6-16(b), respectively. An excellent agreement is also shown between the equivalent residual strain obtained analytically and calculated from Equation 7 as illustrated in Fig. 6-17. The presence of outliers is almost negligible which enhances the confidence of using the proposed expressions. The simplicity and robustness of the proposed expressions is an advantage for increasing their applicability during the design phase.

6.10 Application of the Proposed Procedure

The proposed method is suitable to be implemented by engineers during the preliminary design phase for estimating the residual performance of RC frames exposed to extreme standard fire conditions. The current study represents a step toward developing an integrated approach for considering all the components of the RC frames subjected to different loading conditions and exposed to various fire curves. This research assumes that the global behavior of the frame system is merely affected by the deterioration taking place in columns subjected to pure axial loads. This implies that beams and eccentrically loaded columns are either perfectly insulated against fire or are not exposed to critical temperatures capable of affecting their residual performance. The proposed procedure considers the interaction between the entire frame system and the fire-damaged columns in terms of connections' stiffness and load path. The fire-exposed columns are considered

in the analysis as isolated members using equivalent spring model whose stiffness is determined from the stiffness of the entire frame.

The steps required to adopt the proposed procedure are discussed in view of the 20 stories frame structure shown in Fig. 6-18. The frame is composed of 8 m long 300×450 mm RC beams made of normal weight concrete with f'_c of 35 MPa and reinforced with grade 400 MPa steel bars. The 300×400 mm columns are 3.6 m long with reinforcement ratio of 0.04 and are constructed of the same materials as the beams. The moment of inertia of both member types is determined assuming cracked cross-sections (i.e. $I_{beam} = 0.35I_g$ and $I_{column} = 0.7I_g$) where I_g is the gross moment of inertia of the considered member. The frame is loaded by subjecting the beams to a uniformly distributed load of 33 kN/m along the entire span. ASTM E119 standard fire is assumed to spread in the first floor of the building for 1.5 hours followed by a gradual cooling phase according to ISO 834 specifications. Beams and corner columns are assumed not to be significantly influenced by fire, while the interior columns (i.e. columns IC1 and IC2) are exposed to fire from all sides. To determine the residual performance of the frame, the proposed procedure is discussed with reference to column IC1 in Fig. 6-18. The structural analysis is performed using the commercially available ETABS [32] finite element software.

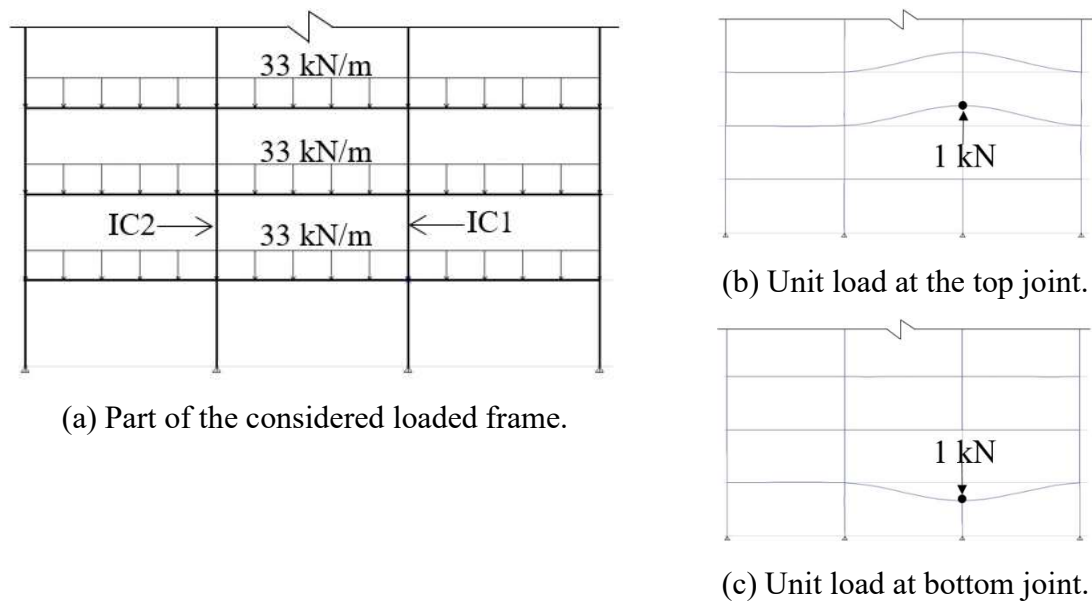


Figure 6-18: Description of the proposed analysis procedure

- 1) Determine the equivalent axial stiffness (k_δ) of the spring shown in Fig. 6-3(b) that represents the vertical stiffness of the structural system at that point. This is performed by replacing the examined column with a unit load acting at each joint individually as shown in Figs. 6-18(b) and 6-18(c). The structural analysis is then performed on the frame to get the corresponding displacement of the considered joint. k_δ for each joint is calculated as the ratio between the unit load to the induced displacement. The total equivalent axial stiffness (k_δ) is then determined by considering the two joints as springs in series according to Equation 8.

$$k_\delta = \frac{(k_\delta)_1(k_\delta)_2}{(k_\delta)_1 + (k_\delta)_2} \quad (8)$$

In this example, $(k_\delta)_1$ is determined as 10,000 kN/m, while $(k_\delta)_2$ is found to be 829,187 kN/m. Thus, k_δ for the isolated column model is 9,881 kN/m.

- 2) Calculate the axial restraint ratio (RD) from k_δ calculated in step 1 and the axial stiffness of column per unit length (EA/L). In this example, RD is found to be 0.012.
- 3) Determine the axial force acting on the considered column by performing structural analysis on the entire frame while the actual loads are added. Column IC1 in this example is subjected to an axial load of 2,383 kN.
- 4) Calculate the applied load level (λ) as the ratio between the applied load and the column axial capacity. In this example, λ is determined as 0.4.
- 5) Determine the residual axial capacity (P_r) and axial stiffness ($(EA)_r$) of the considered column in view of the proposed expressions provided in Equation 4 along with Table 6-2 for rectangular sections. In this case, ω corresponding to the capacity and axial stiffness is 0.531 and 0.311, respectively. For columns IC1, this would be translated into a residual capacity and an axial stiffness of 3,161 kN and 995,923,429 kN, respectively.
- 6) Repeat the same procedure for all other axially loaded columns. In this example, the only other affected column is IC2.
- 7) Adjust the axial capacity and stiffness of the considered columns in the structural program and repeat the analysis. Repeat steps 1 through 6 until the obtained variation in both capacity and stiffness for each column is within an acceptable tolerance.

- 8) Once the residual behavior of all fire-damaged columns is adjusted in the program, the engineer can check the stresses, straining actions and deformation behavior of the frame in both the local and global levels.

6.11 Conclusions

In this chapter, both thermal and sectional analyses are performed aiming at determining the residual behavior of fire-damaged rectangular and circular columns in typical RC frames. The temperature-load history experienced by the exposed members is considered in detail in the analytical study. The model is validated against relevant experimental studies and a parametric study is then carried out to determine the influence of various loading conditions and fire scenarios on the residual properties of the members. The study has led to developing an objective-based method that provides engineers with simplified tools to predict the residual behavior of axially loaded RC columns during the preliminary design phase considering an extreme standard fire scenario. Main findings coming out of this study are as follow:

- 1) Fire duration and member width have the most significant influence on the residual stiffness and capacity of the fire-damaged members.
- 2) The initial load level has minor impact on the residual flexural strength ratio of fire-damaged members.
- 3) Subjecting a member to a moderate initial load before and during heating, both transient and creep strains are developed and counteract thermal expansion tendency of the member.
- 4) Increasing the concrete compressive strength and steel grade is found to have an insignificant impact on the reduction in the residual flexural capacity of the fire-damaged member for all load levels in the examined range.

6.12 References

- [1] Guo, Z. and Shi, X. “Experimental and Calculation of Reinforced Concrete at Elevated Temperatures,” Butterworth-Heinemann, 2011, Oxford, UK.
- [2] CSA. “Design of concrete structures (CAN/CSA A23.3-14),” Cement Association of Canada, 2014, Ottawa, ON.
- [3] ACI Committee 318. “Building code requirements for structural concrete and commentary (ACI 318-14),” American Concrete Institute, 2014, Farmington Hills, MI.
- [4] Eurocode2. “Design of concrete structures- part 1.1: general rules and rules for buildings,” European Committee for Standardization (CEN), 2004, Brussels, Belgium.
- [5] Youssef, M. and Moftah, M. “General Stress-Strain Relationship for Concrete at Elevated Temperatures,” Engineering Structures, Elsevier, 2007, Vol. 29, No. 10, pp. 2618-2634.
- [6] El-Fitiany, S. and Youssef, M. “Assessing the Flexural and Axial Behavior of Reinforced Concrete Members at Elevated Temperatures Using Sectional Analysis,” Fire Safety Journal, 2009, Vol. 44, No. 5, pp. 691-703.
- [7] Schneider, U. “Properties of Materials at High Temperatures: Concrete,” RILEM 1985, Kassel, Germany.
- [8] Anderberg, Y. “Stress and Deformation Characteristics of Concrete at High Temperatures,” Lund Institute of Technology, 1976, Stockholm, Sweden.

- [9] ACI/TMS Committee 216. "Code requirements for determining fire resistance of concrete and masonry construction assemblies (ACI 216.1-07/TMS-216-07)." American Concrete Institute, 2007, Farmington Hills, MI, 28 pp.
- [10] National Research Council Canada (NRCC). "National Building Code of Canada," Associate Committee on the National Building Code, 2015, Ottawa, ON, 708 pp.
- [11] AS-3600. "Concrete Structures," Committee BD-002, 2001, Australia.
- [12] Eurocode 2. "Design of Concrete Structures - Part 1-2: General Rules - Structural Fire Design," European Committee for Standardization (CEN), 2004, Brussels, Belgium.
- [13] Concrete Society. "Assessment, Design and Repair of Fire-Damaged Concrete Structures," The Concrete Society, 2008, Camberley, UK.
- [14] ACI Committee 201. "Guide for Conducting a Visual Inspection of Concrete in Service," American Concrete Institute, 2008, Farmington Hills, MI, USA.
- [15] Hertz, K.D. "Concrete Strength for Fire Safety Design," Magazine of Concrete Research, 2005, Vol. 57, No. 8, pp. 445-453.
- [16] Lie, T.T. "Structural Fire Protection," ASCE Manuals and Reports on Engineering Practice, 1992, Vol. 78, New York, NY.
- [17] ASTM. "Standard Methods of Fire Test of Building Construction and Materials," Test Method E119-01, American Society for Testing and Materials, 2001, West Conshohocken, PA, USA.

- [18] ISO 834. "Fire Resistance Tests, Elements of Building Construction," International Organization for Standardization, 2014, London, UK.
- [19] Tsai, W.T. "Uniaxial Compressional Stress-Strain Relation of Concrete," *Journal of Structural Engineering*, ASCE, 1988, Vol. 114, No. 9, pp. 2133-2136.
- [20] Terro, M.J, "Numerical modeling of the behavior of concrete structures in fire," *ACI Structural Journal*, 1998, Vol. 95, No. 2, pp. 183-193.
- [21] Chang, Y.F., Chen, Y.H., Sheu, M.S. and Yao, G.C. "Residual Stress-Strain Relationship for Concrete after Exposure to High Temperatures," *Cement and Concrete Research*, Elsevier, 2006, Vol. 36, No. 10, pp. 1999-2005.
- [22] Karthik, M. and Mander, J. "Stress-block parameters for unconfined and confined concrete based on a unified stress-strain model," *Journal of Structural Engineering*, ASCE, 2011, Vol. 137, No. 2, pp. 270-273.
- [23] Lie, T.T. "Structural Steel and Fire: More Realistic Analysis," National Research Council, 1976, Ottawa, Canada.
- [24] Alhadid, M. and Youssef, M.A. "Simplified Method to Calculate the Flexural Capacity of Fire-Damaged Reinforced Concrete Beams," *Engineering Structures*, Elsevier, (Under Revision).
- [25] Chen, Y.H., Chang, Y.F., Yao, G.C., Sheu, M.S. "Experimental Research on Post-Fire Behavior of Reinforced Concrete Columns," *Fire Safety Journal*, 2009, Vol. 44, No. 5, pp. 741-748.

- [26] Jau, W.C. and Huang, K.L. "A study of reinforced concrete corner columns after fire," *Cement and Concrete Composites*, Elsevier, 2008, Vol. 30, No. 7, pp. 622-638.
- [27] Yaqub, M. and Bailey, C.G. "Repair of Fire Damaged Circular Reinforced Concrete Columns with FRP Composites," *Construction and Building Materials*, 2011, Vol. 25, No. 1, pp. 359-370.
- [28] Elsanadedy, H., Almusallam, T., Al-Salloum, Y. and Iqbal, R. "Effect of High Temperature on Structural Response of Reinforced Concrete Circular Columns Strengthened with Fiber Reinforced Polymer Composites," *Journal of Composite Materials*, 2016, pp. 1-23.
- [29] Neves, I.C., Rodrigues, J.P.C. and Loureiro, A.D.P. "Mechanical properties of reinforcing and prestressing steels after heating," *Journal of Materials in Civil Engineering*, ASCE, 1996, Vol. 8, No. 4, pp. 189-194.
- [30] Edwards, W.T. and Gamble, W.L. "Strength of Grade 60 Reinforcing Bars After Exposure to Fire Temperatures," *Concrete International*, 1986, Vol. 8, No. 10, pp. 17-19.
- [31] Qiang, X., Bijlaard, F.S.K. and Kolstein, H. "Post-Fire Mechanical Properties of High Strength Structural Steels S460 and S690," *Engineering Structures*, 2012, Vol. 35, pp. 1-10.
- [32] Computers and Structures, Inc. ETABS 15.0.0, 2015, Berkeley, CA.

Chapter 7

7 RESIDUAL BEHAVIOR OF REINFORCED CONCRETE MEMBERS EXPOSED TO FIRE FROM 3 SIDES

The production of concrete as a superior building material led to a consequent civilian renaissance in construction. Unfortunately, despite the enormous advantages of Reinforced Concrete (RC) structures, they deteriorate and lose part of their strength when exposed to fire. The mechanical properties of concrete and reinforcing steel pass through several significant changes during the heating and cooling stages. The post-fire deterioration that occurs in RC structures requires detailed examination to assess their ability to maintain their structural functionality in both the local and global levels. Fortunately, despite the large number of fire incidents involving RC buildings, only few of them experienced partial or full collapse during or after the exposure. Examples of such buildings that experienced the most severe damage are the Windsor tower in Madrid [1], the Jackson Street Apartments in Canada, the Apartment block in Russia [2], the Sampoong Department store in South Korea [3], the Kader toy factory in Thailand [4] and the Skyline plaza in USA [5] among others.

In the current design practice, a preliminary assessment of the damaged members is performed immediately after fire exposure to predict its severity and extent. Visual inspection and non-destructive examination techniques are carried out to identify the maximum temperature reached, fire propagation route, residual strength of concrete, cracking schemes, color changes and smoke characteristics. After that, a decision is made to either repair or demolish the structure depending on the extent of damage and the affordability of the required work. The current design codes are prescriptive and do not explicitly consider temperature-load history and restraint conditions during fire incident. They usually tend to provide fire-resistance ratings of various RC members depending on their cover thickness and cross-sectional dimensions. However, to assess the structural behavior of fire-exposed RC frames, the changes that occur during and after fire should be considered.

The current study extends the analytical procedure discussed in Chapters 5 and 6 to account for the residual capacity, stiffness and deformation behavior of beams and columns exposed to fire from 3 sides. Temperature and load history acting on various RC members in typical RC structures is taken into account to assess their residual structural behavior. The various strain components developed during and after fire are calculated and their influence on changing the residual performance of the damaged members under various restraining conditions is evaluated. The impact of varying the geometrical and mechanical properties of the exposed members as well as the influence of fire duration on their residual structural integrity are examined. The proposed analytical model is validated against relevant experimental studies and found to be with very good agreement. An extensive parametric investigation is then carried out to propose a robust yet simple procedure for researchers and engineers to predict the residual performance of fire-damaged members during the preliminary design phase. The outcome of the current study is an important milestone towards incorporating the objective-based approach into standards and regulations.

7.1 Analysis Stages and Assumptions

During a heating-cooling cycle, the fire-exposed members in a typical RC frame System are subjected to three main loading stages as summarized in the flow chart in Fig. 7-1. Initially, the member is deformed under the influence of the applied load at room temperature. The stiffness and capacity of the intact element are evaluated in this stage to compare them with their residual counterparts at the end of the analysis. The second phase is performed during fire aiming at determining the maximum temperature distribution as well as the residual thermal and transient strains distributions along the cross-section which will be considered as inputs in the post-fire analysis stage. The change in temperature at each point within the member depends on the thermal and physical properties of its composing materials. The interaction between temperature and stress level is taken into account as was discussed in details in Chapter 6. After that, the temperature decreases gradually causing the heat flow to propagate not only to the atmosphere, but also to the inner colder portions of the member. This means that the

maximum temperature at the inner points within the cross-section are attained during the cooling phase. The process continues until thermal equilibrium is achieved and heat is transferred to the colder surrounding environment. Finally, the temperature of the member is completely brought back to the ambient conditions and its residual mechanical properties are determined based on the maximum temperature reached. At this stage of the analysis, if the member survived throughout the first two stages, then the applied load is increased until failure occurs.

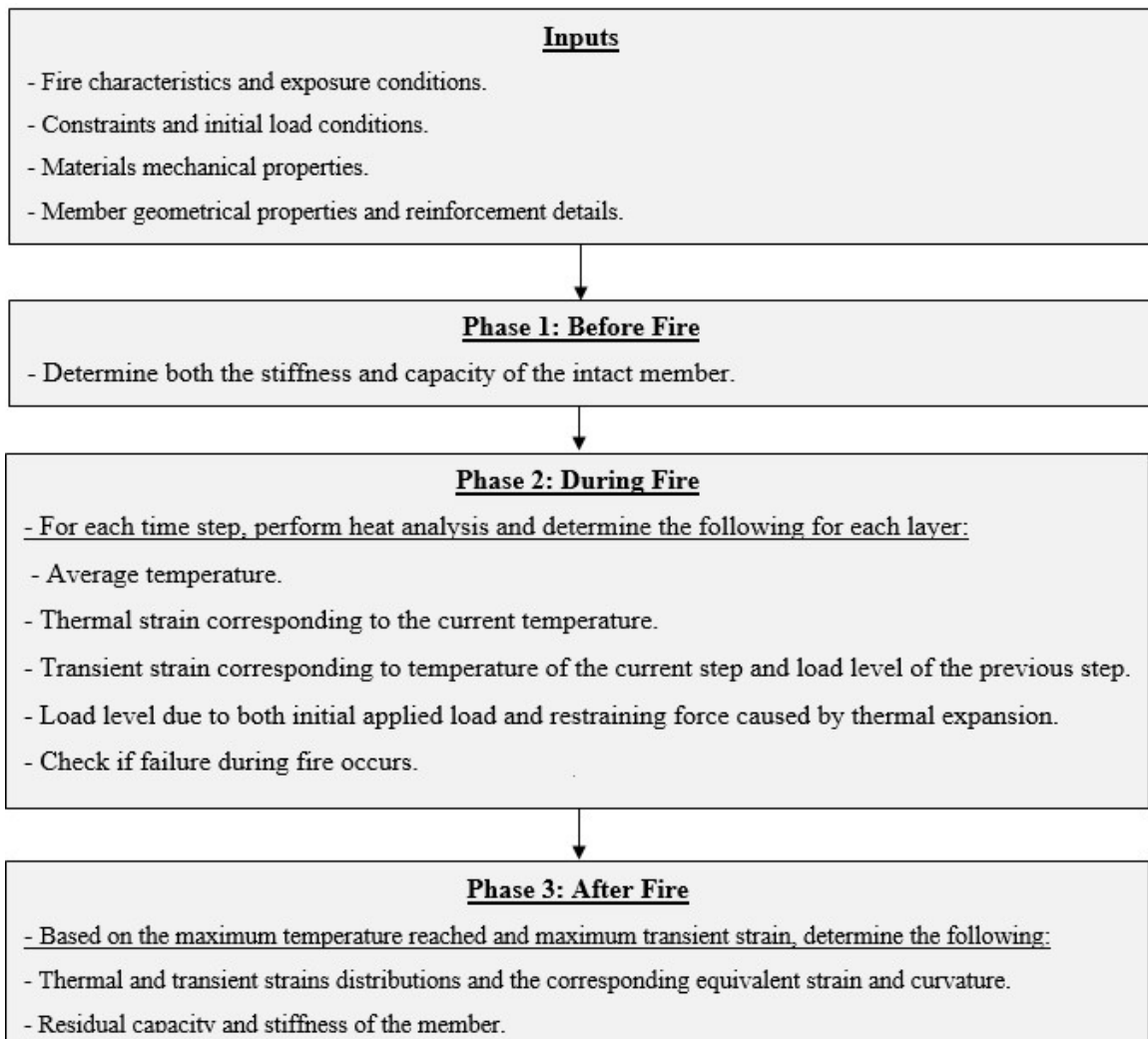


Figure 7-1: Flow chart summarizing the analysis procedure

Material models, constitutive relationships and strain components are the same as those detailed in Chapter 6. The assumptions considered in the analytical model are as follow:

- 1) Cross sections remain plane before and after fire exposure. The validity of this assumption was validated by El-Fitiany and Youssef [6] for temperatures up to 1200°C.
- 2) Perfect bond exists between the steel reinforcement and the surrounding concrete material.
- 3) Spalling of concrete is not considered. This implies that the current work is limited to normal weight concrete.
- 4) Two dimensional heat transfer analysis is considered implying that heat flow is uniform along the member length.
- 5) Influence of concrete tensile cracks on heat flow is neglected in the heat transfer analysis.
- 6) Geometrical nonlinearity is not considered in the analysis.
- 7) Failure of the compression members is not governed by buckling.

7.2 Thermal Analysis

Thermal analysis is performed considering fire exposure from 3 sides that result in the development of both residual thermal strains and curvatures. Heat transfer procedure is similar to the one described in Chapter 6 which is carried out by solving the heat balance formula (Equation 1) in terms of the material thermal conductivity (κ), specific heat (c) and density (ρ). Finite difference method is utilized to solve the differential equation as described by Lie [7].

$$\frac{\partial T}{\partial t} = \frac{\kappa}{c\rho} \left(\frac{\partial^2 T}{\partial x^2} + \frac{\partial^2 T}{\partial y^2} \right) \quad (1)$$

The structural members are exposed to ASTM E119 [8] standard fire during the heating phase and ISO 834 [9] during the cooling phase as described in Equations 2 and 3, respectively.

$$T - T_o = 750 [1 - e^{(-3.79553 \sqrt{t})}] + 170.41\sqrt{t} \quad (2)$$

$$\Delta T = \begin{cases} -10.417 & , t < 0.5 \text{ hr} \\ -4.167(3 - t) & , 0.5 \text{ hr} \leq t < 2.0 \text{ hrs} \\ -4.167 & , t \geq 2.0 \text{ min} \end{cases} \quad (3)$$

where T is the fire temperature in ($^{\circ}\text{C}$), T_o is the initial temperature in ($^{\circ}\text{C}$), ΔT is the change in temperature in ($^{\circ}\text{C}$) and t is the time in hours. Temperature distribution along the cross-sections is calculated twice based on the maximum temperature reached and the residual strength as detailed in Chapter 6.

7.3 Influence of Restraints

The total strain in a typical structural member subjected to elevated temperatures encompasses a mechanical component due to the applied loads and a thermal component due to change in temperature. Temperature distribution within the structural member plays a major role in controlling the member's tendency to expand and/or rotate. In addition, the degrees of freedom at the supports of the structural member dictates its state of stress and deformation behavior based on the kinematic and compatibility conditions. If the restraints are not sufficient to counteract thermal effects, then the structural member experiences change in length (i.e. expansion or contraction) and/or bowing (i.e. deflection) based on the strain gradient generated due to fire. Some hyperstatic (or secondary) stresses are developed merely due to the nonlinear temperature distribution within the section. In typical cast-in-place RC structures, the degrees of freedom in structural members are either partially or fully restrained against free translational and/or rotational movements. Therefore, secondary stresses are developed in a fire-exposed member as a result of the restraints provided by the supports. Translational restraints induce opposing mechanical strains to the intended thermal strains resulting in large compressive stresses. Rotational restraints counteract the rotational tendency of the heated member through large hogging bending moment along the length of the member. Therefore, substantial secondary actions are generated not only due to the non-uniform temperature distribution along the section, but also due to the squashing action caused by

the supports. This implies that restrained RC beams may be subjected to axial force during and after fire. The response of a structural member in a typical RC frame, shown in Fig. 7-2, experiencing either uniform thermal expansion or thermal bowing is discussed.

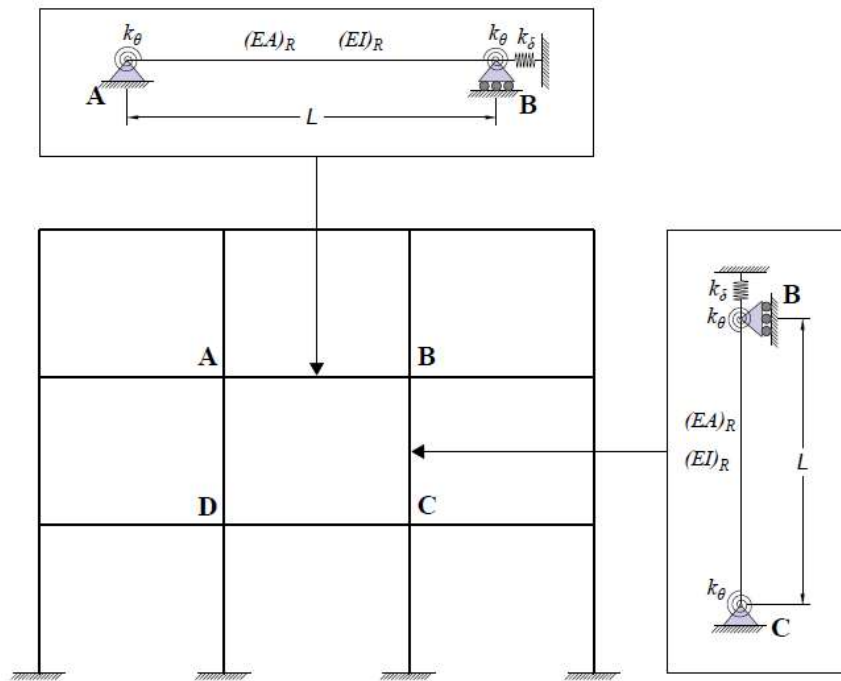


Figure 7-2: A typical RC frame structure illustrating the isolated models

7.3.1 Axial Restraints and Thermal Expansion

If the structural member is fully restrained against deformation, then internal stresses are generated based on the thermal strain that would occur if it was free to undergo thermal expansion. The total strain becomes zero implying that all the thermal strain is converted into a mechanical strain that produces internal stresses in the member. The corresponding restraining axial force depends on the axial rigidity (EA) of the structural member at the given uniform temperature value. If the fire persists and the member kept expanding, then the structural member will either reach the concrete crushing strain or the steel yielding strain. In the first case, the structural member will fail and will no longer be structurally useful. In the other case, the additional strain is stored as plastic strain without increase in stress within the steel bars [10]. RC members in typical frame structures are partially

restrained against translational movements. Therefore, their behavior is somewhere in between the lower limit of free expansion and the upper limit of fully restrained members. The magnitude of the restraining action provided by the supports depends on the stiffness exerted by the frame on the member's ends. This axial translational restraint can be modeled as a spring with a stiffness of (k_δ) as illustrated in Fig. 7-3.

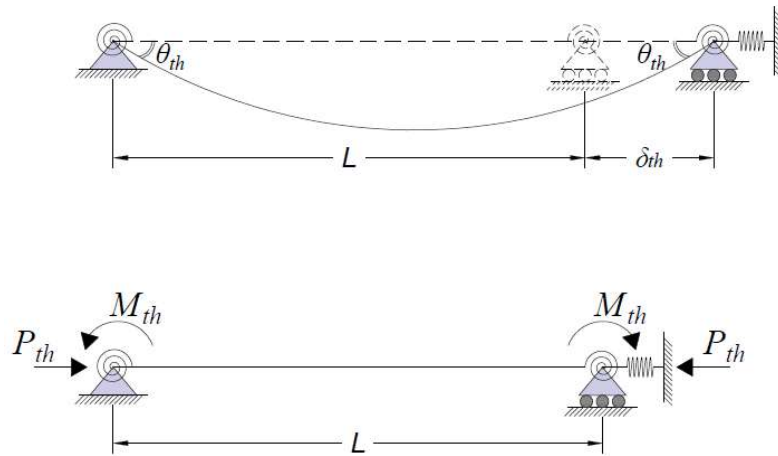


Figure 7-3: Restrained beam model after exposure to elevated temperatures

The resulting restraining axial force (P_{th}) caused by thermal expansion is derived based on the virtual work method and given in Equation 4.

$$P_{th} = \frac{(EA)_T(\varepsilon_{th})_T}{1 + \left[\frac{(EA)_T}{k_\delta L} \right]} \quad (4)$$

Where $(EA)_T$ is the axial stiffness of the structural member at temperature (T); $(\varepsilon_{th})_T$ is the corresponding thermal strain at temperature (T); and L is the length of the structural member. Setting k_δ to an infinitesimally small value results in negligible restraining force implying the case of free expansion. On the other hand, if k_δ has an extremely large magnitude, all thermal strain is counteracted by the generated axial force simulating the case of fully restrained member. For any other values of k_δ , part of the thermal strain will

be cancelled out by the generated thermal force whereas the remaining part will cause thermal expansion in the member.

7.3.2 Rotational Restraints and Thermal Bowing

In fully restrained structural members against rotation, additional constant bending moment is developed along the length to counteract the thermal curvature that would have been produced if the member is free to rotate. Therefore, the original shape of the member is maintained due to the constant bending moment which relies on the flexural stiffness (EI) of the heated member. The heated member fails if the generated bending moment developed exceeds its flexural capacity. At early fire stages, the flexural capacity is large and close to that at ambient conditions since the deterioration in mechanical properties of both concrete and steel are minimal. However, the produced thermal gradient is very large resulting in large bending moment to counteract the anticipated curvature. As the fire continues, the flexural capacity decreases due to the greater loss in strength and stiffness of both materials. But, temperature distribution within the section becomes more uniform and the resulting bending moment decreases as well. This implies that flexural failure of the member may not occur even for longer fire durations. The behavior of RC members in typical frames is neither free to rotate nor fully restrained, but rather somewhere in between these two extremes. The extent of the rotational restraint relies on the capability of the adjacent frame elements to counteract the anticipated thermal rotations at the member's ends. Using the virtual work method, the generated restraining bending moment (M_{th}) is given in Equation 5 as a function of the equivalent rotational spring stiffness (k_θ); flexural stiffness of the structural member at a given temperature $(EI)_T$; thermal curvature at a given temperature $(\phi_{th})_T$; and the length of the heated member (L).

$$M_{th} = \frac{(EI)_T(\phi_{th})_T}{1 + \left[\frac{2(EI)_T}{k_\theta L} \right]} \quad (5)$$

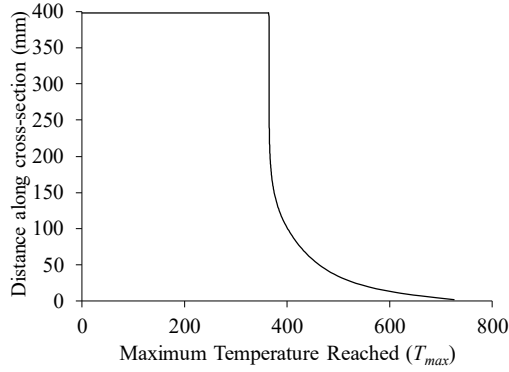
As shown in Equation 5, decreasing k_θ to a very small value significantly reduces the thermal bending moment causing it to approach the case of free rotation. However, increasing it to very large values causes a rise in the restraining moment to cancel out all

the anticipated thermal curvature in a similar manner to a fully constrained member. For intermediate values of k_θ , bending moment is generated to prevent part of the curvature from forming while allowing the other part to induce lateral deformation along the member length.

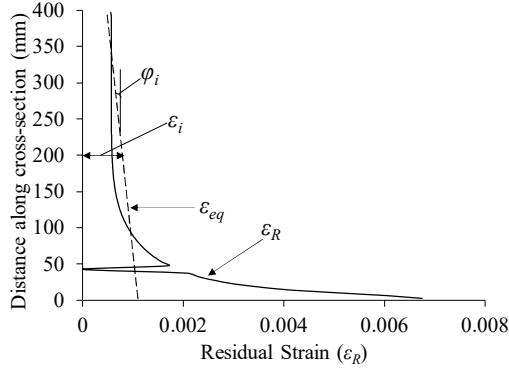
7.4 Equivalent Residual Strain of RC Members Heated from 3 Sides

The distribution of various strain components along the cross-section of a RC beam that has a width of 200 mm, height of 400 mm, longitudinal reinforcement ratio of 0.005 after exposure to heat for 0.5 hr is shown in Fig. 7-4. At ambient conditions, the compressive strength of concrete is 25 MPa and the yield strength of the embedded steel bars is 300 MPa. The maximum temperature reached during the entire heating-cooling cycle and the corresponding transient strain for different initial loading conditions is illustrated in Figs. 7-4(a) and 7-4(b), respectively.

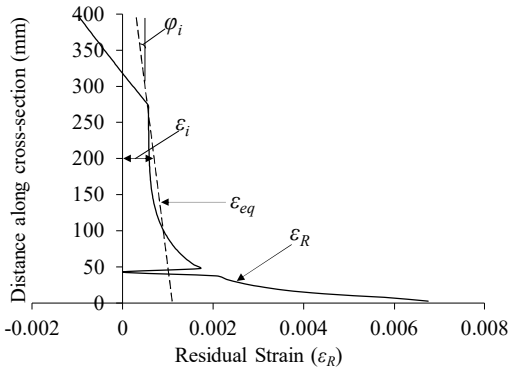
The initial load level (λ) represents the ratio between the applied moment and the flexural capacity of the beam at ambient temperature. The location of the induced compressive stresses is determined from finding out the location of the neutral axis corresponding to the applied moment. Transient strain is then calculated at each concrete layer within the compression zone in terms of the layer temperature and the stress level (f_c/f_c') acting on it. Fig. 7-4(b) shows that for the same flexural load level in beams, transient strain developed in hogging moment sections are significantly larger than their counterparts in the sagging moment sections. This is justified by the fact that transient strain, which develops in the compression zone, increases by increasing the concrete temperature.



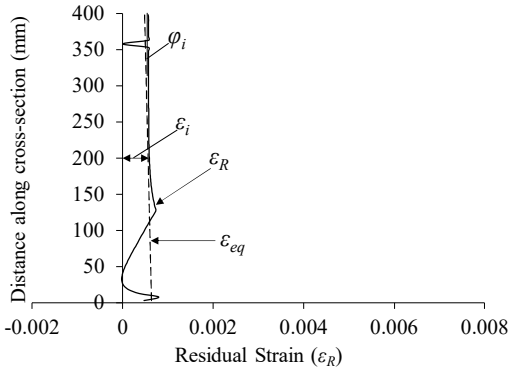
(a) Maximum temperature reached



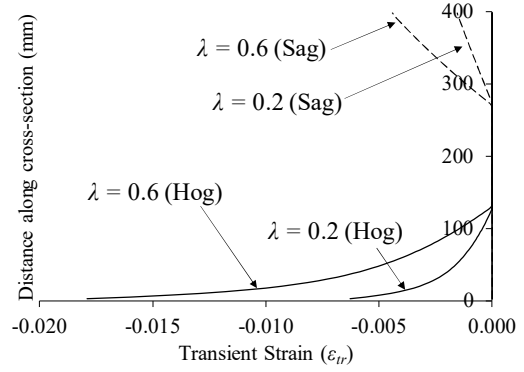
(c) ϵ_R and ϵ_{eq} (Sagging, $\lambda = 0.0$)



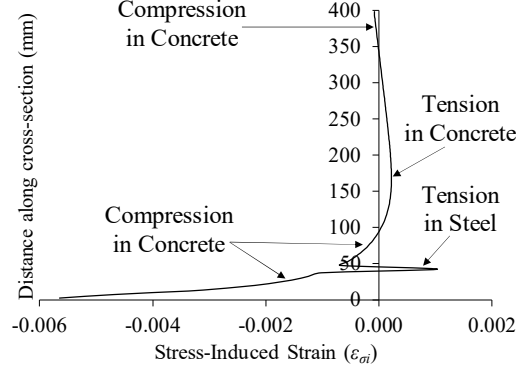
(e) ϵ_R and ϵ_{eq} (Sagging, $\lambda = 0.2$)



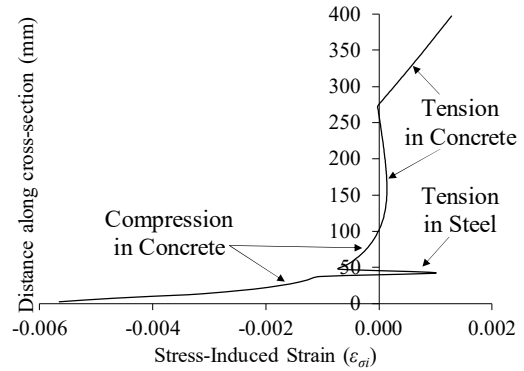
(g) ϵ_R and ϵ_{eq} (Hogging, $\lambda = 0.2$)



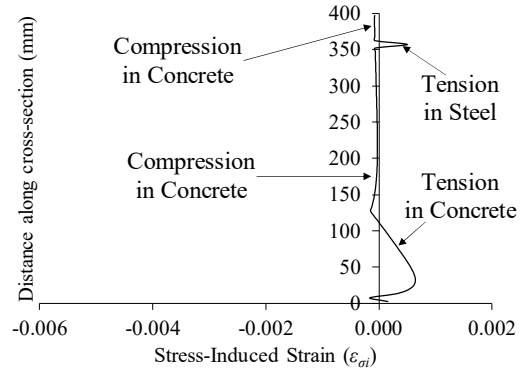
(b) ϵ_{tr} corresponding to $\lambda = 0.2$ and 0.6



(d) $\epsilon_{\sigma i}$ (Sagging, $\lambda = 0.0$)



(f) $\epsilon_{\sigma i}$ (Sagging, $\lambda = 0.2$)



(h) $\epsilon_{\sigma i}$ (Hogging, $\lambda = 0.2$)

Figure 7-4: Strain distributions across a typical beam heated from 3 sides

The residual free thermal strain (ε_{th}), which develops in unstressed concrete after fire, is negligible if the maximum temperature does not exceed 300°C but it may reach as high as 40% of the ultimate thermal strain at a temperature of about 700°C due to the irreversible produced internal cracks. The nonlinear thermal strain distribution is attributed to the extremely low thermal conductivity of concrete causing temperature variation to become nonlinear. If the beam is not initially loaded, transient strain does not develop and the residual strain (ε_R) becomes identical to the thermal strain (ε_{th}) component as shown in Fig. 7-4(c). Since plane sections remain plane after exposure to fire [6], an equivalent linear residual thermal strain (ε_{eq}) distribution is developed in the fire-damaged beams instead of the non-uniform ε_R distribution. The ε_{eq} strain profile is fully described using two parameters which are the equivalent residual thermal strain at centroid (ε_i), and the equivalent residual thermal curvature (φ_i). The difference between the residual strain (ε_R) and the equivalent strain (ε_{eq}) represents the stress-induced strain ($\varepsilon_{\sigma i}$) as shown in Fig. 7-4(d). The latter strain component is obtained by performing iterations to obtain the values of ε_i and φ_i that satisfy equilibrium condition.

Figs. 7-4(e) and 7-4(f) illustrate the ε_R distribution along the cross-section of beams subjected to ($\lambda = 0.2$) initial flexural load in both sagging and hogging moment sections, respectively. Since the beams are loaded during fire, transient strain is developed with negative sign in the locations of compressive stresses. For sagging moment sections, this strain has a minor influence of changing the force resultant acting obtained from $\varepsilon_{\sigma i}$ shown in Fig. 7-4(f). However, in hogging moment sections, $\varepsilon_{\sigma i}$ significantly alleviates the expansion near the beam soffit where thermal expansion is maximum. The higher the load level and temperature during the heating phase, the higher the tendency for the member to experience contraction rather than expansion after it is cooled down [11]. The same observation was proven experimentally as reported by Anderberg [12] and Guo and Shi [11] among others. The same procedure was performed by El-Fitiany and Youssef [6] for RC sections during fire exposure.

7.5 Strength Analysis

Sectional analysis method for evaluating the residual moment-curvature ($M-\phi$) and load-axial strain ($P-\varepsilon$) relationship of RC elements subjected to a complete heating-cooling cycle is carried out based on the maximum temperature distribution along the cross-section. The kinematic and compatibility conditions are considered in view of the corresponding residual mechanical properties and stress-strain relationships of both concrete and steel. The residual stress-induced thermal strain ($\varepsilon_{\sigma i}$) is taken into account as initial strains when performing the sectional analysis procedure. If the member is not restrained against thermal expansion, then the equivalent residual thermal strain results in initial deformations without affecting the stresses within the member. However, if the member is fully restrained, then the residual strains are considered to produce initial stresses before applying the external load. For other constraint conditions, Equations 4 and 5 are used to determine the amount of initial stresses and the corresponding initial deformations.

The failure criterion of the RC element is defined by crushing of concrete once the strain in any of the sectional layers reaches the residual ultimate strain (ε_{cuR}). The ultimate compressive strain (ε_{cu}) of concrete at failure is taken as 0.0035 at ambient conditions [13]. Regarding the post-cooling stage, Alhadid and Youssef [14] proposed and validated an expression of the residual ultimate strain of concrete as the difference between the residual strain at peak stress (ε_{oR}) and its counterpart at ambient conditions (ε_o) as given in Equations 6 and 7.

$$\varepsilon_{cuR} = \varepsilon_{cu} + (\varepsilon_{oR} - \varepsilon_o) \quad (6)$$

$$\frac{\varepsilon_{oR}}{\varepsilon_o} = \begin{cases} 1.0 & , 20^\circ\text{C} < T \leq 200^\circ\text{C} \\ \left(\frac{-f'_c}{10} + 7.7 \right) \left[\frac{e^{(-5.8+0.01)}}{1 + e^{(-5.8+0.01T)}} - 0.0219 \right] + 1.0 & , 200^\circ\text{C} < T \leq 800^\circ\text{C} \end{cases} \quad (7)$$

7.6 Validation

The capability of the proposed model to predict the structural performance of fire-exposed RC members was previously validated in Chapters 5 and 6 in view of the experimental results obtained by Kodur *et al.* [15], Haddad *et al.* [16], Chen *et al.* [17], Jau and Huang [18], Yaqub and Bailey [19] and Elsanadedy *et al.* [20].

In this chapter, the experimental work performed by Guo and Shi [11] is also considered to further validate the proposed model. The experimental program encompassed testing two rectangular RC beams having cross-sectional dimensions of 100×200 mm and an overall length of 2.4 m. The concrete compressive strength at room temperature was 33 MPa and the steel yield strength was 234 MPa. The beams were reinforced with $2\Phi 12$ mm steel bars at the tension and compression sides. In addition to the two sides of the beams, heating of beam (LT) was performed from the tension side and heating of beam (LC) was carried out from the compression side. Both beams were heated to a maximum temperature of 800°C and kept for 10 minutes before cooling down naturally to room temperature. After 20 hours, the beams were subjected to positive and negative bending moments until failure occurs. Fig. 7-5 compares the $M-\phi$ diagrams of beams LC and LT obtained experimentally with the ones determined using the proposed model. A very good agreement between both curves can be shown with a percent difference of 4.3% and 7.4% in the ultimate capacity of beams LT and LC, respectively; and a percent difference of 3.8% and 6.1% in the stiffness for the same consecutive beams, respectively. The residual initial curvatures caused by the free thermal expansion obtained from the proposed model are slightly lower than those obtained experimentally. This variation can be attributed to the sensitivity of the adopted thermal expansion model to the experimental conditions and concrete mix that it was derived from. Also, the cooling phase adopted in the model follows the ISO 834 provisions which may be different from the actual natural cooling conditions followed in the lab. In addition, the loading rate was not mentioned and it may have some influence on the obtained $M-\phi$ diagrams if it was performed in a relatively quick rate. Overall, the agreement between the experimental and analytical results is good.

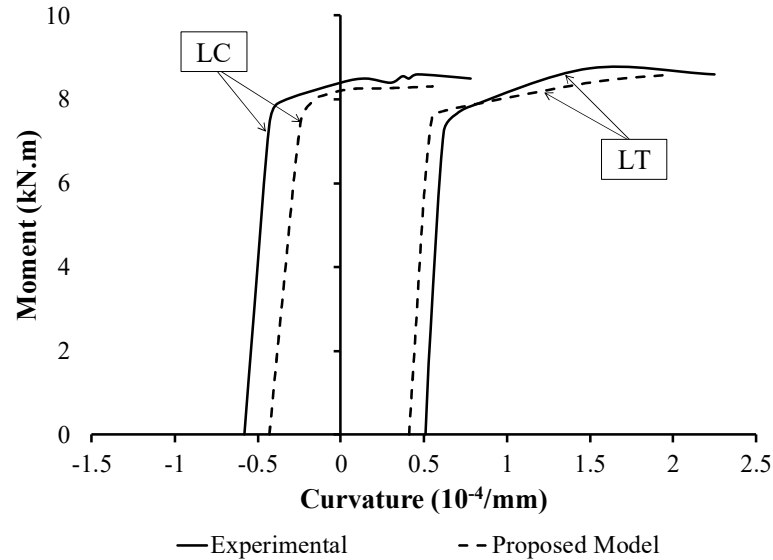


Figure 7-5: Validation of the proposed model in view the $M-\phi$ diagram obtained by Guo and Shi (2011).

7.7 Parametric Study

The influence of various factors on the post-fire behavior of RC members are studied in view of the proposed and validated analytical model. The main parameters are the concrete compressive strength (f'_c), steel yield strength (f_y), member height (h_c), member width (b_c), steel reinforcement ratio (ρ), fire duration (t_f), axial restraint stiffness (k_δ), flexural restraint stiffness (k_θ), initial load level (ζ) and heat exposure direction. The values of the chosen parameters are set based on the practical considerations in the design of typical RC buildings and duration of typical fire incidents. The mechanical properties for concrete are defined in terms of concrete compressive strength as 25 MPa and 35 MPa; and defined for steel in terms of yield strength as 350 MPa and 450 MPa. The chosen widths and heights of the analyzed members range from 200 mm to 500 mm and from 400 mm to 600 mm with an increment of 100 mm, respectively. The initial axial load level acting on the member before fire exposure are taken as 0%, 20% and 40% to simulate the cases of a beam, a lightly loaded column and a moderately loaded column, respectively. Elements subjected to large initial load during a standard fire are not considered as they may exhibit severe failure before the end of the cooling phase and

consequently their residual properties are usually not of structural importance. The studied members are exposed to heat from three sides. The members not subjected to axial load are considered beams and reinforced with $\rho = 0.005, 0.001$ and 0.0015 at the tension side. The axially loaded members are considered as columns and are reinforced with a total of 0.002 or 0.004 reinforcement ratio equally distributed at the top and bottom surfaces. The axial and flexural restraint stiffness range from very small values that account for unrestrained elements to very large values that represent almost fully restrained elements. Each section is analyzed 3 times to account for maximum fire durations of $0.5, 1.5$ and 2.5 hours beyond which a cooling phase proceeds. Therefore, a total of 5994 different cases are considered in the analysis.

7.8 Influence of Study Parameters

The residual behavior of the fire-damaged members is discussed in this section in view of the members listed in Table 7-1 which details their geometrical and mechanical properties.

Table 7-1: Geometrical and mechanical properties of the discussed sections.

Member	t (hr)	f'_c (MPa)	f_y (MPa)	b (mm)	h (mm)	ρ
M1	1.5	35	350	400	500	0.02
M2	2.5	35	350	500	600	0.02
M3	2.5	25	350	500	600	0.02
M4	2.5	35	450	300	400	0.02
M5	0.5	35	350	500	600	0.02
M6	1.5	35	350	500	600	0.02
M7	2.5	35	350	500	600	0.04
M8	2.5	35	350	300	600	0.02
M9	2.5	35	350	400	600	0.02
M10	2.5	35	350	500	400	0.02
M11	2.5	35	350	500	500	0.02

An examination of Figs. 7-6(a) and 7-6(b) reveals the variations in the $M-\phi$ relationship resulting from 3-sides and 4-sides heat exposure for member M1 in Table 7-1 subjected to $\lambda = 0.0$ and 0.2, respectively. When the member is unrestrained and unloaded during fire exposure, thermal expansion is produced in concrete and steel layers depending on the maximum temperature reached in each layer. If the member is heated from 4 sides, then equilibrium is achieved at zero curvature due to symmetric temperature distribution along the cross-section. However, sections heated from 3 sides only experience non-uniform temperature variation along the section with a maximum value close to the heated side and a minimum value near the unheated surface. This results in initial curvature in the member in order to maintain equilibrium as indicated in Fig. 7-6(a). On the other hand, when the member is subjected a moderate initial load before and during heating, both transient and creep strains are developed and counteract thermal expansion tendency of the member. Therefore, at this load level, initial curvature of the member heated from 3 sides approaches zero while achieving equilibrium as shown in Fig. 7-6(b). If the initial load is further increased, then the member may experience opposite initial curvature due to the significant influence of transient strain. These comparisons reveal the significance of tracking the temperature-load history on capturing the residual structural performance of the fire-damaged members. The influence of the considered parameters on the residual behavior of RC member is discussed in this section with reference to Table 7-1.

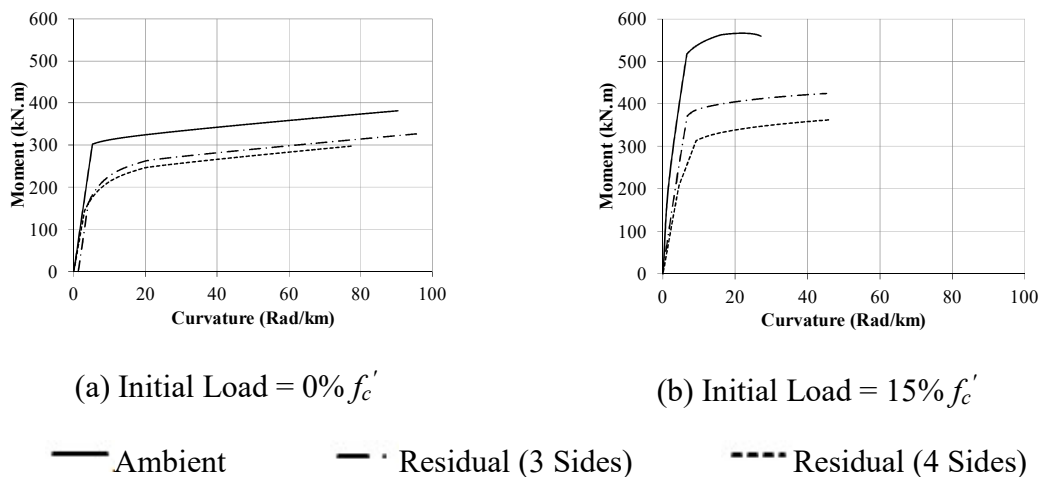


Figure 7-6: Ambient and residual $M-\phi$ diagrams for a typical member corresponding to different initial loads.

7.8.1 Concrete Compressive Strength (f'_c)

Fig. 7-7(a) shows that increasing the concrete compressive strength has an insignificant inverse relationship on the residual flexural capacity of the fire-damaged member for all load levels in the examined range. The decreasing rate can be justified by the more reduction in compressive strength of the stronger concrete after fire. Hence, the reduction in concrete contribution within the compression zone becomes more pronounced and results in the observed larger decrease relative to the original capacity.

The residual thermal strain (including the transient strain component) after a complete heating-cooling phase is illustrated in Fig. 7-8(a). Loading the member during fire significantly alters the developed residual average thermal strain. When the member is unloaded, it tends to expand due to the internal chemical and physical processes in the material itself. At relatively high temperatures (i.e. more than 300°C), internal cracks also form which prevent the member from returning completely to its initial length after cooling resulting in residual deformation. However, the initial applied load hinders the formation of such cracks and consequently reduces the expected expansion during and after fire. If a combination of relatively large initial load (i.e. about $0.4 f'_c A_g$) and high temperature, the member tends to contract as both the transient and creep strain components exceed the thermal strain. As expected, heating from all sides results in higher temperature within the section and consequently more pronounced variation of the residual thermal strain. For the examined range, concrete compressive strength is found to have a negligible influence on the residual thermal strain of the heated member. The use of normal strength concrete infers that no spalling is encountered which could otherwise significantly affect the residual thermal strain.

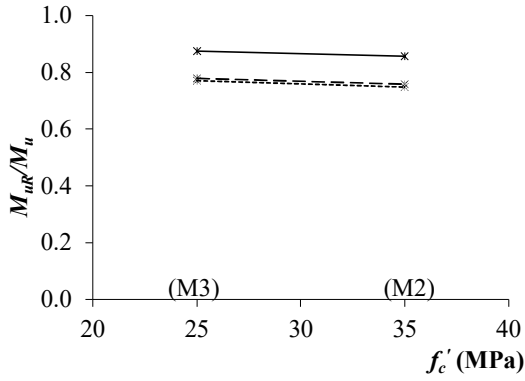
7.8.2 Steel Yield Strength (f_y)

Increasing steel grade from 350 MPa to 450 MPa results in a further reduction in the residual flexural capacity of the fire-damaged member as shown in Fig. 7-7(b). The reason lies in the more pronounced reduction in residual yield strength for the steel bars of higher grade that was accounted for in the material models. Regarding thermal strain, Fig. 7-8(b), varying the steel yield strength is found to have a negligible influence on its

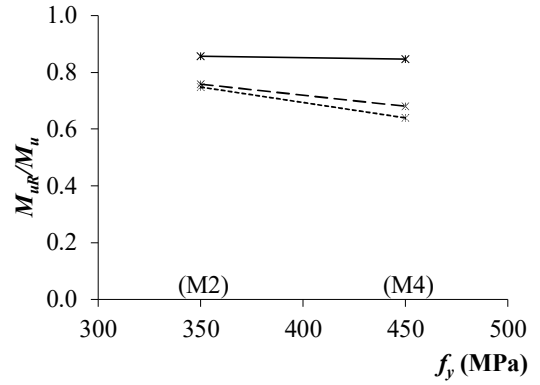
residual value. This is attributed to the fact that the residual thermal strain in all cases did not exceed the elastic range of the steel bars. Hence, it depends merely on the residual elastic modulus of steel that was mostly restored after the specified fire conditions.

7.8.3 Fire Duration (t)

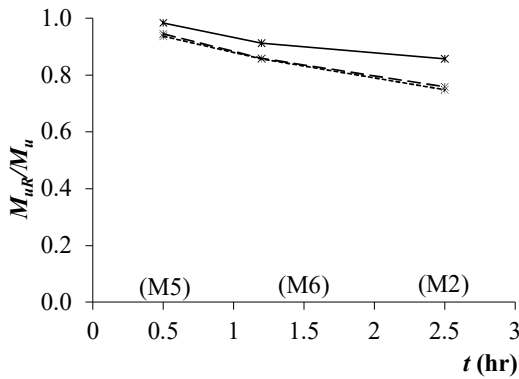
Fig. 7-7(c) indicates that the longer the fire duration, the lower the residual flexural capacity ratio of the member. This is explained by the fact that increasing fire duration causes more rise in temperature which consequently result in further deterioration of materials. In addition, the amount of time required to bring the member back to ambient conditions increases with fire duration. This provides even more time for heat to transfer to the inner elements within the concrete member causing the higher increase in temperature. Fire duration has the most tremendous influence on the variation of the residual thermal strain of RC members as indicated in Fig. 7-8(c). For unloaded members, increasing the fire duration from 0.5 hr to 2.5 hrs resulted in increasing the residual thermal strain by 3.6 folds and 4.2 folds for 3-sides and 4-sides heating, respectively. The higher temperature results in the formation of more internal cracks that counteract the member's tendency to go back to its initial position at ambient conditions. On the other hand, loaded members experience more contraction as fire duration increases since the influence of transient strain becomes more remarkable for the same load level. It is worth mentioning that under a certain loading and temperature combination, the member could restore its initial size even after prolonged fire duration as shown in the case with axial load level of $0.2 f_c' A_g$.



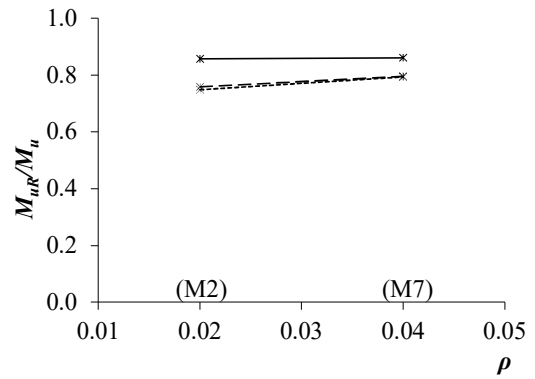
(a) Concrete compressive strength.



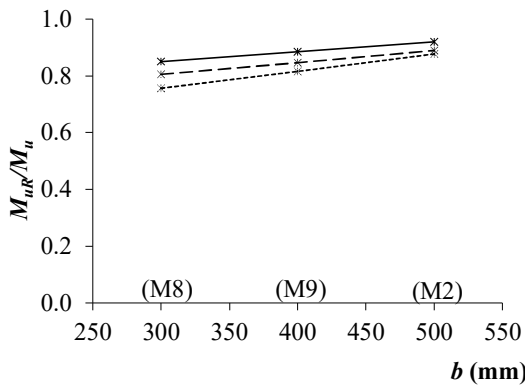
(b) Steel yield strength.



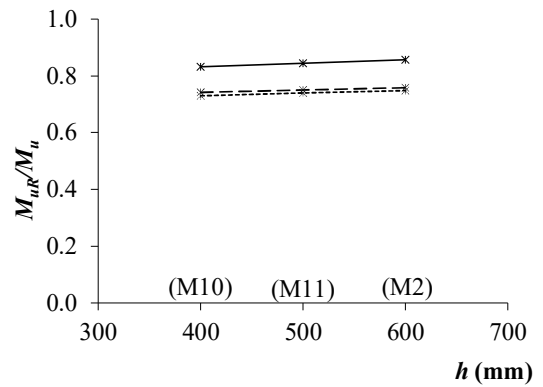
(c) Fire duration (heating phase).



(d) Steel reinforcement ratio.



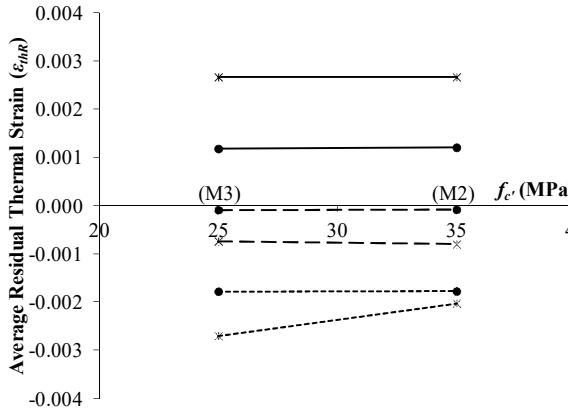
(e) Width of cross-section.



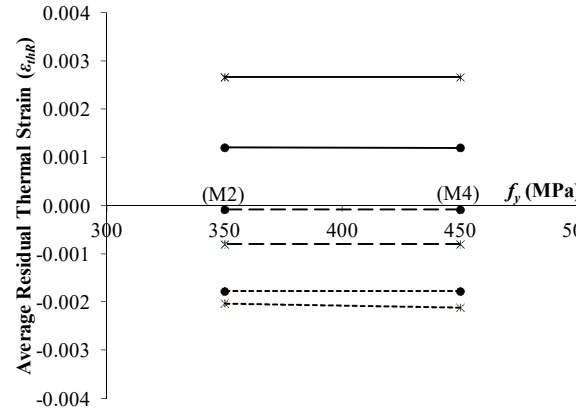
(f) Height of cross-section.

Heating from 3 Sides: —*— ALL = 0% f'_c —x— ALL = 15% f'_c -*- ALL = 30% f'_c

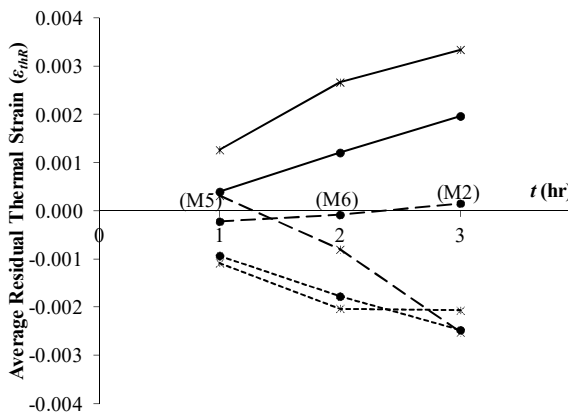
Figure 7-7: Effect of the parameters on the residual flexural capacity.



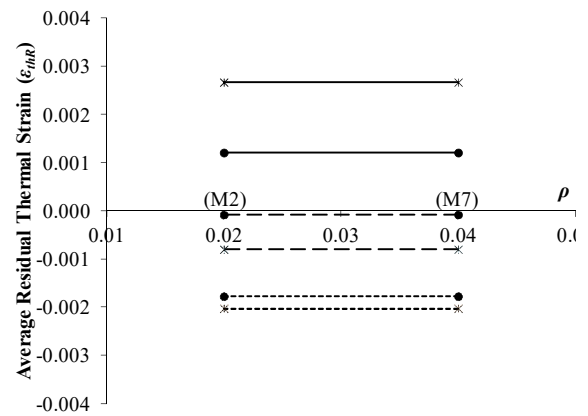
(a) Concrete compressive strength.



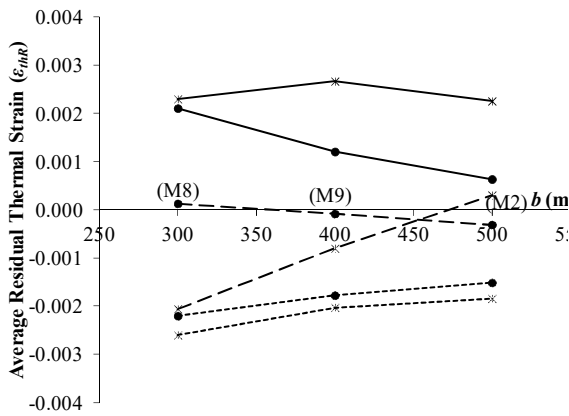
(b) Steel yield strength.



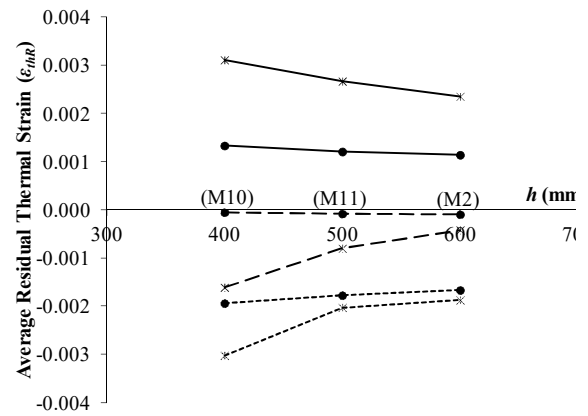
(c) Fire duration (heating phase).



(d) Steel reinforcement ratio.



(e) Width of cross-section.



(f) Height of cross-section.

Heating from 3 Sides: ● ALL = 0% f'_c ● ALL = 15% f'_c ● ALL = 30% f'_c
 Heating from 4 Sides: * ALL = 0% f'_c * ALL = 15% f'_c * ALL = 30% f'_c

Figure 7-8: Effect of the parameters on the average residual thermal strain (including transient strain).

7.8.4 Steel Reinforcement Ratio (ρ)

Increasing the steel reinforcement ratio in unloaded members results in a 3% reduction in residual strength ratio as indicated in Fig. 7-7(d). This insignificant decrease is attributed to the higher impact of the larger steel area in representing the unrecovered portion of yield strength after fire. However, when the same member is subjected to load during heating, a direct relationship between the reinforcement ratio and flexural strength regain is shown. The reason can be justified by the influence of the initial compressive stresses in delaying crack formation in concrete. Varying the reinforcement ratio from 2% to 4% results in an imperceptible variation in the residual thermal strain at all initial load levels. This is attributed to the fact that steel bars have a negligible influence on heat transfer within RC members due to their high thermal conductivity and low thermal inertia relative to the surrounding concrete material.

7.8.5 Width of Cross-Section (b)

The parametric study revealed that increasing the width of the cross-section results in maintaining higher residual flexural strength after fire as shown in Fig. 7-7(e). This larger residual capacity is caused by the lower temperature increase within the wider member as it requires more heat energy to increase its temperature. For the same fire duration, concrete within the inner parts of the wider member experience lower increase in temperature and consequently more recovery after fire. The influence of strength recovery in steel bars is neglected since concrete cover is the same in all specimens causing the maximum temperature reached in all steel bars to be the same. Increasing the cross-sectional width from 300 mm to 500 mm results in about 6%, 8% and 9% increase in the residual capacity ratio of members subjected to initial load of 0.0, $0.2 f'_c A_g$ and $0.4 f'_c A_g$, respectively. Fig. 7-8(e) indicates that cross-sectional width of the member has a large influence on its residual thermal strain. Changing the member's width affects the time required for heat energy to raise the temperature of the inner concrete core. Increasing the cross-sectional width from 300 mm to 500 mm results in decreasing this strain by approximately 65% and 33% for members heated from 3 sides and 4 sides, respectively. The lower percentage for the latter case is justified by the higher temperature distribution within the cross-section when the member is heated from 4

sides. Loading the member prior to heating decreases expansion caused by thermal strain and may result in length shortening as encountered for members with the largest axial load level.

7.8.6 Height of Cross-Section (h)

The influence of increasing the section height is found to have a positive impact on strength recovery of the heated RC members as indicated in Fig. 7-7(f). The higher material content of the larger members requires more heating time to increase their temperature to the same level of smaller members. In addition, increasing the member height shifts the concrete core away from the corners where the maximum temperature condensation exists. These two reasons result in lower concrete degradation and after fire and therefore more strength recovery is detected. Increasing the section height decreases the effect of elevated temperature on altering the member's original length after cooling. The variation follows the same trend detected by changing the beam width for both the unloaded and loaded cases but to less extent. This lower influence explained by the heating configuration by which the two opposite sides representing the section height are exposed to fire in both the 3-sides and 4-sides heating schemes.

7.8.7 Restraints against Thermal Expansion

Figure 7-9 illustrates the influence of restraining member M1 against thermal expansion on the developed axial loads. The member is initially subjected to a $(0.2 f_c')$ axial load and is exposed to an ASTM E119 heating phase for 1.5 hrs. As temperature increases, the member tendency to undergo thermal expansion increases causing the restraints to counteract this potential movement depending on their stiffness relative to the member. The change in the applied compressive load is characterized by a mild increase followed by a gradual degradation with time. In the first stage, the member's stiffness remains close to that at ambient conditions as the temperature increase within the member is relatively low. Thus, an increase in restraining force is observed to hinder the higher thermal expansion tendency exhibited by the member.

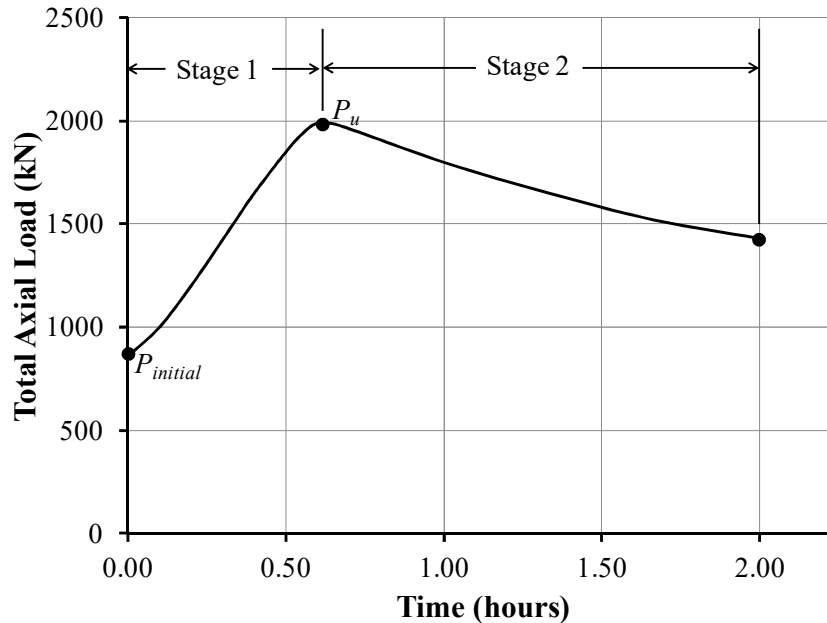


Figure 7-9: Variation of total axial load acting on member 1 during ASTM E119 fire exposure and ($20\%f_c'$) initial axial load level.

In the shown case, the extra restraining force is shown to be about 140% higher than the initial applied load. However, after certain period of time, the temperature within the member becomes relatively high causing the stiffness degradation to become more pronounced. Thus, the forces required to resist the larger thermal expansion of the member drops. The axial force required to restrain the member keeps decreasing as a result of the continuous reduction in stiffness caused by elevated temperatures as indicated in stage 2.

The residual thermal strain (including transient strain component) slightly decreases with increasing the stiffness of constraints. Since thermal strain is always independent from the restraint conditions, the aforementioned observation indicates that the transient strain developed in the member due to the restraining compressive forces is just little higher than its unrestrained counterpart. This small variation is justified by the relatively low temperature within the section at the instance when the extra restraining load is maximum (i.e. end of stage 1). This means that the load-temperature combination does not allow the development of much larger post-fire transient strain than the one generated in the unrestrained case.

The influence of restraining the member against thermal expansion during heating is found to slightly increase its post-fire stiffness and capacity. This is explained by knowing that the transient strain component developed under compressive stresses significantly alleviates the extent of thermal expansion, which means that the overall thermal expansion pushing the stiffer supports is smaller than that exerted on unrestrained supports. Thus, the larger residual axial forces developed in the restrained members are not very large to significantly alter the residual capacity of the member. The residual deformation experienced by unrestrained members is larger than their restrained counterparts. The degree of axial restraint has a minor influence on changing the residual capacity of the fire-damaged member.

7.9 Regression Analysis and Proposed Expressions

The residual axial and flexural behaviors of RC members subjected to different initial load levels and exposed to various fire scenarios are assessed in light of the extensive parametric study. Determining the temperature distribution within the member and performing sectional analysis considering the various strain components and the residual materials' mechanical properties are tedious and require a sequence of nested iterations that may not be convenient for researchers and engineers in during the preliminary design phase. Hence, based on the analytical results conducted on the 5994 specimens, some expressions are developed to determine the residual axial capacity, stiffness and residual thermal strains of fire-exposed beams and columns heated from 3 sides. The accuracy of these expressions is validated for the examined parameters range.

The difference in $M-\phi$ behavior between a typical intact and fire-exposed beams is illustrated in Fig. 7-10. Typically, both stiffness and capacity of fire-damaged beams drop depending on their mechanical characteristics, geometrical properties, load history, support conditions and fire scenario. In Chapter 5, a procedure was proposed to calculate the residual ultimate moment of fire-exposed beams based on stress-block concept. In this chapter, statistical analysis is performed to evaluate plot the entire $M-\phi$ diagram.

This requires the evaluation of residual elastic stiffness $(EI)_R$, residual yield moment $(M_y)_R$ and initial curvature (ϕ_i) .

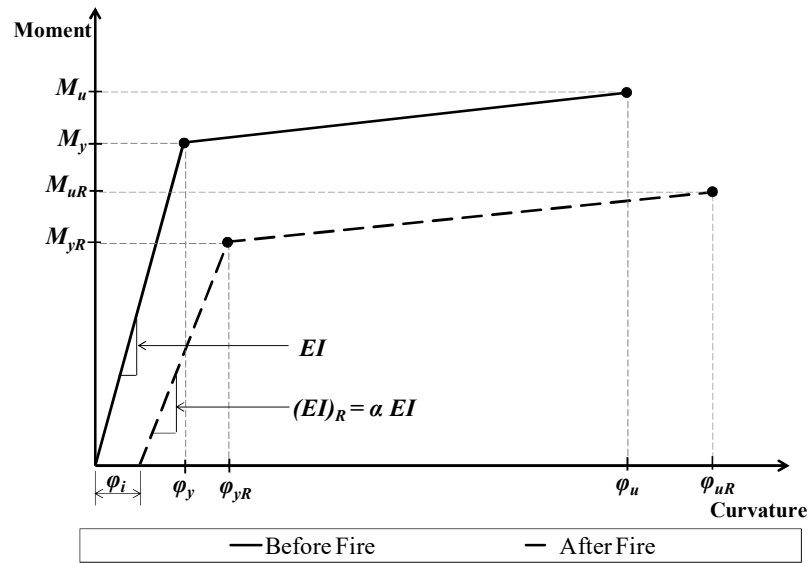


Figure 7-10: Variation of $M-\phi$ diagram between ambient and post-fire conditions.

7.9.1 Residual Flexural Stiffness of Fire-Exposed Beams-Column Elements

The post-fire elastic stiffness $(EI)_R$ of RC members subjected to either sagging or hogging moment and exposed to heat from their soffit and two sides can be estimated using Equation 8 that was developed through multiple regression analysis.

$$\frac{(EI)_R}{(E_c I_g)} = (0.875\lambda^2 - 0.675\lambda + 1)^n \left(A_1 + A_2 t + A_3 f'_c + A_4 f_y + A_5 b + A_6 h + A_7 \rho + A_8 \frac{\sqrt{b}}{t^2} + A_9 \frac{\rho b h}{t^3} \right) (-0.22R_\theta^2 + 0.37R_\theta + 1.0) (A_{10})^{R_d} \quad (8)$$

Where E_c is the secant elastic modulus for concrete at ambient conditions and can be calculated as $4500\sqrt{f'_c}$ (MPa); I_g is the gross moment of inertia (mm^4); t is fire duration (hr); f'_c is concrete compressive strength (MPa); f_y is steel yield strength (MPa); b is section width (m); h is section height (m); ρ is steel reinforcement ratio; λ is initial axial

load level, R_d is restraint ratio and n is a factor to account for the loading condition (1 for sagging moment and 0.77 for hogging moment). The coefficients $A_i (i=1,2,3,4,5,6,7,8,9,10)$ are given in Table 7-2 in terms of the load application condition and fire duration. A very good match between the analytical results and the predictions obtained from Equation 8 are found as indicated in Fig. 7-11 for both sagging and hogging moment sections.

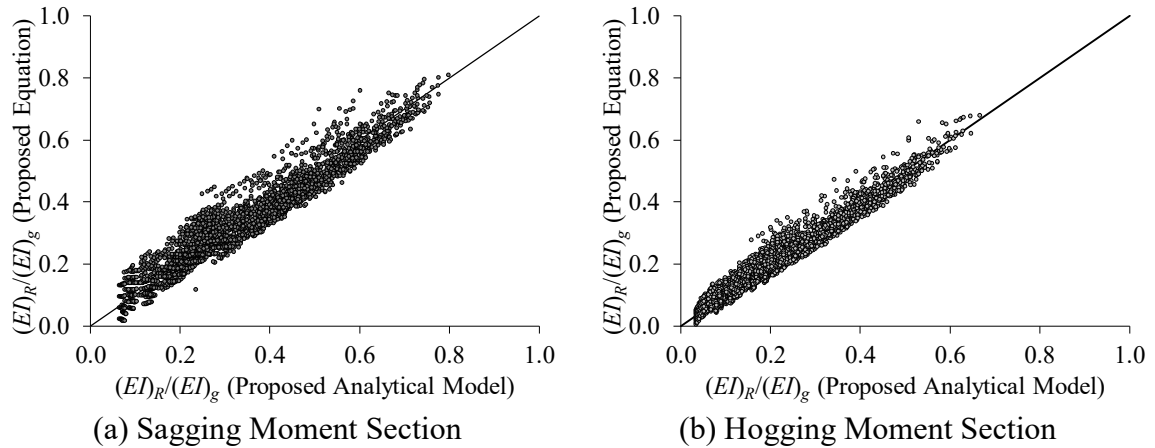


Figure 7-11: Validation of Equation 8 to predict $(EI)_R/(EI)_g$ in fire-exposed beams.

Table 7-2: Coefficients for Equation 8

A_i	Sagging		Hogging	
	$0.5 \leq t < 1.0 \text{ hr}$	$1.5 \leq t \leq 2.5 \text{ hrs}$	$0.5 \leq t < 1.0 \text{ hr}$	$1.5 \leq t \leq 2.5 \text{ hrs}$
A_1	7.5754×10^{-1}	2.5556×10^{-1}	4.9755×10^{-1}	6.7210×10^{-2}
A_2	-6.5976×10^{-1}	-1.1397×10^{-1}	-5.3439×10^{-1}	-6.8090×10^{-2}
A_3	-1.4786×10^{-3}	1.2820×10^{-4}	-7.4930×10^{-4}	6.6050×10^{-4}
A_4	-2.5632×10^{-4}	-2.1784×10^{-4}	-1.0631×10^{-4}	-6.8800×10^{-5}
A_5	7.9210×10^{-1}	9.0350×10^{-1}	5.5731×10^{-1}	4.6185×10^{-1}
A_6	6.6030×10^{-2}	-3.1450×10^{-2}	1.8560×10^{-1}	1.1141×10^{-1}
A_7	1.9262×10^1	6.3157	1.2882×10^1	1.9706
A_8	-1.8403×10^{-1}	-6.4782×10^{-1}	-1.3912×10^{-1}	-3.3707×10^{-1}
A_9	3.3822	1.7794×10^2	4.0724	1.3628×10^2
A_{10}	7.5754×10^{-1}	2.5556×10^{-1}	4.9755×10^{-1}	6.7210×10^{-2}

It is worth mentioning that the term $(E_c I_g)$ is the elastic uncracked stiffness of the concrete section and does not represent its effective stiffness at ambient temperature. Therefore, the reduction ratio obtained from Equation 8 does not represent directly the drop in stiffness of beam sections due to fire exposure. It shows the variation of the

equivalent residual stiffness $(EI)_R$ relative to $(E_c I_g)$, which is taken as a reference value while performing the regression analysis. Considering $E_c I_g$ as a reference point significantly simplifies the calculation procedure as both E_c and I_g for concrete beam sections can be determined easily. The same procedure was adopted in an analytical study and was included in the ACI 318-08 to calculate the effective stiffness at ambient conditions. It was also implemented by E-Fitiany and Youssef [21] to evaluate the equivalent flexural stiffness of fire-exposed beams during fire.

7.9.2 Residual Yield Moment of Fire-Exposed Beams

The residual yield moment capacity of fire-exposed beams $(M_y)_R$ heated from 3 sides and subjected to sagging moment can be obtained from the proposed Equation 9 as a proportion from the yield moment at ambient conditions (M_y) .

$$\frac{(M_y)_R}{(M_y)} = 0.4805 - 0.1317t + 0.00266f'_c + 0.0001566f_y + 1.3226b - 0.00527h - 4.7083\rho + \frac{0.085964}{t} - 2.07993 \frac{b^3}{\sqrt{t}} \quad (9)$$

A reduction factor of 0.65 must be multiplied by the output of Equation 9 if the considered beam is exposed to fire for more than 2 hrs and possesses all of the following properties: $b \leq 0.2$ m, $\rho \geq 0.015$ and $f_y \geq 450$ MPa. The definition of the parameters is similar to the ones used in Equation 8.

If the beam is subjected to hogging moment, then Equation 10 should be used to estimate the residual yield moment $(M_y)_R$.

$$\frac{(M_y)_R}{(M_y)} = 0.4610 - 0.1727t + 0.00275f'_c - 0.0001169f_y + 1.69266b + 0.18648h - 5.6957\rho + \frac{0.0507}{t} - 2.9719 \frac{b^3}{\sqrt{t}} \quad (10)$$

A reduction factor of 0.60 must be multiplied by the value obtained from Equation 10 if the beam is exposed to fire for more than 2 hrs and has the same properties mentioned for Equation 9. A comparison between the analytical results and the predictions of Equations 9 and 10 shows a good agreement for both sagging and hogging moment cases (Fig. 7-12). It is worth mentioning that Equations 9 and 10 are developed considering that the strain-hardening modulus of the steel bars is 2% of its modulus of elasticity. Therefore, if yielding plateau is assumed constant, then the reduction in yield moment is taken equal to that obtained for ultimate moment in Chapter 5.

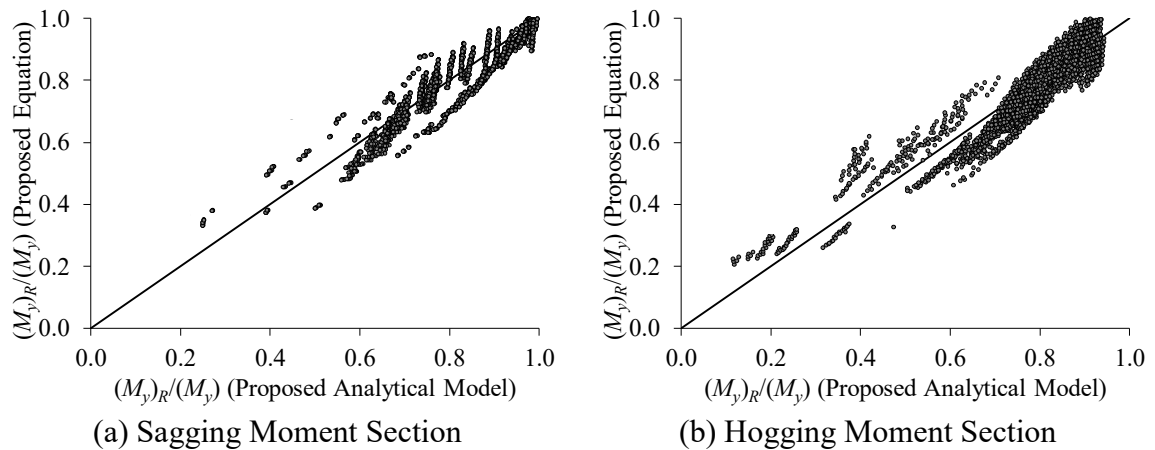


Figure 7-12: Validation of Equations 9 and 10 to predict $(M_y)_R/(M_y)$ in beams.

7.9.3 Residual Thermal Curvature (φ_i) of Fire-Exposed Beams

The residual curvature in beams subjected to sagging and hogging moments after exposure to fire is given in Equations 11 and 12, respectively. These expressions are developed by performing statistical analysis on the results from the parametric study.

$$\varphi_i = \exp[(-0.1165t - 0.1323)\lambda_f] \left[5.6452 \times 10^{-7} - 3.9423 \times 10^{-6}t + 6.305 \times 10^{-9}f'_c + 1.088 \times 10^{-9}f_y + 2.72 \times 10^{-6}b - 1.299 \times 10^{-6}h + 2.623 \times 10^{-5}\rho - 2.558 \times 10^{-7}t^4b^3 + 4.4312 \times 10^{-6} \frac{t}{\sqrt{h}} - 5.22 \times 10^{-7} \frac{\rho f_y^{0.3333}}{h^2} \right] \quad (11)$$

$$\varphi_i = \exp[(-0.8835t - 5.8114)\lambda_f] \left[6.983 \times 10^{-6} + 2.608 \times 10^{-6}t + 2.3 \times 10^{-8}f'_c + 3.3 \times 10^{-9}f_y + 9.5 \times 10^{-8}b - 1.331 \times 10^{-5}h + 8.6285 \times 10^{-5}\rho - 9.53 \times 10^{-7} \frac{t^2b}{\sqrt{h}} + 6.704 \times 10^{-6} \frac{tb^2}{h} \right] \quad (12)$$

In these equations, λ_f is the ambient flexural load level acting on the beams. Fig. 7-13 shows a very good fit between the proposed analytical results and the values of φ_i calculated from Equations 11 and 12 for both sagging and hogging moments.

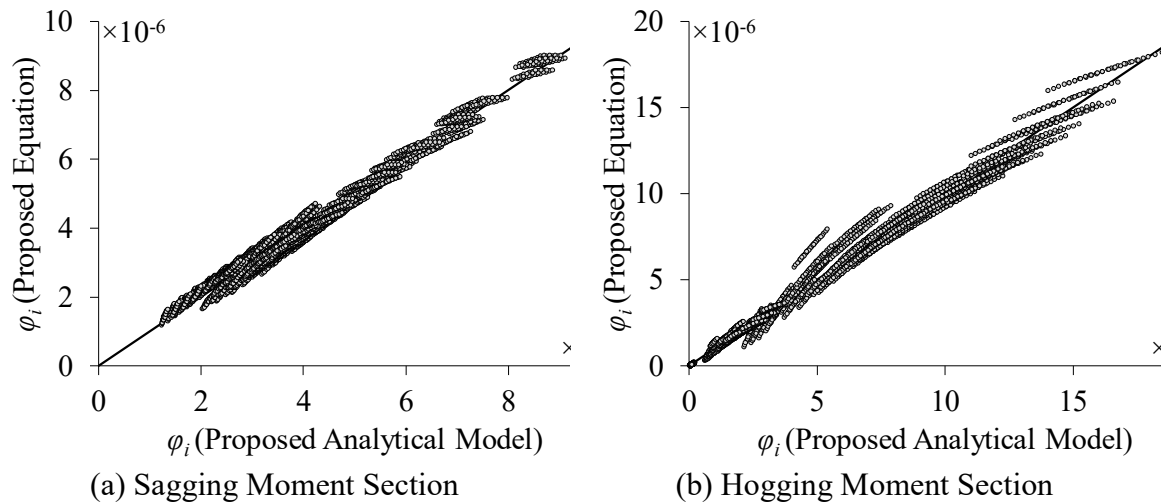


Figure 7-13: Validation of Equations 11 and 12 to predict φ_i in fire-exposed beams.

7.9.4 Residual Thermal Strain (ε_i) of Fire-Exposed Beams

In a similar statistical approach to the previous developed expressions, the post-fire residual thermal strain in beams can be predicted from Equations 13 and 14 for both sagging and hogging moment sections, respectively.

$$\varepsilon_i = (1.667t^2 - 2.333t + 1.12)(c_1t^2 + c_2t + c_3) \left[1.621 \times 10^{-3} + 1.83 \times 10^{-3}t - 1.874 \times 10^{-5}f'_c - 1.56 \times 10^{-6}f'_y - 9.719 \times 10^{-4}b + 2.482 \times 10^{-3}h - 1.703 \times 10^{-2}\sqrt{\rho} - 5.65 \times 10^{-3}tb^3 + 7.038 \times 10^{-4}bt^2 + 9.5 \times 10^{-4} \frac{b}{\sqrt{h}} \right] \quad (13)$$

$$\varepsilon_i = (0.75t^2 - 0.95t + 1.0)(c_1t^2 + c_2t + c_3) \left[1.115 \times 10^{-3} + 9.992 \times 10^{-4}t - 1.304 \times 10^{-5}f'_c - 1.1 \times 10^{-6}f'_y - 5.498 \times 10^{-4}b + 1.704 \times 10^{-3}h - 4.289 \times 10^{-2}\rho + 5.9 \times 10^{-7} \frac{t^2}{\rho} - 5.928 \times 10^{-4}bh^3 \right] \quad (14)$$

Where the coefficients c_1 , c_2 and c_3 in Equations 13 and 14 can be obtained from Table 7-3 in terms of the axial (R_D) and rotational (R_θ) restraint ratios.

Table 7-3: Coefficients for Equations 13 and 14

ci	Sagging (Equation 13)			Hogging (Equation 14)			
	$R_D = 0.0$	$R_D = 0.5$	$R_D = 1.0$	$R_D = 0.0$	$R_D = 0.5$	$R_D = 1.0$	
$R_\theta = 0.0$	c1	0.0000	0.1100	0.1450	0.0000	0.1210	0.1537
	c2	0.0000	-0.5800	-0.6600	0.0000	-0.6380	-0.6996
	c3	1.0000	0.9825	0.8938	1.0500	1.0808	0.9474
$R_\theta = 0.5$	c1	-0.0250	0.1150	0.1300	-0.0270	0.1417	0.1430
	c2	-0.0200	-0.6000	-0.6200	-0.0216	-0.7392	-0.6820
	c3	0.9663	0.9713	0.8475	1.0436	1.1966	0.9323
$R_\theta = 1.0$	c1	-0.0150	0.1150	0.1300	-0.0155	0.1318	0.1400
	c2	-0.0600	-0.6000	-0.6100	-0.0618	-0.6876	-0.6570
	c3	0.9538	0.9713	0.7925	0.9824	1.1131	0.8535

7.9.5 Residual Moment-Curvature Diagram of Fire-Exposed Beams

To plot the approximate bi-linear $M-\phi$ diagram, the following steps are followed:

- 1) Plot the $M-\phi$ diagram of the intact member by calculating the flexural stiffness (EI), yield moment (M_y), ultimate moment (M_u) and ultimate curvature (ϕ_u).
- 2) Calculate the member's residual flexural stiffness (EI)_R from Equation 8; residual yield moment (M_y)_R from Equations 9 or 10; residual flexural capacity (M_u)_R as given in Chapter 5 and residual curvature (ϕ_i) from Equations 11 or 12.
- 3) Obtain the residual yield curvature (ϕ_y)_R by extending a line from the Cartesian point ($\phi_i, 0.0$) with a slope of (EI)_R until reaching (M_y)_R.

7.9.6 Residual Axial Capacity and Stiffness of Columns Heated from 3 Sides

Expressions to predict the residual axial capacity and stiffness of columns heated from 4 sides were previously provided in Chapter 6. The residual behavior of columns heated from 3 sides is found to be different from the former case. Therefore, Equation 15 is developed to predict the reduction in both axial capacity and secant stiffness at different load levels for the 3 sides heating scheme.

$$\omega = A_1 + A_2\lambda + A_3f'_c + A_4f_y + A_5\rho + A_6b + A_7h + A_8\frac{\rho bh}{\lambda} + A_9\frac{(f'_c)^{0.12}}{\rho\sqrt{f_y}} \quad (15)$$

The coefficients $A_{i(i=1,2,3,4,5,6,7,8,9)}$ are listed in Table 7-4 for various reduction ratios (ω) depending on the restraint condition and fire duration during the heating phase. The developed Equation 15 is validated against the analytical results and shown to be in very good agreement.

7.9.7 Residual Thermal Strain in Columns Heated from 3 Sides

The residual thermal strain of columns heated from 4 sides was previously determined in Chapter 6. However, the residual deformation behavior varies when fire acts from 3 directions only. Therefore, Equation 16 is proposed to determine the residual thermal strain after fire.

$$\varepsilon_i = E_1 + E_2 t + E_3 f'_c + E_4 f_y + E_5 b + E_6 h + E_7 \rho + E_8 \frac{t^{4.6}}{b} + E_9 (bh)^{-\sqrt{t}} \quad (16)$$

The coefficients $E_{i(i=1,2,3,4,5,6,7,8,9)}$ are given in Table 7-5 in terms of restraint condition (R_D) and initial axial load level (λ). The proposed Equation 16 is found to be with an excellent agreement with the analytical results.

Table 7-4: Coefficient for Equation 15

ω	A_i	$R_D = 0$ (Unrestrained)			$R_D = 0.5$ (Partially Restrained)			$R_D = 1$ (Fully Restrained)		
		$t = 0.5$ hr	$t = 1.5$ hrs	$t = 2.5$ hrs	$t = 0.5$ hr	$t = 1.5$ hrs	$t = 2.5$ hrs	$t = 0.5$ hr	$t = 1.5$ hrs	$t = 2.5$ hrs
$\frac{P_r}{P_o}$	A_1	8.1669×10^{-1}	6.5733×10^{-1}	5.4430×10^{-1}	7.4177×10^{-1}	6.5408×10^{-1}	5.7891×10^{-1}	7.4018×10^{-1}	5.8365×10^{-1}	4.866×10^{-1}
	A_2	-7.795×10^{-2}	-1.313×10^{-1}	-1.33×10^{-1}	-5.441×10^{-2}	-5.670×10^{-2}	-7.320×10^{-2}	-4.561×10^{-2}	-3.853×10^{-2}	-5.153×10^{-2}
	A_3	-6.832×10^{-4}	-1.021×10^{-3}	-1.405×10^{-3}	-1.074×10^{-3}	-1.524×10^{-3}	-1.628×10^{-3}	-1.011×10^{-3}	-1.696×10^{-3}	-1.808×10^{-3}
	A_4	7.0560×10^{-5}	8.4030×10^{-5}	1.2723×10^{-4}	1.0856×10^{-4}	9.5010×10^{-5}	1.1445×10^{-4}	1.0458×10^{-4}	1.3285×10^{-4}	1.7591×10^{-4}
	A_5	2.2530	3.0030	4.4510	3.7820	2.8450	3.9010	3.5160	4.6420	6.2600
	A_6	8.1689×10^{-2}	1.6751×10^{-1}	2.0341×10^{-1}	7.6004×10^{-2}	1.2334×10^{-1}	1.4797×10^{-1}	7.5724×10^{-2}	1.1580×10^{-1}	1.3495×10^{-1}
	A_7	6.4173×10^{-2}	1.1268×10^{-1}	1.2380×10^{-1}	8.9771×10^{-2}	1.2523×10^{-1}	1.2093×10^{-1}	9.4421×10^{-2}	1.2703×10^{-1}	1.1917×10^{-1}
	A_8	-7.929×10^{-3}	-1.989×10^{-2}	-2.71×10^{-2}	-8.131×10^{-3}	-8.761×10^{-3}	-1.580×10^{-2}	-4.889×10^{-3}	-3.609×10^{-3}	-7.086×10^{-3}
	A_9	2.6310×10^{-3}	3.3110×10^{-3}	6.0390×10^{-3}	5.3730×10^{-3}	1.7730×10^{-3}	3.5510×10^{-3}	4.5520×10^{-3}	6.4260×10^{-3}	9.4780×10^{-3}
$\frac{(EA_i)_r}{EA_i}$	A_1	8.3825×10^{-1}	7.8500×10^{-1}	8.8340×10^{-1}	8.2297×10^{-1}	7.5770×10^{-1}	6.7150×10^{-1}	8.2128×10^{-1}	6.0330×10^{-1}	7.7020×10^{-1}
	A_2	-3.1340×10^{-3}	-5.704×10^{-2}	-8.910×10^{-2}	-4.554×10^{-3}	-1.106×10^{-2}	-1.562×10^{-1}	-4.763×10^{-3}	-3.013×10^{-2}	-1.157×10^{-1}
	A_3	-2.9527×10^{-4}	2.7500×10^{-5}	-1.569×10^{-4}	-3.649×10^{-4}	-5.690×10^{-4}	-7.836×10^{-4}	-2.314×10^{-4}	-7.846×10^{-4}	-7.587×10^{-4}
	A_4	-8.0700×10^{-6}	-8.539×10^{-5}	-1.398×10^{-4}	-1.570×10^{-6}	-6.480×10^{-5}	-2.100×10^{-5}	7.0000×10^{-8}	6.850×10^{-5}	-3.080×10^{-5}
	A_5	6.9890×10^{-1}	-3.3300	-6.1620	1.2439	-2.6330	8.8100×10^{-1}	1.1462	1.0010	-2.7690
	A_6	8.1168×10^{-2}	3.2529×10^{-1}	3.0654×10^{-1}	7.9445×10^{-2}	3.3534×10^{-1}	2.9655×10^{-1}	7.7152×10^{-2}	3.6265×10^{-1}	2.9353×10^{-1}
	A_7	6.2174×10^{-2}	1.0192×10^{-1}	9.7100×10^{-2}	6.6000×10^{-2}	9.2306×10^{-2}	1.0355×10^{-1}	6.6439×10^{-2}	9.2790×10^{-2}	1.0263×10^{-1}
	A_8	6.040×10^{-4}	-1.696×10^{-2}	-2.690×10^{-2}	-6.010×10^{-4}	5.7700×10^{-3}	-4.698×10^{-2}	-1.204×10^{-3}	8.900×10^{-4}	-2.739×10^{-2}
	A_9	-1.0580×10^{-3}	-1.544×10^{-2}	-2.528×10^{-2}	-2.030×10^{-4}	-1.449×10^{-2}	-8.120×10^{-3}	-2.940×10^{-4}	-6.530×10^{-3}	-1.764×10^{-2}
$\frac{(EA_{0.4})_r}{EA_{0.4}}$	A_1	8.3995×10^{-1}	2.7290×10^{-1}	3.7750×10^{-1}	8.0898×10^{-1}	4.1200×10^{-2}	1.2420×10^{-1}	7.6169×10^{-1}	1.3880×10^{-1}	8.7400×10^{-2}
	A_2	-3.4650×10^{-3}	-1.841×10^{-1}	-3.810×10^{-1}	-6.450×10^{-4}	-7.419×10^{-2}	-2.214×10^{-1}	-3.379×10^{-3}	-8.432×10^{-2}	-1.06×10^{-1}
	A_3	-4.2852×10^{-4}	-1.282×10^{-3}	-1.348×10^{-3}	-6.219×10^{-4}	-1.805×10^{-3}	-2.021×10^{-3}	-7.85×10^{-4}	-1.793×10^{-3}	-2.039×10^{-3}
	A_4	-1.6600×10^{-6}	2.5450×10^{-4}	2.4360×10^{-4}	2.6140×10^{-5}	4.4700×10^{-4}	4.2950×10^{-4}	4.6660×10^{-5}	3.9080×10^{-4}	4.8890×10^{-4}
	A_5	9.9070×10^{-1}	1.1391×10^{-1}	8.9110	2.0805	1.4033×10^{-1}	1.3260×10^{-1}	3.5533	1.0941×10^{-1}	1.2289×10^{-1}
	A_6	8.6218×10^{-2}	3.8753×10^{-1}	3.5079×10^{-1}	7.6908×10^{-2}	4.6985×10^{-1}	3.4707×10^{-1}	7.6130×10^{-2}	4.8313×10^{-1}	3.4730×10^{-1}
	A_7	6.8570×10^{-2}	1.1699×10^{-1}	1.1977×10^{-1}	7.0058×10^{-2}	1.1333×10^{-1}	1.1773×10^{-1}	7.4052×10^{-2}	1.2732×10^{-1}	1.1262×10^{-1}
	A_8	-1.5990×10^{-3}	-5.363×10^{-2}	-1.140×10^{-1}	-8.050×10^{-4}	-4.530×10^{-3}	-3.588×10^{-2}	-2.280×10^{-4}	-1.197×10^{-2}	4.4400×10^{-3}
	A_9	-6.9900×10^{-4}	2.0370×10^{-2}	1.3620×10^{-2}	1.5890×10^{-3}	2.7410×10^{-2}	2.4030×10^{-2}	5.0110×10^{-3}	2.0040×10^{-2}	2.1540×10^{-2}
$\frac{(EA_{0.8})_r}{EA_{0.8}}$	A_1	1.2910×10^{-1}	1.1100	8.9000×10^{-1}	7.0000	-1.0800	-7.200×10^{-1}	6.0700	-8.900×10^{-1}	1.600×10^{-1}
	A_2	0.0000	-5.3100	-4.4500	-8.300×10^{-1}	-2.4700	-1.6700	-8.900×10^{-1}	-2.2500	-1.3900
	A_3	0.0000	-2.5900	-2.1400	-5.2100	-3.9100	-1.6400	-4.7700	-3.1600	-2.2300
	A_4	9.4000×10^{-1}	3.0800	1.9900	3.1700	5.5900	3.7200	3.7300	5.5200	2.9800
	A_5	-6.5200	1.9400	1.3200	1.5200	3.3900	2.5600	1.5300	3.2700	1.9900
	A_6	1.1215×10^{-2}	3.1800×10^{-1}	2.3450×10^{-1}	1.4300×10^{-1}	3.6570×10^{-1}	2.3460×10^{-1}	1.3690×10^{-1}	3.8120×10^{-1}	2.6000×10^{-1}
	A_7	0.0000	1.4450×10^{-1}	1.0890×10^{-1}	1.6020×10^{-1}	1.5310×10^{-1}	1.1400×10^{-1}	1.5380×10^{-1}	1.6900×10^{-1}	1.2670×10^{-1}
	A_8	0.0000	-2.0300	-6.800×10^{-1}	-1.000×10^{-1}	-9.100×10^{-1}	3.3000×10^{-1}	-1.900×10^{-1}	-1.1400	3.100×10^{-1}
	A_9	1.2910×10^{-1}	1.4900	9.9000×10^{-1}	8.0000×10^{-1}	3.1400	2.4000	8.5000×10^{-1}	3.0500	1.8200

Table 7-5: Coefficient of Equation 16

E_i	$R_D = 0$ (Unrestrained)			$R_D = 0.5$ (Partially Restrained)			$R_D = 1$ (Fully Restrained)		
	$\lambda = 0.0$	$\lambda = 0.2$	$\lambda = 0.4$	$\lambda = 0.0$	$\lambda = 0.2$	$\lambda = 0.4$	$\lambda = 0.0$	$\lambda = 0.2$	$\lambda = 0.4$
E_1	1.5970×10^{-4}	-6.3690×10^{-5}	-3.8110×10^{-4}	-1.4039×10^{-4}	-2.0152×10^{-4}	-3.9570×10^{-4}	-2.1777×10^{-4}	-2.5416×10^{-4}	-4.118×10^{-4}
E_2	6.7450×10^{-5}	-9.9740×10^{-5}	-3.4650×10^{-4}	-2.4966×10^{-4}	-2.9193×10^{-4}	-3.7787×10^{-4}	-2.7889×10^{-4}	-3.2846×10^{-4}	-4.019×10^{-4}
E_3	5.9000×10^{-6}	-1.0900×10^{-6}	-5.390×10^{-6}	-2.7100×10^{-6}	-3.5900×10^{-6}	-5.6300×10^{-6}	-2.6200×10^{-6}	-5.0800×10^{-6}	-5.870×10^{-6}
E_4	-7.0000×10^{-8}	0.0000	2.2000×10^{-7}	5.0000×10^{-8}	6.0000×10^{-8}	2.8000×10^{-7}	7.0000×10^{-8}	1.5000×10^{-7}	2.6000×10^{-7}
E_5	-3.5235×10^{-4}	7.1700×10^{-6}	1.9635×10^{-4}	1.6603×10^{-4}	2.3122×10^{-4}	2.8654×10^{-4}	2.2061×10^{-4}	2.8139×10^{-4}	3.2832×10^{-4}
E_6	-4.1350×10^{-5}	6.6150×10^{-5}	2.8579×10^{-4}	5.3170×10^{-5}	1.0500×10^{-4}	1.6644×10^{-4}	7.4880×10^{-5}	1.2022×10^{-4}	1.4722×10^{-4}
E_7	-8.9990×10^{-3}	2.9634×10^{-3}	1.5928×10^{-2}	7.1963×10^{-3}	8.6660×10^{-3}	1.6385×10^{-2}	8.6940×10^{-3}	1.0437×10^{-2}	1.7727×10^{-2}
E_8	1.0900×10^{-6}	6.1000×10^{-7}	7.4000×10^{-7}	2.6500×10^{-6}	2.7100×10^{-6}	2.8400×10^{-6}	2.7800×10^{-6}	2.9300×10^{-6}	3.180×10^{-6}
E_9	6.0900×10^{-6}	3.5600×10^{-6}	6.9900×10^{-6}	5.7000×10^{-7}	3.3000×10^{-7}	1.7000×10^{-7}	8.6000×10^{-7}	8.0000×10^{-7}	-2.300×10^{-7}

7.9.8 Residual Thermal Curvature in Columns Heated from 3 Sides

In Chapter 6, the symmetric axially loaded columns were exposed to uniform heating from 4 sides. Therefore, curvature due to elevated temperatures did not develop during and after fire. However, when the columns are heated from 3 sides, temperature distribution within the section becomes asymmetric. Both the thermal and transient strain components respond to this change in temperature and the section bends in order to maintain equilibrium. Based on the results obtained from the parametric study, Equation 17 is proposed to evaluate the residual curvature in columns heated from 3 sides only.

$$\varphi_i = E_1 + E_2 t + E_2 t^2 + E_3 f'_c + E_4 f_y + E_5 b + \frac{E_6}{h^3} + E_7 \rho + E_8 t^2 b \quad (17)$$

The coefficients $E_{i(i=1,2,3,4,5,6,7,8)}$ are presented in Table 7-6 in terms of restraint condition (R_D) and initial axial load level (λ). The outcomes of Equation 17 are validated against the analytical results and found to be in a very good agreement.

Table 7-6: Coefficient of Equation 17

E_i	$R_D = 0$ (Unrestrained)			$R_D = 0.5$ (Partially Restrained)			$R_D = 1$ (Fully Restrained)		
	$\lambda = 0.0$	$\lambda = 0.2$	$\lambda = 0.4$	$\lambda = 0.0$	$\lambda = 0.2$	$\lambda = 0.4$	$\lambda = 0.0$	$\lambda = 0.2$	$\lambda = 0.4$
E_1	-6.858×10^{-7}	-7.109×10^{-7}	-6.893×10^{-7}	-6.769×10^{-7}	-6.486×10^{-7}	-6.501×10^{-7}	-6.024×10^{-7}	-5.643×10^{-7}	-6.046×10^{-7}
E_2	1.115×10^{-6}	1.107×10^{-6}	1.109×10^{-6}	1.101×10^{-6}	1.010×10^{-6}	1.046×10^{-6}	9.796×10^{-7}	8.790×10^{-7}	9.725×10^{-7}
E_3	-1.385×10^{-7}	-1.374×10^{-7}	-1.380×10^{-7}	-1.367×10^{-7}	-1.254×10^{-7}	-1.302×10^{-7}	-1.216×10^{-7}	-1.091×10^{-7}	-1.210×10^{-7}
E_4	2.055×10^{-9}	2.910×10^{-9}	2.575×10^{-9}	2.028×10^{-9}	2.655×10^{-9}	2.429×10^{-9}	1.805×10^{-9}	2.310×10^{-9}	2.259×10^{-9}
E_5	3.450×10^{-10}	3.553×10^{-10}	3.548×10^{-10}	3.405×10^{-10}	3.242×10^{-10}	3.346×10^{-10}	3.030×10^{-10}	2.820×10^{-10}	3.112×10^{-10}
E_6	7.232×10^{-7}	7.260×10^{-7}	7.164×10^{-7}	7.138×10^{-7}	6.623×10^{-7}	6.757×10^{-7}	6.353×10^{-7}	5.762×10^{-7}	6.284×10^{-7}
E_7	6.954×10^{-8}	6.907×10^{-8}	6.896×10^{-8}	6.864×10^{-8}	6.301×10^{-8}	6.504×10^{-8}	6.109×10^{-8}	5.482×10^{-8}	6.049×10^{-8}
E_8	4.184×10^{-6}	4.452×10^{-6}	3.890×10^{-6}	4.129×10^{-6}	4.062×10^{-6}	3.668×10^{-6}	3.675×10^{-6}	3.534×10^{-6}	3.412×10^{-6}
E_9	-1.849×10^{-8}	-1.598×10^{-8}	-1.666×10^{-8}	-1.825×10^{-8}	-1.458×10^{-8}	-1.571×10^{-8}	-1.625×10^{-8}	-1.268×10^{-8}	-1.461×10^{-8}

7.10 Proposed Procedure to Analyze Fire-Damaged RC Members

A method to assess the residual behavior of RC frame structures partially or fully exposed to fire is proposed in view of the extensive parametric study performed. The procedure is iterative and requires modeling the structure using any commercially available structural analysis software.

The analysis commences by first modeling the geometry, loading cases and ambient material properties of the frame structure using a finite element software. This step is usually performed earlier during designing the structure under normal loading and exposure conditions. The procedure is then carried out as detailed in the following steps for each of the fire-damaged members in the frame:

- 1) Isolate each damaged member and determine the stiffness of the supports. This is performed by replacing the member with a unit load and recording the associated deformation.
- 2) Determine the axial load level (λ) and flexural load level (λ_f) acting on the member due to the applied load by performing structural analysis on the full model.

- 3) Determine the residual properties of the fire-exposed members by utilizing the proposed Equations 8 through 16.
- 4) Adjust the residual stiffness of each fire-exposed member in the finite element model in view of the results calculated in step 3.
- 5) Apply the residual thermal expansion and thermal curvature on each fire-exposed member. This can be performed by assigning temperature variation in each member that result in the same ϵ_i and ϕ_i .
- 6) Perform the analysis on the model considering the modified properties and applied thermal loads. The deformed shape and straining actions can be obtained.
- 7) Check whether the fire-exposed members are resisting the applied loads in view of their residual capacity obtained from the proposed Equations.

7.11 Conclusions

In this chapter, both thermal and sectional analyses are performed aiming at determining the residual behavior of fire-damaged members in typical RC frames. The temperature-load history experienced by the exposed members is considered in detail in the analytical study. The model is validated against relevant experimental studies and a parametric study is then carried out to determine the influence of various loading conditions and fire scenarios on the residual properties of the members. The study has led to developing an objective-based method to allow engineers to preliminarily evaluate the deterioration in fire-damaged members. Main findings coming out of this study are as follow:

- 1) The influence of support conditions should be taken into account in the analysis of fire-damaged RC members. The ability of the frame in providing translational and/or rotational restraints to the supported members increases the induced force axial and/or bending moment necessary to counteract the anticipated thermal deformations of the member. The magnitude of these additional restraining forces relies on the residual stiffness of the damaged member; the restraining stiffness provided by the adjacent frame elements; and the initial load level acting on the heated member.

- 2) Variation in temperature can result in substantial stresses in statically indeterminate structures which must be considered in the design. These stresses can be accounted for by modifying the fixed end forces depending on the axial and rotational rigidities of the supports.
- 3) Subjecting a member to a moderate initial load before and during heating, both transient and creep strains are developed and counteract thermal expansion tendency of the member.
- 4) Increasing the concrete compressive strength is found to have an insignificant inverse relationship on the reduction in the residual flexural capacity of the fire-damaged member for all load levels in the examined range.
- 5) Fire duration and member width have the most significant influence on the residual stiffness and capacity of the fire-damaged members.

7.12 References

- [1] Denoël, J.F. “Fire Safety and Concrete Structures,” FEBELCEM - Federation of Belgian Cement Industry, 2007, Brussel, Belgium, 90 pp.
- [2] Beitel, J.J. and Iwankiw, N.R. “Historical Survey of Multi-Story Building Collapses Due to Fire,” Jensen Hughes, FPE 3rd Quarter, 2005.
- [3] Park, T.W. “Inspection of Collapse Cause of Sampoong Department Store,” Forensic Science International, 2012, Vol. 217, No. 1-3, pp. 119-126.
- [4] Shepherd, E. “Kader Fire Aftermath: Industrial Failure,” Occupational Safety and Health, Asian Labor, 2003, Update 47.
- [5] Schellhammer, J., Delatte, N. and Bosela, P. “Another Look at the Collapse of Skyline Plaza at Bailey’s Crossroads, Virginia,” Journal of Performance of Constructed Facilities; 2013, Vol. 27, No. 3, pp. 354-361.
- [6] El-Fitiany, S. and Youssef, M. “Assessing the Flexural and Axial Behavior of Reinforced Concrete Members at Elevated Temperatures Using Sectional Analysis,” Fire Safety Journal, Elsevier, 2009, Vol. 44, No. 5, pp. 691-703.
- [7] Lie, T.T. “Structural Fire Protection,” ASCE Manuals and Reports on Engineering Practice, 1992, No. 78, New York, NY..
- [8] ASTM. “Standard Methods of Fire Test of Building Construction and Materials,” Test Method E119-01, American Society for Testing and Materials, 2001, West Conshohocken, PA.
- [9] ISO. “Fire Resistance Tests, Elements of Building Construction, ISO 834,” International Organization for Standardization, 2014, London, UK.
- [10] Usmani, A.S., Rotter, J.M., Lamont, S., Sanad, A.M. and Gillie, M. “Fundamental principles of structural behavior under thermal effects,” Fire Safety Journal, 2001, Vol. 36, No. 8, pp. 721-744.

- [11] Guo, Z. and Shi, X. "Experimental and Calculation of Reinforced Concrete at Elevated Temperatures," Butterworth-Heinemann, Elsevier, 2011, pp. 168-188.
- [12] Anderberg, Y. "Stress and Deformation Characteristics of Concrete at High Temperatures," Lund Institute of Technology, 1976, Stockholm, Sweden.
- [13] CSA. "Design of Concrete Structures (CAN/ CSA A23.3-14)," Cement Association of Canada, 3rd Ed., 2014, Ottawa, ON, 297 pp.
- [14] Alhadid, M.M. Youssef, M.A. "A Simplified Method to Calculate the Flexural Capacity of Fire-Damaged Reinforced Concrete Beams," Engineering Structures, Elsevier, (Under Revision).
- [15] Kodur, V.K.R., Dwaikat, M.B. and Fike, R.S. "An Approach for Evaluating the Residual Strength of Fire-Exposed RC Beams," Magazine of Concrete Research, 2010, Vol. 62, No. 7, pp. 479-488.
- [16] Haddad, R., Shannag, M. and Moh'd, Alaa. "Repair of heat-damaged RC shallow beams using advanced composites," Materials and Structures, 2008, Vol. 41, No. 2, pp. 287-299.
- [17] Chen, Y.H., Chang, Y.F., Yao G.C. and Sheu, M.S. "Experimental research on post-fire behaviour of reinforced concrete columns," Fire Safety Journal, 2009, Vol. 44, No. 5, pp. 741-748.
- [18] Jau, W. and Huang, K. "A study of reinforced concrete corner columns after fire," Cement and Concrete Composite, 2007, Vol. 30, No. 7, pp. 622-638.
- [19] Yaqub, M. and Bailey, C.G. "Repair of Fire Damaged Circular Reinforced Concrete Columns with FRP Composites," Construction and Building Materials, 2011, Vol. 25, No. 1, pp. 359-370.
- [20] Elsanadedy, H., Almusallam, T., Al-Salloum, Y. and Iqbal, R. "Effect of High Temperature on Structural Response of Reinforced Concrete Circular Columns

Strengthened with Fiber Reinforced Polymer Composites,” *Journal of Composite Materials*, 2016, pp. 1-23.

[21] El-Fitiany, S. and Youssef, M. “Simplified Method to Analyze Continuous Reinforced Concrete Beams during Fire Exposure,” *ACI Structural Journal*, 2014, Vol. 111, No. 1, pp. 145-155.

Chapter 8

8 STRUCTURAL PERFORMANCE OF JACKETED FIRE-EXPOSED REINFORCED CONCRETE MEMBERS IN FRAME STRUCTURES CONSIDERING SLIP INFLUENCE

Concrete is classified as one of the most superior materials in resisting elevated temperatures owing to its low thermal conductivity and significantly high thermal inertia. Throughout their intended life span, reinforced concrete structures are designed to exhibit adequate behavior in terms of both strength and serviceability. Unfortunately, exposing such structures to elevated temperatures has tremendous implications on their expected performance due to degradation of the composing materials, generation of residual stresses and alteration of deformation behavior. The mechanical properties of concrete are barely reduced when the maximum temperature reached is below 250°C to 300°C [1]. However, in typical fire scenarios where enough fuel and good ventilation exist, temperature significantly exceeds these limits. In such conditions, concrete experiences remarkable cracking between the aggregate and the cement paste due to the variation in thermal properties between them. At temperatures above 600°C, significant chemical reactions and physical changes take place resulting in substantial deterioration causing the structural members to become structurally useless. The deterioration becomes more pronounced when the temperature of the embedded steel reinforcement exceeds 500°C [2] as they experience permanent drop in yield strength.

Comprehensive assessment and mitigation processes should be performed to ensure that the structure demonstrates acceptable safety and serviceability criteria depending on its functionality. Redesign of the structural members requires the evaluation of the behavior of repaired members in comparison with their intact counterparts. Among the various rehabilitation techniques of reinforced concrete members, jacketing using reinforced concrete layers is commonly used worldwide. It has the advantage of restoring, or even exceeding, both strength and stiffness of the fire-damaged structural members while maintaining their excellent fire resistance and thermal properties. The repair procedure

according to this technique encompasses the removal of the damaged concrete, treatment of the existing steel bars, roughening of the exposed concrete surface, and adding new concrete layers (and additional reinforcement if needed). The procedure followed in practice to repair fire-exposed concrete members is similar to that adopted for repairing corroded reinforced concrete structural elements.

The influence of interfacial slip between the concrete jacket and the original concrete member on the residual strength and deformation behavior of fire-damaged elements is not previously investigated. In practice, full bond is assumed between the concrete core and the attached concrete layers provided that some criteria are satisfied [3]. The error associated with this assumption may become relatively significant and could result in larger deformations and lower capacity of the structure.

In addition, the increased dimensions of the repaired structural members and the alteration in their mechanical properties lead to a remarkable change in their stiffness. The modified characteristics of the repaired members affect the load path in the entire frame. Thus, repair of fire-exposed members should be performed considering the global behavior of the entire frame and the mutual interaction between the composing structural members. In the current design practice, the capacity of the repaired fire-exposed members is carried out usually for each member separately while ignoring the consequent stress redistribution taking place in other structural elements.

The current study aims at investigating the changes in the structural behavior of RC frames associated with exposure to standard fire before and after jacketing. It also examines the influence of interfacial slip on the structural performance of jacketed fire-exposed RC members. The work described in this chapter is performed as a culmination of previous analytical studies that resulted in proposing simplified calculation procedures that address both the interfacial slip in jacketed members (Chapters 3 and 4) and the residual characteristics of fire-exposed members (Chapters 5, 6 and 7). A brief description of the material mechanical properties and analysis considerations adopted in those studies is first presented. The structural performance of the repaired fire-exposed members is compared to that obtained for both intact and unjacketed fire-damaged

members. A procedure is described to assist engineers during the design phase to predict the behavior of RC frame systems exposed to severe fire incidents and repaired with concrete jacket.

8.1 Applicability of the Proposed Method

This section discusses the applicability of the proposed method for analyzing RC frame systems by presenting a brief summary of the assumptions and analytical work considered in Chapters 3 through 7.

8.1.1 Analysis Main Assumptions

Several assumptions were made and validated by the authors when performing the thermal and structural analyses. Firstly, thermal analysis was performed considering that the structural members are exposed to ASTM E119 standard fire during the heating phase up to the specified fire duration (t_f), beyond which ISO 834 gradual cooling curve was adopted. Heat flow was assumed to be uniform along the member length and consequently two dimensional heat transfer analysis was performed on the cross-section. After reaching the maximum temperature, concrete thermal properties were assumed to maintain their ultimate values since thermal properties of concrete are irreversible [4-6]. Throughout the heating-cooling cycle, cross sections are assumed to remain plane along the entire span. This assumption was validated for temperatures up to 1200°C [7]. The proposed work is limited to normal weight concrete and consequently spalling was neglected. Perfect bond is assumed to exist between the steel reinforcement and the surrounding concrete material. The influence of concrete tensile cracks on heat flow was neglected in the heat transfer analysis. In case of compression members, failure was not governed by buckling. Hence, geometrical nonlinearity was not considered in the analysis.

8.1.2 Mechanical Characteristics Before, During and After Fire

After exposure to elevated temperatures, the mechanical properties and structural characteristics of concrete are altered and do not exhibit complete recovery. These permanent variations result in considerable weakening of the structural members as

indicated by the drop in both stiffness and capacity. They also cause permanent expansion or contraction in the fire-exposed members depending on the state of stress during heating. The literature is ample with empirical models that describe the residual behavior of concrete exposed to various heating and loading conditions. The calculation procedures described by the authors in Chapters 5 to 7 were proposed in view of the constitutive relationship given by the general form of Tsai [8] to represent the compressive stress-strain relationship of concrete at all stages. During fire, the reduced compressive strength due to fire (f'_{cT}) proposed by Hertz [5] is adopted; whereas, concrete strain at peak stress at elevated temperatures (ϵ_{oT}) is determined by Terro [9] formula. The post-fire mechanical properties are calculated based on the expressions provided by Chang [10].

Regarding the steel reinforcement, full recovery of mechanical properties is usually attained unless temperature exceed 500°C. The constitutive relationship of steel described by Karthik and Mander [11] was implemented in the proposed analytical model proposed by the authors as it conveniently combines the initial elastic response, yield plateau and strain hardening stages in a rigorous form. At elevated temperatures, Lie [12] model was adopted as it implicitly includes the reduction in yield strength due to fire. The post-fire mechanical properties of steel were obtained from the experimental work provided by Felicetti *et al.*, Neves *et al.* and Qiang *et al.* [2,13,14].

8.1.3 Residual Strain Components

The proposed calculation procedure and the developed expressions in Chapters 5 through 7 account for load-temperature interaction and explicitly consider the various strain components developed throughout the heating-cooling phase. The total strain (ϵ_t) developed along the cross-section of RC structural member during and after fire encompasses four categories: stress-related strain (ϵ_m) due to the applied loads, free thermal strain (ϵ_{th}) due to change in temperature, creep strain (ϵ_{cr}) due to change in molecular arrangement, transient strain (ϵ_r) due to interaction between compressive load and temperature in concrete. Free thermal strain of both concrete and steel bars is determined from EN 1992-1-2 (Eurocode) [15] proposed expressions. Regarding the transient and creep strains, the empirical model proposed by Terro [9] is adopted as it

determines the value of both strain components simultaneously in terms of load induced thermal strain (ε_{LITS}).

8.1.4 Temperature-Load Interaction

The actual deformation behavior and residual stresses induced in the fire-exposed members are highly dependent on the simultaneous interaction between temperature and the applied loads. In unrestrained members, the residual transient strains are calculated considering the constant applied load throughout the heating-cooling cycle. However, restraining the member induces additional compressive stresses that counteract its tendency to expand. The magnitude of the extra restraining forces depends on the stiffness of the member, temperature distribution along the cross-section, degree of restraint and the influence of transient strain. During heating, the aforementioned factors vary with time resulting in continuous fluctuation of the restraining force. These implications were considered in the proposed analytical model by performing simultaneous thermal and sectional analyses at each time increment throughout the heating-cooling cycle. Therefore, the influence of interaction between temperature and load level on the member's post-fire capacity and deformation behavior was explicitly implemented in the analysis.

8.1.5 Description of the Frame System and Fire Scenarios

Fig. 8-1 shows an elevation view of a 3 stories frame structure considered in the analysis. The cross-sectional dimensions and reinforcement of the composing intact members are presented in Fig. 8-2. Both beams and columns are constructed using normal weight concrete with f_c' of 35 MPa and reinforced with grade 400 MPa steel bars that have a strain hardening stiffness of 1% of their elastic stiffness. The reinforcement ratio of beams and columns are predefined as 0.0106 and 0.03, respectively. The columns are assumed not to change cross-sectional dimensions along the entire height of the building. The moment of inertia of both member types is determined assuming cracked cross-sections (i.e. $I_{beam} = 0.35I_g$ and $I_{column} = 0.7I_g$) where I_g is the gross moment of inertia of the considered member. The frame is loaded by subjecting the beams to a uniformly

distributed load of 25 kN/m along the entire span. The own weight of the structural members is considered as part of the applied uniform load acting on the beams only.

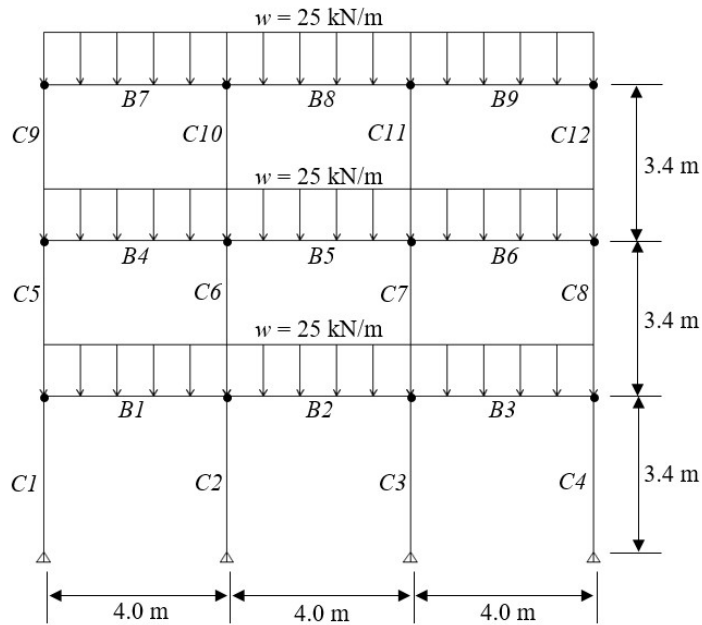


Figure 8-1: Elevation view of the frame model showing load pattern

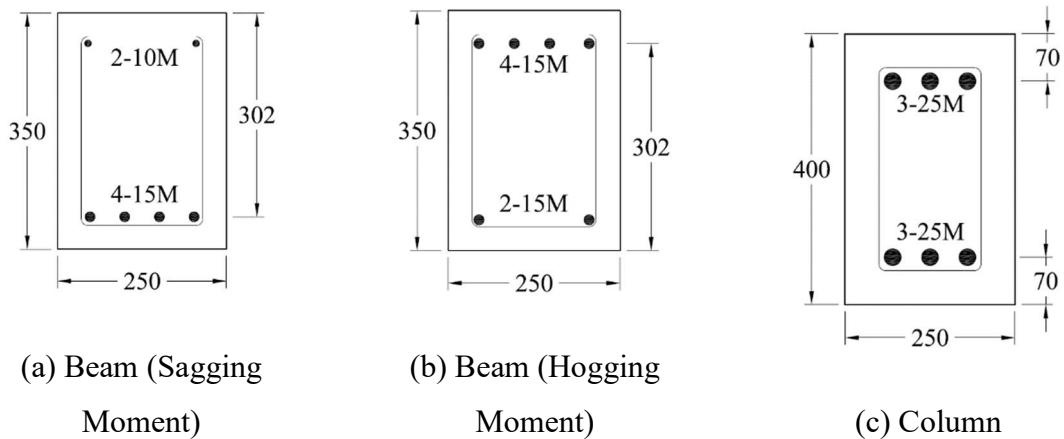


Figure 8-2: Cross-sectional views of the sections in the analyzed RC frame

After fire, the exposed members are repaired using concrete jackets as shown in Fig. 8-3 for both beams and columns. The jacket thickness is assumed to take a value of 100 mm that lies within the practical recommended range [16]. The area of the jacket steel bars is determined to maintain the reinforcement ratio in the jacketed section similar to that in the original section. The sizes and spacing between the steel bars are determined in accordance with A23.3-14 (CSA 2014). The provided jacket shear reinforcement is assumed to be sufficient to counteract the applied shear force minus the shear capacity of the fire-damaged section. The optimum jacket thickness and reinforcement configuration can be accurately calculated by assuming different values and performing the same analysis procedure again on the repaired frame.

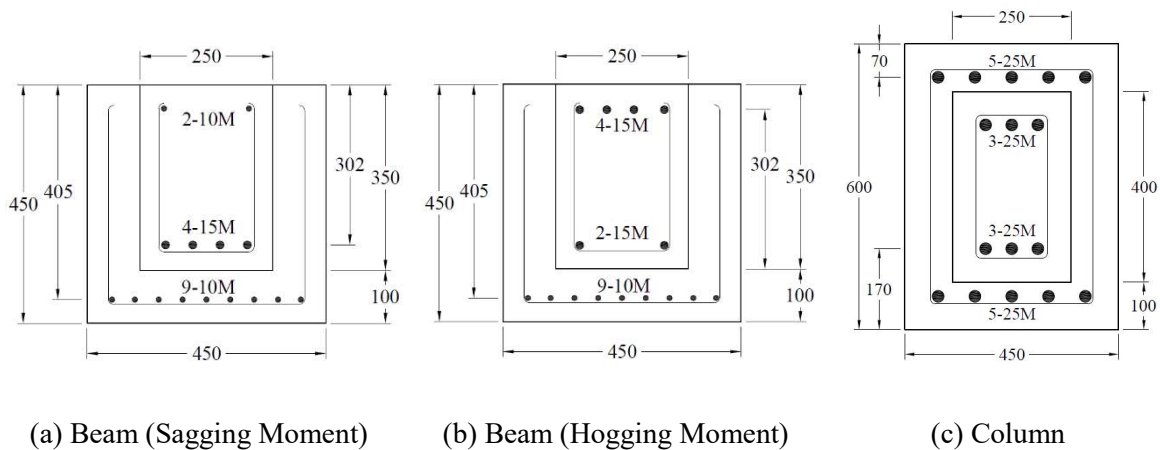


Figure 8-3: Cross-sectional views of the jacketed sections in the RC frame

The spread of fire in the considered frame is chosen based on two commonly encountered scenarios in real life as shown in Fig. 8-4. The first one represents the case where fire is spread in the first floor where storage areas are usually encountered. This provides sufficient fuel and ventilation for fire to propagate before the intervention of fire brigades. The second case is spread of fire from one side along the elevation of the building. This case usually occurs due to the role of façade material in providing the required fuel, the outstanding ventilation caused by direct exposure to atmosphere and the fast fire propagation in the vertical direction.

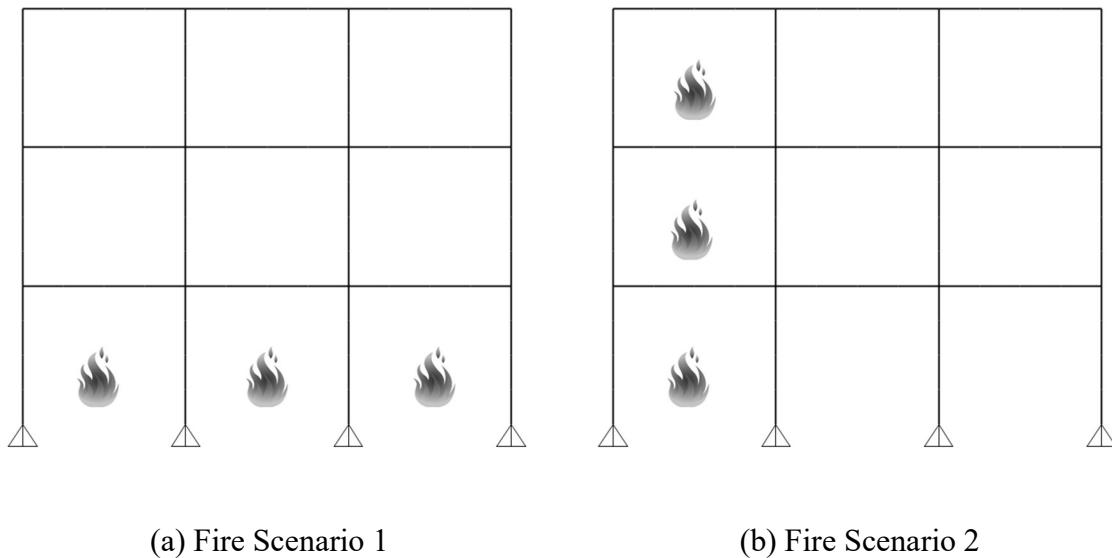


Figure 8-4: Elevation view of the frame model showing load pattern

The calculation procedure encompasses two main stages. The first one is the determination of the residual properties of the fire-exposed members and the modified characteristics of the jacketed members. This step is performed by identifying the fire-exposed members and applying the relevant procedure described in Chapters 3 through 7 to obtain their local behavior. The next analysis stage is conducted by adjusting the stiffness of the affected members in the finite element model and apply the residual thermal strains and curvatures as temperature load. The resulting straining actions and deformation represent the expected behavior of the modified frame.

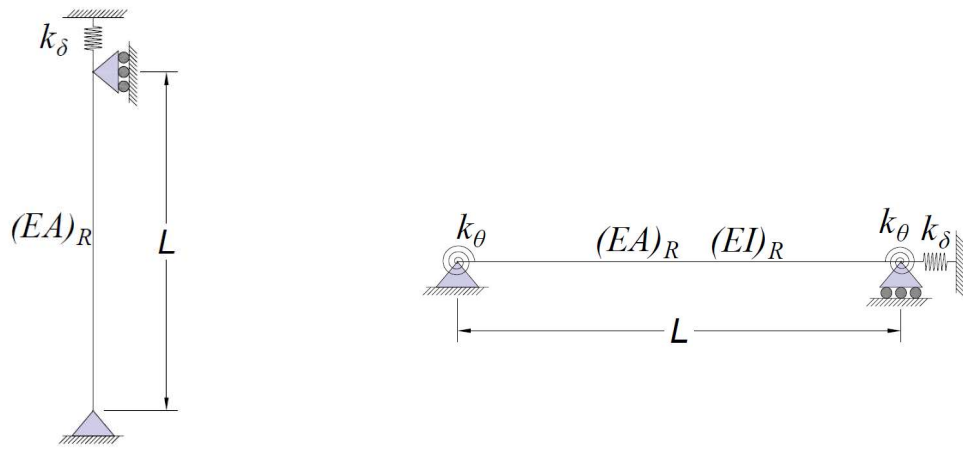
8.2 Local Behavior of the Affected Frame Members

The local structural performance of the fire-exposed members before and after jacketing is determined in this section. According to the two fire scenarios considered in the analysis, beams B1, B2, B3, B4 and B7 and columns C1, C2, C3, C4, C5, C6, C9 and C10 are directly affected by fire. The residual capacity, stiffness and thermal deformations in the affected columns and beams after exposure to fire are determined with reference to Chapters 5 through 7. Then, the modified stiffness and capacity of the

jacketed members are obtained considering interfacial slip as described in the procedure proposed in Chapters 3 and 4.

8.2.1 Support Conditions of the Considered Members

Fig. 8-5 shows the isolated model of both columns and beams composing the frame system. The structural performance of each member can be determined by separating it from the unloaded frame and assigning the appropriate boundary conditions and stiffness.



(a) Isolated Column Model.

(b) Isolated Beam Model.

Figure 8-5: Isolated models of the different structural members in the frame

The axial and flexural restraints provided by the frame are modeled as springs with stiffness of k_δ and k_θ , respectively. The spring stiffness can be obtained from the finite element model by replacing the considered member with a unit load (or moment) acting on the adjacent joints. The process is repeated twice by applying the unit load (or moment) at each joint separately and recording the resulting deformation. The stiffness of the spring at each joint is calculated as the magnitude of the applied load (or moment) divided by the corresponding deformation at the same degree of freedom. The equivalent stiffness (k_{eq}) is then calculated considering springs in series from Equations 1.

$$(k)_{eq} = \frac{(k)_1(k)_2}{(k)_1 + (k)_2} \quad (1)$$

Figs. 8-6(a) and 8-6(b) illustrate the aforementioned procedure to obtain the axial stiffness of the spring (k_δ) at the lower and upper supports of column C6, respectively. The stiffness provided by the frame at the lower support is higher than that at the upper support as indicated by the smaller deformation in the former case under the same applied load. The same procedure is performed again to obtain the axial stiffness at the left and right supports of beam B1 as shown in Figs. 8-6(c) and 8-6(d), respectively.

The smaller deformation at the right support reflects the influence of the additional frame members in the two adjacent bays on resisting the deformation. Regarding the flexural stiffness of the springs, Figs. 8-6(e) and 8-6(f) show the deformed shape of the frame when beam B1 is replaced with a unit moment acting on the left and right supports, respectively.

The deformation at the interior support is shown to be lower than its counterpart at the exterior support as expected. Tables 8-1 and 8-2 list the equivalent spring stiffness for the columns and beams under consideration, respectively.

Table 8-1: Axial spring stiffness and restraint ratios of the considered columns

Column	Spring Axial Stiffness, k_δ (N/mm)			R_D
	Top Support	Bottom Support	Equivalent	
C1	2.557×10^3	Pin	2.557×10^3	3.255×10^{-3}
C2	8.315×10^3	Pin	8.315×10^3	1.051×10^{-2}
C3	8.315×10^3	Pin	8.315×10^3	1.051×10^{-2}
C4	2.557×10^3	Pin	2.557×10^3	3.255×10^{-3}
C5	1.750×10^3	7.813×10^5	1.746×10^3	2.225×10^{-3}
C6	5.515×10^3	7.874×10^5	5.477×10^3	6.946×10^{-3}
C9	3.114×10^2	3.922×10^5	3.112×10^2	3.972×10^{-4}
C10	2.555×10^3	3.953×10^5	2.539×10^3	3.232×10^{-3}

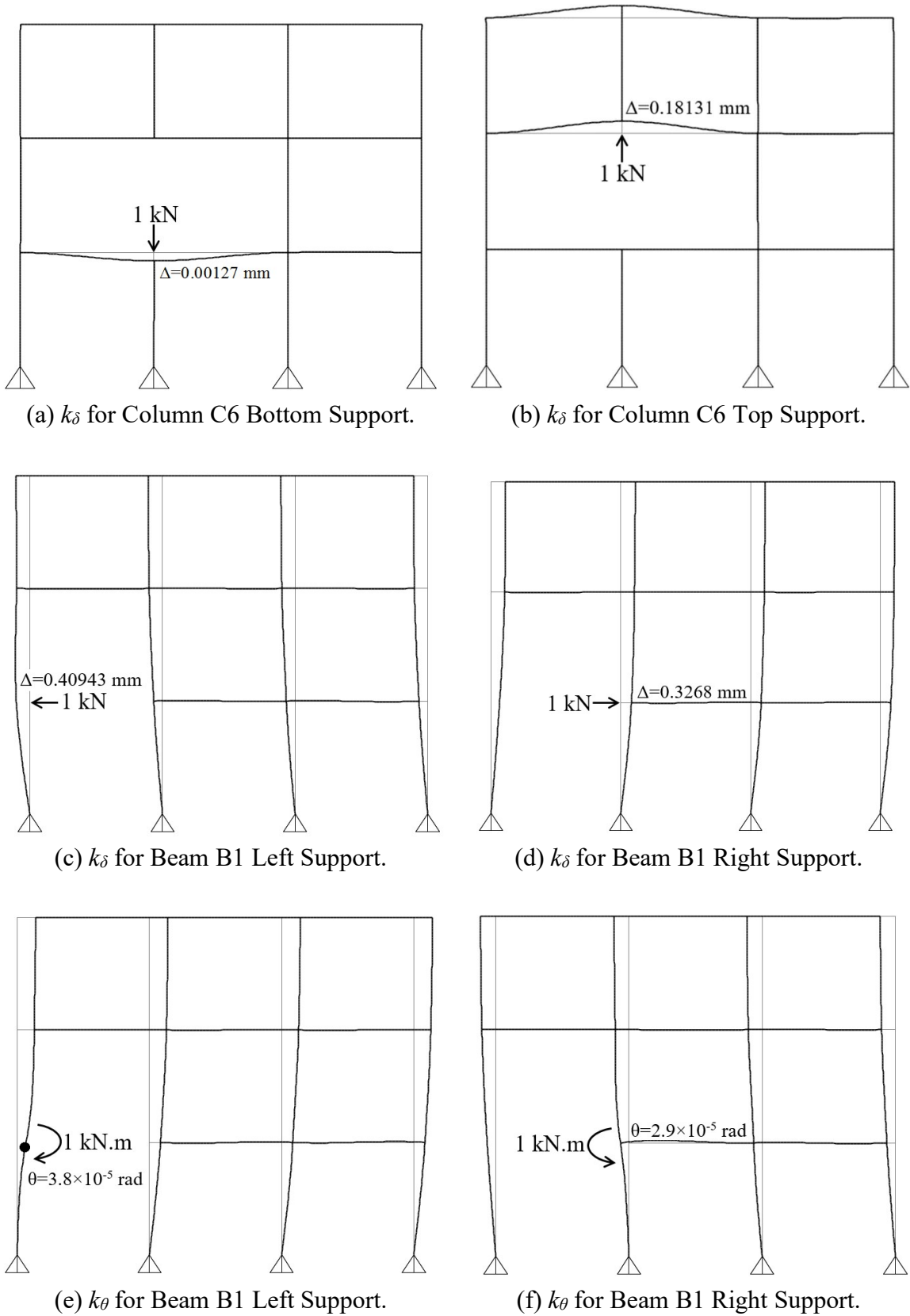


Figure 8-6: Isolated models of the different structural members in the frame

Table 8-2: Axial and flexural spring stiffness and restraint ratios of the considered beams

Beam	Spring Axial Stiffness, k_δ (N/mm)			R_D	Spring Rotational Stiffness, k_θ (N.mm/rad)			R_θ
	Left Support	Right Support	Equivalent		Left Support	Right Support	Equivalent	
B1	2.442×10^3	3.060×10^3	1.358×10^3	2.327×10^{-3}	2.610×10^{10}	3.466×10^{10}	1.489×10^{10}	0.516
B2	3.006×10^3	3.006×10^3	1.503×10^3	2.575×10^{-3}	3.544×10^{10}	3.544×10^{10}	1.772×10^{10}	0.559
B3	3.060×10^3	2.442×10^3	1.358×10^3	2.327×10^{-3}	3.466×10^{10}	2.610×10^{10}	1.489×10^{10}	0.516
B4	1.524×10^3	1.829×10^3	8.311×10^2	1.425×10^{-3}	3.182×10^{10}	3.951×10^{10}	1.762×10^{10}	0.558
B7	5.796×10^2	1.275×10^3	3.984×10^2	6.837×10^{-4}	5.757×10^9	2.520×10^{10}	4.686×10^9	0.251

Having determined the equivalent spring stiffness for each member, the restraint ratios are then calculated. These ratios represent the degree of restraint that is obtained by comparing the actual spring stiffness to the stiffness of perfectly fixed members. Detailed discussion about the axial and flexural restraints was provided in Chapter 7. The axial restraint ratio (R_D) and the flexural restraint ratio (R_θ) can be evaluated from Equations 2 and 3, respectively.

$$R_D = \frac{1}{1 + \left[\frac{EA}{k_\delta L} \right]} \quad (3)$$

$$R_\theta = \frac{1}{1 + \left[\frac{2EI}{k_\theta L} \right]} \quad (4)$$

Where EA is the axial stiffness of the considered section (N), EI is the flexural stiffness of the considered member (N.mm^2) and L is the member length (mm). The values of R_D and R_θ for the considered columns and beams are calculated and listed in Tables 8-1 and 8-2, respectively.

8.2.2 Initial Load Level Acting on the Members

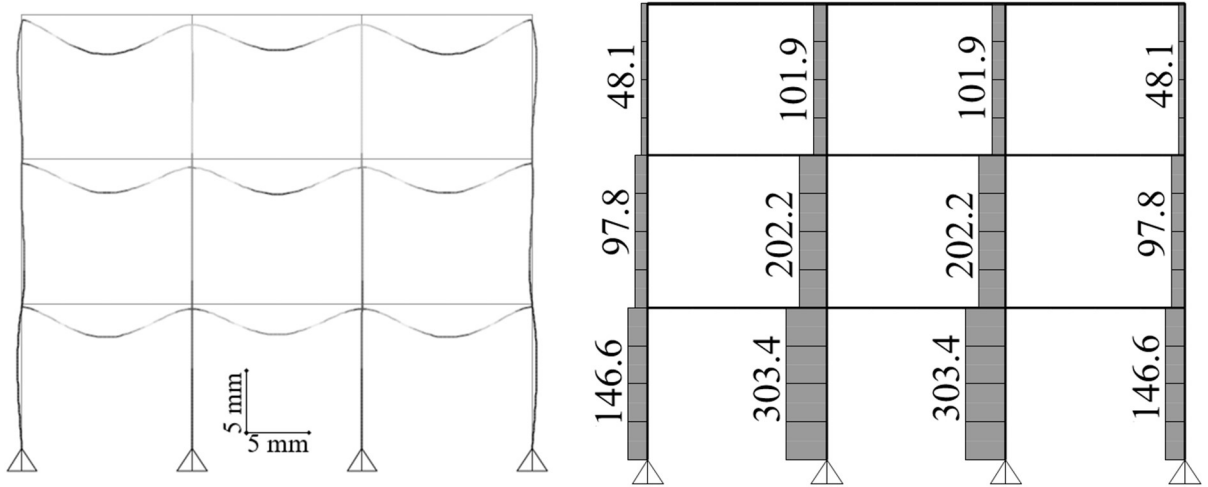
The axial initial load level (λ) in columns and the flexural initial load level (λ_f) in beam are required as inputs in the expressions proposed in Chapters 1 through 5. For instance, the interfacial slip in jacketed members is found to depend on the initial load level prior

to jacketing. The influence of slip on the flexural response of jacketed beams becomes less pronounced if they are initially loaded before the application of the additional concrete layers. Regarding the post-fire behavior of RC members, the initial load level acting on the member significantly alters the deformation behavior and the residual stresses. These changes occur due to the simultaneous influence of temperature and load on the development of transient strain component as discussed in section 7 of Chapter 6 and section 5 of Chapter 7.

The axial capacity of the typical column section is calculated as 4,595 kN based on the provided material properties and geometrical characteristics. The flexural capacity of all beams is calculated for both the sagging and hogging moment sections shown in Figs. 8-1(a) and 8-1(b) as 99.5 kN.m and 102.6 kN.m, respectively. To determine the load level acting on each member, the axial force, shear force and bending moment distributions are obtained from the structural analysis program on the intact frame system as shown in Fig. 8-7. The axial load level is then calculated by dividing the axial load acting on each member on its axial capacity. The flexural load level in beams is calculated twice to account for both the sagging moment and hogging moment sections. If jacketing of undamaged members is to be carried out, then the smaller negative moment value is chosen as it results in larger interfacial slip. However, if jacketing is performed on fire-exposed members, then the negative moment at both sides of the beam should be considered in the analysis. Tables 8-3 and 8-4 detail the initial load levels acting on the examined columns and beams, respectively.

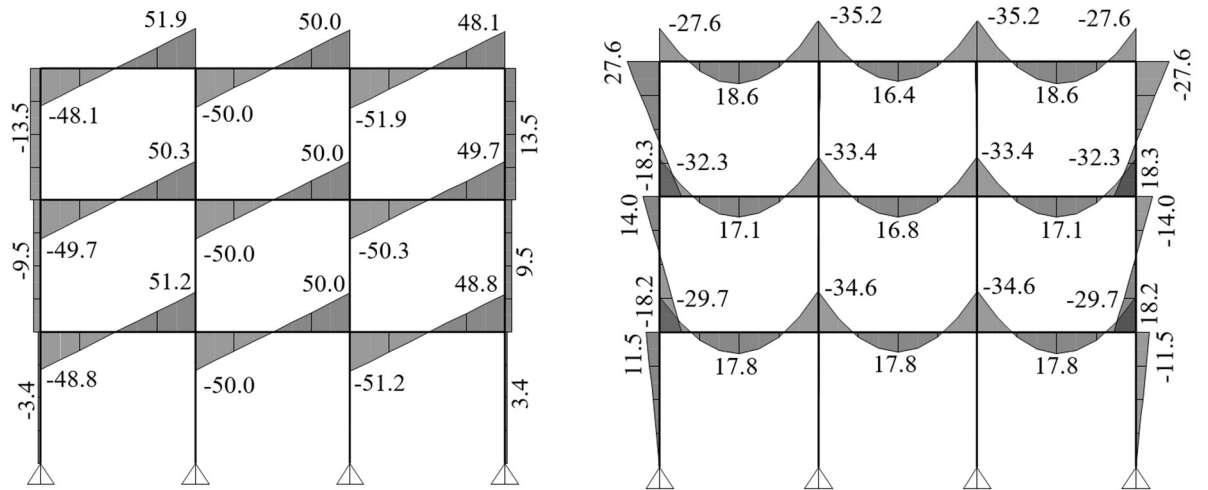
Table 8-3: Initial load level and residual properties of the fire-exposed columns

Column	λ	$\frac{P_r}{P_o}$	$\frac{(EA_i)_r}{EA_i}$	$\frac{(EA_{0.4})_r}{EA_{0.4}}$	$\frac{(EA_{0.8})_r}{EA_{0.8}}$	P_r (N)	$(EA_i)_r$ (N)	$(EA_{0.4})_r$ (N)	$(EA_{0.8})_r$ (N)
C1	0.032	N.A.	N.A.	N.A.	N.A.	N.A.	N.A.	N.A.	N.A.
C2	0.066	0.6025	0.3907	0.3267	0.2937	2.77×10^6	1.04×10^9	8.70×10^8	7.82×10^8
C3	0.066	0.6025	0.3907	0.3267	0.2937	2.77×10^6	1.04×10^9	8.70×10^8	7.82×10^8
C4	0.032	N.A.	N.A.	N.A.	N.A.	N.A.	N.A.	N.A.	N.A.
C5	0.021	N.A.	N.A.	N.A.	N.A.	N.A.	N.A.	N.A.	N.A.
C6	0.044	0.6064	0.3922	0.3298	0.2972	2.79×10^6	1.04×10^9	8.78×10^8	7.91×10^8
C9	0.010	N.A.	N.A.	N.A.	N.A.	N.A.	N.A.	N.A.	N.A.
C10	0.022	0.6103	0.3936	0.3329	0.3006	2.80×10^6	1.05×10^9	8.86×10^8	8.00×10^8



(a) Deformed Shape.

(b) Axial Force Distribution.



(c) Shear Force Distribution.

(d) Bending Moment Distribution.

Figure 8-7: Deformation shape and straining actions in the intact frame

Table 8-4: Initial load level and residual properties of the fire-exposed beams

Beam	λ	$\lambda_{f(Sag)}$	$\lambda_{f(HogLeft)}$	$\lambda_{f(HogRight)}$	$(EI)_{R,Sag}$ (kN.m ²)	$(EI)_{R,Hog}$ (kN.m ²)
B1	0.000	0.180	0.289	0.337	5.172×10^3	2.701×10^3
B2	0.000	0.180	0.337	0.337	5.196×10^3	2.713×10^3
B3	0.000	0.180	0.337	0.289	5.172×10^3	2.701×10^3
B4	0.000	0.173	0.315	0.326	5.196×10^3	2.713×10^3
B7	0.000	0.188	0.269	0.343	4.932×10^3	2.575×10^3

8.2.3 Residual Stiffness and Capacity of Columns Heated from 4 Sides

A procedure to evaluate the residual axial stiffness and capacity of axially loaded columns exposed to fire along their perimeter was proposed in Chapter 6. The reduction ratio (ω) given in Equation 6 take into account the geometrical properties, reinforcement ratio, mechanical characteristics, support conditions and fire duration.

$$\omega = A_1 + A_2\lambda + A_3f'_c + A_4f_y + A_5\rho + A_6\frac{\rho f_y}{f'_c} + A_7b + A_8h \quad (6)$$

Where λ is the initial load level at ambient conditions, f'_c is the concrete compressive strength (MPa), f_y is the steel yield strength (MPa), ρ is steel reinforcement ratio, b is section width (m), h is section height (m). The coefficients $(A_i)_{i=1,2,3,4,5,6,7,8}$ are given in Table 6-2 in Chapter 6 as functions of the axial restraint ratio (R_D) and fire duration at the end of the heating phase (t) in hours. For fire duration or axial restraint values not listed in the table, linear interpolation should be performed considering the actual values.

Columns C2, C3, C6 and C10 satisfy the conditions where the procedure can be applied as they are exposed to fire from four sides and possess geometrical and mechanical properties that are within the recommended range as mentioned in Chapter 6. The reduction ratios in capacity, initial axial stiffness, 40% secant axial stiffness and 80% secant axial stiffness are calculated using an Excel spreadsheet and reported in Table 8-3. The axial capacity and elastic stiffness at ambient conditions are found to be 4,595 kN

and 2.66×10^6 kN, respectively. The values of the residual axial capacity and stiffness for the examined columns are then evaluated by multiplying the reduction ratio with the corresponding property as shown in Table 8-3.

8.2.4 Residual Stiffness and Capacity of Columns Heated from 3 Sides

The residual behavior of columns exposed to fire from 3 sides is different from the case of four-sides heating. This variation is attributed to the non-uniform temperature distribution within the cross-section of the former case resulting in both thermal deformation and curvature. Consequently, the residual thermal and transient strains are also changed as they are highly dependant on the temperature distribution within the member. In addition, the deterioration in the mechanical properties of members exposed to fire from four sides is expected to be more pronounced as higher temperatures are reached for a longer cooling period than three-sides heating. In Chapter 7, expressions are developed based on an extensive parametric study to evaluate the residual capacity and stiffness of fire-exposed columns. A similar approach for columns heated from 4 sides is followed by calculating a reduction ratio (ω) in both capacity and secant stiffness at 0%, 40% and 80% of the ultimate capacity. Equation 7 shows the proposed expression for ω that accounts for the material used, cross-sectional dimensions, support conditions and fire duration.

$$\omega = A_1 + A_2\lambda + A_3f'_c + A_4f_y + A_5\rho + A_6b + A_7h + A_8 \frac{\rho bh}{\lambda} + A_9 \frac{(f'_c)^{0.12}}{\rho\sqrt{f_y}} \quad (7)$$

The parameters in Equation 7 are the same as the ones shown in Equation 6 with the same units. The coefficients $A_{i(i=1,2,3,4,5,6,7,8,9)}$ are listed in Table 7-4 in Chapter 7 in terms of the restraint condition and fire duration during the heating phase.

An examination of the considered frame reveals that the edge columns C1, C4, C5 and C9 are heated from 3 sides. The residual capacity and stiffness of the fire-exposed members are calculated and reported in Table 8-5. As expected, the residual properties for columns heated from 3 sides are larger than their counterparts heated from 4 sides for the same fire duration.

Table 8-5: Initial load level and residual properties of the fire-exposed columns

Column	$\frac{P_r}{P_o}$	$\frac{(EA_i)_r}{EA_i}$	$\frac{(EA_{0.4})_r}{EA_{0.4}}$	$\frac{(EA_{0.8})_r}{EA_{0.8}}$	P_r (kN)	$(EA_i)_r$ (kN)	$(EA_{0.4})_r$ (kN)	$(EA_{0.8})_r$ (kN)
C1	0.8345	0.5664	0.3724	0.3292	3.83×10^3	1.51×10^9	9.91×10^8	8.76×10^8
C4	0.8345	0.5664	0.3724	0.3219	3.83×10^3	1.51×10^9	9.91×10^8	8.57×10^8
C5	0.8350	0.5670	0.3730	0.3331	3.84×10^3	1.51×10^9	9.93×10^8	8.87×10^8
C9	0.8336	0.5692	0.3739	0.3301	3.83×10^3	1.52×10^9	9.95×10^8	8.79×10^8

8.2.5 Maximum Temperature Distribution in Beams

The knowledge of maximum temperature (T_{max}) distribution along the cross-section and at the location of the steel bars is essential to determine the residual capacity of the fire-exposed beams. Various studies (Gao *et al.*, Wickström, Abbasi and Hogg) [17, 18,19] have been performed to determine temperature distribution at the end of the heating phase (T_{hot}) in concrete sections exposed to a standard fire. In the current study, the continuous rise in temperature within the cross-section during the cooling phase is taken into account as discussed in Chapter 5. Firstly, the method proposed by Gao *et al.* (2014) to determine the temperature distribution reached before the initiation of the cooling phase due to its simplicity compared to other approaches. Then, the calculation procedure described in view of the proposed Equations 3 through 7 in Chapter 5 is carried out to determine a factor (η) that varies along the cross-section and represents the ratio between T_{max} and T_{hot} . The value of $(d/h_c)_{peak}$ that represent the normalized distance from the beam soffit to the balance heat transfer point is defined in Fig. 5-4 in Chapter 5 and is evaluated as 0.427 for the examined beams. Fig. 8-8 shows the both T_{max} and T_{hot} distributions obtained by applying Gao *et al.* [17] method and the procedure described in Chapter 5 of this study, respectively.

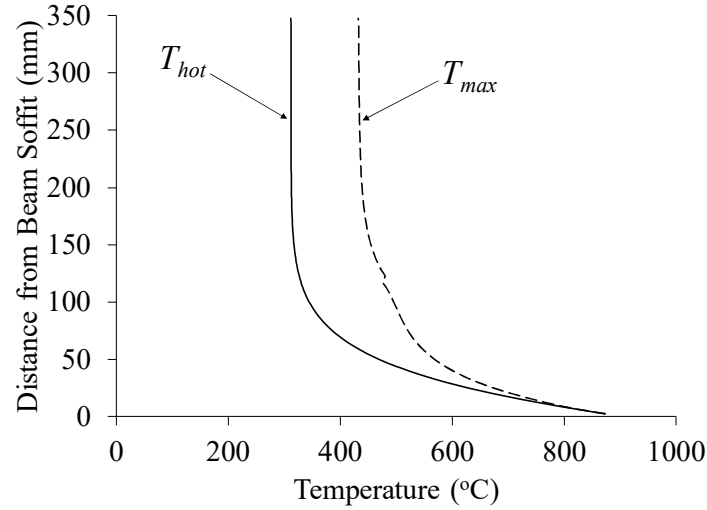


Figure 8-8: Temperature distribution along the beam cross-section

Regarding the temperature of the embedded steel bars, it must be evaluated at their exact location rather than considering the average temperature of the concrete layer they lie in. Wickström [18] proposed and validated a simplified method to predict the temperature at any point inside concrete sections at a given fire duration. Equations 8 through 11 are a compact form of the calculation procedure provided by Wickström [18] that can be implemented to calculate the temperature rise (T_{xy}) at a distance of (x) from one side of the beam and a distance of (y) from its soffit.

$$T_{xy} = T_f [\eta_w (\eta_x + \eta_y - 2\eta_x \eta_y) + \eta_x \eta_y] \quad (8)$$

$$\eta_w = 1 - 0.616 \left(\frac{1550 \sqrt{T} t}{\sqrt{kc\rho}} \right)^{-0.88} \geq 0.0 \quad (9)$$

$$\eta_x = -2.18 + 0.23 \ln \left[\left(\frac{kt}{c\rho a_c} \right)^2 \frac{1}{x^2 (b-x)^2} \right] \geq 0.0 \quad (10)$$

$$\eta_y = \left[0.23 \ln \left(\frac{kt}{c\rho a_c y^2} \right) - 1.09 \right] \geq 0.0 \quad (11)$$

Where T_f is the fire temperature, t is fire duration (hr), b is width of the cross-section (m), η_w is the ratio between the temperature rise of the surface and the fire, η_x is the ratio

between the temperature rise of an interior point x and the surface, η_y is the ratio between the temperature rise of an interior point y and the surface, k is thermal conductivity of concrete = $1.6 \text{ Wm}^{-1}\text{K}^{-1}$, ρ is concrete density = 2400 kg/m^3 , c is the specific heat of concrete = $1000 \text{ Jkg}^{-1}\text{K}^{-1}$, a_c is thermal diffusivity of normal weight concrete = $417 \times 10^{-9} \text{ m}^2/\text{s}$. Wickström[18] showed that the error associated with assuming constant material properties during heating is acceptable for heat transfer analysis.

The dimensionless compartment time factor (Γ) is used to convert any fire type into an equivalent ISO 834 standard fire that was adopted by Wickström [18]. Since the calculation procedures in the current study are developed considering ASTM E119 standard fire during the heating phase, determination of the factor Γ should be carried out. The fire temperature corresponding to the specified fire duration (t) of 1.5 hrs is first calculated according to ASTM E119 curve given in Equation 12.

$$(T_f)_{ASTM} - T_{initial} = 750 [1 - e^{(-3.79553 \sqrt{t})}] + 170.41\sqrt{t} \quad (12)$$

Then, the time (t^*) required for an ISO 834 standard fire to reach the same temperature as the one calculated considering ASTM E119 heating scenario is evaluated from Equation 13.

$$(T_f)_{ISO} - T_{initial} = 345 \log_{10}(480 t^* + 1) \quad (13)$$

The factor Γ is then calculated as the ratio between the equivalent ISO 834 fire duration (t^*) and the actual fire duration (t) considering ASTM E119 fire. By performing the aforementioned procedure, Γ is found to be equal to 0.794 corresponding to fire durations of $t = 1.5$ hrs, $t^* = 1.19$ hrs and fire temperature $(T_f)_{ASTM} = (T_f)_{ISO} = 951.5^\circ\text{C}$.

The temperature at the end of the heating phase (T_{hot}) for each steel bars in both the sagging and hogging moment sections is calculated from Equations 8 through 11 and reported in Table 8-6. Having determined T_{hot} , Equation 8 in Chapter 5 is used to calculate the corresponding maximum temperature reached (T_{max}) considering the complete heating-cooling cycle. The values of the calculated T_{max} for all steel bars are shown in Table 8-6.

Table 8-6: Temperature and residual yield strength in the beams reinforcement

Bar Location	x (mm)	y (mm)	η_x	η_y	η_w	T_{hot} (°C)	T_{max}/T_{hot}	T_{max} (°C)	f_{yR}/f_y	f_{yR} (MPa)
Bottom (Corner)	48	48	0.355	0.508	0.413	399.2	1.319	526.7	0.958	383.1
Bottom (Interior)	100	48	0.154	0.508	0.413	303.4	1.556	472.1	0.984	393.7
Top (Corner)	48	302	0.355	0.000	0.413	169.6	1.000	169.6	0.990	395.9
Top (Interior)	100	302	0.154	0.000	0.413	90.7	2.657	240.9	0.989	395.4

8.2.6 Residual Flexural Capacity of the Fire-Exposed Beams

A procedure to evaluate the residual moment capacity of fire-exposed beams after a complete heating-cooling cycle was proposed in Chapter 5 in view of the stress-block concept. The developed expressions and calculation algorithm is suitable for sections subjected to either sagging or hogging moments. The volume of the equivalent stress-block after exposure to fire can be given according to Equation 14.

$$C_{CR} = \alpha_{1R} f'_{cR} \beta_{1R} c b \quad (14)$$

Where α_{1R} represents the ratio of the average stress in rectangular compression stress block to the concrete compressive strength; β_{1R} is the ratio of rectangular compression stress-block depth to the distance between the extreme compression fiber and the neutral axis; f'_{cR} is the average residual compressive strength of concrete in the compression stress-block; c is the neutral axis depth; and b is the width of the beam cross-section.

The values of the stress-block parameters (α_{1R} and β_{1R}) can be determined from the expressions developed from statistical analysis as shown in Equations 10 and 11 in Chapter 5. These expressions were developed for a range of fire duration, cross-sectional dimensions, steel reinforcement ratio and mechanical properties for positive and negative moment sections. The coefficients used in Equations 10 and 11 are obtained from Table 5-2 in Chapter 5 in terms of the load condition and fire duration at the end of the heating phase. Considering the properties of the beams and the fire exposure conditions in the examined frame system, the values of α_{1R} and β_{1R} are calculated as 0.903 and 0.765 for

the sagging moment section, and determined as 0.676 and 0.987 for the hogging moment section, respectively.

To obtain the residual compressive strength (f'_{CR}), Equation 12 proposed for sagging moment sections and Equations 13 and 14 developed for hogging moment sections in Chapter 5 are adopted. The calculated values of f'_{CR} is determined as 18.6 MPa and 9.4 MPa for the sagging and hogging moment sections, respectively. The reduction in concrete compressive strength is more pronounced when the beam is subjected to negative moment since the compression block becomes in direct exposure to fire from 3 sides as opposed to the positive moment case. Linear interpolation is performed between Equations 13 and 14 for the sagging moment case since the beam width lies between the two ranges for each equation.

The next step is to evaluate the residual maximum strain at the extreme compression fiber (ϵ_{maxR}) from the proposed Equations 1 and 15 in Chapter 5 for the positive moment section and Equation 16 in Chapter 5 for the hogging moment section. When calculating ϵ_{maxR} in the sagging moment section, maximum temperature (T_{max}) in the compression zone can be obtained directly from the obtained Fig. 8-8. The value of the residual strain at peak stress (ϵ_{oR}) can be obtained from the empirical expressions provided by Chang *et al.* (2006) and shown in Equation 15 in terms of concrete compressive strength (f'_c) and the corresponding peak strain (ϵ_o) at ambient conditions.

$$\frac{\epsilon_{oR}}{\epsilon_o} = \begin{cases} 1.0 & , 20^\circ\text{C} < T_{max} \leq 200^\circ\text{C} \\ \left(\frac{-f'_c}{10} + 7.7 \right) \left[\frac{\exp(-5.8 + 0.01T_{max})}{1 + \exp(-5.8 + 0.01T_{max})} - 0.0219 \right] + 1.0 & , T_{max} > 200^\circ\text{C} \end{cases} \quad (15)$$

By performing the calculations, the values of ϵ_{maxR} in both the sagging and hogging moment sections are found to be equal to 0.00489 and 0.0122, respectively. The larger ϵ_{maxR} obtained in the latter case is attributed to the higher temperature near the beam soffit where the compression stress-block in the hogging moment section is located.

The residual yield strength (f_{yR}) of the steel bars is calculated using Equation 2 in Chapter 5 that was proposed in this study considering the experimental studies performed by

Felicetti and Gambarova [13] and Neves *et al.* [2]. The values of f_{yR} for the steel bars in the considered beam sections are calculated and detailed in Table 8-6. Regarding the residual elastic modulus of steel, it is considered not to be affected by the heating-cooling cycle at all temperature levels and can be taken equal to its original value before fire [2, 13, 20]

After obtaining the residual properties of the fire-exposed beam, the residual capacity is calculated in a similar procedure to the stress-block concept described in CSA A23.3-14 for intact sections. Fig. 8-9 illustrates the strain profile, residual stresses and equivalent forces in a typical beam section. Equilibrium condition in the section is applied and the location of the neutral axis (c) is calculated as 56.9 mm and 54.4 mm for both sagging and hogging moment sections, respectively. The residual moment capacity (M_R) is found to be 83.6 kN.m and 81.2 kN.m for the same sections, respectively.

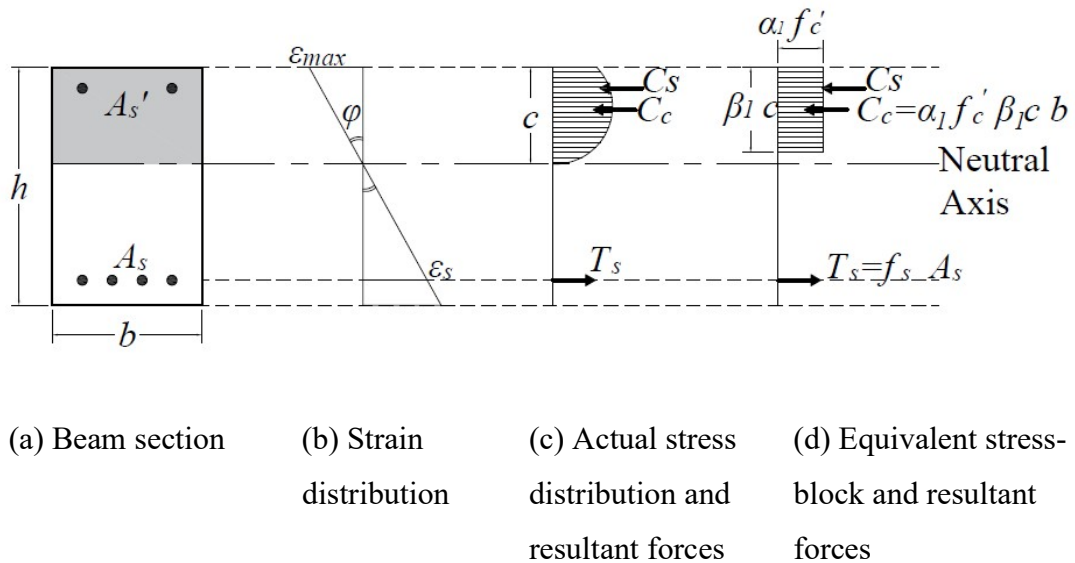


Figure 8-9: Strain profile and residual stress-block definition

8.2.7 Residual Stiffness of the Fire-Exposed Beams

The residual flexural stiffness of fire-exposed beams can be calculated using the expressions proposed in this study and provided in Equation 8 in Chapter 7. The expressions were developed considering the material properties, cross-sectional dimensions, reinforcement ratio, fire duration, initial axial load level and support

conditions for both sagging and hogging moment sections. The calculation procedure commences by calculating the flexural stiffness at ambient condition as the product of concrete elastic modulus (E_c) and the gross moment of inertia (I_g) of the beam section. The concrete elastic modulus can be estimated as $4500\sqrt{f'_c}$ (MPa) for normal weight concrete. The ambient flexural stiffness of the considered beams is calculated and found to be equal to 2.378×10^4 kN.m². The next step is to evaluate the effective residual stiffness after exposure to fire from Equation 8 in Chapter 7. The calculated ratios between $(EI)_R$ and $(EI)_g$ are evaluated for beams B1, B2, B3, B4 and B7 subjected to sagging moment as 0.2175, 0.2185, 0.2175, 0.2185 and 0.2074, respectively. Similarly, these values are obtained as 0.1136, 0.1141, 0.1136, 0.1141 and 0.1083 for the beams subjected to hogging moment, respectively. The effective residual flexural stiffness of the considered beams is calculated and listed in Table 8-4.

8.2.8 Residual Thermal Deformations in Beams

After exposure to fire, residual thermal strains and curvatures are induced in the beams causing residual stresses and deformations. The generated strains are highly dependant on the support conditions and the temperature-load history during the entire heating-cooling cycle. In Chapter 7, regression analysis was performed based on the results of an extensive parametric study that culminated in developing expressions to estimate the residual equivalent strain (ε_i) and curvature (φ_i) defined in section 5 of Chapter 7. The values of ε_i and φ_i for the beams considered in the analysis are calculated and listed in Table 8-7. The restraint conditions are obtained from Table 8-2 and the initial applied loads acting on the beams are obtained from Table 8-4 that were calculated previously.

Table 8-7: Residual thermal strains and curvatures in the considered beams

Beam	$\varepsilon_i(\text{Sag})$	$\varepsilon_i(\text{Hog})$	$\varphi_i(\text{Sag})$	$\varphi_i(\text{HogLeft})$	$\varphi_i(\text{HogRight})$
B1	3.408×10^{-3}	2.041×10^{-3}	6.333×10^{-6}	1.295×10^{-6}	9.197×10^{-7}
B2	3.379×10^{-3}	2.031×10^{-3}	6.333×10^{-6}	9.197×10^{-7}	9.197×10^{-7}
B3	3.408×10^{-3}	2.041×10^{-3}	6.333×10^{-6}	9.197×10^{-7}	1.295×10^{-6}
B4	3.379×10^{-3}	2.032×10^{-3}	6.346×10^{-6}	1.076×10^{-6}	9.948×10^{-7}
B7	3.597×10^{-3}	2.184×10^{-3}	6.317×10^{-6}	1.494×10^{-6}	8.812×10^{-7}

8.2.9 Residual Thermal Deformations in Columns

In a similar manner of estimating the residual thermal strains in beams, a procedure is proposed in Chapters 6 and 7 to evaluate the equivalent residual strains and curvatures in RC columns after exposure to fire from 4 sides and 3 sides, respectively. For the former case, Equation 5 along with Table 7-3 in Chapter 7 are used to calculate the residual thermal strain (ε_i) in columns C2, C3, C6 and C10. The values of ε_i calculated for the aforementioned columns are listed in Table 8-8.

Table 8-8: Residual thermal strains and curvatures in the considered columns

Column	ε_i	φ_i
C1	3.899×10^{-4}	2.73×10^{-6}
C2	6.898×10^{-4}	0.000
C3	6.898×10^{-4}	0.000
C4	3.899×10^{-4}	2.73×10^{-6}
C5	3.913×10^{-4}	2.83×10^{-6}
C6	6.998×10^{-4}	0.000
C9	3.954×10^{-4}	2.91×10^{-6}
C10	7.1378×10^{-4}	0.000

Linear interpolation is performed when substituting in Equation 5 to account for the actual initial load level acting on each column as given in Table 8-3. This step is important as the applied load level and the restraining conditions that exist during the heating-cooling cycle have a significant influence on the residual deformation shape of fire-exposed columns. Resisting the expansion tendency of the columns during fire is found to generate irreversible transient strains that counteract the residual thermal strain. Thus, the column can either expand or contract after fire. This may not be an issue if the column is analyzed separately; however, the anticipated deformed shape is required when analyzing a full frame system.

For columns heated from 3 sides, both residual strains (ε_i) and curvatures (φ_i) are detected after fire. In Chapter 7, a procedure was proposed by performing a statistical analysis considering different columns characteristics, fire durations, restraining conditions and

initial applied load. Equation 16 in Chapter 7 is used to calculate ε_i for columns C1, C4, C5 and C9; whereas, Equation 17 is adopted to evaluate φ_i developed in the same columns. The calculated values are shown in Table 8-8.

8.2.10 Behavior of Jacketed Beams

In the current practice, analysis of jacketed RC beams is performed by neglecting the interfacial slip between the original concrete and the attached layers. Assuming a monolithic behavior may result in higher estimates for stiffness and/or capacity in the composite section. Therefore, a calculation algorithm was developed in Chapters 3 and 4 to account for the potential change in behavior due to slip in both structurally determinate and continuous beams, respectively. The proposed procedure is performed in two main stages. Firstly, a bilinear moment-curvature diagram is obtained for the jacketed section assuming full composite action. This requires the determination of the yield moment, yield curvature, ultimate moment and ultimate curvature of the jacketed section. After that, the proposed monolithic factors given in Equations 15 through 23 are used to adjust the calculated yield and ultimate capacities as well as the corresponding curvatures depending on the surface treatment condition. In this case study, the coefficient of interfacial friction (μ) is taken as 0.4 to account for a partial composite action with untreated surfaces. This case results in the maximum potential reduction in both stiffness and capacity of the jacketed beams.

The jacketing scheme and reinforcement configuration shown in Fig. 8-3 are considered in the analysis. To calculate the yield moment and the corresponding curvature of the composite section, the stress-block parameters (α_1) and (β_1) are derived based on Scott *et al.* [21] model as shown in Equations 16 and 17, respectively.

$$\alpha_1 = \frac{\left(\frac{\varepsilon_c}{\varepsilon_o}\right) - \left(\frac{1}{3}\right)\left(\frac{\varepsilon_c}{\varepsilon_o}\right)^2}{\beta_1} \quad (16)$$

$$\beta_1 = \frac{4 - \left(\frac{\varepsilon_c}{\varepsilon_o}\right)}{6 - \left(\frac{2\varepsilon_c}{\varepsilon_o}\right)} \quad (17)$$

Where ε_c is the concrete strain at the extreme compression fiber and ε_o is the peak strain. These parameters allow the determination of the moment and the corresponding curvature at any ε_c value. When calculating the compression concrete in the core part of the jacketed section, the residual compressive strength (f'_{cR}) obtained from Equations 12 through 14 in Chapter 5 is considered. The error associated with this assumption is minor because the neutral axis at section yield is slightly larger than that at calculated at ultimate. This results in a more conservative assumption since the average f'_{cR} possesses a lower value when calculated over the smaller compression block area where the temperature is maximum. Also, the influence of varying the concrete compressive strength at ambient conditions on the flexural capacity of the beam is relatively insignificant. The residual yield strength of the core reinforcing bars is obtained from Table 8-6 depending on the location of each bar. Table 8-9 shows the outputs involved in the calculation of the yield and ultimate moments and their corresponding curvatures. The flexural stiffness of the jacketed section considering full composite action is calculated from the knowledge of the moment and the corresponding curvature for the different loading cases. The elastic stiffness (EI) are found to be 25,732 kN.m² and 18,184 kN.m² for the sagging and hogging moment sections, respectively.

Table 8-9: Calculation of yield and ultimate moment capacities of the beams

Case	Concrete				Core Secondary Steel		Core Main Steel		Jacket Steel		Φ (rad/km)	M_n (kN.m)	
	ε_c $\times 10^{-3}$	C (mm)	α_1	β_1	C_c (kN)	ε_s' $\times 10^{-3}$	C_s' (kN)	ε_s $\times 10^{-3}$	T_s (kN)	ε_{sJ} $\times 10^{-3}$			T_{sJ} (kN)
Sagging (Yield)	0.88	123.7	0.54	0.70	541.3	0.54	21.5	1.27	202.8	2.00	360	7.1	182.7
Sagging (Ultimate)	3.50	72.8	0.81	0.90	618.7	1.19	47.7	11.0	306.5	11.60	360	48.1	215.8
Hogging (Yield)	0.61	93.5	0.40	0.69	401.2	-0.35	-28.3	2.0	316.3	0.314	56.6	6.5	118.2
Hogging (Ultimate)	2.44	9.6	0.93	0.78	109.6	-35.5	-153	99.6	316.3	-8.99	-360	253.9	118.2

The monolithic factors α_y^{+ve} , α_y^{-ve} and α_u^{-v} are calculated according to the procedure described in section 13 of Chapter 4 and found to be equal to 1.024, 1.013 and 1.014, respectively. The initial load level required to perform the procedure is obtained from Table 8-4 for the different sections. The elastic stiffness is adjusted based on the obtained

monolithic factors to account for interfacial slip and found to be equal to 25,129 kN.m² and 17,603 kN.m² for the sagging and hogging moment sections, respectively.

8.3 Global Structural Behavior of the Considered Frame

To evaluate the deformation behavior and straining actions developed within the members, the frame is modelled and analyzed using SAP2000 finite element software. The analysis is performed considering both the undamaged, fire-exposed and repaired conditions. A discussion related to the structural behavior of the considered frame in view of the two aforementioned fire scenarios is presented in this section.

8.3.1 Fire Scenario 1

The first fire scenario represents the case of fire propagation in the first floor. The side columns C1 and C4 are exposed to fire from three sides; whereas, the interior columns C2 and C3 are exposed to fire from all four sides. Beams B1, B2 and B3 are exposed to elevated temperature from their soffit and two vertical sides. The residual properties of the fire-exposed members are evaluated in the previous section. The influence of residual thermal strain and curvature on the post-fire strength and capacity of the different structural elements was considered in the proposed calculation algorithm in terms of the temperature-load history and support conditions. If the members are to be analyzed individually, then the residual deformations will cause them to either expand or contract. However, if the members are considered to be part of the entire frame system, then these deformations cause secondary stresses in the other frame elements and should be accounted for. In SAP2000, the calculated residual strain (ε_i) can be considered as an applied temperature load (ΔT) given in terms of the coefficient of thermal expansion of concrete as shown in Equation 18. Similarly, the residual curvature (φ_i) is considered as a linear temperature gradient acting along the thickness as given in Equation 19.

$$\Delta T = \frac{\varepsilon_i}{\alpha} \quad (18)$$

$$\frac{\Delta T}{h} = \frac{\varphi_i}{\alpha} \quad (19)$$

The appropriate temperature loads are applied on the beam elements by first identifying the sagging and hogging moment regions as indicated in Table 8-7. The columns heated from 4 sides are subjected to a uniform temperature load corresponding to ε_i , while the columns exposed to fire from 3 sides are subjected to both uniform and gradient temperature loads corresponding to both ε_i and φ_i as indicated in Table 8-8, respectively.

The deformation shape and straining actions developed in the fire-exposed frame according to the first fire scenario are obtained using SAP2000 as shown in Fig. 8-10.

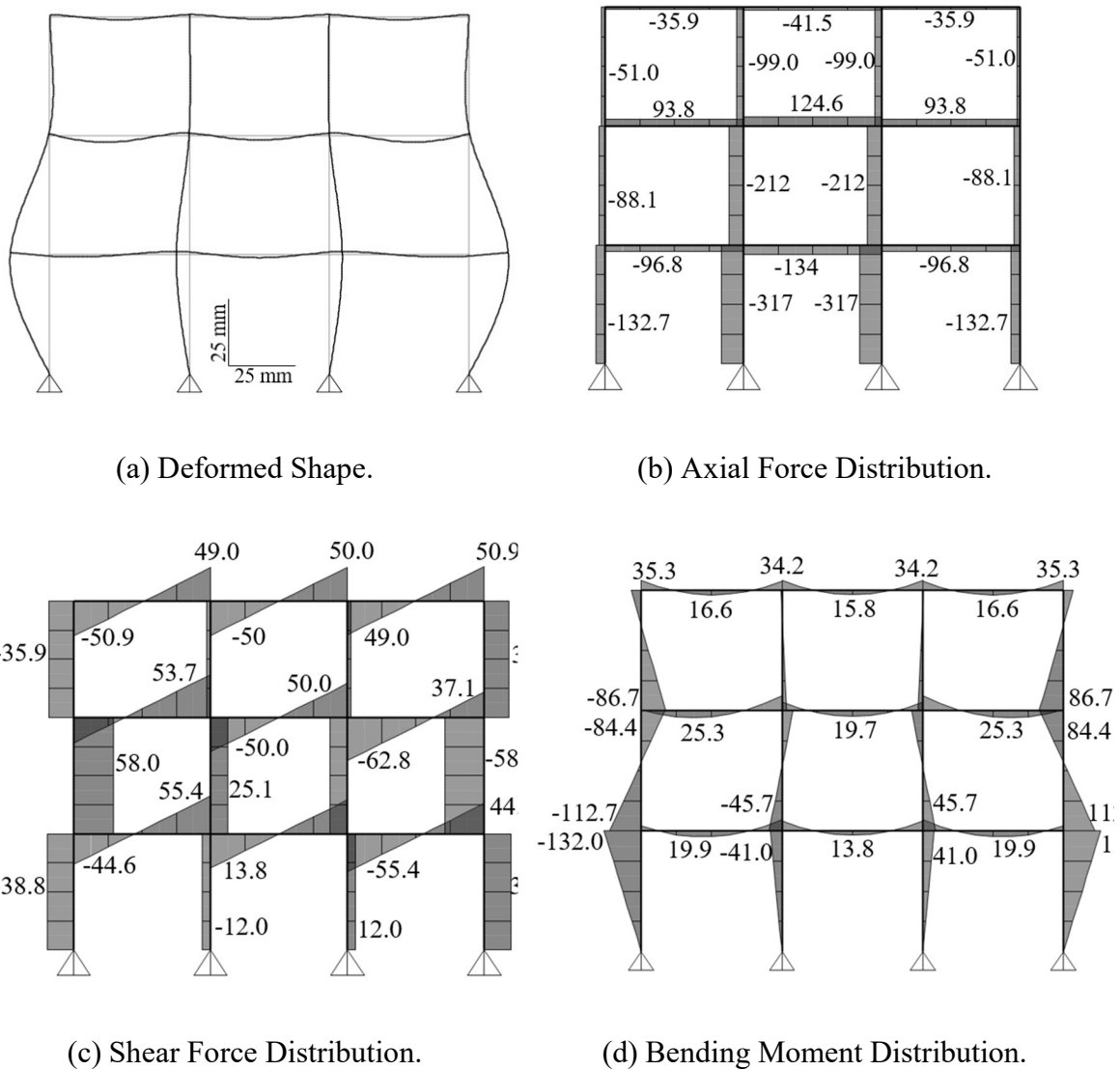


Figure 8-10: Deformation shape and straining actions in the fire-exposed frame (scenario 1)

Comparing these results with their counterparts in the intact frame shown in Fig. 8-7 reveals the significant change in deflected shape and forces redistribution. These variations are attributed to the deterioration in the residual properties of the affected structural members and the development of secondary stresses generated from the temperature loads acting on the fire-exposed beams and columns. The amount of the secondary stresses and deformations are governed by the axial and rotational restraints provided by the frame. The capability of the fire-exposed frame in resisting the developed straining actions is assessed in view of the residual capacity of each member as determined in the previous section. For this fire scenario and loading conditions, all members are found to pass the check.

After fire, the fire-exposed members are repaired using concrete jackets according to the configuration schemes shown in Fig. 8-3. The stiffness of the jacketed beams considering interfacial slip between the new and original concrete layers is implemented in the model. Regarding the columns, full composite action is considered as they are jacketed from 4 sides and subjected mainly to axial loads. The repair procedure is assumed to relieve the structure by reducing the secondary deformations before applying the jacketing material. Fig. 8-11 illustrates the changes in both the deflected shape and force distribution caused by repairing the affected members. The results show that the deformations are greatly reduced as the stiffness of the repaired structural members exceeds the original values of the intact members.

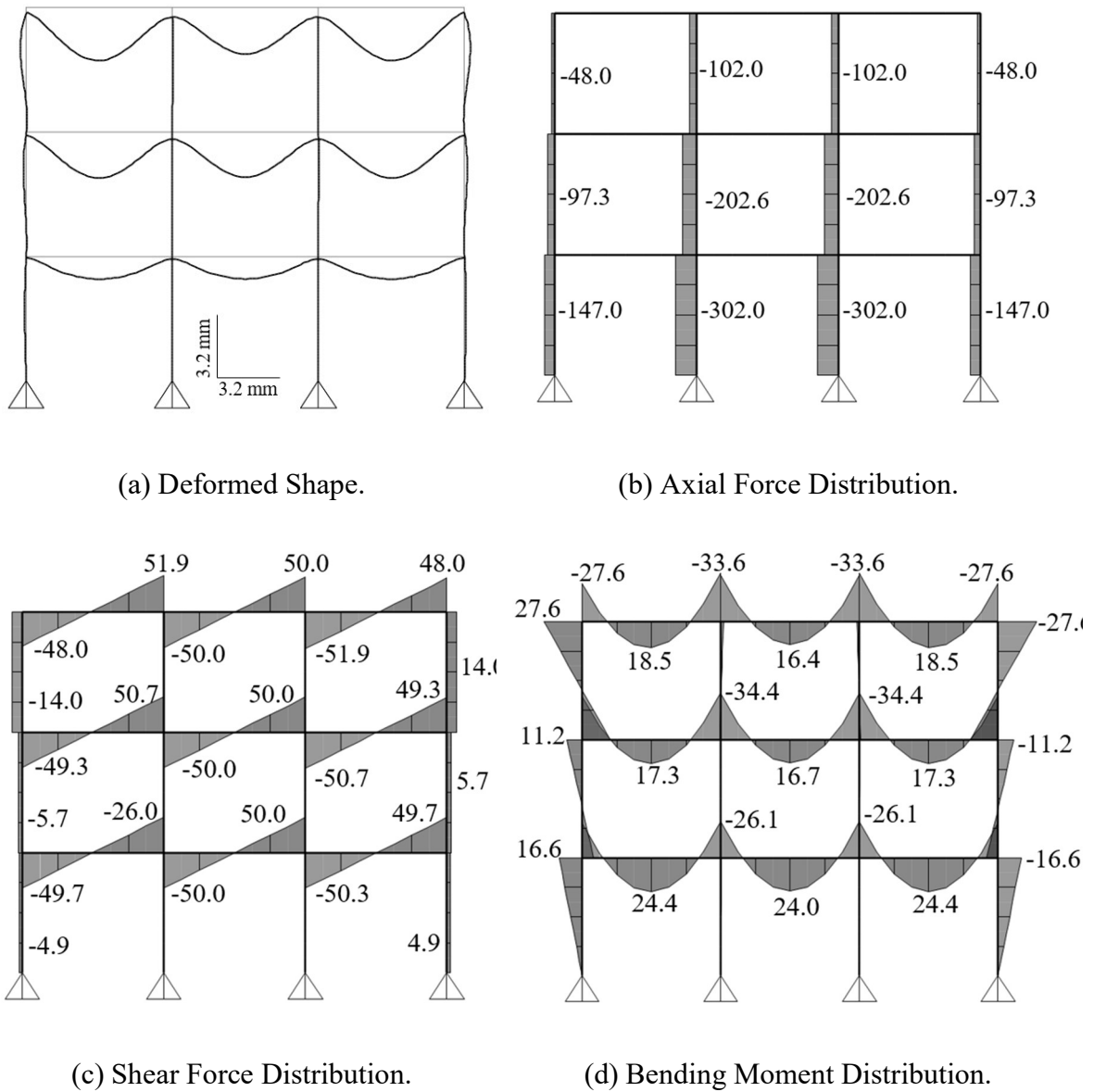


Figure 8-11: Deformation shape and straining actions in the jacketed frame (scenario 1)

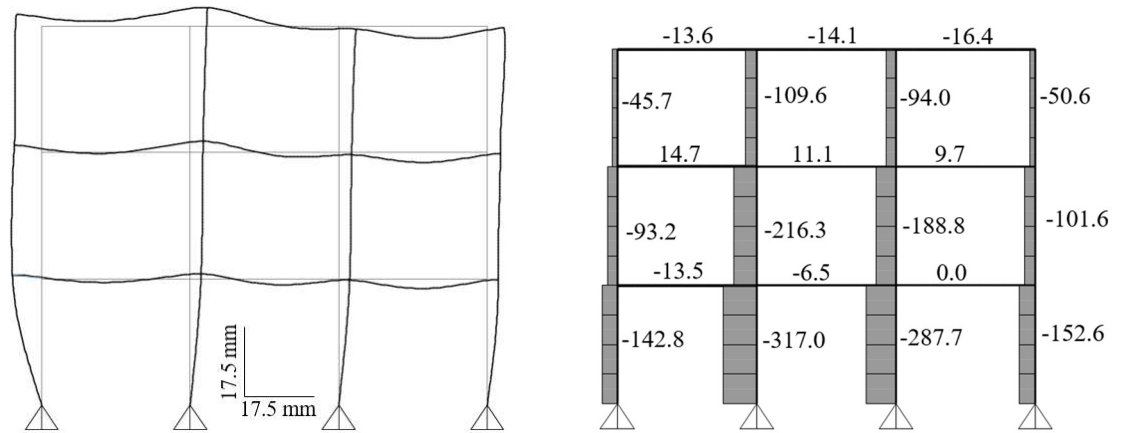
8.3.2 Fire Scenario 2

The first second fire scenario simulates a situation where fire is developed and propagated along the vertical direction from one side of a building. In this scenario, columns C1, C5 and C9 are exposed to fire from three sides; whereas, the interior columns C2, C6 and C10 are exposed to fire from all four sides. Beams B1, B4 and B7

are considered to be exposed to fire from 3 sides even in the case where the upper side of the beam is in the vicinity of fire. This is justified by assuming that perfect insulation is provided by the floor cover which significantly decreases the heat transferred by radiation to the concrete beam. Also, heat transfer by convection is minimized due to the upward movement of the hot gases that have lower density than the cooler air [21]. The effective residual stiffness of the fire-exposed members is considered in the model as an input. The temperature loads representing the residual thermal strains and curvatures are applied to the affected members in a similar manner to fire scenario 1.

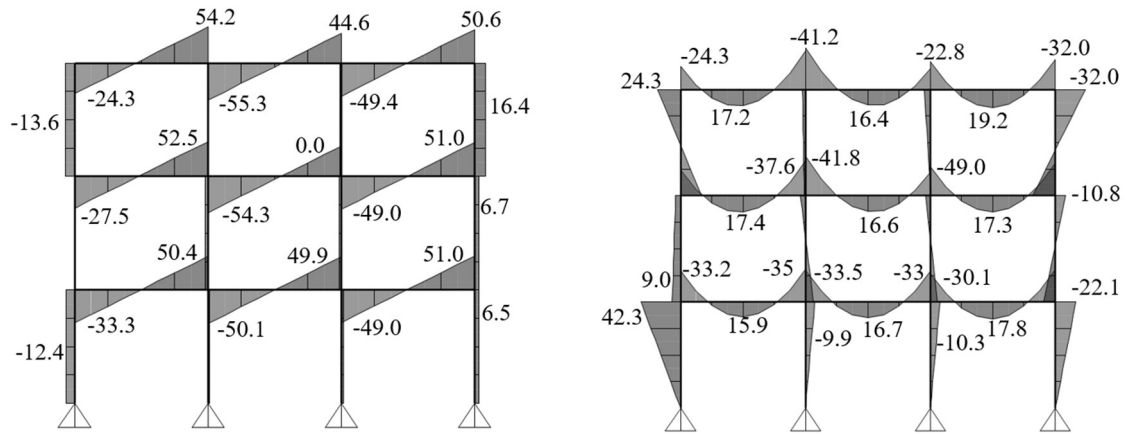
The deformation behavior of the fire-exposed frame is shown in Fig. 8-12(a), while the axial force, shear force and bending moment distributions are shown in Figs. 8-12(b), 8-12(c) and 8-12(d), respectively. The affected members are shown to experience larger displacements and rotations than their intact counterparts. This is attributed to both the permanent residual portion of thermal expansion that generated during fire and the drop in stiffness associated with material deterioration and residual strains. Shear forces become is more pronounced in the fire-exposed frame than the intact case due to the restraining forces generated at the beam-column joints. Similarly, the bending moment is also increase due to balance the secondary stresses caused by the equivalent temperature loads.

Jacketing the deteriorated members is found to have a remarkable improvement on the deformation and load distribution as shown in Fig. 8-13. The vertical displacements are reduced in the first bay that was exposed to elevated temperatures. This is attributed to the significant increase in the stiffness of both beams and columns affected by fire. Shear forces and moments in the columns are significantly reduced due to the reduction in the residual stresses after the application of the concrete jackets.



(a) Deformed Shape.

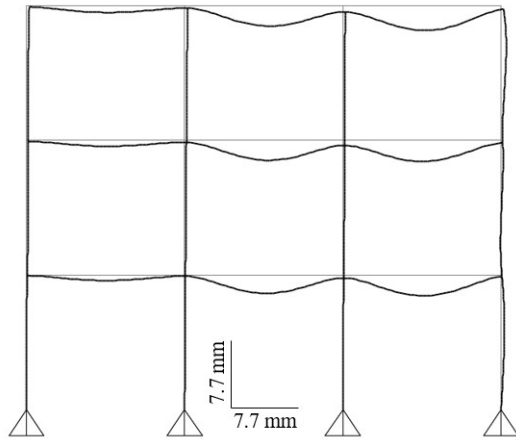
(b) Axial Force Distribution.



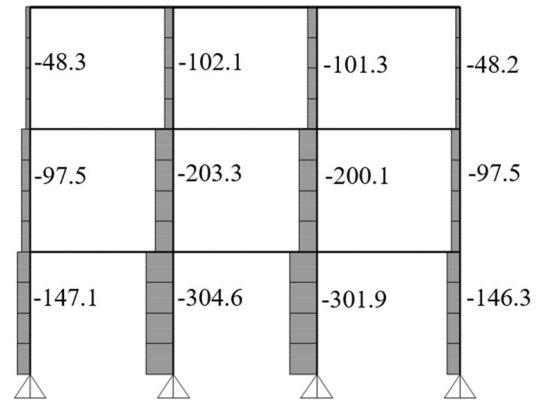
(c) Shear Force Distribution.

(d) Bending Moment Distribution.

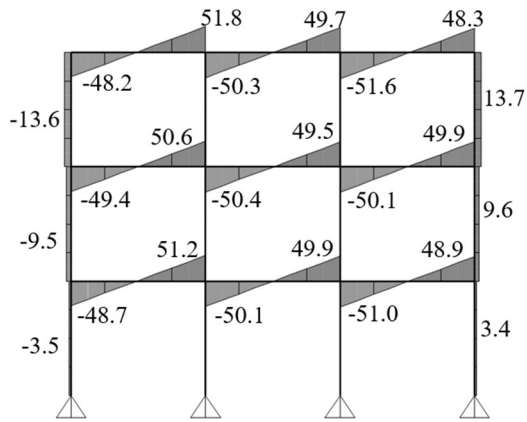
Figure 8-12: Deformation shape and straining actions in the fire-exposed frame (scenario 2)



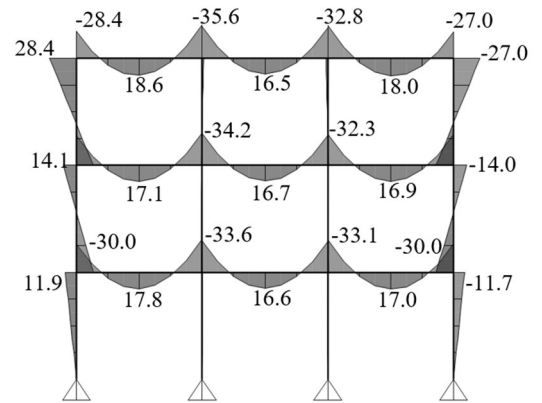
(a) Deformed Shape.



(b) Axial Force Distribution.



(c) Shear Force Distribution.



(d) Bending Moment Distribution.

Figure 8-13: Deformation shape and straining actions in the jacketed frame (scenario 2)

8.4 Summary and Conclusions

The residual behavior of a typical fire-exposed RC frame is investigated in this chapter considering two commonly encountered fire scenarios. The analysis is performed according to the calculation procedures proposed and validated in the current study. The fire-exposed members are isolated from the frame and their residual stiffness, capacity and thermal strains are evaluated. The main factors affecting their residual behavior are the mechanical properties, geometrical characteristics, reinforcement ratio, fire exposure scenarios, support conditions and temperature-load interaction during the entire heating cooling cycle. The effective residual stiffness is considered as an input in the structural analysis model to account for the deterioration of the fire-exposed members. The residual thermal strains and curvatures are considered as temperature loads acting on the heated members. The deformation shape and straining actions developed in the frame system are obtained by performing the structural analysis using any commercially available software like SAP2000. The capability of the fire-exposed members to resist the applied loads is determined in view of the corresponding residual capacity. The local and global behavior of the repaired frame is then assessed considering interfacial slip in the jacketed beams. The analysis approach described in the case study can be extended for any other frame system provided that it satisfies the range of parameters considered in the statistical studies discussed in Chapters 3 through 7.

8.5 References

- [1] Khoury, G. "Effect of Fire on Concrete and Concrete Structures," *Progress in Structural Engineering and Materials*, 2000, Vol. 2, No. 4, pp. 429-447.
- [2] Neves, I. Rodrigues and J. Loureiro, A. "Mechanical properties of reinforcing and prestressing steels after heating," *Journal of Materials in Civil Engineering*, 1996, Vol. 8, No. 4, pp. 189-194.
- [3] Monks, W.L. "Tests to determine the bond strength between gunite and dense concrete," London, Cement and Concrete Association, Jan 1968, DN 2020.
- [4] Schneider, U. "Concrete at High Temperatures - A General Review," *Fire Safety Journal*, 1988, Vol. 13, No. 1, pp. 55-68.
- [5] Hertz, K.D. "Concrete Strength for Fire Safety Design," *Magazine of Concrete Research*, 2005, Vol. 57, No. 8, pp. 445-453.
- [6] Franssen, J.M. and Kodur, V. "Residual Load Bearing Capacity of Structures Exposed to Fire," *Proceedings of the 2001 Structures Congress and Exposition*, Washington, 2004, Vol. 109, pp. 1-12.
- [7] El-Fitiany, S. and Youssef, M. "Assessing the Flexural and Axial Behavior of Reinforced Concrete Members at Elevated Temperatures Using Sectional Analysis," *Fire Safety Journal*, 2009, Vol. 44, No. 5, pp. 691-703.
- [8] Tsai, W.T. "Uniaxial Compressional Stress-Strain Relation of Concrete," *Journal of Structural Engineering*, 1988, Vol. 114, No. 9, pp. 2133-2136.
- [9] Terro, M.J. "Numerical modeling of the behavior of concrete structures in fire," *ACI Structural Journal*, 1998, Vol. 95, No. 2, pp. 183-193.

- [10] Chang, Y.F., Chen, Y.H., Sheu, M.S. and Yao, G.C. "Residual Stress-Strain Relationship for Concrete after Exposure to High Temperatures," *Cement and Concrete Research*, 2006, Vol. 36, No. 10, pp. 1999-2005.
- [11] Karthik, M., Mander, J. "Stress-block parameters for unconfined and confined concrete based on a unified stress-strain model," *Journal of Structural Engineering*, 2011, Vol. 137, No. 2, pp. 270-273.
- [12] Lie, T.T. "Structural Steel and Fire: More Realistic Analysis," National Research Council, 1976, Ottawa, Canada.
- [13] Felicetti, R., Gambarova, P. and Meda, A. "Residual behavior of steel rebars and R/C sections after a fire." *Construction and Building Materials*, 2009, Vol. 23, No. 12, pp. 3546-3555.
- [14] Qiang, X., Bijlaard, F. and Kolstein, H. "Post-Fire Mechanical Properties of High Strength Structural Steels S460 and S690," *Engineering Structures*, Elsevier, 2012, Vol. 35, pp. 1-10.
- [15] Eurocode2. "Design of concrete structures- part 1.1: general rules and rules for buildings," European Committee for Standardization (CEN), 2004, Brussels, Belgium.
- [16] Ersoy, U., Tankut, T. and Suleiman, R. "Behavior of Jacketed Columns," *ACI Structural Journal*, 1993, Vol. 90, No. 3, pp. 288-293.
- [17] Gao, W.Y., Dai, J.G. and Teng, J.G. "Simple Method for Predicting Temperatures in Reinforced Concrete Beams Exposed to a Standard Fire," *Advances in Structural Engineering*, Vol. 17, No. 4, pp. 573-589.
- [18] Wickström, U. "A Very Simple Method for Estimating Temperature in Fire Exposed Concrete Structures," *Proceeding of New Technology to Reduce Fire Losses and Costs*, Elsevier, 1986, New York, NY.

- [19] Abbasi, A., Hogg, P.J. "A Model for Predicting the Properties of the Constituents of a Glass Fibre Rebar Reinforced Concrete Beam at Elevated Temperatures Simulating a Fire Test," *Composites Part B: Engineering*, 2004, Vol. 3, No. 5, pp. 384-393.
- [20] Malhotra, H.L., "Design of Fire-Resisting Structures," Bishopbriggs and Glasgow, Surrey University Press, 1982, 226 pp.
- [21] Scott, B., Park, R. and Priestley, M. "Stress-strain behavior of concrete confined by overlapping hoops at low and high strain rates." *ACI Structural Journal*, 1982, Vol. 79, No. 1, pp. 13-27.
- [22] Flint, G., Usmani, A., Lamont, S., Lane, B. and Torero, J. "Fire Induced Collapse of Tall Buildings," *Proceedings of the fourth International Workshop on Structures in Fire*. 2006, Aveiro, pp. 415-426.

Chapter 9

9 SUMMARY AND CONCLUSIONS

The current research work has presented a simple, practical and rational approach to evaluate the local and global behavior of fire-exposed RC members before and after repair with concrete jackets. This procedure is a milestone towards developing an objective-based approach convenient in both the research and office design levels. The behavior of the frame is analyzed considering various heating and loading conditions. The thermal and transient strains are considered explicitly in the models to account for the residual deformation after fire. The interfacial slip between the original sections and the added jackets are also considered in the analysis by developing a calculation approach. The following sections summarize the work performed in each chapter and the recommended future work.

9.1 Background and Literature Review

The dissertation commenced by presenting a literature review about fire safety procedures adopted in Canada, the concept of standard fire and the thermal analysis procedure adopted in the analytical model. A summary of the residual mechanical properties and stress-strain relationship of both concrete and reinforcing steel bars was then presented. Finally, the influence of repairing RC members with concrete jackets before and after exposure to fire was discussed.

9.2 Analysis of Reinforced Concrete Beams Strengthened using Concrete Jackets

An investigation of the influence of RC jackets on the flexural behavior of both determinate and continuous RC beams was discussed. Geometrical properties and mechanical characteristics of the RC members are considered. The influence of surface treatment and interfacial behavior is examined in view of relevant material models found

in literature. Sectional analysis procedure is performed to account for the variations in aforementioned factors in determining the overall behavior of the structural members. A parametric study is conducted in view of the validated model and showed that slip can affect the behavior of jacketed members to some extent depending on the considered parameters. For the beams considered in the analysis, ductile failure mode characterized by yielding of tension steel bars followed by concrete crushing at the extreme compression fiber was observed. The influence of the examined parameters on the deformation behavior of the jacketed beams was almost identical in both sagging and hogging moment regions. A method is proposed to evaluate the complete load-deformation curve considering slip effect.

9.3 Simplified Approach to Assess the Capacity of Fire-Damaged Reinforced Concrete Beams

Maximum temperature distribution along a typical beam section and the post-fire flexural capacity of RC beams were investigated in Chapter 5. The analysis procedure commences by performing thermal analysis to evaluate heat distribution within the cross-section followed by sectional analysis taking into consideration the residual mechanical properties and constitutive relationships of both concrete and steel. An extensive parametric study was performed considering the validated model and culminated in proposing different expressions to evaluate the residual flexural capacity of beams using the concept of stress-block parameters. In addition, a method for evaluating the maximum temperature distribution within the cross-section and at specific locations was proposed and validated. The simplified approach is convenient for engineers to easily and quickly calculate the expected residual capacity of beams within a structure after exposure to fire.

9.4 Residual Axial Behavior of Restrained Reinforced Concrete Columns Damaged by a Standard Fire

Both thermal and sectional analyses were carried out to evaluate the post-fire behavior of fire-exposed rectangular and circular columns in RC frame structures. Consideration of

load-temperature history acting on the members were explicitly accounted for. An analytical model was developed using MATLAB programming language to track the full behavior of axially loaded columns after fire. The study revealed that fire duration and cross-sectional dimensions are main factors that govern the residual behavior of columns. The interaction between temperature and load were shown to be of great importance in the analysis as they affect the restraining forces and consequently the residual transient strain component.

9.5 Residual Behavior of Reinforced Concrete Members Exposed to Fire from Three Sides

Exposure to fire from three sides causes non-uniform temperature distribution within the cross-section and consequently imposes residual thermal curvatures after fire. This Chapter was a continuation of Chapter 6 since the same analytical model was used with some modifications to account for curvatures and bending stresses. A parametric investigation was performed on different specimens with various mechanical properties, cross-sectional dimensions, support conditions and initial load levels. Statistical analysis was then performed on the obtained results to propose and validate regression equations that can be used to estimate the residual capacity, stiffness and thermal deformations in fire-exposed columns.

9.6 Structural Performance of Jacketed Fire-Exposed Reinforced Concrete Members in Frame Structures Considering Slip Influence

The post-fire performance of typical RC frames is discussed in view of a case study that encompasses two fire scenarios. The analysis is performed according to the calculation procedures proposed and validated in Chapters 3 through 8. Residual stiffness is calculated for the fire-exposed members and applied as inputs in the finite element model. Residual thermal deformations are converted into temperature loads that are applied on the frame. Load redistribution associated with the variation in both stiffness

and applied temperature loads was evaluated using the SAP2000. The residual capacity of each member was calculated using the proposed calculation approach. The capability of each member to withstand the fire event taking into account the mutual interaction with other members was assessed. Deformation shape and straining actions in the entire frame was determined considering intact, fire-exposed and repaired members.

9.7 Recommendations for Future Work

The assigned objectives of this study were achieved. However, further experimental and analytical work is needed to:

- 1) Extend the proposed approach to consider the effect of fire on the residual behavior of prestressed concrete members.
- 2) Further validate the use of the proposed model by experimentally examining the structural behavior of jacketed fire-damaged members.
- 3) Investigate the behavior of fire-exposed frame systems under various static and dynamic loading conditions.
- 4) Predict the shear capacity of fire-exposed RC members.
- 5) Determine the influence of initially applied eccentric loads on the residual capacity and stiffness of the fire-exposed members.

Curriculum Vitae

Name: Mohammed Monir Ajan Alhadid

Post-secondary Education and Degrees: United Arab Emirates University
Al Ain, Abu Dhabi, United Arab Emirates
2004-2009 B.Sc.

United Arab Emirates University
Al Ain, Abu Dhabi, United Arab Emirates
2009-2011 M.Sc.

Western University
London, Ontario, Canada
2012-2016 Ph.D.

Honours and Awards: Mitacs Accelerate Fellowship
2016

Related Work Experience Teaching Assistant
United Arab Emirates University
2009-2011

Teaching Assistant
Western University
2012-2016

Publications:

- Alhadid, M. and Youssef, M. (2016). Analysis of Reinforced Concrete Beams Strengthened Using Concrete Jackets. *Engineering Structures*, 132, 172-187.
- Alhadid, M. and Youssef, M. (2016). Residual Axial Behavior of Fire-Damaged Reinforced Concrete Columns. *Proceedings of the 5th International Structural Specialty Conference on Resilient Infrastructure*, CSCE, STR-898, 1-4 June, London, ON, Canada.
- Alhadid, M. and Youssef, M. (2015). Strengthening and Repair of Reinforced Concrete Beams Using Concrete Jackets. *Proceedings of the Michigan State University Conference on Strengthening of Structures under Extreme Loading*, PROTECT 2015, 28-30 June, East Lansing, Michigan, USA.
- Alhadid, M. and Youssef, M. (2013). Structural Behavior of Jacketed Fire-Damaged Reinforced Concrete Members: A Review. *Proceedings of the 3rd Specialty Conference on Disaster Prevention and Mitigation*, CSCE, DIS-023, 29 May - 1 June, Montréal, Québec, Canada.